UNIVERSIDADE DE SÃO PAULO

Instituto de Química

Graduate Program in Chemistry

Mariana Pires Figueiredo

Iron-based Layered Double Hydroxides aiming biomaterials: structure, composition, and polymer composites

Revised version of the thesis. The original version is available in the Graduate Program Office (GPO) at the Institute of Chemistry

São Paulo

Deposited at the GPO:
October 15th 2021

Mariana Pires Figueiredo

Hidróxidos Duplos Lamelares à base de Ferro como biomateriais: estrutura, composição e compósitos poliméricos

Thesis presented to the *Instituto de Química*
of the *Universidade de São Paulo* to the obtainment
of the Doctor of Chemistry degree

Supervisor: *Profa. Dra. Vera Regina Leopoldo Constantino*

São Paulo

2021

Ficha Catalográfica elaborada eletronicamente pelo autor, utilizando o programa desenvolvido pela Seção Técnica de Informática do ICMC/USP e adaptado para a Divisão de Biblioteca e Documentação do Conjunto das Químicas da USP

Bibliotecária responsável pela orientação de catalogação da publicação: Marlene Aparecida Vieira - CRB - 8/5562

P667i Pires Figueiredo, Mariana Iron-based layered double hydroxides aiming biomaterials: structure, composition, and polymer composites / Mariana Pires Figueiredo. - São Paulo, 2021.
300 p.

Tese (doutorado) - Instituto de Química da Universidade de São Paulo. Departamento de Química Fundamental.
Orientador: Constantino, Vera Regina Leopoldo

1. Biomateriais. 2. Materiais híbridos orgânico inorgânicos. 3. Compósitos poliméricos. 4. Liberação modificada de espécies bioativas. 5. Regeneração tecidual. I. T. II. Constantino, Vera Regina Leopoldo, orientador.

“Iron-based Layered Double Hydroxides aiming biomaterials: structure, composition, and polymer composites”

"Hidróxidos Duplos Lamelares à base de ferro como biomateriais: estrutura, composição e compósitos poliméricos"

MARIANA PIRES FIGUEIREDO

Tese de Doutorado submetida ao Instituto de Química da Universidade de São Paulo como parte dos requisitos necessários à obtenção do grau de Doutora em Ciências - no Programa de Química.

Profa. Dra. Vera Regina Leopoldo Constantino

(Orientadora e Presidente)

APROVADA POR:

Prof. Dr. Flavio Maron Vichi
IQ - USP

Prof. Dr. Jairo Tronto
UFV

Prof. Dr. Ruben Dario Sinisterra Millan
UFMG

SÃO PAULO

18 de agosto de 2021

Dedico esta tese à minha amada mãe, Ana Maria Fernandes Pires Figueiredo

Acknowledgements
Agradecimentos

I would like to thank to
Agradeço à/ao

Vera Regina Leopoldo Constantino, por ter feito com que eu me apaixonasse pela química inorgânica; por ser minha referência em didática e comprometimento com o ensino. Obrigada por representar tanto em minhas bases químicas e por ter me ensinado tanto; por ter me aceito como sua orientanda e por ter me depositado confiança ao longo de todos esses anos.

André Eduardo Zaidan, por ter me apresentado à universidade pública e à ciência e por ter me mostrado que era possível alcançá-las, auxiliando-me academicamente e emocionalmente ao longo desta jornada. Por me inspirar com seu profundo interesse pelo conhecimento, com seu pensamento crítico, e por suas ações serem fiéis aos seus ideais e pensamentos. Espero conseguir traduzir com simplicidade, porém com fidelidade e formalismo, a grandiosidade da química, assim como você faz com a física e com a matemática.

Ana Maria Fernandes Pires Figueiredo, por me inspirar com tamanha bondade; por todos os anos de seu esforço para que eu pudesse estudar e para que eu tivesse oportunidades; por você ter me dito uma certa vez "não importa qual o seu sonho ou quão difícil ele possa ser, eu vou te apoiar". Seu apoio me possibilitou tantas coisas, dentre elas esta tese, à qual dedico a você.

José Roberto Nubié Figueiredo por me incentivar a me aventurar nas ciências exatas, por me introduzir à química, por ter estudado comigo; por ter estado comigo em tantos exames que prestei, me incentivando nos momentos de frustração e vibrando comigo nos momentos de conquistas.

Roberta Pires Figueiredo de Mendonça por ter me ajudado a permanecer no ensino superior, me amparando material e emocionalmente. Serei sempre para você, e para a linda família que construiu, como as águas do mar, que mesmo que se recolham, sempre retornam à praia. Não importa de qual oceano estaremos mais perto no futuro, as águas sempre nos conectarão.

Luísa Figueiredo de Mendonça, por fazer crescer amor aonde quer que o seu sorriso chegue e por me motivar a lutar pela carreira científica e poder contribuir, mesmo que um pouquinho, para que sua geração tenha acesso a mais tecnologias e qualidade de vida.

Renata Figueiredo Pilon por ter me ajudado a tomar a decisão de mudar os rumos da minha educação, em direção às desafiadoras Universidades Públicas e aos anos de intenso estudo e dedicação. Por estar sempre ao meu lado, vibrando e vivenciando comigo. Por ser minha segunda mãe.

Rafael Medeiros de Mendonça, Iesa Nubié Figueiredo, Renato Pilon, Maria Aparecida Gazotti Vallim, Bruno Figueiredo Pilon e Cristiana Heideier Pilon por terem vibrado comigo tantas vezes ao longo dessa jornada.

Aparecida Ignácio Patzina, Renê Eduardo Zaidan e Daniel Érick Zaidan por me acolherem e por dividirem comigo tantos momentos felizes; por me incentivarem a galgar a entrada na USP e por serem suporte emocional e material ao longo de todos esses anos.

Caroline Silva de Matos, por ter feito meus olhos brilharem pelos materiais lamelares numa conversa ao acaso no metrô de SP, o que determinou meus rumos científicos; por me inspirar com seu tamanho interesse pela educação e pela ciência; por contribuir para que o meio acadêmico seja mais humano e justo; por ser essa pessoa sem igual; por ser suporte, estar sempre presente e por compartilhar comigo uma linda e atemporal amizade. A você e ao Felipe Teixeira Maragni por serem os melhores pais acadêmicos.

Victor Vendruscolo, meu grande amigo, por ser paciente com minhas séries de HDLs de ferro e por me ajudar na obtenção de espectros desde a iniciação científica; por fazer parte desta tese cientificamente e também afetivamente; por ser um parceiro científico sem igual. Sua genialidade química me inspira.

Vagner R. Magri pela amizade, por me inspirar com tamanha responsabilidade no laboratório e na condução dos experimentos e com seu interesse em aprofundar o quão mais possível o conhecimento científico.

Denise Eulálio pela amizade, por não medir esforços para amparar quem quer que seja que careça de ajuda ao seu redor; por me inspirar com sua garra, dedicação, disposição e comprometimento científico.

Vanessa Sakai, por ter me presenteado com sua amizade leve e divertida e por ter me agraciado com palavras sábias nas mais oportunas situações.

Rafael Macedo pelas diversas situações em que me ajudou e de maneira despretensiosa; por me inspirar com tamanha maturidade científica e por contribuir com a manutenção do senso crítico na ciência.

Alfredo Duarte pelo registro de imagens lindas e únicas dos HDLs e por me motivar com seu profundo interesse pela relação entre a composição, a estrutura e as propriedades dos materiais.

Lucas Urbano, Bruna Mayumi Usuginu e Ana Carolina Cruz da Silva, bem como todos os atuais estudantes e os que passaram pelo LaSoL e ajudaram a escrever sua história como um ambiente regado à amizade e parceria.

Ana Paula Curcio, por ser meu maior exemplo de resiliência nos estudos e na ciência; por me inspirar com sua busca contínua pelo conhecimento; por ter me presenteado com uma amizade atemporal, regada de carinho, cuidados, suporte e muita alegria; por ser para mim família.

Juliana Gallego pela amizade, por estar ao meu lado ao longo dessa jornada, me motivando com seu entusiasmo em aprender e cada vez mais desenvolver habilidades.

Professor Ivan Hong Jun Koh, Ana Maria C. R. P. F. Martins e Rodrigo B. Souza pela valiosa colaboração e por propiciarem uma convivência agradável e alegre.

Professora Helena Petrili e Eduardo Diaz Suarez pela valiosa colaboração e pelas alegres reuniões.

Professor Jocelyne Brendlé for accepting me in the IS2M, for being my supervisor, and for have been so supportive. Your learnership and positivity inspire me.

Professor Lionel for receiving me at IS2M and for the academic support.

Faicka Houssen for make me happy going to the IS2M office even during European summer and for the friendship.

All technicians, students, and stuff of IS2M.

Professor Guy Schlatter for having been so participative in each step of the development of my project at ICPEES and for having taught me so much from the design of functional materials to polymeric materials' characterization. It was a great pleasure working with you.

Professor Anne Hébraud, for welcoming me at ICPEES, for the great contribution in the development of my internship project, and for inspiring me reinforcing our space as women scientists.

Géraldine Layrac, for the partnership, for have worked side-by-side with me, and for have supported me daily at ICPEES.

Saeel Momin for being such a great friend and for the patience with my *frenchenglish*. Please, don't be mad at me because I asked you to go to work with me on French Labor Day. I cannot say sorry, otherwise the drug release curves shown in Chapter 6 would not be so nice, but I am very grateful to you!

Chayma Mahmoudi for all the support during my days at Strasbourg when you inspired me with compassion and friendship.

All technicians, students, and stuff of ICPEES.

Professor César Viseras for integrating me in your research group; for have always considered and encouraged my ideas; for being a practical and supportive supervisor, especially during the beginning of the pandemic when you have propitiated me valuables collaborations and alternatives to conduct the research despite all difficulties.

Brenda Lini for the friendship and partnership; for inspiring me with your critical thinking, as well as with your responsibility performing the experiments. The Chapter 8 of this thesis only exists because of you.

Fátima García-Villén for being absolutely compromised in any task you do, and Ana Borrego-Sánchez for always look for best data acquisition and results interpretation; both of you for being kind and support students work at the lab, finding the best solutions for the more variable problems.

Professor Ignacio Sainz-Diaz, a very kind person who I had the pleasure to collaborate and learn so more much with.

Alexander de La Luz, Carlos Pimentel, Professor Giuseppina Sandra, Dalila Mieli, Silvia Rossi, and Alessandra Rossi for the valuable collaboration.

Kiara Montriel for spire me with your care with others and for being such a unique person. Thank you for the friendship, for the support, and for sharing with me the renaissance after the quarantine, when Granada flowered for us.

All technicians, students, and stuff of the *Faculdad de Farmacia* of the *Universidad de Granada*.

Professor Christine Taviot-Guého for the great contribution to my thesis, sharing with me part of your strong knowledge concerning structure and composition of Layered Double Hydroxide materials, and for kindly have welcomed me in Clermont-Ferrand.

Professora Liliana Marzorati pela valiosa experiência que me propiciou na disciplina "Prática de Ensino de Química", onde me deu liberdade para criar, experimentar e aprender tanto.

Professores Breno P. Espósito, Lucas C. V Rodrigues, Flávio M. Vichi, Denise Petri, Susana Torresi, Antônio C. Borin e Mauro C. C. Ribeiro por possibilitarem ativa participação de monitores durante os estágios PAE.

Alex Inague pela amizade e por ter estado sempre presente ao longo da minha jornada acadêmica.

Eduardo Delago, Laís S. de Matos e Ronaldo Costa Amaral pelos cafés e conversas valiosas.

Equipe docente, técnica, administrativa, de segurança e de limpeza do IQUSP. Em especial, Professor Thiago R. L. C. de Paixão, por me inspirar com sua liderança responsável e democrática, bem como com sua didática e comprometimento em sala de aula, e por sempre se colocar à disposição para ajudar os estudantes em qualquer situação; Valderez Gomes e Carolina Santos pela simpatia todas as manhãs e pela amizade; Maria Suelen pelo fornecimento de um ambiente de trabalho próprio e pelas conversas diárias; Vanderlei P. de Oliveira e Milton C. S. Oliveira por ajudarem tanto o/as estudantes com paciência e tamanha atenção; Fernanda Dib Cordeiro e Fátima Maria de Jesus J. Mazzine por sempre me receberem na diretoria com carinho e por toda assistência provida; Alceu Totti, por atenciosamente me treinar no uso de equipamentos desde a iniciação científica e por ser sempre tão gentil. Michele Rocha, Vânia A. B. B. Silva, Adriana Y. Matsukuma e Victor B. Astuto pelas análises na Central Analítica e pelo convívio sempre muito agradável; Patrícia B. di Vitta e David B. de Oliveira por

gentilmente ensinarem e orientarem os estudantes quanto às boas práticas de armazenamento de reagentes e resíduos e tratamento dos mesmos; Maria Aparecida P. Lopes, Ricardo A. A. Couto e Armando Henrique dos Santos pela inestimável ajuda na organização e no funcionamento da pesquisa no LaSoL.

Ao Társis Mendes Germano, por cada minuto naquela sala de difração de raios-X que poderia ter sido silêncio ou formalidade, porém que foram ricos momentos em que você buscou entender os meus materiais e obter os melhores resultados e me apresentou desde uma colaboração acadêmica até Darcy Ribeiro, música e poesia. Társis e Mônica pelo carinho e pelas cervejas.

Raquel M. Urteaga for inspiring me being such a dedicated student and researcher; for thinking always ahead and working hard to achieve your dreams and goals.

Fernanda e Rodolfo pela valiosa amizade, por terem me acompanhado e me incentivado ao longo de todo doutorado.

Adriana Valério e Rebeca Bayeh por terem sido meu combustível na reta final da escrita desta tese. Obrigada pela amizade e sororidade. Vocês são maravilhosas!

Às agências Fundação de Amparo à Pesquisa do Estado de São Paulo (processos FAPESP 2014/15900-0–Iniciação Científica, 2016/13862-9 – Doutorado Direto, 2018/22726-7–BEPE e 2018/22782-4–BEPE) e Conselho Nacional de Desenvolvimento Científico e Tecnológico (processo CNPq 140827/2016-1–Doutorado Direto) pelo apoio financeiro.

Finally, I'm thankful to all those who believed and believe in education and science as mechanisms of intellectual and material development and ways to reduce society inequalities.
Por fim, agradeço a todas e todos que acreditaram e que acreditam na educação e na ciência como mecanismos de desenvolvimento intelectual e material, e como caminhos para redução de desigualdades sociais.

ABSTRACT

Pires Figueiredo, M. **Iron-based Layered Double Hydroxides aiming biomaterials: structure, composition, and polymer composites.** 2021. 300 p. PhD Thesis - Graduate Program in Chemistry. Instituto de Química, Universidade de São Paulo.

Layered Double Hydroxides (LDHs) are considered promising materials to compose pharmaceutical formulations and medical devices mainly by their capacity to act as carriers for anionic bioactive species. LDHs are mostly composed by Mg^{2+} and Zn^{2+} as divalent cations and Al^{3+} (exogenous) as trivalent cation. The substitution of aluminium by an endogenous metal, such as Fe^{3+}, is of great interest for the development of even more promising LDHs for acting as biomaterials. However, the Fe^{3+} incorporation into the LDH structure has led to impure materials, also the intercalation of organic anions into these materials has been challenging. In this regard, the present work deals with two main aims: 1) to improve the applicability of Fe^{3+}-LDH materials by the comprehension of their structure, composition, and properties; and 2) to develop advanced polymeric medical devices, such as implantable surgical membranes and therapeutic wound dressings, based on pure Fe^{3+}-LDH phases.

Concerning aim number 1), in the first part of the thesis it was investigated the effect of Fe^{3+} in the formation of LDH phase and the limit of aluminium substitution by iron allowing the isolation of pure LDH phases also capable to intercalate bioactive species. First, two series of $Mg_2Fe_yAl_{(1-y)}(OH)_6$-Cl and $Zn_2Fe_yAl_{(1-y)}(OH)_6$-Cl LDHs, intercalated with chloride anions, with *y* equal to 0, 0.25, 0.50, 0.75, or 1 were studied. Then, all pristine LDH-Cl materials were submitted to ion-exchange of Cl^- by anions derived from the non-steroidal anti-inflammatory drug naproxen (NAP), a model organic compound. Lastly, LDH materials with nominal layer compositions $Mg_2Fe_yAl_{(1-y)}(OH)_6$ and $Zn_2Fe_yAl_{(1-y)}(OH)_6$, with *y* equal to 0, 0.25, 0.5, 0.75, or 1, aiming carriers for bioactive species were also prepared by the coprecipitation (one-pot) method in the presence of abietate anions (ABI), derived from abietic acid, a natural product that presents several biological properties (*i.e.* bactericidal, fungicidal, anti-inflammatory).

Along each series of materials, phase purity was evaluated using several analytical techniques combined with a crystal-chemical and geometrical reasoning that allowed the comparison between the composition of the bulk samples (considering the possible contribution of amorphous phases other than LDH) and the composition of the respective crystalline LDH phases. In general, phase purity was achieved for *y* values lower or equal to 0.5, which corresponds to half of the Al^{3+} content substituted by Fe^{3+}. Compositions considered pure and able to intercalate NAP or ABI organic anions in satisfactory amounts (*i.e.* the weight of the organic anion representing more than 25 % of the weight of the hybrid organic-inorganic LDH) were selected to compose polymeric devices according to the aim number 2) of this thesis, *i.e.* $Mg_2Fe_{0.5}Al_{0.5}(OH)_6$ and $Zn_2Fe_{0.5}Al_{0.5}(OH)_6$ layer compositions intercalated with Cl^-, NAP, or ABI anions. Approaches for the modulation of the release rate of the bioactive species intercalated into LDHs were explored and *in vitro* cytotoxicity assays were performed as a function of the composition of the materials. Polymeric membranes were prepared by different methods: electrospinning or casting. LDHs showed promising as components of the medical devices providing advantages from the mechanical, pharmacological, and biological points of view in comparison to the polymer-drug systems.

The results presented in this thesis, which include detailed structural analyses, the synthesis of several Fe^{3+}-LDH materials able to intercalated bioactive species, as well as the development of promising polymeric membranes containing Fe^{3+}-LDHs, are expected to advance even more the applicability of LDH as biomaterials.

Keywords: iron(III), proper compositional determination, bioactive species, intercalation compounds, polymeric membranes, *in vitro* drug release, *in vitro* biocompatibility

RESUMO

Pires Figueiredo, M. **Hidróxidos Duplos Lamelares à base de Ferro como biomateriais: estrutura, composição e compósitos poliméricos**. 2021. 300 p. Tese (Doutorado) - Programa de Pós-Graduação em Química. Instituto de Química, Universidade de São Paulo.

Hidróxidos Duplos Lamelares (HDLs) são considerados materiais promissores para comporem formulações farmacêuticas e dispositivos biomédicos, destacando-se pela possibilidade de atuarem como carregadores de espécies bioativas aniônicas. HDLs são compostos em sua maioria pelos cátions divalentes Mg^{2+} e Zn^{2+} e pelo cátion trivalente Al^{3+} (exógeno). A substituição do cátion Al^{3+} por um metal endógeno, tal como o Fe^{3+}, é de grande interesse para o desenvolvimento de HDLs ainda mais adequados para atuação como biomateriais. Contudo, as tentativas de incorporação do Fe^{3+} na estrutura do HDL têm conduzido à formação de materiais impuros, bem com a intercalação de ânions orgânicos nesses materiais tem se mostrado desafiadora. Nesse sentido, o presente trabalho tem como objetivos principais: 1) aumentar a aplicabilidade dos Fe^{3+}-HDLs através da compreensão da estrutura, da composição, e de propriedades desses materiais e 2) desenvolver dispositivos biomédicos poliméricos avançados baseados em Fe^{3+}-HDLs, tais como membranas cirúrgicas implantáveis e curativos dérmicos.

Com relação ao objetivo 1), na primeira parte desta tese foi estudado o efeito dos cátions Fe^{3+} na formação dos HDLs e na obtenção de fases puras contendo a maior quantidade possível de cátions Al^{3+} substituídos por Fe^{3+} e capazes de intercalar espécies bioativas. Primeiramente, foram sintetizadas e estudadas duas séries de HDLs de composição nominal $Mg_2Fe_yAl_{(1-y)}(OH)_6$-Cl e $Zn_2Fe_yAl_{(1-y)}(OH)_6$-Cl, intercalados com ânions cloreto, com valores de *y* iguais a 0; 0,25; 0,50; 0,75 ou 1. Posteriormente, os HDLs-Cl foram submetidos à reação de troca iônica dos ânions Cl^- por ânions derivados do anti-inflamatório não esteroidal naproxeno (NAP), um fármaco modelo. Por fim, HDLs de composição nominal lamelar $Mg_2Fe_yAl_{(1-y)}(OH)_6$ e $Zn_2Fe_yAl_{(1-y)}(OH)_6$, com *y* igual a 0; 0,25; 0,5, 0,75 ou 1, visando intercalar espécies bioativas também foram produzidos pelo método da coprecipitação na presença de ânions abietato (ABI), derivados do ácido

abiético, um produto natural que apresenta diversas propriedades biológicas (*i.e.* bactericida, fungicida, anti-inflamatória).

A pureza de fase de cada série de materiais foi avaliada por diversas técnicas analíticas combinadas com um raciocínio químico-cristalino e geométrico que permitiu a comparação entre a composição das amostras como um todo (considerando a contribuição de fases amorfas diferentes da HDL) e a composição das respectivas fases cristalinas de HDL. Em geral, pureza de fase foi alcançada para valores de *y* menores ou igual a 0,5, correspondendo à substituição de metade do conteúdo de Al^{3+} por Fe^{3+}. Composições consideradas puras e capazes de intercalar quantidades satisfatórias de ânions NAP ou ABI (*i.e.* massa do ânion orgânico representando mais de 25 % da massa do HDL híbrido orgânico-inorgânico) foram selecionadas para compor os dispositivos poliméricos segundo o objetivo 2) desta tese, *i.e.* materiais de composição lamelar $Mg_2Fe_{0,5}Al_{0,5}(OH)_6$ and $Zn_2Fe_{0,5}Al_{0,5}(OH)_6$ intercalados com ânions Cl^-, NAP ou ABI. Foram explorados mecanismos de modulação da taxa de liberação das espécies bioativas, bem como foram realizados testes de citotoxicidade em função da composição dos HDLs. Membranas foram produzidas por diferentes métodos: eletrofiação ou *casting*. Os LDHs mostraram-se promissores para compor formulações poliméricas biomédicas proporcionando vantagens do ponto de vista mecânico, farmacológico e biológico em comparação aos sistemas formados apenas por polímero-fármaco.

Espera-se que os resultados apresentados nesta tese, que incluem profunda análise estrutural, a síntese de diversas composições de Fe^{3+}-HDLs capazes de intercalar espécies bioativas aniônicas, bem como o desenvolvimento de membranas poliméricas promissoras baseadas em Fe^{3+}-HDLs, avancem ainda mais a aplicabilidade dos HDLs como biomateriais.

Palavras-chave: ferro(III), correta determinação composicional**,** compostos de intercalação, espécies bioativas, membranas poliméricas, liberação de fármacos *in vitro*, bicompatibilidade *in vitro*

LIST OF FIGURES

LIST OF TABLES

SUMMARY

Chapter 1: Introduction

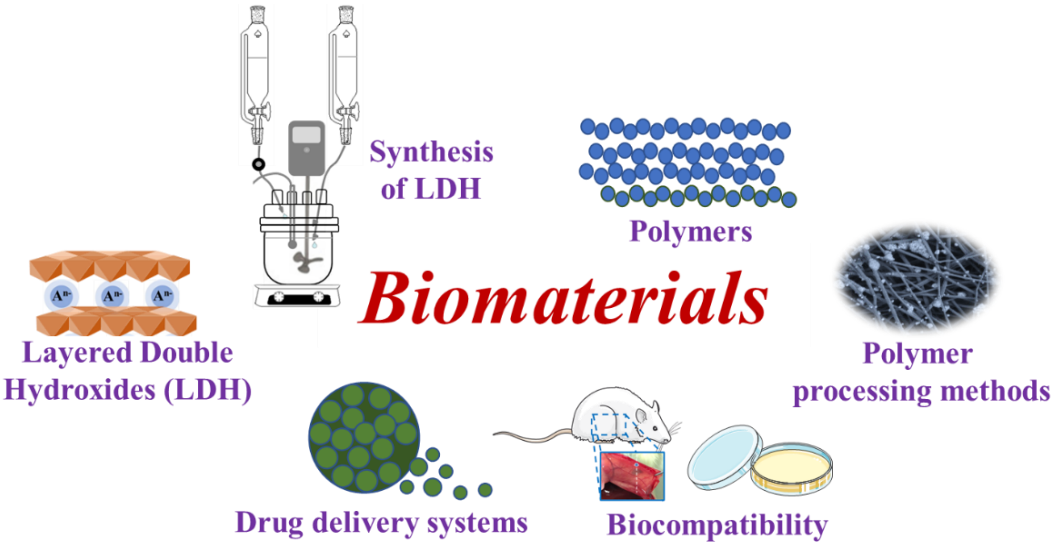

1. Introduction

Searching for more effective therapies to treat human diseases and improve life expectancy and quality is a constant effort in our society, implying in the discovery of more effective drugs and formulations and the development of materials able to compensate the loss of functions of body structures and improve the healing process, such as bone[1,2] and muscles constructs[3], and skin wound dressings[4,5], respectively.

New drugs have been commonly discovery through screening species from nature. Although more advanced techniques have been applied, such as those based on genomic and genetic approaches, the process resulting in the commercialization of new and more effective drugs still takes more than one decade and costs millions of dollars.[6] In this way, existing drugs may be re-profiled, optimizing time and costs. Re-profile can be done by far-reaching examination of a drug action at the molecular level aiming to better identify mechanisms of actions and causes of side effects.[7] As a consequence, drugs application can be expanded to other diseases and drug derivatives may be synthesized. In the same direction, drug delivery systems, also called drug carriers, have been developed to improve the efficacy of marketplace drugs.[8] Drug carriers interact with bioactive species in a manner that propitiate therapeutic benefits, as for instance, the control of the release rate, the destination of the drug to a specific site of action (targeted delivery), the improvement of biological and physicochemical properties, and the decrease in side effects.[8,9] Examples of commercialized drug carriers are liposomes[10], polymeric micelles[11], and magnetic nanoparticles[12].

Adequate chemical structures to act as drug carriers, body recovery assistants, or substitute materials of body constituents are considered biomaterials, defined as *"a substance that has been engineered to take form, which, alone or as a part of a complex system, is used to direct, by control of interactions with components of living systems, the course of any therapeutic or diagnostic procedure"*.[13] Biomaterials may be of different natures[14], from inorganic to organic, or a combination of both in an intimate contact at nanometer and molecular level, resulting in hybrid organic-inorganic materials. Two or more inorganic or organic materials with different physical and chemical properties may also be combined, whose contact dimension comprises a larger scale (from nano to

macro), originating composites with improved properties in comparison with the individual constituents. Specifically regarding to materials to assist damaged body organs or tissues, synthetic and natural polymers and their composites play a central role and are widely studied.[15,16]

To be in contact with living systems, biomaterials are expected to present biocompatibility, which can be referred as *"...the ability of a biomaterial to perform its desired function with respect to a medical therapy, without eliciting any undesirable local or systemic effects in the recipient or beneficiary of that therapy, but generating the most appropriate beneficial cellular or tissue response in that specific situation, and optimizing the clinically relevant performance of that therapy."*[17] Biocompatibility may be accessed through *in vitro, ex-vivo* or *in vivo* tests.[18,19] In all cases, the statement of the biocompatibility of a material is dependent of the local of application, the doses, and time. Considering the high complexity of living systems, diverse *in vitro* and *in vivo* tests may be combined.

Layered double hydroxides (LDHs) comprise interesting naturally obtained and also easily synthesized inorganic materials that present diverse compositions and properties, thus finding application in several fields, such as health[20,21], catalysis[22,23], electrochemical sensors[24], energy[25] and environment related domains[26]. Especial attention has been directed to their medical uses since many compositions are promising for application as biomaterials. LDHs can intercalate anionic bioactive species, originating organic-inorganic hybrid materials. This class of materials has been extensively studied not only as drug carriers[27], but also for application as vectors for gene therapy[28], for therapeutic coupled to diagnosis purposes (theragnostic)[29], and tissues engineering[30]. LDH/polymer composites have also been studied for the development of even more effective biomaterials.[31]

LDHs studied for biological applications usually contain Al^{3+} cations (Al-LDHs) in their compositions. Although no toxic effects have been related to Al-LDHs and their biocompatibility have been attested through different *in vitro* and *in vivo* tests,[32–35] the substitution of aluminum by endogenous metals, such as Fe^{3+}, is interesting to avoid still poorly investigated possible long-term and dose-dependent toxic effects and may generate new and even more promising materials.

In the next sections, structure, compositions, properties and bioapplications of LDHs, and more specifically LDHs composed by iron, are discussed, as well as promising bioactive species to compose LDH biomaterials. Furthermore, promising polymers and techniques to prepare polymeric membranes containing LDHs will be presented aiming medical devices.

1.1. Layered Double Hydroxides (LDHs)

1.1.1. LDHs structure and composition

As shown in **Figure 1.1A**, LDH structure is formed by basic octahedral units containing M^{2+} or M^{3+} metallic cations in the center, hexacoordinated by hydroxyl anions, and hydrated anions (A^{n-}), and presents general formula $[M^{2+}_{(1-x)}M^{3+}_{x}(OH)_2](A^{n-})_{x/n}\bullet zH_2O$.[36] The condensation of the octahedrons originates layers (**Figure 1.1B** – top view) presenting a residual positive charge compensated by the anions present between the layers (**Figure 1.1C** – frontal view). LDH layers can stack one on another with two different symmetries: rhombohedral or hexagonal.[36] Hydrotalcite and pyroaurite minerals, with formulae $[Mg_3Al(OH)_8](CO_3^{2-})_{0.5}\bullet 4H_2O$ and $[Mg_3Fe(OH)_8](CO_3^{2-})_{0.5}\bullet 4.5H_2O$, respectively, crystallize in 3R rhombohedral symmetry (**Figure 1.1B** and **1.1C**). The unity cell parameter *a* is equal to *b,* and *c* parameter equal to 3d, with d representing the basal spacing, *i.e.* equivalent to the thickness of one layer plus the interlayer spacing. The mineral syögrenite, a polytype of pyroaurite, presents another symmetry, 2H hexagonal, where *a* parameter is equal to *b,* but *c* parameter equal to 2d. 3R symmetry is commonly observed for synthetic LDHs.[37]

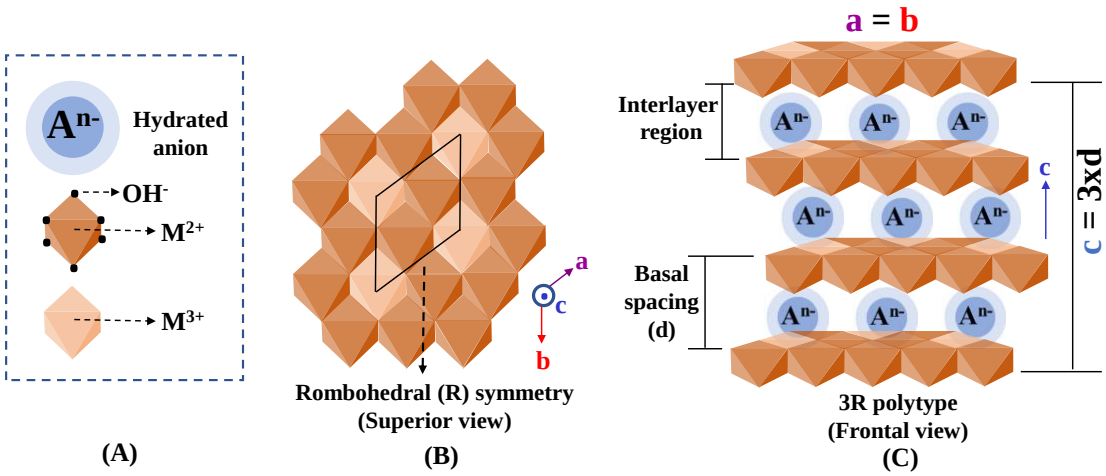

Figure 1.1.(A) LDHs constituents: basic octahedral structures and hydrated anions, (B) LDH layer (top view), and (C) LDH structure (frontal view) corresponding to the 3R polytype.

Di- and trivalent cations able to compose LDH layers are restricted by their ionic radii, that is observed to be close to the one of the Mg^{2+} (0.72 Å in a 6-coordinated site).[38] This condition is satisfied by several metallic cations, such as Zn^{2+}, Fe^{2+}, Fe^{3+}, Al^{3+}, Co^{2+}, Co^{3+}, Ni^{2+}, Ni^{3+}, Mn^{2+}, and Mn^{3+}. The *x* value, the amount of the trivalent cation in the layer, is another adjustable parameter and a source of diversity in the LDH structure. By changing *x*, the charge density in the layers can be modulated and, therefore, the anions amount and arrangement between the layers.[36] For minerals, *x* is usually equal to 0.25 (M^{2+}/M^{3+} molar ratio equal to 3), while for synthetic LDHs it is observed to be $0.2 \leq x \leq 0.33$, in general, which means M^{2+}/M^{3+} molar ratios between 4 and 2. Values of *x* out of this range may conduct to $M(OH)_2$ and $M(OH)_3$ into separated phases.[39] Additionally, when *x* is lower than 0.33, Pauling's rule restricts the occupancy of adjacent metallic sites by trivalent cations, conducting to a cation-ordered idealized structure.[40] Since the *a* (equal to *b*) cell parameter is dependent of both M^{2+} and M^{3+} ionic radii, it can indicate if the incorporation of the cations is in agreement with the nominal value of *x*. Finally, LDH may experience guest-host interaction, where the interlayer reservoir may accommodate from simple small inorganic anions (such as Cl^-, NO_3^-, or CO_3^{2-}) to macrostructures such as the deoxyribonucleic acid (DNA) macromolecule or plasmids[41–43]. LDH is generally abbreviated by $M^{2+}{}_RM^{3+}$-A, where R is the molar ratio between the di- and trivalent cations.

1.1.2. LDH synthetic methods: coprecipitation and ion-exchange

Several synthetic methods have been applied for the preparation of LDH, such as coprecipitation[44], ion-exchange[45], reconstruction[46], sol-gel[47], and the urea method[48]. Post-synthesis (aging) treatments, such as hydrothermal[49] and microwave[50] radiation, are also employed to improve LDHs properties, such as crystallinity and particles size.[39] In general, LDHs synthesis in the laboratory and in an industrial scale is easy and economically practicable, since these materials are usually prepared in an aqueous medium, at room or mild temperature values, at atmospheric pressure, and applying not expensive reagents, as in the case when prepared by the coprecipitation method, the most applied synthetic route for the preparation of simple inorganic or organic-inorganic hybrid LDHs. It consists of mixing an Arrhenius base, such as NaOH or KOH, and an aqueous solution containing M^{2+} and M^{3+} cations in the desired molar ratio. In water, some metallic cations can form (oxy)hydroxide complexes.[39] By increasing the pH of the medium, cations charge is balanced by increasing the number of negatively charged ligand coordinated to the metallic center until the coprecipitation and condensation, or solids conversion, into LDH.[39] The pH value of precipitation is dictated by the solubility product of the related $M(OH)_2$ and $M(OH)_3$ hydroxides. Thus, the pH value must be higher enough to propitiate the coprecipitation of both M^{2+} and M^{3+} cations.[36] The coprecipitation reaction at constant pH leads to well structurally organized LDHs. In this modality of the coprecipitation method, as soon as the salt's solution is added into the aqueous medium compartment containing the anions to be intercalated, previously dissolved or coming from de counter anions of the $M_n(A^{n-})_2$ and $M_n(A^{n-})_3$ salts, the base solution is concomitantly added to keep the pH value constant. When it is desired the intercalation of anions other than carbonate and products with high purity, an inert atmosphere is recommended to avoid atmospheric CO_2 dissolution in the alkaline reaction medium. **Figure 1.2A** shows the schematic representation of the semi-automatized system applied in studies presented in this thesis for the preparation of LDHs by coprecipitation reaction at constant pH and heating in some cases, in which an automatic titrator is coupled to the system and the addition rate of the salt's solution is manually adjusted.

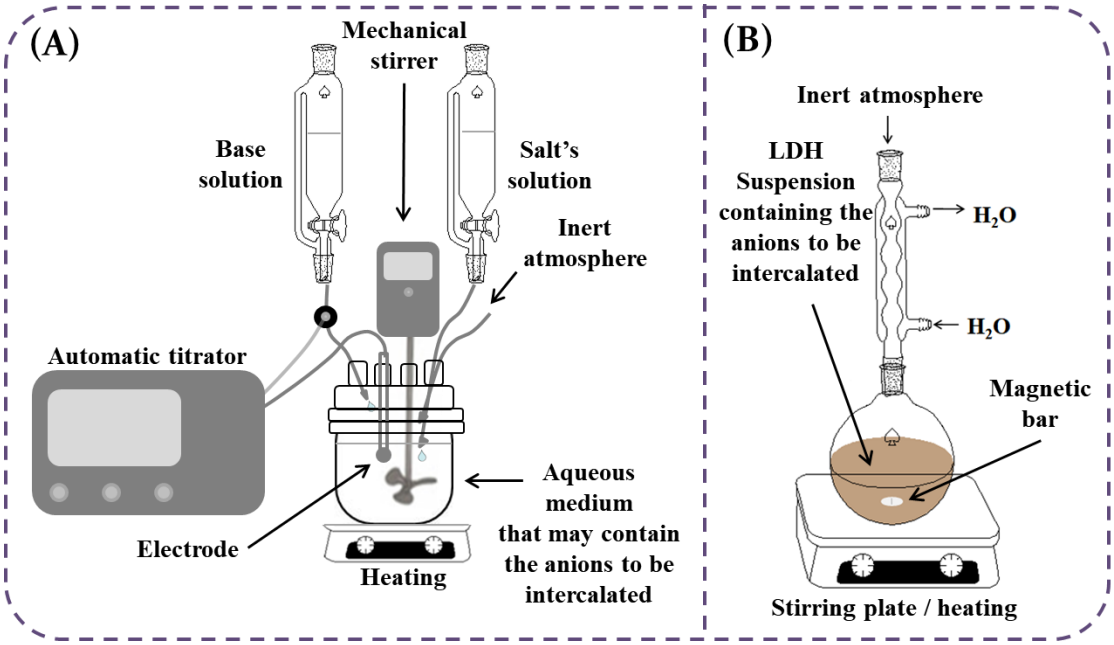

Figure 1.2. Schematic representation of the apparatus applied for the synthesis of LDH.

The synthesis of LDHs intercalated with anions that compete with hydroxide ions by the coprecipitation with the cations may hinder the application of the coprecipitation method.[39] Moreover, the intercalation of organic anions into LDH may not occur by applying the coprecipitation reaction.[51,52] In such cases, anions such as phosphate and oxalate have to be intercalated by ion-exchange reaction into previously prepared LDHs.[39] The order of intercalation preference of the main inorganic anions is given by[53]:

$$CO_3^{2-} > HPO_4^{2-} > HAsO_4^{2-} > CrO_4^{2-} > SO_4^{2-} > MoO_4^{2-} > OH^- > F^- > Cl^- > Br^- > NO_3^-$$

Therefore, the intercalation preference of anions to originate precursors LDHs to participate of ion-exchange reactions is the inverse, in which NO_3^-, Br^-, and Cl^- are easily deintercalated. **Figure 1.2B** shows the synthetic apparatus applied in this thesis for ion -exchange reaction consisting of suspending LDH particles in a solution containing the anions to be intercalated, under stirring, room temperature or under heating, and inert atmosphere if desired to avoid carbonate contamination.

1.1.3. LDHs as biomaterials

LDH composed by Mg^{2+} or Zn^{2+} as divalent cations and Al^{3+} as trivalent cations are being investigated to act as biomaterials. LDH containing Mg^{2+} and Al^{3+} intercalated

with CO_3^{2-} anions is applied as the antiacid Talcid®, patented by Bayer AG.[54] More than a basic material able to neutralize gastric acids, LDH is demonstrated to accelerate gastric ulcer healing[55], having a role in the expression of Epidermal Growth Factor, that stimulate cell growth and differentiation, and its receptors in normal and ulcerated gastric mucosa of rats[56], interesting characteristics to be explored in terms of tissue healing. In this way, simple inorganic LDHs only or combined with polymers, may act as biofunctional bone substitutes.[57,58] Their nanoscale 3D organized structure is able to support cells, to release cell growth factors, and to act as a scaffold for bone growth. The combination of the inorganic matrix with polymers can mimic bones, conferring gains in mechanical strength and remodeling facilities. The combination of inorganic matrices, such as LDH and hydroxyapatite, originates advanced materials able to induce the formation of high-quality bone.[30]

Besides the described bioactivity of LDHs, essentially related to the presence of metallic cations, the intercalation of anionic drugs allows the development of diverse pharmaceutical formulations and medical devices. The intercalation of many bioactive species into LDH has being studied, such as: non-steroidal anti-inflammatories[59], amino acids[60], vitamins[61], anticarcinogenic drugs[62], antibodies[63], and deoxyribonucleic acid segments[41,43]. LDHs have shown, in general, a great intercalation yield, being possible to reach more than 99 %.[64] Moreover, it is expected to prolong the release rate of the guest species and may protect it from light, heat, or chemical degradation.[20] Simply as a passive drug carrier, LDH is already promising. Additionally, research involving targeted therapies, specifically for cancer therapies, is in development.[65] A simple advantage of an intrinsic characteristic of LDH against cancerous cells consists in its faster particles degradations and release of intercalated species in the more acidic media of extracellular tumor cells compared to healthy tissues.[66] Another strategies consist in functionalize LDH structure with an external chemical entity able to interact with tumor microenvironment or in hybridizing the surface with magnetic particles to guide them towards the tumor.[65]

The *in vitro* biocompatibility of LDHs has being studied concerning cell cytotoxicity and viability,[67] hemolysis,[33] lipid peroxidation,[68] and with the generation of reactive species of oxygen[67], among other tests. Cytotoxicity tests may be classified

according to the type of measurements performed, such as changes in color and luminescence intensity, for instance. The colorimetric Methyl Thiazolyl Tetrazolium (MMT) assay, based on mitochondrial dehydrogenase activity measurement, is frequently applied for the evaluation of LDHs cytototoxicity[68–72]. MTT method is based on the action of mitochondrial dehydrogenase in the cytochrome b and c sites. By cleaving the tetrazole ring and reducing the MTT, the yellow color is substituted by purple, from crystalline and insoluble in water formazan. Formed crystals are dissolved in organic solvents, such as dimethylsulfoxide, quantified, and their amount is proportional to surviving cells and metabolic activity. Although the number of works concerning the evaluation of the *in vivo* performance of LDH is still lower compared to *in vitro* assays, different tests have been applied, for instance, intravenous[35] or subcutaneous and intramuscular implantation[73]. It is interesting to note that, LDHs studies aiming at biomaterials are mostly composed by Mg^{2+} or Zn^{2+} divalent cations and by Al^{3+} divalent cation, exogenous. Although *in vitro* and *in vivo* studies have not, in general, indicated possible toxicity of Al-LDHs, there is a lack of studies about aluminum effect considering long-term treatments and dose. Furthermore, Al^{3+} cations absorption has been associated with neurotoxicity and general tissue accumulation[74–76]. In this way, its partial or complete substitution by endogenous metals, such as iron, is desired to originate biomaterials composed only by essential metals and able to be completely metabolized.[77]

1.1.4. Iron-based LDHs as biomaterials

Although much less studied than Al-LDHs, Mg_RFe and Zn_RFe LDHs have been reported for catalysis[78,79], agriculture[80], energy conversion/storage[81,82], as adsorbents for environmental remediation in its layered phases or as oxides after calcination[83–93], and more rarely for organic anions loading and delivery[94]. Iron-based LDHs (Fe^{3+}-LDHs) are difficult to characterize due to their quite low crystallinity and the presence of crystalline and/or amorphous impurities. X-ray diffraction patterns of Fe^{3+} containing LDH clearly indicate a lower structural organization with broad and less intense peaks compared to Al^{3+} containing LDHs[93,95]. Moreover, Fe-K radiation fluorescence under Cu-K alpha X-ray radiation affects the X-ray diffraction pattern

baseline[96], ascending by increasing 2θ degrees, and leads to an important decrease in the signal to noise ratio making phases identification challenging. **Appendix A** shows results of a search in *Web of Science*[97] database for the evaluation of synthetic parameters usually applied for the preparation of Mg_RFe and Zn_RFe LDHs and evaluation of the formed products. The search was made applying the entering sentence "M Fe Layered Double Hydroxides", with M equal to Mg^{2+} or Zn^{2+}, for all years until 19th May 2021. Synthetic methods were restricted to coprecipitation and ion-exchange. Papers that did not specify the molar ratio between the cations, pH value of synthesis, XRD quality is too low precluding proper phases attribution, or suppress XRD pattern (or showed XRD results for small 2θ range) were excluded. Additionally, synthesis starting from Fe^{2+} species with further oxidation to Fe^{3+} were also excluded. **Table A.1** (**Appendix A**) compiles 49 works and 122 materials. The following information was extracted from these works: expected LDH composition (nominal M^{2+}/M^{3+} molar ratio, M nature, and intercalated anion), synthetic method, pH, post-synthesis treatment, obtained crystallographic phase(s) (LDH, LDH and side phase(s), or side phase(s) only) assigned by the authors and/or by our criteria and expertise. Some of these works are commented on below. Base on the materials analyzed in **Table A.1**, **Figure 1.3** shows the percentage of the materials concerning Mg_RFe and Zn_RFe-LDHs, as well as the percentage of the materials in which LDH and /or side phase(s) or only LDH phase was identified by XRD for each of them. Most of the works are related to Mg_RFe-LDHs and the formation of side phases are observed for both Mg and Zn compositions, although much more common in Zn materials. Phase segregation also tends to occur when increasing the value of the M^{2+}/Fe^{3+} molar ratios, combined with the application of thermal treatment. Such conditions conduct to the appearance of XRD peaks not attributed to the corresponding LDH materials and frequently, for Zn-LDHs, peaks related to $Zn(OH)_2$ and ZnO species[84,85,88,98–108]. For instance, Morimoto *et al.*[109] investigated the effect of different aging temperature values (25, 50, 75, 100, 125, and 150 °C) on the formation of hematite in Mg_RFe-Cl (R = 2, 3, and 4) samples and observed that hematite formation is favored as higher the iron content and higher the temperature; this fact was explained by the decrease of LDH dehydroxylation temperature with the increase in the iron amount.

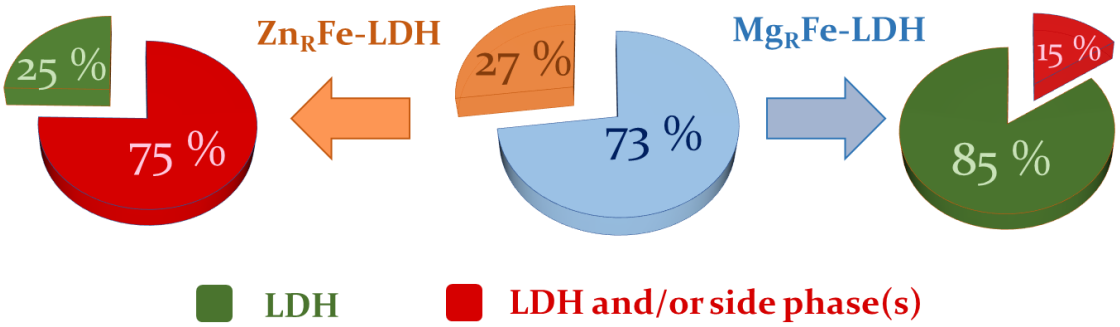

Figure 1.3. Percentage of materials in which LDH and /or side phase(s) (in red) or only LDH phase (in green) was identified by XRD for the Mg$_R$Fe- (in blue) and Zn$_R$Fe-LDHs (in orange), according to **Table A.1 – Appendix A**.

Concerning Fe-LDHs as biomaterials, most of the works are related to inorganic phases, intercalated with simple anions such as NO_3^-, Cl^-, or CO_3^{2-}. For instance, inorganic Mg$_R$Fe LDHs were evaluated as phosphates binders for oral administration[110], for enzyme adsorption[98], or also as osteogenesis enhancers by covering Ti plates[111], bone[99], and orthopedic implants[112] with LDH. The preparation of organic-inorganic hybrid Fe-LDH seems not to be simple. For instance, L-ascorbate intercalation into the Mg_3Fe LDH was possible by the reconstruction method but not by coprecipitation[51,94,113]. Ding *et al.*[52] studied the intercalation of ibuprofenate anions into Zn_3Al, Mg_3Al, and Mg_3Fe LDHs by coprecipitation reaction and showed that superficial anions absorption occurred preferentially over intercalation for the iron-based LDH. The incorporation of phenylalanine into the Zn_3Fe LDH by different synthetic methods (coprecipitation, ion-exchange, and reconstruction) was reported by Seftel *et al.*[106] However, XRD data do not endorse the formation of the LDH phase for all compositions and also indicated the presence of Fe_2O_3 as an impurity for the LDH intercalated with nitrate, applied as starting phase for anions exchange reaction. These studies show the difficulty to intercalate organic anions into Fe^{3+} containing LDH by the most common coprecipitation method. Even for the simplest materials containing inorganic anions between the layers, it is difficult to obtain pure LDH phases in the presence of iron and to verify the crystallographic phase purity due to their low structural organization. Although still dealing with phase impurity, more recent studies have shown positive results concerning Fe-LDHs as host biomaterials. Both Mg$_R$Fe and Zn$_R$Fe LDH, with different R values, were studied by Balcomb *et al.*[100] aiming their application as nonviral gene delivery vehicles and their performances were compared to the

compositions containing Al^{3+} cations. Samples based on iron presented impurities, evidenced by XRD data. However, DNA binding was successful for all LDH samples, thus able to protect the macromolecule from degradation by nucleases in comparison with unbound DNA. DNA-LDH systems were able to efficiently deliver DNA into mammalian cells. Furthermore, all samples showed low cytotoxicity (cell viability higher than 80 %), human embryonic kidney 293 *cells* viability was over 100 %, and higher values were observed for Fe-containing LDH than for Al-LDHs. A device for co-delivery of ligand (adenosine) and ligation activator (leachate Mg^{2+} cations) was prepared based on the Mg_2Fe LDH composition[114]. Phase's purity could not be analyzed by XRD, since the diffractograms only showed a restricted region concerning possible basal planes of LDH, and related characterization techniques were not sufficient to prove materials purity. *In vitro* culture cells data showed that the nanohybrid promoted osteogenic differentiation of stem cells. Furthermore, it presented healing abilities when injected into the tibial bone of rats.

The partial substitution of Al^{3+} by Fe^{3+} cations may be an alternative to reduce aluminum amount in the LDH but also to achieve better structure organization as a benefit. A progressive insertion of Fe^{3+} into LDH compositions may also be an interesting strategy to determine the optimum substitution degree aiming pure phases, minimal structural organization to assist materials characterization and structure/composition determination. These are important features to be considered allowing the development of advanced biomaterials. In this way, Pires Figueiredo et al. published a previous work concerning the synthesis and characterization of LDHs composed by Mg^{2+} or Zn^{2+} as divalent cations and Fe^{3+} and Al^{3+} in the same proportion as trivalent cations, and intercalated with chloride anions, named $Mg_2Fe_{0.5}Al_{0.5}$-Cl and $Zn_2Fe_{0.5}Al_{0.5}$-Cl compositions[115]. Naproxen was intercalated by ion-exchange in an appreciable amount in both materials, whose weight percentage (wt %) of NAP was equal to 35 and 29 % for the Mg and Zn-LDH, respectively. Drug release was kept for around 4 days in phosphate buffer solution. Moreover, it was attested the pristine LDHs-Cl biocompatibility through intramuscular implants in rats. Interestingly, the *in vivo* study also showed that Fe^{3+} modulates the formation of collagen during the tissue regeneration process. Type-I collagen was predominant in the presence of both $Mg_2Fe_{0.5}Al_{0.5}$-Cl and $Zn_2Fe_{0.5}Al_{0.5}$-Cl materials, differently from the results obtained for the Mg_2Al-Cl and Zn_2Al-Cl LDH

materials, in which collagen formation was guided by the divalent cation nature and a predominance of type-III collagen was observed for the Zn_2Al matrix[116]. These results directed our efforts for the understanding of iron-based LDH structure and composition to advance the application of such promising materials.

1.1.5. Guest species for intercalation into LDHs

1.1.5.1. Naproxenate anions

Non-steroidal anti-inflammatory drugs (NSAIDs) are formed by a heterogeneous group of compounds containing one or more aromatic rings bonded to an acid group. They are weak acids that act mainly in inflamed tissues and bond significantly to plasma albumin.[117] NSAIDs comprise the most studied class of drugs for intercalation into LDH drug carriers.[59] Prolonged uses of NSAIDs are associated with several side effects, mainly related to the gastrointestinal tract, such as ulcerative stomatitis, esophagitis, ulcerations, among many others.[118] LDH's antiacid property, where hydroxide ions from the layers are responsible for acids neutralization buffering action[119], and the possibility to promote a modified drug release offer advantages to compose oral formulations of NSAIDs, expecting to decrease the side effects described above. It is also demonstrated that LDH basicity favors permeation of NSAIDs through gastrointestinal mucosa[59]. Literature pertaining to LDHs aiming a controlled release of NSAIDs indicates that the release rate may vary from hours to days, depending on LDH composition, morphology, particle size, and particle aggregation state. Also, LDH can intercalate the anionic form of NSAIDs, which presents greater solubility. Moreover, LDH may load an amount of drug per volume unit that is higher than its solubility, releasing it in concentration rates along time that are under saturation. In this way, it is said that LDH may overcome the low solubility of NSAIDs in aqueous medium when intercalated into LDH, improving the viability of oral administration, allowing the dissolution and absorption of the active principles in the body.[59]

Naproxen, (S)-(+)-6-methoxy-a-methyl-2-naphtalenacetic acid, consists of a naphthalene aromatic moiety containing a propionate and a carboxylic side groups[120],

as shown in **Figure 1.4**. Literature counts with several works concerning the intercalation of naproxenate anions (NAP), deprotonated naproxen, into Mg_RAl and Zn_RAL LDHs[121–130] and just two works concerning the NAP intercalation into iron-based LDHs. The work of del Arco *et al.*[131] reports NAP intercalation into the $Mg_2Fe_{0.1}Al_{0.9}$ LDH, with a low amount of iron. Higher iron amounts were applied for the preparation of the $Mg_2Fe_{0.5}Al_{0.5}$-NAP and $Zn_2Fe_{0.5}Al_{0.5}$-NAP LDHs, in our previous work.[115] Therefore, NAP is applied in this thesis as a model drug, but still carrying innovation concerning its intercalation into iron-enriched LDHs.

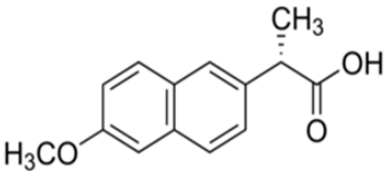

Figure 1.4. Chemical structure of naproxen.

Topical administration of NSAIDs can be seen as an alternative to overcome gastrointestinal side effects arising from the oral administration route. Local administration may leads to an increase in the local concentration of the drug in subjacent tissues, which can also reaches the bloodstream, performing a systemic action.[132] Transdermal release of naproxen and its sodic form has being studied in formulations in form of gel[133], polymeric film[134,135], polymeric nanoparticle[136], and microemulsion[137]. LDHs intercalated with NAP may compose topical formulations, such as therapeutic dressings, being possible to propitiate a NAP modified release and to improve physical properties of polymers and gels.[31,138]

1.1.5.2. Abietate anions

Rosin, also called colophony, is mainly obtained from pines and is a source of several substances primarily used for plant protection. Rosin is composed by 90 – 95 % of monocarboxylic acids diterpenoids with general formula $C_{19}H_{29}COOH$, mainly tricyclic carbon skeletons, such as abietic acid (HABI), whose chemical structure is shown in **Figure 1.5**, and neutral compounds.[139] Rosin, isolated components and its derivatives find many uses in cosmetics and dermatologic formulations. They present bactericidal, fungicidal, antiulcer, cardiovascular, and anti-inflammatory activities.[140],[141]

Bactericidal property of HABI and derivatives have been proved against common bacteria, such as *Escherichia coli* and *Pseudomonas aeruginosa,* and also *Staphylococcus aureus* strains and its methicillin-resistant biofilms. [142,143]

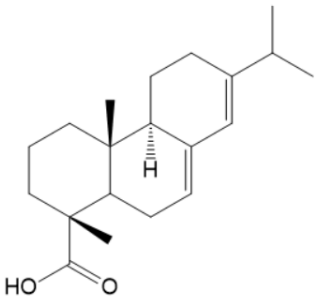

Figure 1.5. Chemical structure of abietic acid.

HABI was investigated for anticancer therapy as an antimetastatic adjuvant agent to act with the anticarcinogenic drug taxol. Studies carried *in vivo,* on mice, showed that HABI was able to reduce metastases in the lung by about 92.8 %, through inhibition of melanoma cells migration, invasion and mobility. Also, it improved the taxol activity.[144] Another paper reported the role of HABI on wound healing.[145] Briefly, wound healing involves a sequence of overlapped well-coordinated steps: (1) hemostasis, (2) inflammation, (3) proliferation, and (4) remodeling.[146] HABI enhanced *in vitro* angiogenesis, an important process occurring in early phases of wound healing, consisting of new blood vessel formation, and accelerated *in vivo* wound healing in mice.

As discussed above, LDHs can propitiate a series of advantages to the guest species *via* intercalation. Poor solubility of non-ionized HABI in water (1.2×10^{-5} mol L^{-1} at 20 °C)[147] can be overcame by intercalating deprotonated HABI (ABI) into LDH. Moreover, the combination of ABI and LDH properties can originate enhanced formulations for diverse diseases and the hybrid can also compose interesting topical formulations aiming to assist wound healing, such as solid dressings.

The interaction between LDH and ABI, addressed in this thesis, is a new issue and only two works could be found in the literature: a study concerning the development of a nickel catalyst based on Ni_RAl-LDH for rosin hydrogenation;[148] and the application of colloidal suspensions of calcined Mg_RAl LDHs to remove HABI/ABI from solution through superficial adsorption. The latter work takes advantage of *memory effect*, in which LDH structure is rebuilt from oxides obtained from LDH calcination in the

presence of the anion to be intercalated (however ABI intercalation into LDH was not proved or discussed)[149].

1.1.6. LDH-polymer composites

The combination of polymers and LDH particles forming nanocomposites dates from the 2000's and aims to improve mechanical, thermal, and optical properties of polymers.[150–153] In the pharmaceutical field, primary studies were related to the oral administration route. Although LDHs tends to promote a sustained drug release in pH medium close to the physiologic values, when in contact with acidic medium, such as of the stomach, the inorganic matrix is rapidly dissolved, accelerating the release rate of the intercalated species. Enteric coating is a technique in which capsules surface is covered by a polymeric layer protecting them from dissolution in the stomach, directing the active ingredient to be preferentially absorbed in the intestine.[154] For instance, Li *et al.*[155] prepared Mg_2Al LDH particles intercalated with the NSAID fenbufen coated with Eugragit® (copolymer of methacrylic acid and methyl methacrylate) and it was verified the inhibition of the drug release due to the interaction of carboxylic groups of the polymer with the LDH surface. Still in the direction to turn LDHs into even more interesting therapeutic vehicles, M. Mahkam *et al.*[156] showed that the nanocomposite consisting of the Zn_2Al LDH and alginate entrapping insulin propitiate a slower drug release in comparison to the LDH in the absence of alginate.

In the breakthrough of administration routes other than the oral, LDH-polymer composites are studied for topical ocular applications[157], as a suspension, and for skin applications, in the form of cream[158], gels[159], or membranes[160], aiming a controlled release of bioactive species. As discussed in the section 1.1.3, *LDHs as biomaterials*, LDH-polymer composites also find application in tissues engineering field, being studied as bone substitutes and more recently as dressings aiming wound healing[161]. As wound dressings, the polymer acts as more than a physical barrier to the wound, as a mechanism for exudates removal, or as a support for LDH particles[162]; it may also impose diffusional barriers to drug release, assisting drug release modulation and participating of wound healing process, improving cells adhesion and migration. On its turn, LDH can propitiate a controlled release of species that can promote a faster and

painless wound healing process, such as anti-inflammatories[59,121] and bactericidal[163–165] agents. Moreover, the LDH structure may experience a M^{2+} and M^{3+} cations leaching process, especially in acid media such as the skin (pH value range 4–7[166]), and such cations are involved in collagen neogenesis, verified thought *in vivo* model[73,115], as discussed above, thus playing a role in tissue regeneration process.

1.1.6.1. Preparation of polymer/LDH membranes

1.1.6.1.1. Electrospinning and electrospraying methods

The application of a high voltage electrostatic field charging the surface of a polymer solution leading to the ejection of the liquid jet through a spinneret dates from centuries ago.[167] During the liquid ejection, the solvent evaporates giving rise to an electrosprayed or electrospun polymer, depending on operation conditions such as the tension and the distance between the spinneret and the collector, the polymer molar mass and concentration, the vapor pressure of the applied solvent, the solution viscosity, etc. When a strong electric field is established between the metallic needle and a conductive collector, the droplet exiting the needle takes the shape of the so-called *Taylor cone* from which a charged jet is propelled.[168] During its flight travel in the air, the charged jet is subjected to whipping movements while the solvent evaporates. Thereby the jet elongates and solidifies. A dry fibber with an average diameter ranging from tens of nm to few of microns is deposited on the collector in the form of a nonwoven mat. The first patent describing the electrospinning operation was deposited in 1934.[169] However, it started being described in more detail from 2000s, since the physics of the process started to be better understood. When a suspension is submitted to a similar setup to electrospinning, dispersed particles from fine droplets are collected and the process is called electrospraying.[170] **Figure 1.6** illustrates both electrospinning and electrospraying procedures.

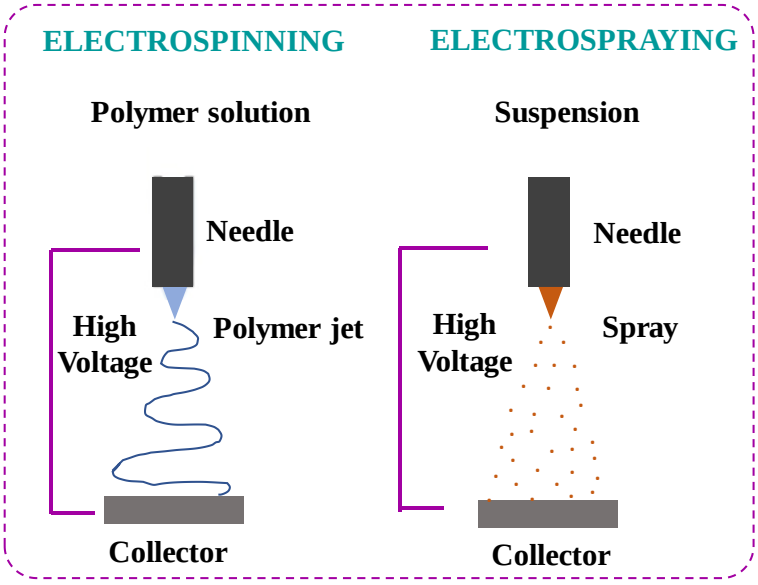

Figure 1.6. Schematic representation of electrospinning and electrospraying procedures.

Electrospun membranes find applications in diverse areas, such as the food industry and agriculture[171], electrochemistry for energy storage[172], and medicinal devices development. In this last field, wound healing purpose has to be highlighted[173] because electrospun nanofibrous mats mimic the extracellular matrix components and enable cells growth and differentiation. Fibers possess a high surface area/volume ratio and high porosity, able to create nutrient gradients.[170] Thus, polymer matrix by itself is promising to be applied as wound dressings or implantable devices, supporting damaged tissues and improving tissue regeneration.

Polymeric membranes containing LDH particles may originate promising multifunctional composites, combining healing properties of both electrospun fibers and LDH, and also the ability of LDH to sustain the release of intercalated bioactive species. In literature, electrospun-LDH interaction occurs via the introduction of particles inside polymeric fibers. This design is obtained by suspending LDH in the polymer solution which is further electrospun.[174] However, such approach frequently leads to the formation of beads, turning fibers less homogeneous. Bead occurrence tends to increase with the increase in LDH percentage in the composites. For instance, Valarezo *et al.*[174] obtained homogeneous fibers containing the Zn_2Al LDH intercalated with amoxicillin when LDH percentage in the membrane was equal to 3 wt%. However, the formation of beads was observed for membranes with 5 and 7 wt% of LDH. In the same work, amoxicillin *in vitro* release was also studied for the membrane presenting 3 % wt of LDH,

and was observed to be slow, extending for more than 20 days. Since aiming the production of homogenous fibers, bead formation limits the amount of LDH in the composites. Furthermore, as shown in the work of Gao *et al.*[175], fiber diameter tends to increase as the LDH amount increases. Yang *et al.*[176] prepared poly(lactic-co-glycolic acid) electrospun membranes containing 5 wt% of Mg_3Al LDH intercalated with flurbiprofen acetyl. Heterogeneous fibers diameter was observed. Additionally, less than 40 % of the drug was released after 5 days. A slow release of diclofenac from poly(caprolactone) electrospun fibers containing Mg_3Al LDH particles was also observed in the work of Tammaro *et al.*[177], where after 240 days only 50 % of the drug was released.

Although electrospun membranes containing LDH drug carriers inside the fibers have shown to sustain the release of the guest species for a long time, a desired characteristic for pharmaceutical formulations, the technology involved in the development of advanced drug delivery devices may count on mechanisms to modulate the drug release rate, adjusting the formulation characteristics according to the application, *e.g.* drug chemical structure and physical-chemical properties, disease type and treatment. The combination of polymer electrospinning and LDH electrospraying techniques may offer a greater variety of designs aiming for such fine control of the polymeric device's specifications, as shown in this thesis.

1.1.6.1.2. Solvent casting method

Solvent evaporation[178,179], also called casting method, is a cheap and simple technique for polymeric membranes preparation and is an alternative to more complex methods, such as electrospinning or extrusion, for instance, inclusive when such cited methods are not viable. By casting, the polymer is solubilized in a suitable solvent or mixture of solvents. After solubilization, the polymer solution is spread on a substrate then submitted to evaporation under ambient or controlled pressure, humidity, and temperature conditions. Polymer precipitates as a consequence of the evaporation of the solvent, forming the polymeric membrane. **Figure 1.7** shows a schematic representation of the casting method for the preparation of a simple polymeric membrane.

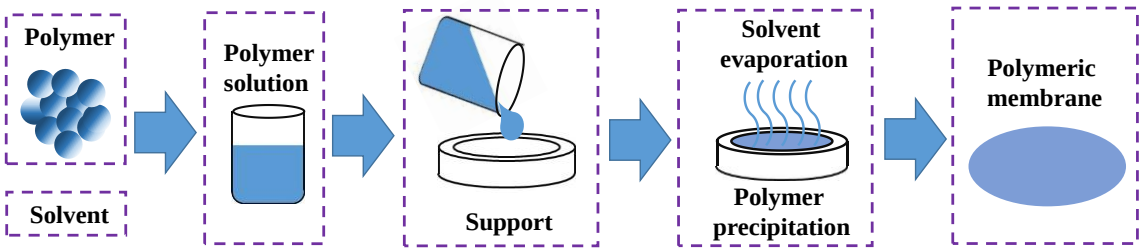

Figure 1.7. Schematic representation of the preparation of a polymeric membrane by the casting method.

The casting method also allows polymer chains impregnation with chemical entities that can be previously solubilized and added to the polymer solution or be solubilized in the polymer solution. Similarly, composite membranes can be prepared by suspending insoluble particles in the polymer solution.

The casting method is being employed for the preparation of LDH-polymer composites membranes aiming different applications, such as exchange membrane fuel cells[180,181], for removal of contaminants[182], and as biomedical devices for controlled release of drugs[183].

1.1.6.2. Polymers used in biomedical devices

1.1.6.2.1. Poly(lactic acid)

Poly(lactic acid) (PLA), 2-hydroxy propionic acid, is a polyester formed by the condensation of lactic acid units, whose chemical structure is presented in **Figure 1.8**. Besides being non-toxic and biocompatible, it is biodegraded in physiologic conditions through hydrolysis of ester bond backbone to products that are easily excreted by kidneys.[184] PLA is synthesized from renewable and abundant resources, such as corn starch, potato, or sugar cane.[185] Since biobased and biodegradable, PLA is defined as an eco-friendly polymer. PLA production spends from 25 to 55 % less energy compared to polymers obtained from petroleum. Moreover, PLA is thermoplastic and presents physical properties (*e.g.* thermal, mechanical, and optical) comparable to other commercial polymers, such as polystyrene, poly(ethylene terephthalate), and polypropylene. Thus, it is a promising substitute to petrol-based polymer in plasticulture and packing industry.[184,186]

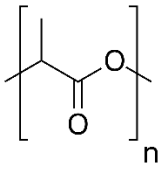

Figure 1.8. Chemical structure of PLA.

Although PLA is approved by the Food and Drug Administration (FDA) with respect to more intimate contact with biological fluids, medical applications of PLA were initially limited due to processing issues. High molar weight polymer is now possible and PLA can be submitted to diverse techniques, such as injection, extrusion, blow molding, thermoforming, and electrospinning.[185]

PLA may compose diverse biomedical devices, such as implantable membranes and dressings aiming drug delivery[187] and absorbable sutures[188], arising special attention for the development of biomaterials for tissue and organ engineering. In this way, PLA composites grafting bone implants are found to stimulate bone integration and promote hard tissue regrowth.[186] PLA polymer devices may hold species such as bio-signaling and growth factors to enhanced cell adhesion and proliferation, promoting wound healing.

1.1.6.2.2. PEBAX®2533 member of the poly(ether)-block-poly(amide) family

PEBA comprises a wide family of synthetic thermoplastic elastomer block copolymers formed by polyether (PE) that confer elasticity, called soft portions, and by polyamide (PA) units that confer rigidity to the chains, called hard segments. PEBA attracts attention due to its unique mechanical performance and also due to the possibility to modulate polymer properties by changing the compositions of the PE and PA units and the proportions among them.[189] PEBAX®MED are compositions indicated to medical applications. Some characteristics that make PEBAX®MED promising to medical applications include the ease with which it can be sterilized, being resistant to detergents, bleach and anti-infective agents, high selectivity and permeability, and long-term stability.[190] PEBAX®2533 applied in this work is composed

of 80 wt % poly(tetramethylene oxide) and 20 wt % poly(amide)-12, as PE and PA portions, respectively (**Figure 1.9**).

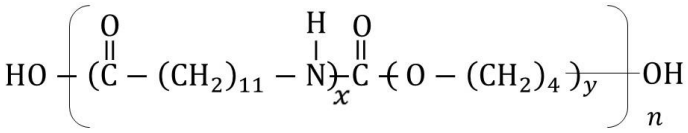

Figure 1.9. Chemical structure of PEBAX®2533.

PEBAX® is already applied for the production of catheters[191,192] and angioplasty balloons[193]. However, in literature, studies involving PEBAX® are mostly focused on gases separation. Zhang *et al.*[194] studied the performance of PEBAX®2533, PEBAX®3533, and PEBAX®4033 membranes containing tween 20 for separation of CO_2 and N_2 gases, prepared by solvent casting method. Nafisi *et al.*[195] prepared a membrane composed by a dual layer PEBAX®2533 obtained by casting method and zeolitic imidazolate metal-organic framework (MOF) as filler for CO_2 capturing. Ardestani *et al.*[196] fabricated PEBA nanocomposites, with PEBA composed by poly(amide)$_6$ and polyethylene oxide portions, by dip-coating a ceramic support by PEBA solution for purposes of separation of CO_2 and N_2 gases. Thanakkasaranee *et al.*[197] prepared PEBAX®MH165 films with temperature-dependent permeation, also by casting method. Besides gas separation, PEBA membranes have being studied for solvent sorption[198] and bio-ethanol recovery[199] by applying MOV / PEBAX®2533 membrane. Other studies concern the improvement of PEBAX® properties, such as the work of Shirole *et al.*[200], in which it were developed shape memory composites prepared sandwiching electrospun poly(vinyl alcohol) fibers with PEBAX®-6333, and the work of Oliveira *et al.*[201], in which silver nanoparticles were immobilized into PEBAX®2533 membranes prepared by casting method, conferring a bactericidal property for the composite.

To the best of our knowledge, despite the studies presented in this thesis, no works could be found concerning PEBA and LDH composites.

Chapter 2: Aims and Organization of the Thesis

2. Aims and organization

2.1. Aims of the thesis

The main aims of this thesis are to study the incorporation of Fe^{3+} cations into LDH structure and develop Fe^{3+}-LDHs and their polymer composites to act as biomaterials.

More specifically:

(1) to obtain LDHs composed by as higher as possible amount of Fe^{3+} cations;

(2) to study the influence of Fe^{3+} in structural and compositional properties of LDHs;

(3) to evaluate possible impurities from the Fe^{3+}-LDHs synthesis and properly determining the composition of the samples;

(4) to study the intercalation of different anionic bioactive species into the Fe^{3+}-LDHs by coprecipitation method and ion-exchange reaction;

(5) to develop polymer/Fe^{3+}-LDHs composites aiming multifunctional therapeutic membranes such as implantable devices or dressings.

2.2. Organization of the thesis

The results presented in this thesis are divided into two main parts, consisting of a total of seven chapters, whose resumed content is displayed in **Figure 2.1**. The first part comprises **Chapters 3**, **4,** and **5**, concerning systematic studies to investigate the progressive incorporation of Fe^{3+} cations into LDH and its effect on the structure, composition, and properties of the materials. In **Chapter 3**, both $Mg_2Fe_yAl_{(1-y)}$-Cl and $Zn_2Fe_yAl_{(1-y)}$-Cl series of LDHs, with *y* equal to 0, 0.25, 0.5, 0.75, or 1, are investigated. The M^{2+}/M^{3+} molar ratio (R) equal to 2 was chosen since it allows a high iron content and, consequently, a higher charge density in LDHs layers, conducting to high drug loading capacity. Chloride anions were chosen due to their intrinsic biocompatibility[202] and the possibility to compose LDHs-Cl acting as biomaterials[73,115]. Synthetic parameters were adjusted aiming to achieve both optimal purity and crystallinity. Iron incorporation and the evaluation of phase purity are central aims explored in **Chapter 3**. Materials were characterized by X-ray diffraction (XRD), infrared (FTIR) and Raman spectroscopies, thermal, and elemental analysis which, in practice, are the usual and basic characterization techniques applied to determine LDH's structure and composition in

literature. Complementary techniques including full-profile refinements of XRD data, geometrical reasoning of LDH structures and pair distribution function (PDF) analysis of X-ray total scattering data are presented as auxiliary techniques to better understand materials structure and to avoid misleading concerning their compositions. The formation of continuous solid solutions for both series is investigated. **Chapters 4** and **5** explore the two most applied techniques for preparation of hybrid organic-inorganic LDHs, *i.e.* ion-exchange and coprecipitation, as well as the influence of the presence of iron in the preparation of the materials by both synthetic methods. More specifically, **Chapter 4** is related to the capacity of the $Mg_2Fe_yAl_{(1-y)}$-Cl and $Zn_2Fe_yAl_{(1-y)}$-Cl pristine LDHs to participate in ion-exchange replacement of Cl^- by NAP anions. The NAP/ M^{3+} molar ratio and the temperature of ion-exchange were also investigated. Moreover, the submission of pristine LDHs to ion-exchange may provide additional information and confirm structural and compositional hypothesis made in **Chapter 3**. In its turn, in **Chapter 5** it is showed for the first time the capacity of LDH to intercalate ABI anions. Both series of LDHs, with $Mg_2Fe_yAl_{(1-y)}$ and $Zn_2Fe_yAl_{(1-y)}$ layer compositions, intercalated with ABI anions were prepared by the coprecipitation (one-pot) method. The same basic characterization techniques applied in **Chapter 3** are used for the evaluation of LDH-ABI and LDH-NAP materials, in some cases including similar studies concerning iron-incorporation and a proper materials composition determination by geometric reasoning of the LDH structure. ABI and NAP were primarily considered as model anions. However, they are also considered promising guest bioactive species, as discussed above. The final purpose of these three studies consists in the preparation of single Fe^{3+}-based LDH phases, containing as higher as possible Fe^{3+} instead of Al^{3+} cations, aiming more adequate LDHs compositions for application as biomaterials, in general, and the preparation Fe^{3+}-LDH/polymer composites, subject of the second part of this thesis.

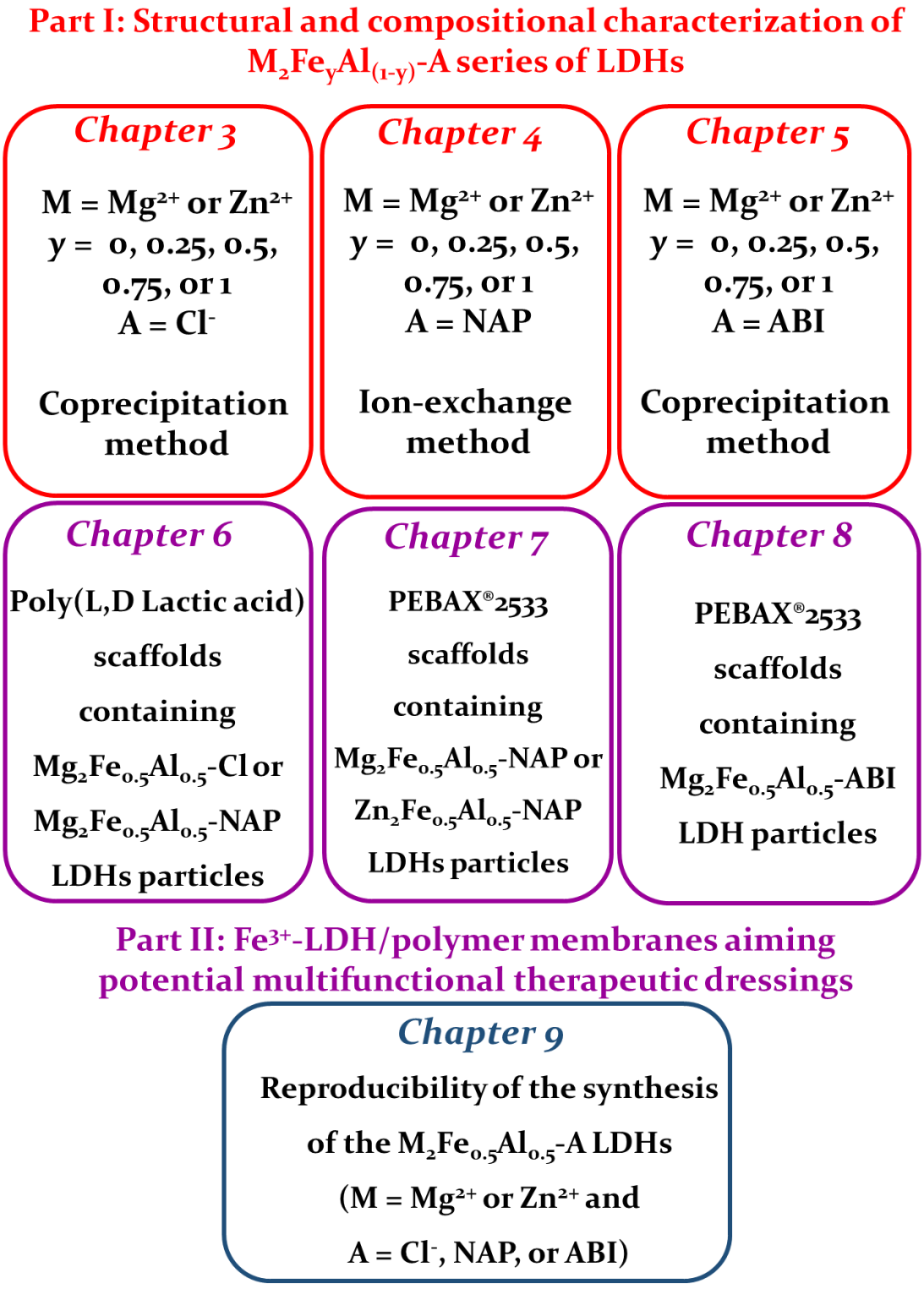

Figure 2.1. Resume of results and discussions divided by chapters.

After careful analysis of the Fe^{3+}-LDH compositions, based on purity and capacity for ABI and NAP anions intercalation, the intermediate layer compositions $Mg_2Fe_{0.5}Al_{0.5}$ and $Zn_2Fe_{0.5}Al_{0.5}$ were selected for further application as components of LDH-polymer composite membranes, in the second part of the results and discussions section. **Chapter 6** presents membranes composed by poly(L,D lactide) (PLA), aiming topical or implantable devices, elaborated from the combination of electrospinning and electrospraying processes, showing interesting properties coming from the presence of both nanofibers and microparticles components. Two kinds of membranes having different structures and made of PLA electrospun nanofibers and drug-loaded LDH electrosprayed microparticles were elaborated in order to modulate the kinetics of drug release, *in vitro* assessed, while avoiding the use of any hydrophilic adjuvant. Multilayer membranes with LDH particles sandwiched between PLA fibrous layers of various thicknesses were studied and compared to membranes in which the LDH particles were entrapped in the fibrous PLA mesh. PLA was chosen as polymer due to its biocompatibility, good mechanical properties, and performance for fibers formation. The $Mg_2Fe_{0.5}Al_{0.5}$-NAP LDH was the chosen solid component. To compare the effect of the organic anions regarding the interaction between LDHs particles and fibers, similar membranes were prepared with the $Mg_2Fe_{0.5}Al_{0.5}$-Cl LDH precursor. **Chapter 7** is concerned with the development of polymer-LDH composites prepared by casting method, based on the PEBAX®2533 (PEBA) polymer and $Mg_2Fe_{0.5}Al_{0.5}$-NAP or $Zn_2Fe_{0.5}Al_{0.5}$-NAP LDHs, aiming multifunctional therapeutic wound dressings. For comparison, pristine PEBA membrane and the membranes containing only NaNAP (not intercalated into LDH) or pristine $Mg_2Fe_{0.5}Al_{0.5}$-Cl or $Zn_2Fe_{0.5}Al_{0.5}$-Cl LDHs were also prepared. Membranes were structurally characterized by XRD, vibrational FT-IR spectroscopy, thermal analysis, vertical mechanical resistance, and static water contact angle. *In vitro* drug release profile and *in vitro* cytotoxicity were assessed. Finally, **Chapter 8** presents for the first time the *in vitro* ABI release profile from the LDH, $Mg_2Fe_{0.5}Al_{0.5}$-ABI composition. Previously, it was determined the NaABI solubility in the same medium and conditions (solution type and temperature) applied for the drug release experiments. The $Mg_2Fe_{0.5}Al_{0.5}$-ABI LDH was applied for the preparation of an LDH-polymer composite based on the same PEBA polymer and prepared by the same method applied in **Chapter 7**, aiming wound dressings. PEBA membrane containing

NaABI was also prepared and studied for comparison. Membranes were structurally characterized by similar methods employed in **Chapter 7**. Finally, **Chapter 9** compiles elemental analysis (metals and carbon percentage) of the $M_2Fe_{0.5}Al_{0.5}$-A LDHs (with A = Cl^-, NAP, or ABI) presented in this thesis and applied in its second part and the associated deviations, important to validate compositional inferences made along with the thesis and also to approximate the production of these materials to the large scale.

Chapter 3: Synthesis and characterization of $Mg_2Fe_yAl_{(1-y)}$-Cl and $Zn_2Fe_yAl_{(1-y)}$ -Cl LDHs: insights on Fe^{3+} incorporation into LDH

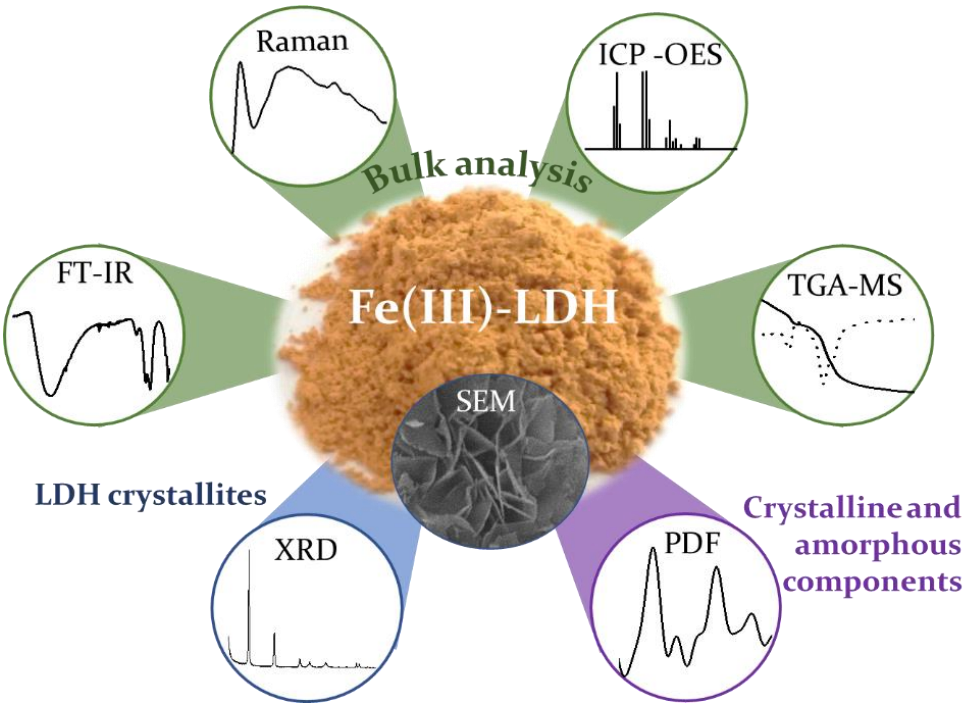

3. Abstract and data presentation

3.1. Abstract

As discussed in the introduction section, LDH and related composites have attracted much attention for biomedical applications and the development of LDH drug carriers composed of endogenous metals, such as Fe^{3+}, is of great interest. However, most of the studies reported so far on iron-containing LDH, mainly focusing on the applications, suffer from insufficient data and limited understanding of the synthesis, the composition, and the structure of these materials. The studies presented in this chapter involve the synthesis of $Mg_2Fe_yAl_{(1-y)}$-Cl and $Zn_2Fe_yAl_{(1-y)}$-Cl LDH materials with the molar ratio between the di and trivalent cations (R) equal to 2 and $0 \leq y \leq 1$, and the use of complementary spectroscopic, microscopic, thermal and scattering techniques for the evaluation of their compositional and structural properties. By combining crystal-chemical reasoning and pair distribution function (PDF) analysis, it was possible to differentiate between contributions from crystalline and amorphous components. For Mg-series, when the iron content exceeds that of aluminium ($y > 0.5$), the compositions were found to slightly deviate from that expected with an increase in the value of R tending to 3. For Zn-series, more heterogeneous samples were obtained. Iron incorporation in the crystalline LDH component was observed up to y equal to 0.75 (nominal value), then an amorphous product was observed for y equal to 1. For $y \geq 0.5$ the presence of the amorphous 2-line ferrihydrite was clearly demonstrated by PDF analysis and it is the major phase for $y = 1$. Although never reported so far, the precipitation of ferrihydrite for the Zn_RFe-based LDHs is not surprising given the synthesis conditions applied, with a pH value of 7.5. As well as providing a reliable approach to the characterization of Fe^{3+}-LDHs, this study also gives useful elements for better understanding and interpreting the results reported in the literature regarding these phases. Results shown in this chapter are published as an article in *the Journal of Alloys and Compounds*, 886 (2021) 161184, Copyright Elsevier (please, see https://doi.org/10.1016/j.jallcom.2021.161184 and the original abstract in **Appendix B**).

3.2. Materials and Methods

3.2.1. Reagents

Magnesium chloride hexahydrate ($MgCl_2 \cdot 6H_2O$) (99 %), zinc chloride ($ZnCl_2$) (≥ 99 %), aluminum chloride hexahydrate ($AlCl_3 \cdot 6H_2O$) (99 %), ferric chloride hexahydrate ($FeCl_3 \cdot 6H_2O$) (98 %), sodium hydroxide (NaOH) (≥ 98 %), D-sorbitol (> 98 %), and absolute ethanol were acquired from Sigma-Aldrich. Deionized water was obtained from a Millipore water purification system.

3.2.2. Synthesis of the $Mg_2Fe_yAl_{(1-y)}$-Cl and $Zn_2Fe_yAl_{(y-1)}$-Cl series

Samples were prepared by the coprecipitation method and labelled according to the starting molar ratios used for the synthesis *i.e.* $M_2Fe_yAl_{(1-y)}$-Cl in which M is either Mg^{2+} or Zn^{2+} with a $M^{2+}/(Al^{3} + Fe^{3+})$ molar ratio that is equal to 2 and *y* corresponding to the substitution molar ratio of Al^{3+} for Fe^{3+}. Preliminary tests were performed on $Mg_2Fe_{0.5}Al_{0.5}$-Cl nominal composition to adjust the following synthetic parameters based on the work of Sun *et al*[203]: salts solution concentration (0.05 and 0.1 mol L^{-1}), temperature (room temperature or 50 °C) and stirring method (magnetic at 400 rpm or mechanical stirring at 900 rpm). A Fisatom plate model 752A was employed for the magnetic stirring and a Fisatom homogenizer model 713D for the mechanical stirring. The pH value was set to 10.5 by the addition of 0.2 mol L^{-1} NaOH solution. The analyses carried out for these tests are presented and discussed in **Appendix B.** Optimal conditions for the synthesis of the $Mg_2Fe_{0.5}Al_{0.5}$-Cl LDH in terms of crystallinity and apparent homogeneity were obtained for a salt solution concentration of 0.05 mol L^{-1}, a mechanical stirring at 900 rpm, and a temperature of 50°C. These conditions were then applied to all members of Mg series. They were also applied for Zn series except for the temperature, since heating may lead to the formation of $ZnO/Zn(OH)_2$ as often reported in the literature[84,85,88,98–108], and the pH set to 7.5 (see **Appendix B**: **Figure B.4** and discussions).

In more details, around 190 mL of 0.05 mol L^{-1} chloride salts solution containing the metal cations in appropriate molar amounts to obtain the iron content (*y* value) 0, 0.25, 0.5, 0.75, or 1 were added into a reactor vessel prefilled with 200 mL of deionized water

under nitrogen flow at an addition rate of 0.4 mL min^{-1}, while the pH value was controlled by the simultaneous addition of a 0.2 mol L^{-1} NaOH solution. Following the completion of the addition of the salt solution (for around 8 hours), the precipitate was left in the solution for one hour at the same temperature and stirring condition, and was then recovered by filtration under reduced pressure, washed with deionized water followed with absolute ethanol and finally dried at room temperature under reduced pressure in a desiccator.

3.2.3. Characterization

X-ray diffractometry (XRD) analysis for the synthesis conditions optimization tests were performed using a D8 Discover Bruker with a LYNXEYE XE-T detector, using CuKα_1/ Kα_2 radiation (1.5406/1.5444 Å) source in Bragg Brentano θ-θ geometry, scan range 1.5 – 70° (2θ) and scan step of 0.05° / 8 s. The subsequent XRD measurements for the characterization of $Mg_2Fe_yAl_{(1-y)}$-Cl and $Zn_2Fe_yAl_{(1-y)}$-Cl series were performed on a Philips X'Pert pro diffractometer equipped with a X'celerator 1D detector (2.122° active length), using CuKα_1/ Kα_2 source in Bragg Brentano θ-θ geometry. XRD patterns were scanned through steps of 0.016°(2θ) from 5 to 90°(2θ).

The lattice parameters for both series were refined using the Le Bail[204] whole powder XRD pattern decomposition method with FullProf suite package[205] and assuming R-3m space group as usually reported for LDH[206]. To properly reproduce XRD peak profile and reach good fits, it was necessary to consider microstructural effects in particular anisotropic size effects related to the platelet morphology of LDH particles. Peak broadening coming from anisotropic size effect was modelled with linear combinations of spherical harmonics[207] as implemented in FullProf which then allowed the calculation of the volume-averaged apparent size of the coherent domains along each reciprocal lattice vector. Dimensions according to the 110 (L_{110}) and 00*l* (L_{00l}) directions are of particular interest being related to the coherence lengths within LDH hydroxide layers and along the stacking direction, respectively. LaB_6 NIST standard was used to correct for instrumental broadening.

The atomic Pair Distribution Functions (PDF) were obtained from X-ray total scattering data collected on a PANalytical Empyrean diffractometer equipped with a

solid state GaliPIX3D detector, a focusing X-ray multilayer mirror, and an Ag anticathode (Kα1 = 0.5594214 Å, Kα2 = 0.5638120 Å). Powder samples were mounted in glass capillaries of 0.7 mm diameter. An empty capillary of the same type was measured in the same way for background subtraction. Data were recorded over the range $1 < 2\theta < 145°$, which corresponds to an accessible maximum value for the scattering vector Q max of 21.4 $Å^{-1}$. Data merging, background subtraction, and Kα2 stripping were done using HighScore Plus software, provided by PANalytical Corporation. It was also used to generate a corrected and normalized total scattering structure functions S(Q) and finally the PDF or G(r) were calculated from the Fourier transforms of the reduced structure functions truncated at 21 $Å^{-1}$. The bulk chemical composition of the materials was used for the normalization of S(Q).

Direct observations of LDH particles from samples involved in optimization tests were obtained by scanning electron microscopy (SEM) using a FE-SEM Jeol JSM 7401F equipment; samples were prepared by simple powder deposition onto double sided adhesive copper tape. A Jeol JSM 6610LV equipment was used for imaging $Mg_2Fe_yAl_{(1-y)}$-Cl and $Zn_2Fe_yAl_{(1-y)}$-Cl sample series after gold sputter coating.

Thermogravimetric analysis coupled to mass spectrometry (TGA-MS) was performed on a Netzsch thermoanalyser model TGA/DSC 490 PC Luxx coupled to an Aëolos 403 C mass spectrometer, using alumina crucibles with a heating rate of 10 °C min^{-1} from room temperature until 1000 °C, under a synthetic air flow of 50 mL min^{-1}, and applying around 10 mg of sample.

Quantitative analyses of Mg, Zn, Fe, and Al were performed by inductively coupled plasma optical emission spectroscopy (ICP-OES) in a Spectro Analytical equipment, Arcos model, at the *Central Analítica* of *Instituto de Química* (*Universidade de São Paulo* – USP). Sampling was executed in duplicate. *A*pproximately 10 mg of solid sample was dissolved with 2 mL of boiling concentrated HNO_3 until complete dissolution. Translucent solutions were transferred to 100 mL volumetric flasks and the volume was adjusted with deionized water.

Fourier transform infrared (FT-IR) spectra of powdered samples were recorded on a Bruker spectrophotometer, model Alpha, in attenuated total reflectance (ATR) mode with a resolution of 4 cm^{-1} and 512 scans in the 4000–400 cm^{-1} range.

Raman spectra were recorded at –100 °C in a Renishaw inVia spectrometer coupled with a Leica optical microscope (RE04) with a CCD detector, using a diode laser at 785 nm (Renishaw HPNIR785), a laser potency of 5 mW (1 % of the maximum beam potency) and quintuple accumulation. Low temperature was applied to limit materials luminescence and samples decomposition. Component analysis of vibrational spectra of LDH samples was performed using *OriginPro® 9* software by applying the Voigt function, product of Gaussian and Lorentzian functions, on baseline discounted curves.[208] The minimum number of component bands was considered for the fitting process, carried out until the obtention of reproducible results with R-Squared (R^2 or the coefficient of determination) values greater than 0.995.

Particle hydrodynamic size distribution of LDH samples involved in optimization tests were measured in a Malvern Zetasizer Nano ZS equipment through dynamic light scattering (DLS). A fifth of a 5 mL Eppendorf tube was filled with the LDH slurry just after the washing procedure plus 4 mL of deionized water. The suspension was submitted to ultrasound bath (Limp-Sonic Ciencor equipment, model LS-3D-3/X) for 2 h. Then, it was added 0.5 mL of a 0.1 mol L^{-1} sorbitol aqueous solution and the suspensions were submitted to the ultrasound bath for two more hours.

3.3. Results

3.3.1. Initial inspection of $Mg_2Fe_yAl_{(1-y)}$-Cl and $Zn_2Fe_yAl_{(1-y)}$-Cl compositional series

XRD patterns of $Mg_2Fe_yAl_{(1-y)}$-Cl and $Zn_2Fe_yAl_{(1-y)}$-Cl samples are showed in **Figures 3.1** and **3.2**, respectively, and they are typical of LDH materials.[39] Bragg peaks were indexed considering a hexagonal cell with R-3m space group, usually reported for powdered LDH by reference to Quintinite and Hydrotalcite crystal minerals[37]. Actually, the relatively low crystallinity of the samples does not allow us to consider another crystal system such as a monoclinic cell as reported elsewhere[209]. It may be recalled that in R-3m space group, the position of the (003) peaks are related to the

interlamellar distance while the (110) peak is related to the distance between adjacent metal cations thus on their ionic radii within the hydroxide layers, and it follows that $a = 2xd_{110}$ and $c = 3xd_{003}$.

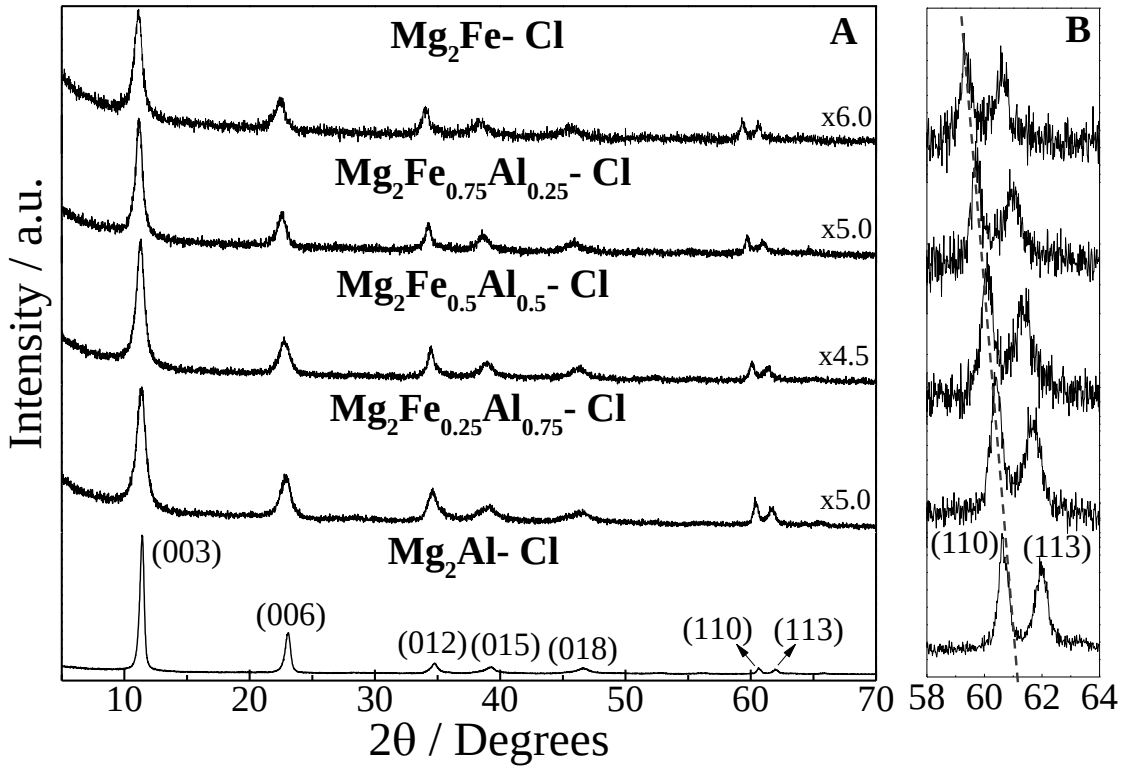

Figure 3.1. (A) XRD patterns of $Mg_2Fe_yAl_{(1-y)}$-Cl samples. (B) Magnification in the 58 – 64° (2θ) range; the dotted line shows the shift of the (110) peak to the left as *y* increases.

For both series, the signal to noise ratio decreases significantly between the first composition (*y* = 0) and the followings, which indicates a decrease of the crystallinity as soon as iron is introduced in LDH layers. Mg-series appears to consist of pure LDH single phases in the whole composition range. The broadening of the Bragg peaks along the series can be related to a progressive loss of structural order and/or a decrease of the coherent domain size. For Zn series, the last composition (*y* = 1) is practically amorphous with only two broad peaks observed on the XRD pattern centered at *ca.* 35.0° and 61.2° (2θ) attributed to amorphous 2-line (2 main lines visualized in XRD) ferrihydrite (FH) as will be demonstrated below in the second part of this study [210–212]. For $Zn_2Fe_{0.75}Al_{0.25}$-Cl sample, one can note the presence of additional low intense peaks identified with an asterisk in **Figure 3.2** and attributed to the presence of $Zn(OH)_2$ and ZnO phases.[213,214]

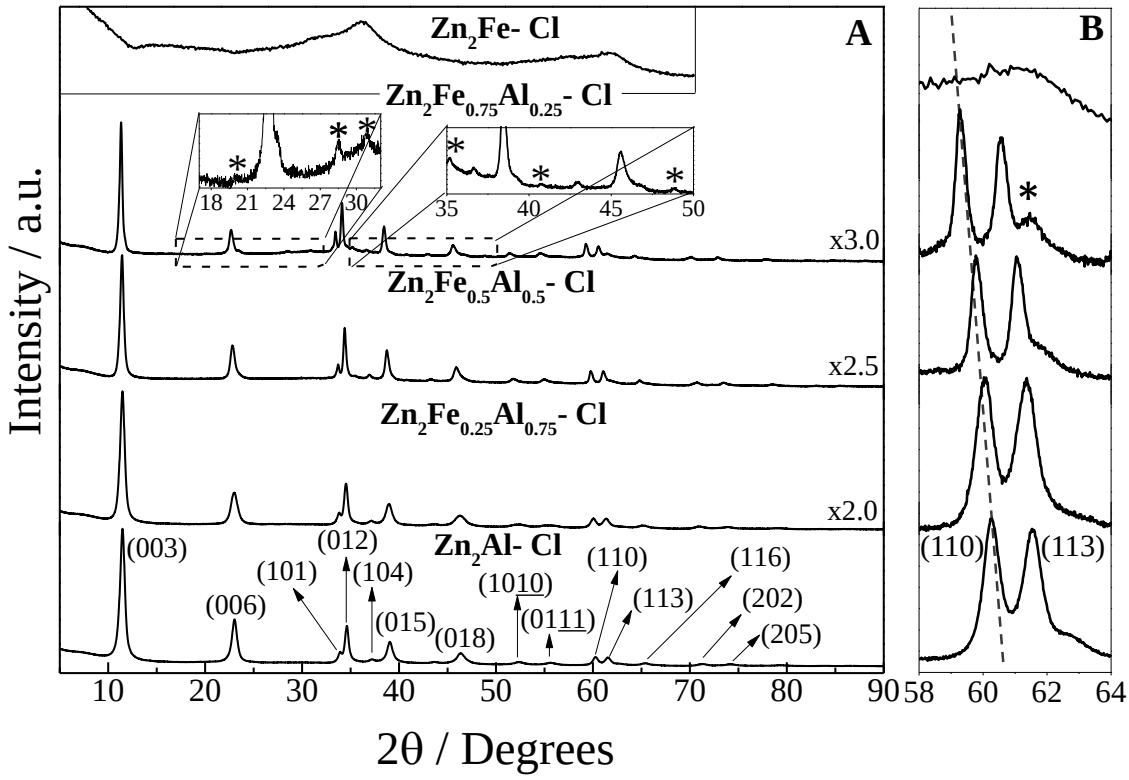

Figure 3.2. (A) XRD patterns of the $Zn_2Fe_yAl_{(1-y)}$-Cl samples; (*) indicates the presence of $Zn(OH)_2$ and ZnO phases. (B) Magnification in the 58 – 64 (2θ) range; the dotted line shows the shift of the (110) peak to the left as *y* increases.

The gradual shift of the (110) peaks towards lower angles for both series (**Figures 3.1B** and **3.2B**) is consistent with the gradual incorporation of Fe^{3+} into the hydroxide layers by substitution of Al^{3+}, with the ionic radii of Fe^{3+} and Al^{3+} in six-fold coordination being 0.645 and 0.535 Å[38], respectively. On the other hand, for $M^{2+}/(Al^{3+}+Fe^{3+})$ molar ratio being constant and close to 2, the charge density of the layers does not change, therefore the interlayer content is not expected to vary and neither is the (003) peak position.

The chemical compositions of the samples are given in **Table 3.1**. Mg, Zn, Al, and Fe elements were quantified by ICP-OES analysis and the analytical error for this analysis is considered to be ± 2 %. For Mg series, the M^{2+}/M^{3+} molar ratios (R) obtained are very close to the value of 2 applied during the synthesis. The amounts of water were deduced from TGA analysis, as discussed further. On the other hand, for Zn series, except for Zn_2Al-Cl and $Zn_2Fe_{0.25}Al_{0.75}$-Cl samples, the chemical compositions of the bulk differ more compared to those expected and the differences are more related to the value of R than to the value of *y*. It may also be noted that for Zn_2Fe-Cl sample the experimental

molar ratio obtained, *i.e.* R = 1.16, is not consistent with the formation of LDH hydroxide layers.

Table 3.1. Bulk chemical composition of the synthesized samples.

Sample	$\frac{M^{2+}}{Al^{3+}}$	$\frac{M^{2+}}{Fe^{3+}}$	$y = \frac{Fe^{3+}}{Fe^{3+} + Al^{3+}}$	$R = \frac{M^{2+}}{Fe^{3+} + Al^{3+}}$	% H_2O[c]
Mg_2Al-Cl	(2.00)[a] 2.04[b]				11.2
$Mg_2Fe_{0.25}Al_{0.75}$-Cl	(2.67) 2.71	(8.00) 8.25	(0.25) 0.25	(2.00) 2.04	12.8
$Mg_2Fe_{0.5}Al_{0.5}$-Cl	(4.00) 4.23	(4.00) 4.01	(0.50) 0.48	(2.06) 2.06	12.4
$Mg_2Fe_{0.75}Al_{0.25}$-Cl	(8.00) 8.27	(2.67) 2.64	(0.75) 0.76	(2.00) 2.00	13.4
Mg_2Fe-Cl		(2.00) 1.96			13.1
Zn_2Al-Cl	(2.00) 1.96				9.5
$Zn_2Fe_{0.25}Al_{0.75}$-Cl	(2.67) 2.59	(8.00) 8.74	(0.25) 0.23	(2.00) 2.00	11.1
$Zn_2Fe_{0.5}Al_{0.5}$-Cl	(4.00) 3.53	(4.00) 3.47	(0.50) 0.50	(2.00) 1.75	9.7
$Zn_2Fe_{0.75}Al_{0.25}$-Cl	(8.00) 7.99	(2.67) 2.51	(0.75) 0.76	(2.00) 1.91	----
Zn_2Fe-Cl		(2.00) 1.16			----

(a) Nominal molar ratios between the cations according to the reagents stoichiometry; (b) experimental molar ratios between the cations determined by ICP; (c) water amount (m/m) released in TGA mass loss event(s) related to dehydration.

The unit-cell parameters *a* and *c* for both sample series given in **Table 3.2** were accurately determined by full-profile refinement of the XRD patterns by the *Le Bail* method for the $M_2Fe_yAl_{(1-y)}$-Cl materials, whose results are shown in **Appendix B** (**Figures B.5** and **B.6**). A linear variation of *a* cell parameter as a function of the amount

of iron (*y)* experimentally measured is observed for both series as shown in **Figure 3.3** which may indicate the existence of a continuous solid solution in the whole domain for Mg series and up to *y* = 0.75 for Zn series. The slopes of the linear regression curves being quite similar, the incorporation of iron into Mg_2Al and Zn_2Al LDH layers is indicated to proceed in the same way. This result may seem surprising in the case of Zn series given the differences in chemical compositions observed between nominal and experimental values (**Table 3.1**), unless it is considered that the crystallised components have a chemical composition different from the bulk and close to that expected.

Table 3.2. *a* and *c* lattice parameters of the hexagonal unit-cell (R-3m) obtained by *Le Bail* refinement of powder X-ray diffraction data, as well as the basal spacing *d*.

Sample	***a*** **(Å)**	***c*** **(Å)**	***d*** **(Å)**
Mg_2Al-Cl	3.04572(8)	23.0085(6)	7.669
$Mg_2Fe_{0.25}Al_{0.75}$-Cl	3.05724(9)	23.194(2)	7.731
$Mg_2Fe_{0.5}Al_{0.5}$-Cl	3.0716(1)	23.283(2)	7.761
$Mg_2Fe_{0.75}Al_{0.25}$-Cl	3.0884(1)	23.478(2)	7.826
Mg_2Fe-Cl	3.1052(2)	23.611(4)	7.870
Zn_2Al-Cl	3.07104(3)	23.1769(4)	7.725
$Zn_2Fe_{0.25}Al_{0.75}$-Cl	3.07933(5)	23.2021(5)	7.734
$Zn_2Fe_{0.5}Al_{0.5}$-Cl	3.09740(3)	23.4670(7)	7.822
$Zn_2Fe_{0.75}Al_{0.25}$-Cl	3.11485(4)	23.5409(5)	7.847

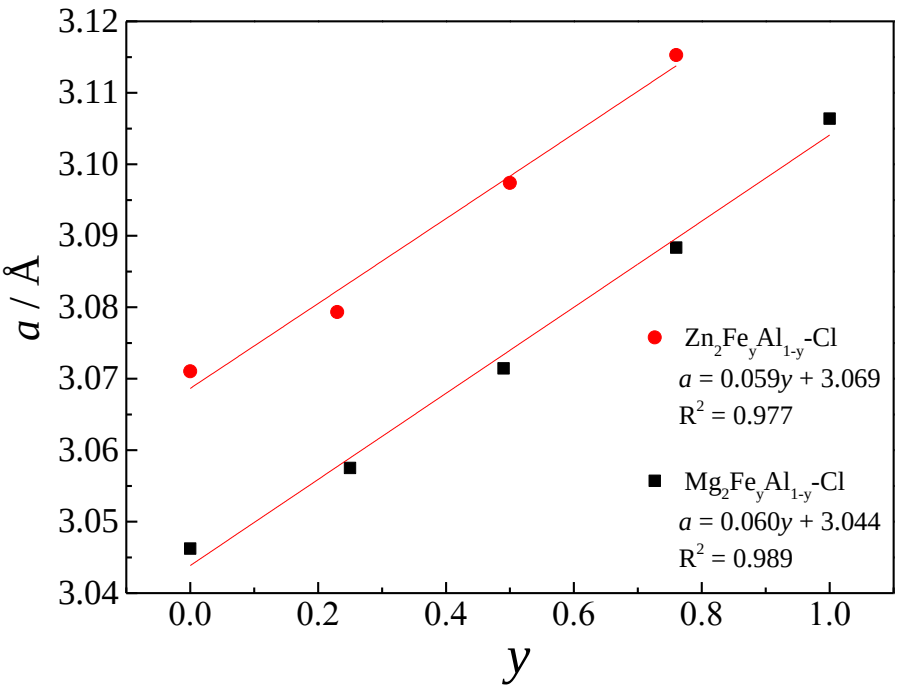

Figure 3.3. Variation of the lattice parameter *a* along $Mg_2Fe_yAl_{(1-y)}$-Cl and $Zn_2Fe_yAl_{(1-y)}$-Cl compositional series as a function of the amount of iron (*y*) experimentally measured.

The variation of the structural and physicochemical properties along both series was also investigated by IR/Raman spectroscopies and thermogravimetric analysis. **Figures 3.4** and **3.5** show the FT-IR spectra of $Mg_2Fe_yAl_{(1-y)}$-Cl and $Zn_2Fe_yAl_{(1-y)}$-Cl samples, respectively, in the 4000-400 cm^{-1} range. Several differences are pointed out between the two series concerning the O-H stretching region in the FT-IR spectra between 3750 and 2700 cm^{-1}, characterized by a very broad band ascribed to the overlap of bands related to the stretching of O-H of the layers and of the water molecules that can be intercalated (surrounding the hydroxylated layer and the confined anion[215]) and/or in the interparticle region. The spectra of Mg_2Al-Cl and Mg_2Fe-Cl samples reveal main broad bands located at about 3397 and 3387 cm^{-1}, respectively, *i.e.* a shift of 10 cm^{-1} in low energy direction is observed when the lighter Al^{3+} is replaced for Fe^{3+} (**Figure 3.4**). The spectral behavior of the Zn-series in the O-H stretching vibration is distinct in relation to the magnesium series (**Figure 3.5**) showing a shift of the broad bands to high energy when Fe^{3+} amount increase in the samples.

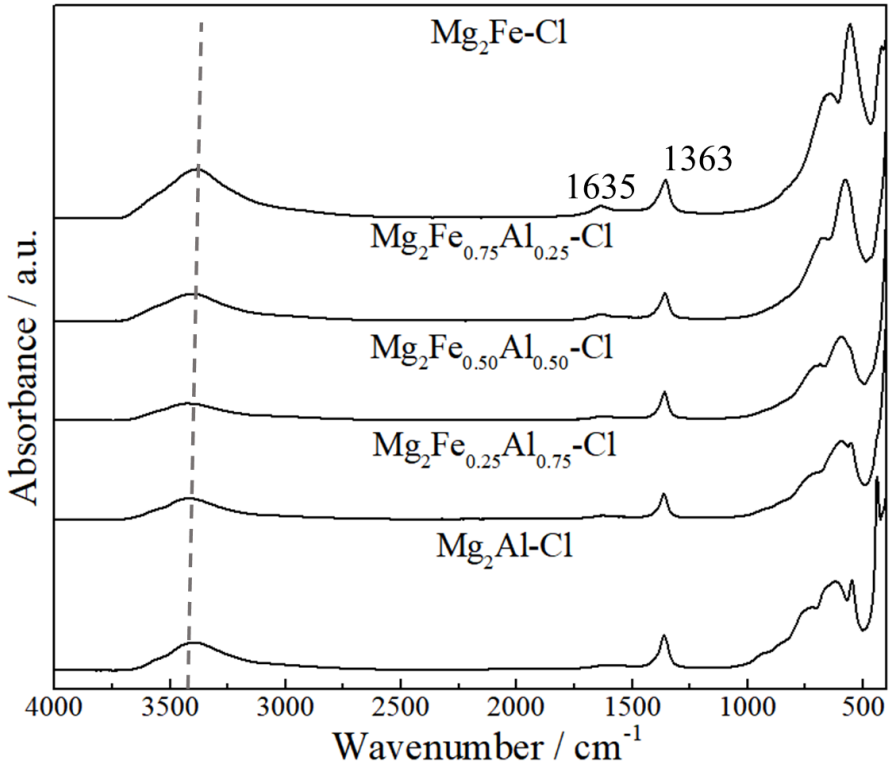

Figure 3.4. FT-IR spectra of $Mg_2Fe_yAl_{(1-y)}$-Cl samples.

The band assigned to the bending mode of water is visualized at around 1635 cm^{-1}. The band at 1360 cm^{-1} is related to the antisymmetric stretching of co-intercalated carbonate anion (CO_3^{2-}), present as a contaminant.[215] In comparison to the other materials, the spectrum of Zn_2Fe-Cl sample, whose LDH phase formation was not confirmed by XRD, shows the band attributed to O-H stretching at 3380 cm^{-1} and the appearance of the band at 1088 cm^{-1} and 1049 cm^{-1} that can be attributed to the Zn-OH twisting and bending modes of the zinc hydrixide[214], respectively, and the bands at 2976 cm^{-1} and 1468 cm^{-1}, that may also be assigned to the zinc oxyde[216] (**Figure 3.5**). The bands at 1468 and 1049 cm^{-1} are also present in the spectrum of the $Zn_2Fe_{0.75}Al_{0.25}$-Cl sample, which impurities were also verified by XRD.

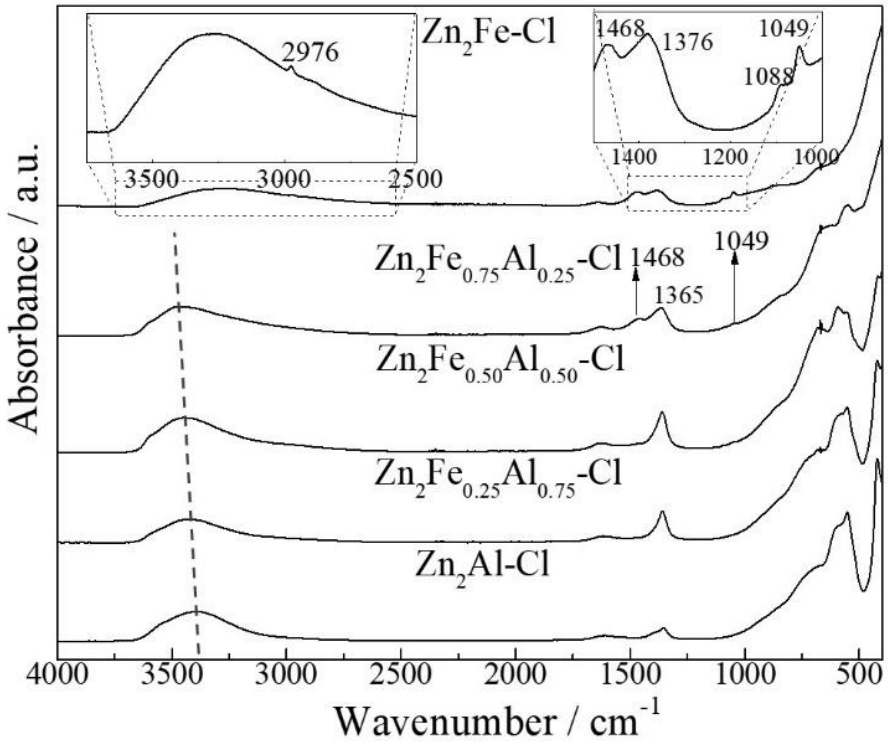

Figure 3.5. FT-IR spectra of $Zn_2Fe_yAl_{(1-y)}$-Cl samples.

Figure 3.6 shows the Raman spectra of $Mg_2Fe_yAl_{(1-y)}$-Cl and $Zn_2Fe_yAl_{(1-y)}$-Cl samples in the 1100 – 200 cm^{-1} range. Spectra of all samples from 1100 to around 600 cm^{-1} are very similar and present broad bands related to vibrational modes of hydroxyl groups and water molecules.[217] The band at 1064 cm^{-1}, present in the spectra of all Mg-LDH samples and with lower relative intensity in the spectra of the $Zn_2Fe_{0.25}Al_{0.75}$-Cl and $Zn_2Fe_{0.75}Al_{0.25}$-Cl samples, can be associated with the symmetric stretching of the CO_3^{2-} contaminant anions.

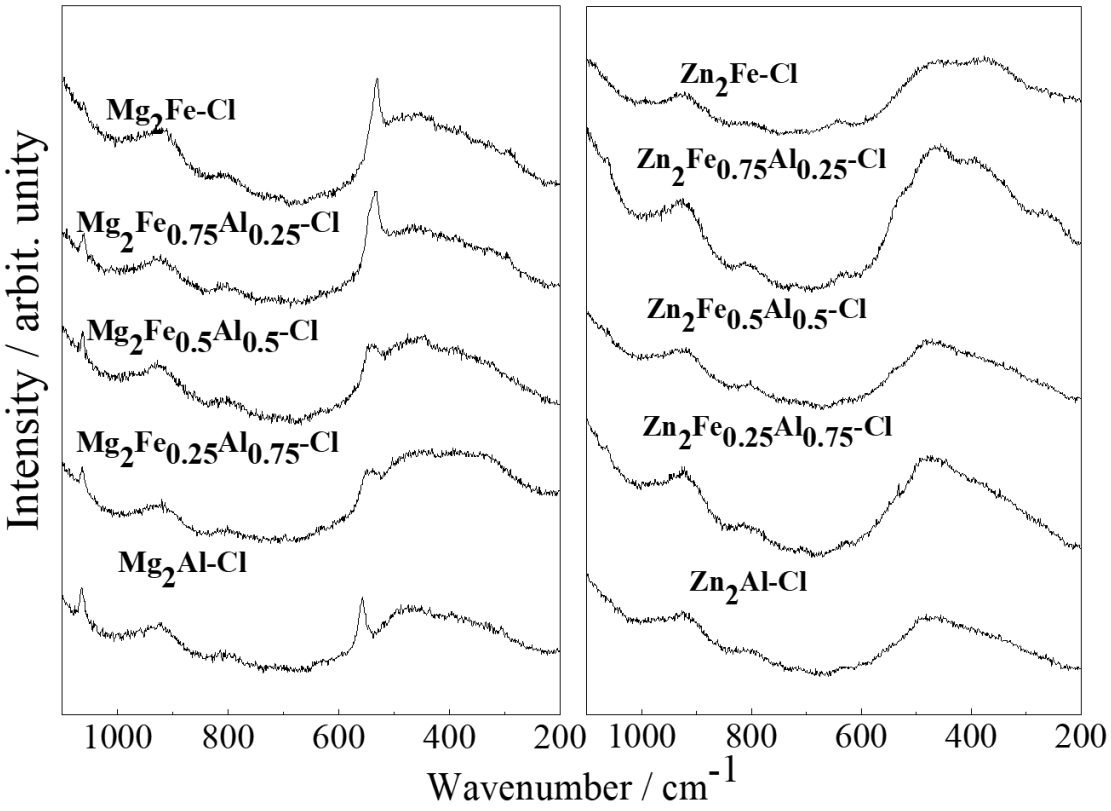

Figure 3.6. Raman spectra of $Mg_2Fe_yAl_{(1-y)}$-Cl (left) and $Zn_2Fe_yAl_{(1-y)}$-Cl samples (right).

Figure 3.7 shows the low frequency region of the FT-IR (1000 – 500 cm^{-1}) and Raman (600 – 200 cm^{-1}) spectra of $Mg_2Fe_yAl_{(1-y)}$-Cl samples, whose bands are attributed to M-OH vibration (rotatory) and M-OH translation (lattice) modes, as reported by Frost and coworkers.[218–220] The band component analysis of the IR spectrum of Mg_2Al-Cl sample shows bands at 550 and 772 cm^{-1} (**Figure 3.7A)** that can be assigned to hydroxide translation modes mainly influenced by the Al^{3+} cations (along with the corresponding deformation mode observed around 940 cm^{-1}) while the band at 610 cm^{-1} is mainly influenced by the Mg^{2+} cations. Along the Mg series, a gradual shift to lower frequency region is observed for the band assigned to M^{3+}-OH from 772 cm^{-1} for y = 0 to 677 cm^{-1} for y = 1, which is consistent with the replacement of Al^{3+} for Fe^{3+} cations due to the increase of the atomic mass of the trivalent cation. The two bands observed at 668 and 864 cm^{-1} can be attributed to the υ_4 and υ_2 modes of interlayer CO_3^{2-} anion, respectively[221]. This indicates a contamination by carbonate anions, better evidenced by the presence of the band at 1360 cm^{-1} characteristic of υ_3 mode (**Figures 3.4.** and **3.5**).

This contamination often takes place during the washing procedure and it is attributed to atmospheric CO_2 solubilization in water.[37] The Raman spectrum of Mg_2Al-Cl in **Figure 3.7B** shows a well-defined band at 558 cm^{-1} assigned to the Al-O-Al translation mode and its progressive downshift along Mg series corroborates XRD data, *i.e.* the aluminum substitution for the heavier Fe^{3+} ion within LDH hydroxide layers. The other bands at 506, 464, 390 and 318 cm^{-1} are related to both Mg/Al-OH translations.[218–220]

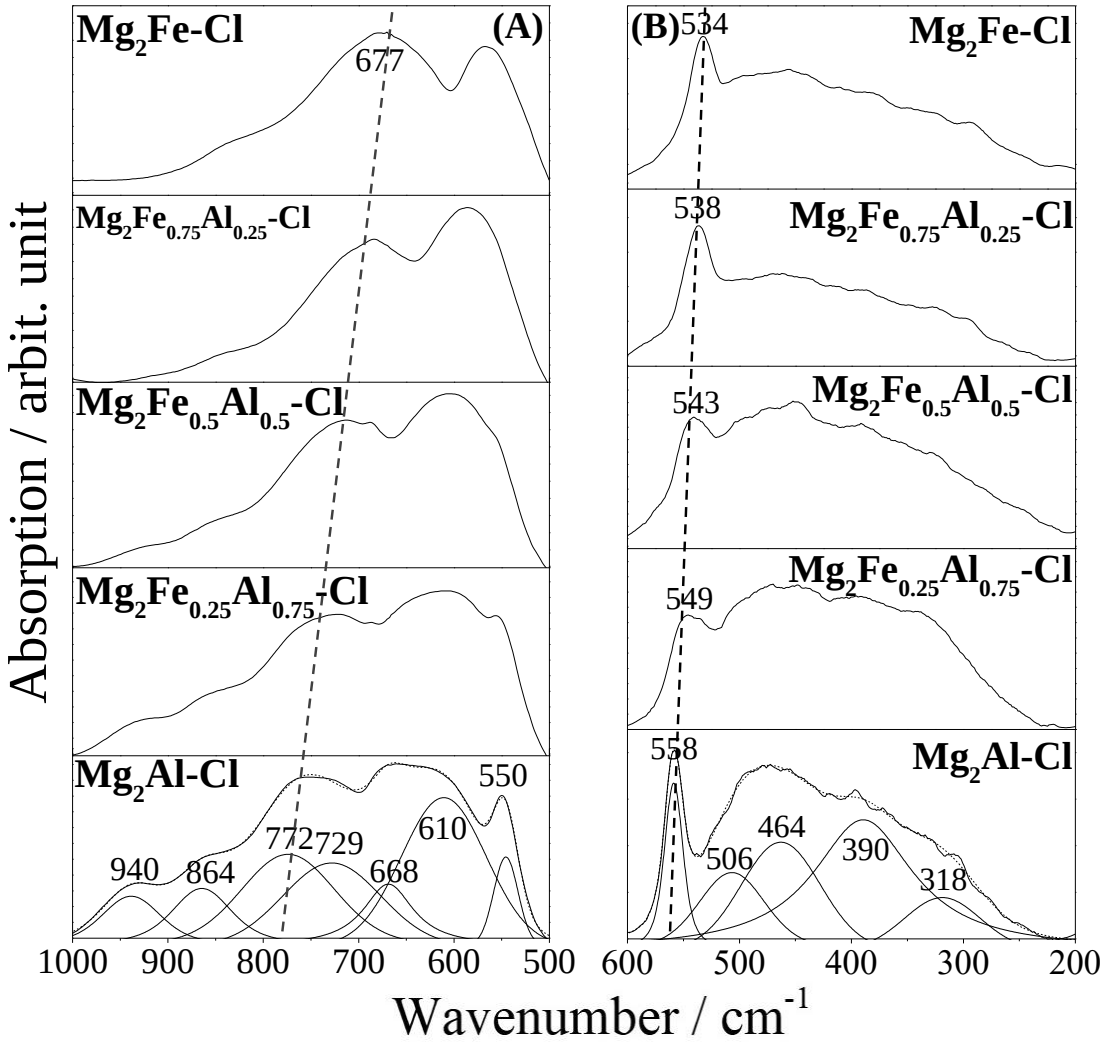

Figure 3.7. (A) FT-IR and (B) Raman spectra of the $Mg_2Fe_yAl_{(1-y)}$-Cl samples.

Similarly, the band component analysis of the FT-IR spectrum of Zn_2Al-Cl in **Figure 3.8A** shows bands at 545 and 741 cm^{-1} assigned to hydroxide translation modes and mainly influenced by the trivalent cation, while the band at 593 cm^{-1} is attributed to Zn-OH translation mode.[222] Due to the proximity of frequency values of these bands and also due to the appearance of impurities upon iron incorporation, the interpretation of

changes along Zn series is not straightforward. The FT-IR spectrum recorded for the sample with composition $y = 1$ can be interpreted by only considering the presence of ZnO/ $Zn(OH)_2$ and FH phases. Indeed, the bands at 564 and 685 cm^{-1} are common to both Zn-based impurities and ferrihydrite, respectively, while the bands at 848 and 882 cm^{-1} can be attributed to solely ZnO/ $Zn(OH)_2$ phases.[212,214,223,224] The presence of ZnO/$Zn(OH)_2$ impurities is further confirmed at higher frequencies (**Figure 3.5**). The interpretation of the Raman spectra for Zn-series is not simple either (**Figure 3.8B**). The shoulder observed at 557 cm^{-1} for Zn_2Al-Cl sample can be tentatively attributed to Al-OH translation mode, by similarity with Mg-series, since it is observed a redshift as the iron content increases. For the sample with composition $y = 1$, the band observed at 370 cm^{-1} may be attributed to FH.[225]

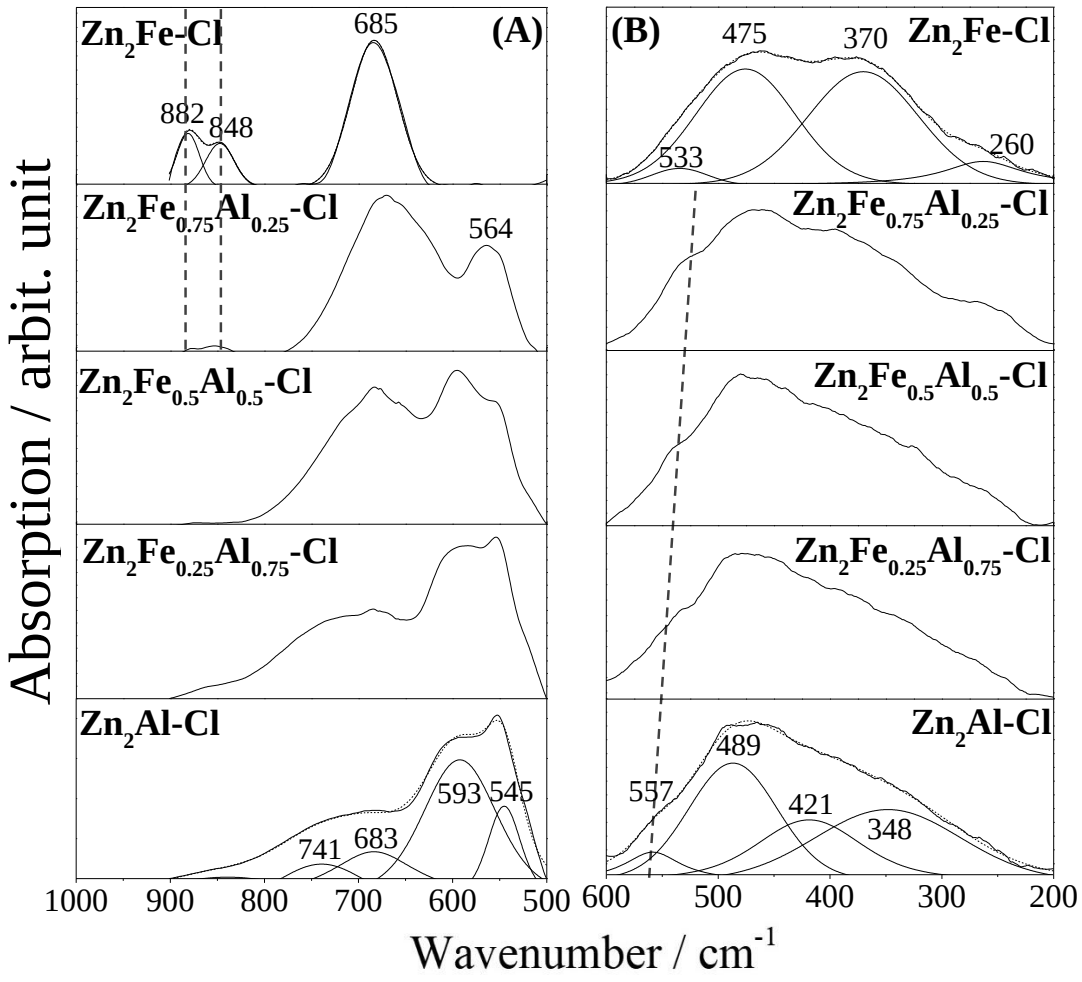

Figure 3.8. (A) FT-IR and (B) Raman spectra of the $Zn_2Fe_yAl_{(1-y)}$-Cl samples.

Focusing on the influence of the $M^{2+/3+}$ cations nature in the MO-H stretching, properties such the ones displayed in **Table 3.3** should be considered to explain the observed trends in LDH series: *(i)* atomic molar mass (MM)[226], *(ii)* effective ionic radii (r)[38], *(iii)* acidity constant of their aqua-complexes (pKa)[227,228], *(iv)* electronegativity (χ_m)[229] of the cations, and *(v)* the solubility product constant (pK_{sp}) of the corresponding $M^{n+}(OH)_n$ hydroxides and the FeOOH phase[230].

Table 3.3. Properties of metallic cations, their aqua-complexes and related hydroxides.

	Mg^{2+}	**Zn^{2+}**	**Al^{3+}**	**Fe^{3+} (high spin)**
MM (g mol^{-1})	24.31	65.41	26.98	55.84
r (Å)[a)]	0.720	0.740	0.535	0.645
pK_a	11.2	9.0	5.0	2.2[228]
χ_m[b)]	1.234	1.336	1.513	1.556
pK_{sp}	11.5	16.2	32.3	38.8

a) for hexacoordinated cations and b) Pauling electronegativity scale.

Based on **Equation 3.1**, with the progressive increase in the reduced mass (μ) because the increase in *y* value (iron) is twice heavier than aluminum), the wavenumber ($\bar{\upsilon}$) related to the M-O stretching decreases, as visualized for both series (**Figures 3.7** and **3.8**).

$$\bar{\upsilon}_{(M-O)} \propto \sqrt{\frac{k_{(M-O)}}{\mu}} \qquad (3.1)$$

The force bond constant ($k_{(M-O)}$) is dependent on the cation position in the periodic table (*i.e.* representative or transition metals, molar mass and electronegativity) and their valences (that is the same for Al and Fe in this work).[231] The bond weakening is expected with the increase in the M-O distance by increasing *y* value. On the other hand, the Fe-O bond is favored compared to the Al-O bond. In fact, the pK_a of M^{3+} aqua-complexes is lower for Fe compared to Al, even with the first possessing lower charge to effective ionic radii relation (Z/r), as can be seen in **Figure 3.9**. Consequently, the lower pK_a is related to the lower solubility product constant (K_{sp}) of FeOOH (frequently expressed as $Fe(OH)_3$ for simplification) compared to $Al(OH)_3$ (**Table 3.3**). The plot of pKa values of aqua-complexes[227,228] for different di and trivalent metals (**Figure 3.9**) that can composed the LDH structure also reveals two tendencies. Clearly, the transition

metal cations experience a stronger interaction with oxygen than the representative metal cations, making MO-H bond weaker and the bond vibrations less energetic, as observed for the Mg-series. Accordingly, Fe^{3+} has a higher covalent index ($\chi_m{}^2 r$) compared to aluminum, which also strengthens the Fe-O bond.[232] Therefore, both M-O length and M-O bond strength affect $k_{(M\text{-}O)}$ value but in opposite directions. In the case of Mg-series, this work suggests that the contribution of reduced mass (μ) is the main factor responsible for changes in the M-OH stretching energy when samples are iron enriched, which consequently affects the MO-H stretching (stronger M-OH bonds promote weaker MO-H linkages).

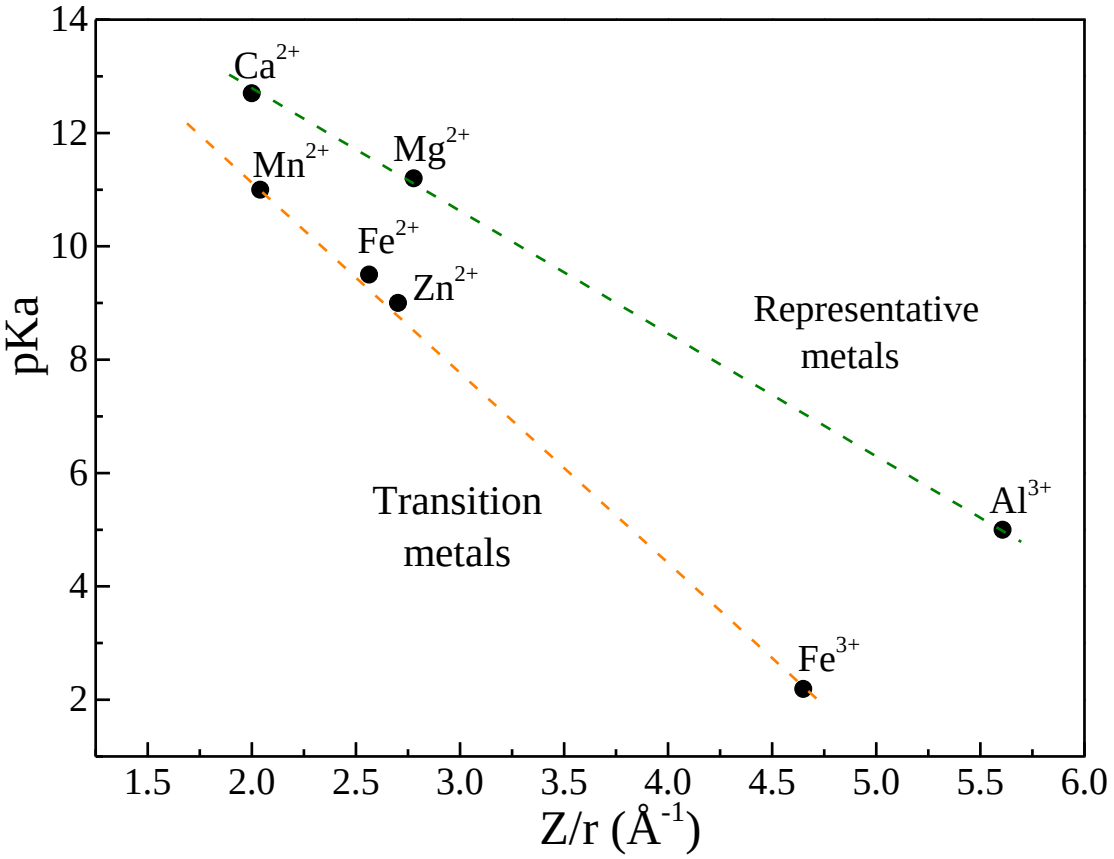

Figure 3.9. Acidity variation of aqua-complexes (expressed by pK_a) as a function of the Z/r relation, where Z is the cation electric charge and r is the ionic radii.

The present hypothesis is supported by the literature for related materials. For instance, for different $M(OH)_2$ brucite-like structured hydroxides having cations with the same electric charge (but with different masses, ionic radii values, and M^{2+}-OH bond covalence contributions), the increase in the M-O distance and the M mass leads to the decrease in O-H stretching energy and such effect is shown to be more pronounced for

transition metals.[233,234] The same tendency is observed for other layered minerals, such as oxyhydroxide MOOH (M = Fe or Al)[235] and clay minerals[236]. The opposite behavior observed for the Zn-series in the 3800 – 3000 cm^{-1} spectral range (**Figure 3.5)** indicate that other factors, beyond the metal atomic mass, are operating, such as the establishment (or not) of water molecule interactions by H-bonding of diverse strength in particular sites (internal or external LDH surfaces, for instance) and with distinct species such as the intercalated anion, the hydroxylated layers or with other water molecules in the interlayer region or in the inter-particles region. Hence, the scenario is multifaceted. The shift of the broad bands to high energy when Fe^{3+} amount increases in the Zn-series cannot be assigned to the higher atomic mass of iron compared to aluminum. Furthermore, the presence of phases as $Zn(OH)_2$ and ZnO for sample with the composition y = 0.75 and ferrihydrite for y = 1 makes the interpretation of shifts in the vibrational bands unpractical.

The thermal behavior of the materials is examined here by coupling thermogravimetric analysis with evolved gas analysis using a mass spectrometer and data are discussed in details considering already reported works[36,237,238]. **Figures 3.10** and **3.11** show the TGA-DTG and MS curves for the $Mg_2Fe_yAl_{(1-y)}$-Cl materials, respectively. Samples present a similar thermal decomposition profile in which three main mass loss events are well visualized by TGA and DTG curves. It was possible to distinguish between interparticle and interlayer water molecules (m/z = 18). The release of weakly bonded interparticle water molecules is observed up to *ca.* 140 °C for all samples of Mg series leading to a peak minimum on the DTG curves located at 100 °C. The release of intercalated water occurred at higher temperature and depended on the iron content with a DTG peak minimum located at about 200 °C for y = 0 which gradually moves to lower temperature as the amount of iron increases to reach a temperature of 150 °C for y = 1. Since these phases have similar water contents (**Table 3.1**) and interlamellar distance (**Table 3.2**), this can only be explained by a weakening of the hydrogen-bonded network in the interlayer space upon iron incorporation. This result is consistent with IR data (**Figure 3.4**) showing a blueshift of the vibrational band at about 3390 cm^{-1} as the iron content increases for Mg-series indicating a weakening of MO-H···OH_2 linkages. For iron rich compositions *i.e.* y = 0.75 and 1, the effect of the

increment of a heavier M^{3+} ion is more pronounced than the mentioned H-bonding influence, shifting the broad band to low energy region. DTG peak minimum related to the decomposition of LDH hydroxide layers (dehydroxylation event) is also lowered as the iron content increases from approximately 350 °C for y = 0 to 290 °C for y = 1. It is interesting to note that a decrease of the dehydroxylation temperature of the same magnitude (ΔT~ -60°C) was also reported for $Mg_3Fe_yAl_{(1-y)}$-CO_3 samples[239]. This decrease of the dehydroxylation temperature can also be attributed to a decrease of the strength of hydrogen bonds in the interlayer space. In the 200-450 °C temperature range and for all samples of Mg-series, MS analysis indicates the release of a fragment m/z = 44 attributed to carbonate species probably adsorbed for those released at low temperature and intercalated for those detected at higher temperature[240].

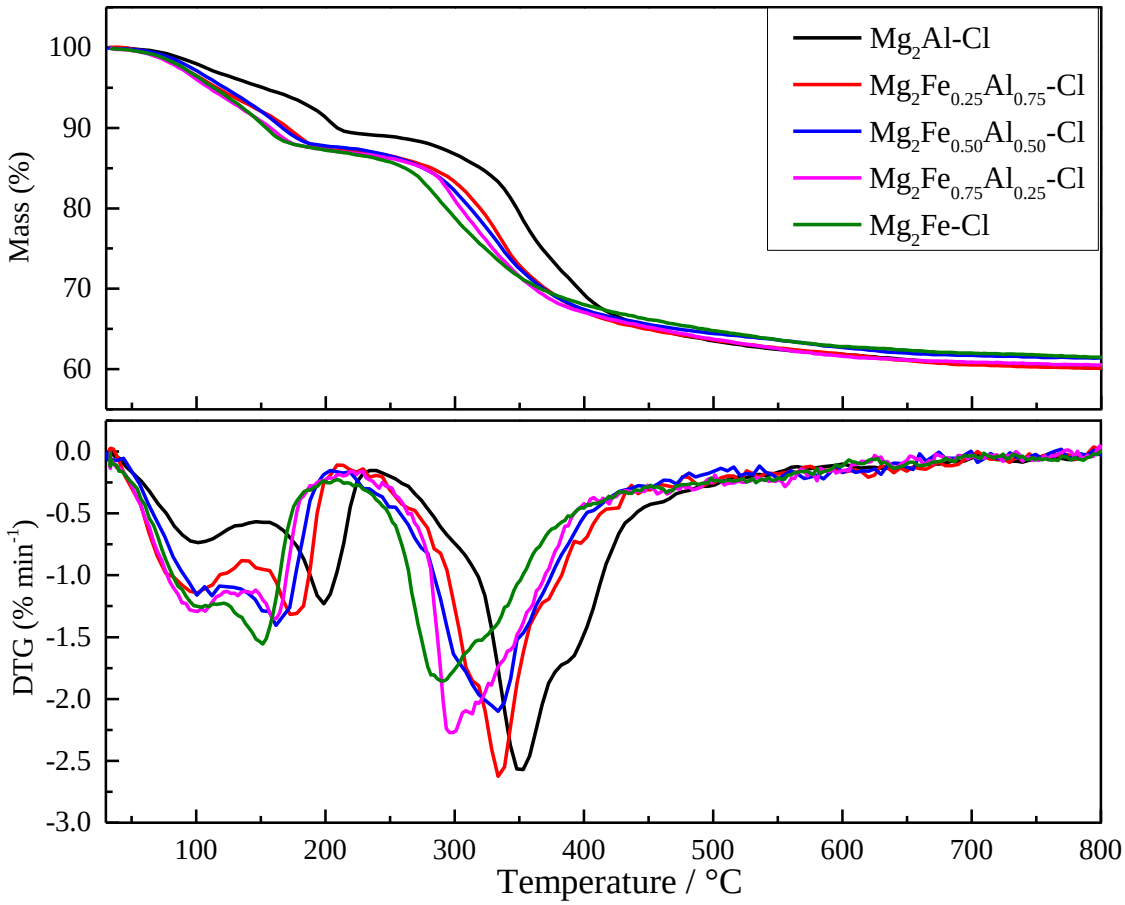

Figure 3.10. TGA and DTG curves of the $Mg_2Fe_yAl_{(1-y)}$-Cl samples. DTG curves were smoothed applying the Netzsch *Proteus*® software.

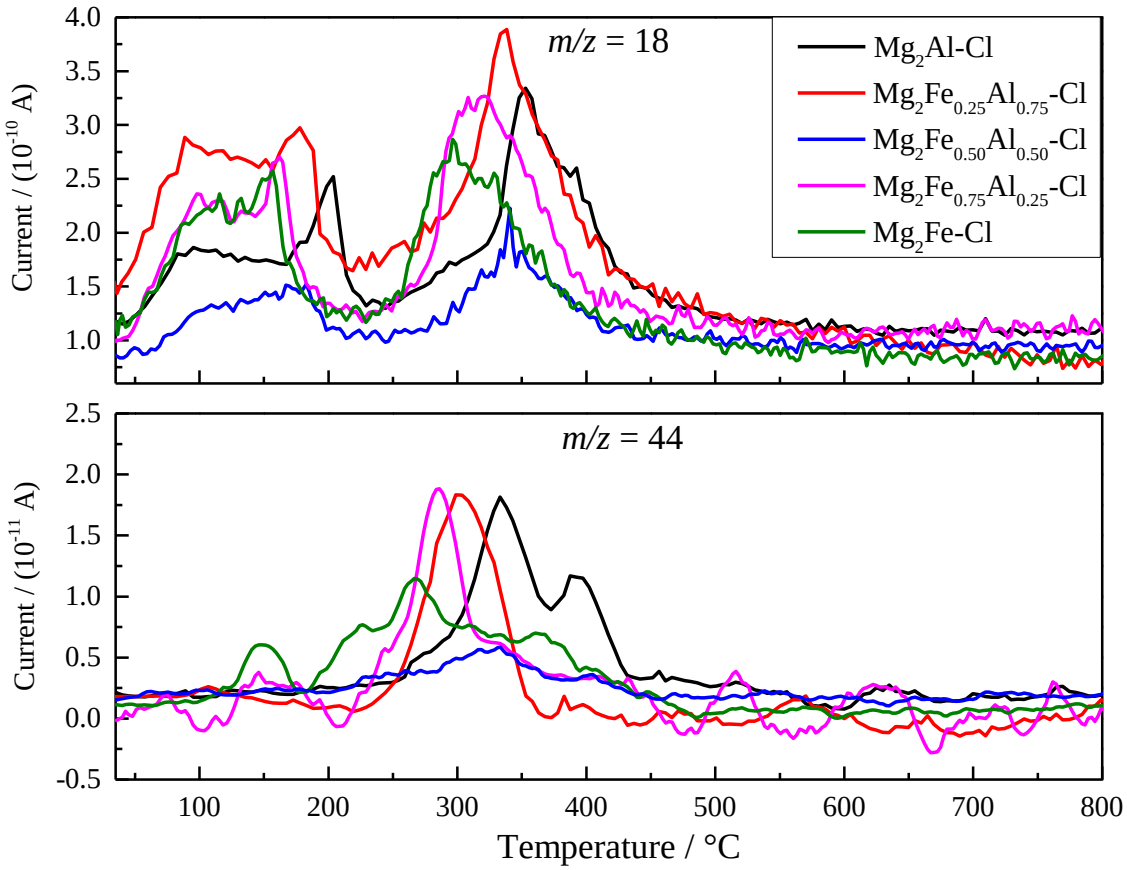

Figure 3.11. MS curves of the $Mg_2Fe_yAl_{(1-y)}$-Cl samples. Curves were smoothed applying the Netzsch *Proteus*® software.

Figures 3.12 and **3.13** show the TGA-DTG and MS curves for the $Zn_2Fe_yAl_{(1-y)}$-Cl materials, respectively. Zn_2Fe-Cl sample is out of the tendencies observed for the Zn-series. DTG curve shows a first mass loss event from room temperature to 280 °C, related to the release of adsorbed water molecules, as observed to LDH, and probably to the material decomposition that presents another DTG event from 280 to 348 °C. Such thermal behavior is in agreement with the formation of ferrihydrite phase, that presents DTA peaks in the ranges 150-200 °C and 300-350 °C[241]. The first one, from room temperature to around 270 °C, is accompanied by the release of water molecules and CO_2. On the other hand, the second event occurs from 270 to 350 °C and is accompanied only by the release of CO_2. Differently from the $Mg_2Fe_yAl_{(1-y)}$-Cl series, in general for the $Zn_2Fe_yAl_{(1-y)}$-Cl materials the loss of adsorbed and intercalated water molecules is shown as only one event. As expect, Zn-LDH materials present smaller thermal stability in comparison with Mg-LDH, as already reported[53,115,242]. Compared to the $Mg_2Fe_yAl_{(1-y)}$-Cl samples, for the Zn-series, in general, the removal of interlayer water starts at low temperature around 100 °C overlapping with the end of the removal of interparticle

weakly bonded water molecules. For the dehydroxylation process, a shift to low temperature of almost the same amplitude (ΔT~ -55°C) is observed from 255 °C for y = 0 to 200 °C for y = 0.75 (setting aside composition y = 1). CO_2 release is also detected between 150 and 400 °C but in lower amounts compared to Mg-series and no signal was measured for Zn_2Al-Cl sample.

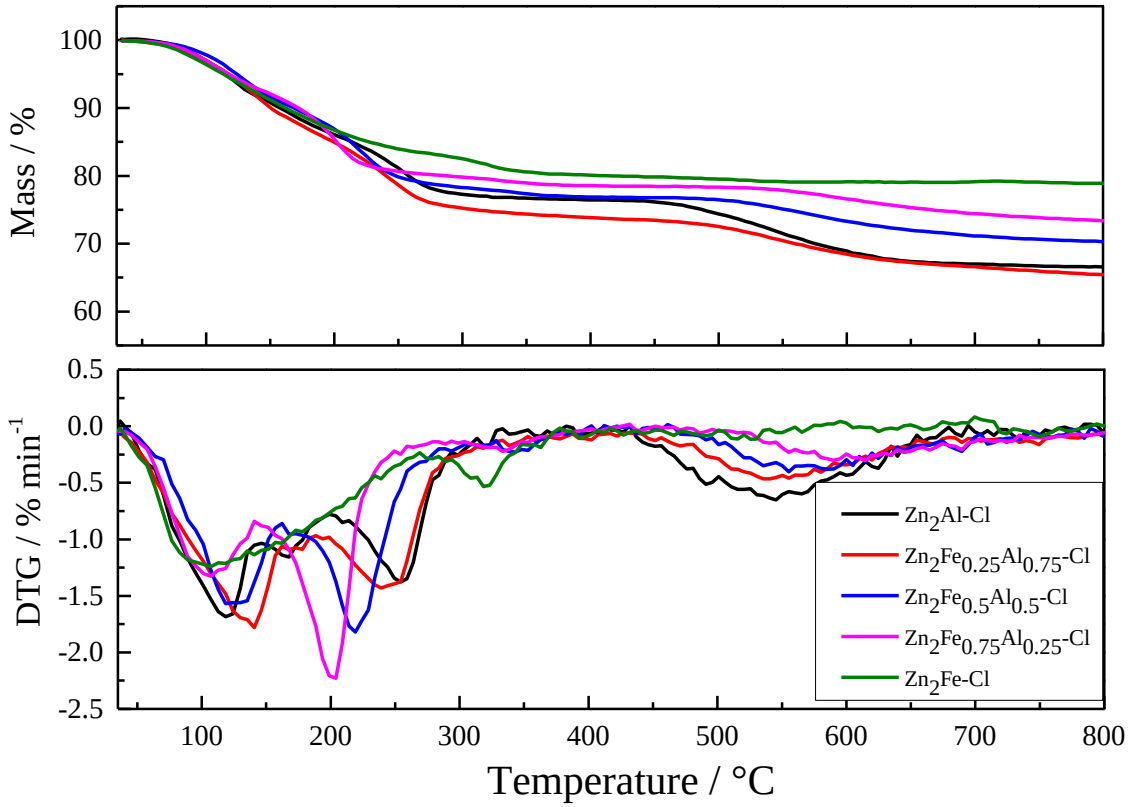

Figure 3.12. TGA and DTG curves of the $Zn_2Fe_yAl_{(1-y)}$-Cl samples. DTG curves were smoothed applying the Netzsch *Proteus*® software.

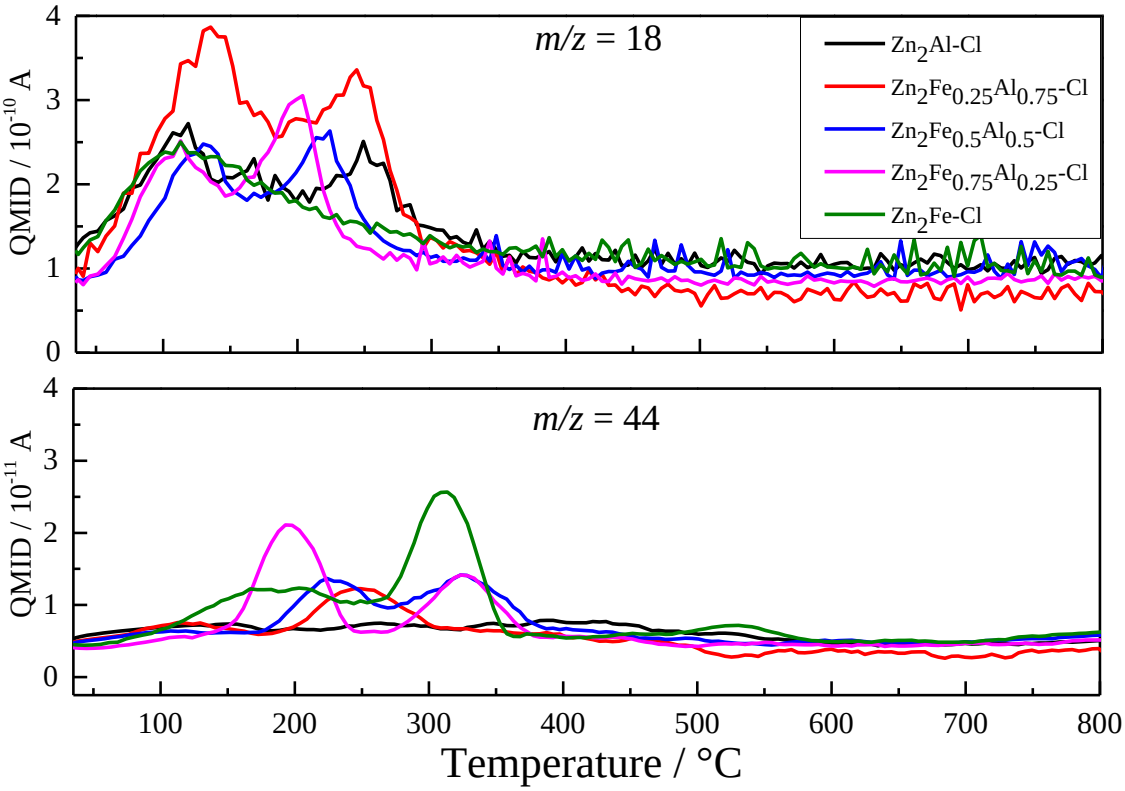

Figure 3.13. MS curves of the $Zn_2Fe_yAl_{(1-y)}$-Cl samples. Curves were smoothed applying the Netzsch *Proteus*® software.

For both series, it is observed the decrease in LDH thermal stability according to the increase in iron amount. Matrix dehydroxylation initiates at 240 and 210 °C for the Mg_2Al-Cl and Mg_2Fe-Cl materials, respectively, and at 200 and 140 °C for the Zn_2Al-Cl and $Zn_2Fe_{0.75}Al_{0.25}$-Cl materials, respectively. Residual mass increases progressively from Zn_2Al-Cl to Zn_2Fe-Cl samples, expected when Al^{3+} is replaced for the heavier Fe^{3+} and considering that anions nature and quantity and hydration degree does not significantly change. The same behavior was not verified for the Mg-LDH, which residual TGA masses changed just slightly. Mg-materials were prepared at pH 10.5 what promoted a higher carbonate amount in the samples compared to the Zn-series. Furthermore, the first series had a higher hydration level than de zinc-materials (**Table 3.1**). Additionally, although the dehydrochlorination process can be indirectly inferred by the loss masses around 450-750 °C, the fragment m/z = 36 was not detectable. The thermal analysis of similar intermediate $Mg_2Fe_{0.5}Al_{0.5}$-Cl and $Zn_2Fe_{0.5}Al_{0.5}$-Cl materials as the ones presented here was performed in the same equipment and analysis conditions but using a macro crucible where it was used ten times higher mass of sample in comparison to this work, the mass signal for HCl was better visualized, reinforcing the equipment limitation[115].

3.3.2. Further insights about the structural incorporation of Fe^{3+} in LDH layers

For Mg series that from preliminary analysis seems to consist of pure phases, the linear trend obtained for the variation of the cell parameter a as a function of y was further investigated based on geometrical reasoning. Indeed, it is possible to calculate the substitution ratio of divalent x and trivalent y cations in LDH from the a lattice parameter and *vice versa*, whichever is known with more confidence, and this can be used as a "sanity test" to validate the formation of solid solution in addition to the application of Vegard's rule[243] (**Figure 3.3**). The geometrical relationships in the octahedral layers of LDH were recently reviewed by Richardson[244,245] providing improved values for the effective radius of the O atom of the hydroxyl ion and a better understanding of the deformation of the metal–oxygen octahedra in the main layer. Thus, it was possible to calculate the theoretical variation of the cell parameter *a* for Mg series using **Equation 3.2**:

$$a = 2\sin\frac{\alpha}{2}(r\mathrm{Mg}^{2+} + r\mathrm{OH}^{-}) - 2\sin\frac{\alpha}{2}(r\mathrm{Mg}^{2+} - (1-y)r\mathrm{Al}^{3+} - yr\mathrm{Fe}^{3+})x \quad (3.2)$$

where x is the fraction of divalent cations, y is the fraction of trivalent ions (*i.e.* Fe^{3+} amount varying from 0 to 1 in our case), α is the O-M-O bond angle within octahedra set to 97.41° for Mg-based LDH and $r\mathrm{OH}^{-}$ is the effective radius of the O atom of the hydroxyl ions of 1.365 Å. The values used for the ionic radii of cations r are those tabulated by Shannon[38] (**Table 3.3**). The cell parameters a are the ones presented in **Table 3.2**.

This theoretical variation is compared to experimental data in **Figure 3.14**. The solid lines represent the theoretical variation of the *a* parameter obtained from **Equation 3.2** against *x* for the different values of *y*. The top line corresponds to y = 1, the lines below are at *y* interval of 0.25 and the last one at the bottom corresponding to y = 0. The filled squares correspond to the experimental values of the cell parameter a obtained from XRD data refinement each associated with the experimental values of x and y determined from chemical analysis, and are compared to open circles giving the expected values of the cell parameter a obtained by application of **Equation 3.2**. It is important to point that the application of **Equation 3.2** for Zn-LDHs presents

limitations, as discussed by Richardson *et al.*[244] As can be seen in **Figure B.7** (**Appendix B**), where the same graph as the one shown in **Figure 3.14** was built for the Zn-series, even applying the α value suggested by a most recent paper[245], theoretical *a* lattice parameter values are too discrepant in comparison to the experimental ones.

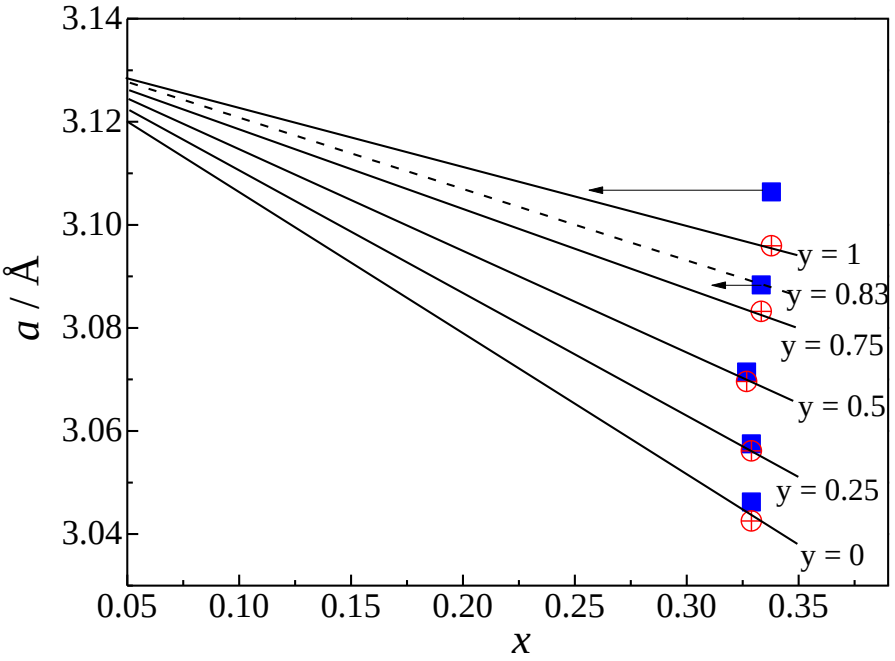

Figure 3.14. Crossed-analysis of XRD and chemical analysis data for the $Mg_{1-x}Fe_yAl_{(1-y)}$-Cl series: theoretical variation of the lattice parameter *a* as a function of the composition of LDH layers in terms of *x* and *y* (solid lines); experimental (filled squares) and expected (open circles) values of the cell parameters *a* for each experimental composition.

This crossed analysis of data can reveal composition and/or cell parameter deviations from expected values for an ideal solid solution. As can be seen, the experimental values for both *a* and *(x, y)* gradually deviate from the expected positions for $y > 0.5$. It is interesting to note that a similar deviation was observed for $Mg_3Fe_yAl_{(1-y)}$-CO_3 series.[239] Since the cell parameters were obtained from refined Bragg peak positions, the present deviations can only be attributed to compositional errors, *i.e.* a composition of LDH crystals slightly different from the bulk powder for iron rich samples. Furthermore, since XRD data of $Mg_2Fe_yAl_{(1-y)}$-Cl series do not show the presence of a crystallized impurity, amorphous second phases must be responsible for this deviation. These compositional inconsistencies can be on the value of *x* or *y*, therefore related to Mg^{2+}/M^{3+} or Fe^{3+}/Al^{3+} molar ratios, respectively. Thus, in the case of $Mg_2Fe_{0.75}Al_{0.25}$-Cl sample, the composition difference between LDH phase and the bulk would be either on *x* with a value of 0.30

instead of 0.33 as indicated by the arrow, or on *y* with a value of 0.83 instead of 0.75 as shown by the dotted line. For Mg_2Fe-Cl sample, the difference can only be related to the value of *x* with a value of 0.25 instead of 0.34 leading to a Mg^{2+}/M^{3+} ratio of 3 instead of 2, in which the missing quantity of iron would still be present but in an amorphous form.

From **Figure 3.3**, considering that *y* is constantly increased by *ca.* 0.25, since *y* and *a* show linear relation, thus it is expected a constant increase in *a*. If the M^{2+}/M^{3+} molar ratio (R) is constant for all samples, then the approach of plotting *a* as a function of *y* can be considered sufficient for a proper verification and estimation of the LDH composition. However, a second inspection considering *x* instead of *y* showed useful and considerable deviations were observed. The linearity observed in **Figure 3.3** and the pronounced deviations observed in **Figure 3.14** could intuitively indicate a contradiction. However, as discussed above, *a* cell parameter depends on both *x* and *y* values, in which the visualized increase in *a* according to the increase in *y* value can also be related to a smaller *y* value related to the crystalline LDH component together with a decrease in *x*, thus increasing the contribution of the larger ionic radii of the Mg^{2+} cations (0.72 Å), and such effect was camouflaged in **Figure 3.3**. Thus, the approaches shown in **Figures 3.3** and **3.14** can be seen as complementary.

Microstructural information can also be extracted from the full profile analysis of the XRD patterns. In the present case, although stacking faults may be present, the sample contribution to the peak widths was assumed to be fully described by size-broadening effects. Using the spherical harmonic model, the coherence lengths along the [00*l*] and [110] directions could be obtained (**Table 3.4**), reflecting the extent of the structural order along the stacking direction (L_z) and in the plane of the hydroxide layers (L_{xy}) respectively. The formation of nanocrystals is observed with dimensions ranging from of 80 - 339 Å. The size and shape anisotropy varies with the amount of iron and the trends are different for the two series. Differences occur from the first compositions *y* = 0. Mg_2Al-Cl nanocrystals are anisotropic in shape with L_{xy}/L_z around 1.4 consistent with a plate-like morphology typical of LDH crystals whereas Zn_2Al-Cl displays more isotropic coherent domains with L_{xy}/L_z around 1.0 and of smaller size. Then, for $Mg_2Fe_yAl_{(1-y)}$-Cl series, the introduction of iron leads immediately to a decrease of the structural coherence lengths with a value of L_z halved and then no longer changes while

in-plane dimension L_{xy} slightly re- increases. The occurrence of stacking faults, visible in the line shape of the o*kl* peaks in the mid -2θ region of the XRD patterns (**Figures 3.1** and **3.2**), can explain the decrease of L_z dimension. On the other hand, for $Zn_2Fe_yAl_{(1-y)}$-Cl series, the structural coherence is somehow improved upon iron incorporation. The greater increase is observed for L_{xy} in-plane dimension, increasing shape anisotropy L_{xy}/L_z around 1.7 for y = 0.75.

Table 3.4. Coherence lengths (Å) of crystalline domains for Mg and Zn series as determined from the modelling of XRD peak broadening by spherical harmonic functions: L_z and L_{xy} are the coherence lengths in the [00*l*] and [110] directions, respectively, also assimilated to the out-of-plane and in-plane dimensions of LDH platelets

	$Mg_2Fe_yAl_{(1-y)}$-Cl				
y	**0**	**0.25**	**0.5**	**0.75**	**1**
L_z (Å)	198	81	80	115	96
L_{xy} (Å)	270	175	187	209	221
	$Zn_2Fe_yAl_{(1-y)}$-Cl				
y	**0**	**0.25**	**0.5**	**0.75**	**1**
L_z (Å)	119	115	150	198	-
L_{xy} (Å)	120	133	278	339	-

SEM analyses of the Mg- and Zn-series are given in **Figures 3.15 and 3.16**, respectively, showing micrometric sized platelets entangled each other typical of LDH morphology. It should be noted that LDH particles observed by SEM are often polycrystalline secondary particles[246], as is likely the case here, resulting from the aggregation/coalescence of the primary nanoparticles as measured from peak shape analysis of XRD data. Nevertheless, the effects described above on the primary nanoparticles for increasing amount of iron reproduce on these secondary assemblies with a net decrease of the particle size for Mg series while maintaining the plate-like morphology whereas for Zn series it is the reverse (except for Zn_2FeCl sample), *i.e.* a net increase of the crystallinity with platelets becoming better defined.

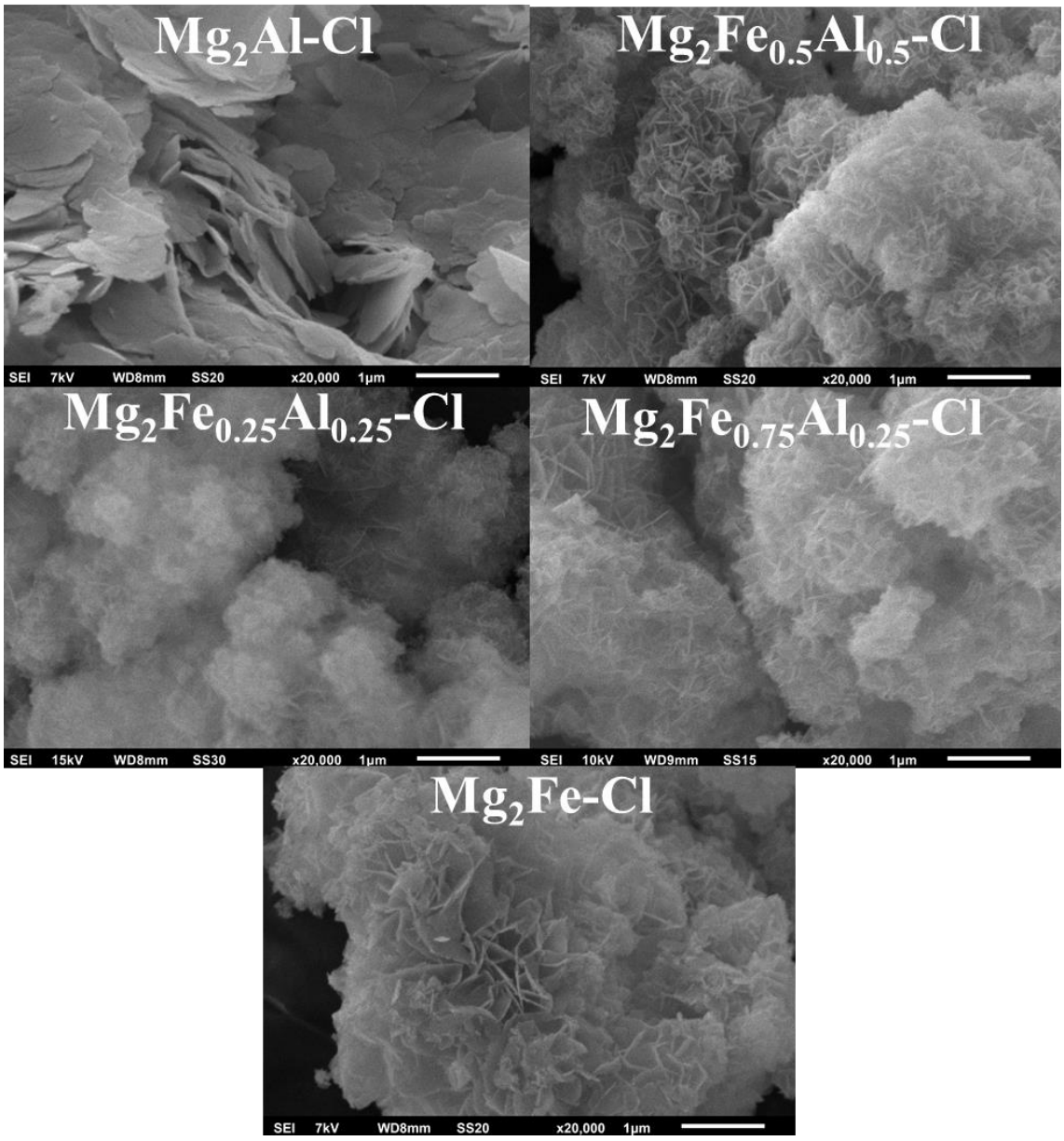

Figure 3.15. Scanning electron micrographs of $Mg_2Fe_yAl_{(1-y)}$-Cl samples.

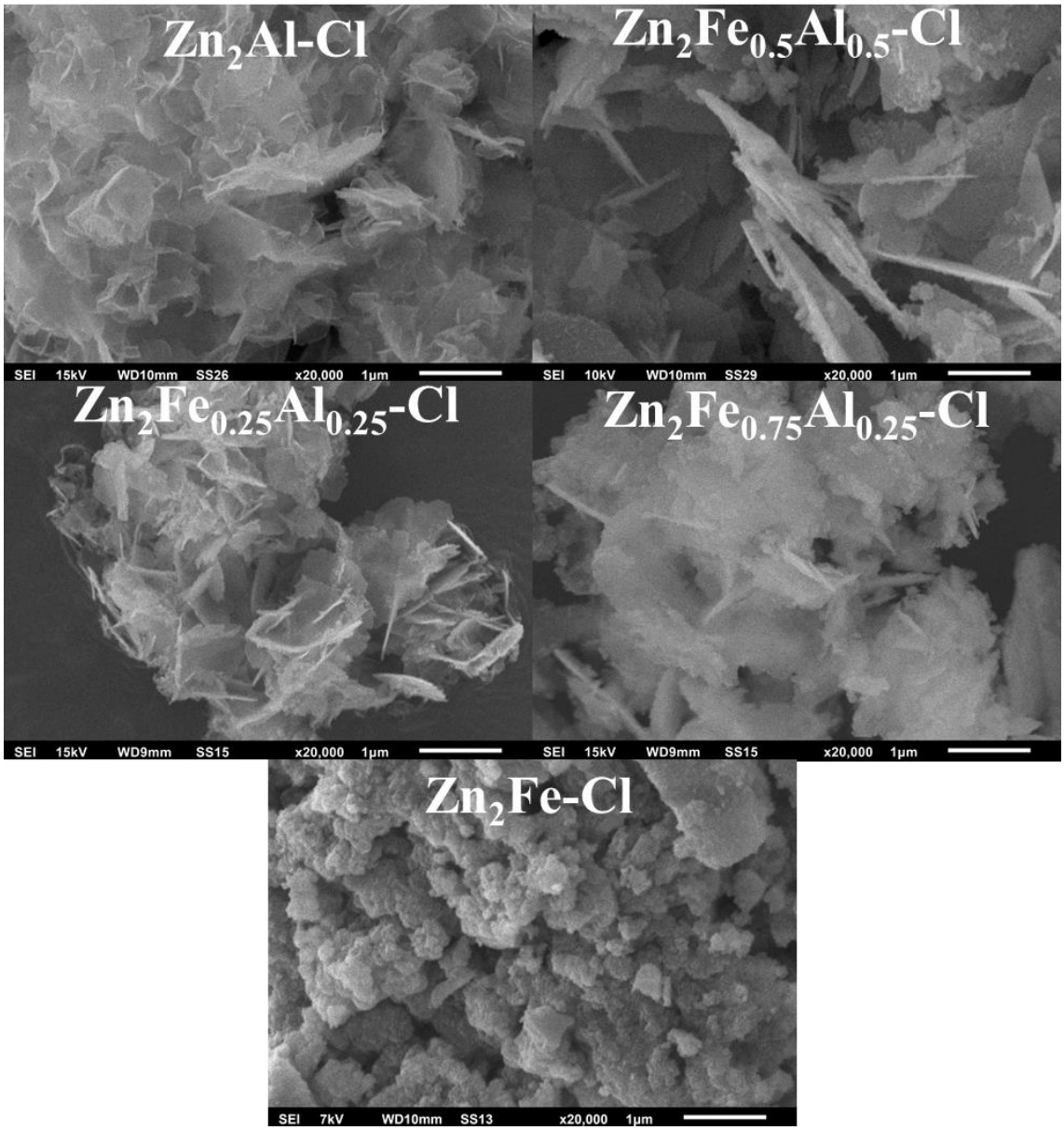

Figure 3.16. Scanning electron micrographs of $Zn_2Fe_yAl_{(1-y)}$-Cl samples.

To link the different results together, in particular XRD data results with the bulk analysis, and better explain the deviation observed for *y* compositions above 0.5 for both series, it was performed X-ray total scattering measurements to investigate the pair distribution function (PDF). As shown by Proffen *et al.*[247], the PDF analysis is an interesting method to investigate systems where crystalline and amorphous structural phases co-exist. In this method, high energy X-ray source and wide-angular range detection are employed, thus a wide range of reciprocal space are probed, that is why such method is frequently called total scattering experiments. Experimental pair

distribution function (G(r)) corresponds to the truncated Fourier transform of a function related to the total scattering structure.[248]

Figures 3.17 and **3.18** show the pair distribution functions G(r) for both series for *r* values up to 200 and 50 Å, respectively. For all samples, it is observed a falloff in the pair correlations intensities around 50 Å (**Figure 3.17**), then there remain peaks weaker in intensity and visible up to 200 Å. Such a falloff in the PDF intensity by increasing *r* is usually attributed to the finite size of the coherent domains. Therefore, it comes that the samples count with contributions of small crystalline domains of 50 Å in size. This result is consistent with a description of LDH particles formed by nanosized subdomains randomly oriented inside the particles, as discussed above. It also follows that the crystallized components characterized above by XRD and having domain sizes between 80 and 340 Å do not represent the majority size of the samples.

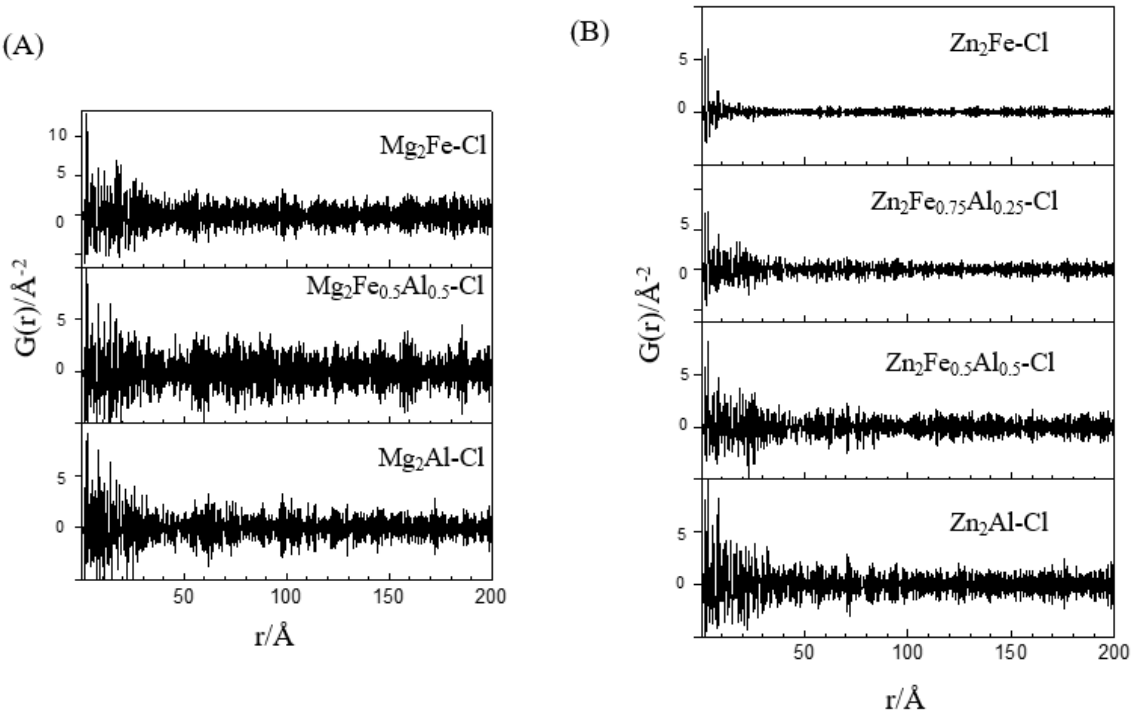

Figure 3.17. Experimental pair distribution function (PDF) for *r* values up to 200 Å for: (A) $Mg_2Fe_yAl_{(1-y)}$-Cl series with *y*= 0, 0.5, and 1; (B) $Zn_2Fe_yAl_{(1-y)}$-Cl series with *y*= 0, 0.5, 0.75, and 1.

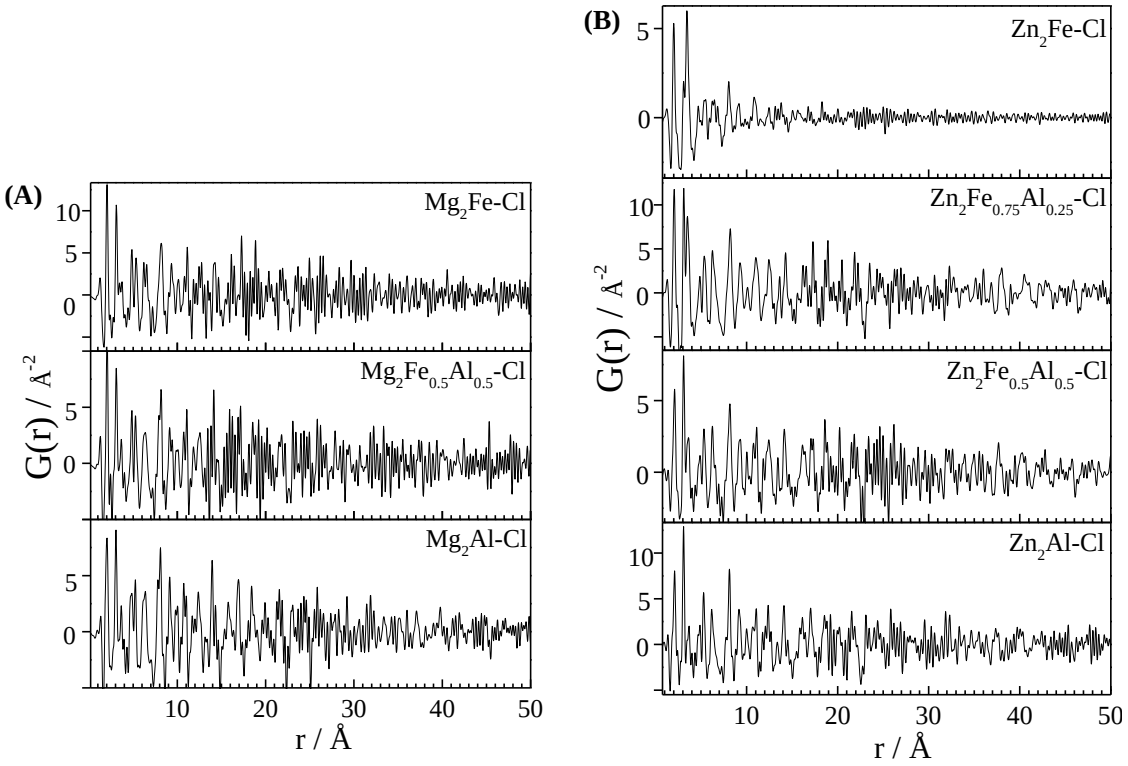

Figure 3.18. Experimental pair distribution function (PDF) also known as G(r) for *r* values below 50 Å for: (A) $Mg_2Fe_yAl_{(1-y)}$-Cl series with *y*= 0, 0.5, and 1; (B) $Zn_2Fe_yAl_{(1-y)}$-Cl series with *y*= 0, 0.5, 0.75, and 1.

The peaks for *r* values below the interlayer distance can be easily assigned to distances within the hydroxide layers. In **Figure 3.19**, P_1 results from a single atomic pair (*i.e.* M-OH in the first nearest neighbor shell) while P_2 results from the contribution of different atomic pairs although dominated by the M---M atomic pair between the first nearest neighbor cations. For Mg series, a gradual evolution of P_1 and P_2 at low *r* PDF peaks is observed in **Figure 3.19A**. For *y* = 0, P_1 displays a shoulder attributed to Al-OH distances which disappear as Al^{3+} ions are replaced by Fe^{3+}; Fe-OH distances being closer to Mg-OH distances, P_1 peak width decreases. The increase of the number of Fe-OH pairs also leads to an increase of the intensity of P_1. Concomitantly and as expected, the position of P_2 which is related to the sum of the ionic radii of M cations is shifted to higher distances and can be compared to the parameter *a* of the rhombohedral cell obtained from Bragg peaks position (**Table 3.2**). While similar values are obtained for *y* = 0 and 0.5, different values are observed for $MgFe_2$-Cl sample with a maximum measured at 3.09 Å for P_2 PDF peak and a value of 3.11 Å for the cell parameter *a*. This indicates that the crystalline component as measured by XRD is not the only phase

contributing to the signal measured by PDF. This result is consistent with chemical/XRD data crossed analysis by Richardson's method given above and suggesting the probable presence of an amorphous phase for $y > 0.5$. For Mg_2Fe-Cl sample, it is also noticed the presence of an additional peak on the PDF at 3.45 Å, which could be attributed to the presence of iron hydroxide species as shown below. On the other hand, changes are more difficult to be observed for Zn series due to the presence of FH, which occurs probably from $y = 0.5$ and is the major phase for $y = 1$ (**Figure 3.19B**). FH is a nano Fe^{3+} oxide material widely present in nature which structure has not been clearly established yet[249]. PDF data profile measured for the Zn_2Fe-Cl sample is very similar to the PDF PDF data reported for 2-line FH by Tang *et al.*[250]. In FH, iron is both tetrahedrally and octahedrally coordinated; the first peak in the PDF at around 2.0 Å is attributed to Fe-O pairs while the peaks at around 3.03 Å and 3.40 Å are mainly ascribed to Fe-Fe correlations between adjacent FeO_6 octahedra linked in edge-sharing and corner-sharing configurations respectively. To the best of our knowledge, this is the first time that FH impurity is so clearly identified in iron containing LDH.

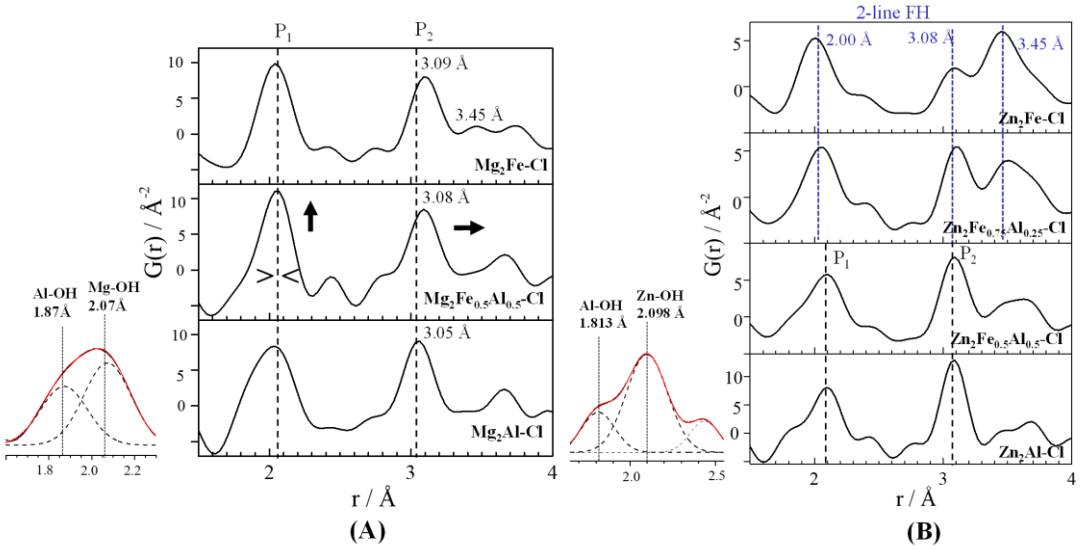

Figure 3.19. Expanded view of PDFs in the range 1-4 Å for (A) $Mg_2Fe_yAl_{(1-y)}$-Cl series with $y = 0$, 0.5, and 1 and (B) $Zn_2Fe_yAl_{(1-y)}$-Cl series with $y = 0$, 0.5, 0.75, and 1. The black dotted lines are anchored to the composition $y = 0$. The blue dotted lines indicate the PDF peaks of 2-line FH. On the left of each Figures, it is given the Gaussian fit of P_1 peak for the composition samples $y = 0$.

Discussion

Iron-containing LDH phases have recently attracted a lot of interest in several application fields in particular the medical one[21,217]. However, most of the studies reported so far suffer from insufficient data concerning the conditions of formation and the determination of the fine chemical composition of Fe-LDH which can hinder the development of applications. Mention should be made to the studies carried out by Rosoz *et al.*[239,251] who examined in detail the composition, structure, solubility, and thermodynamic properties of $[Mg_3Fe_yAl_{(1-y)}(OH)_8](CO_3)_{0.5}\cdot 2.5H_2O$ hydrotalcite - pyroaurite materials with $Mg^{2+}/(Al^{3+} + Fe^{3+})$ molar ratio equal to 3. The other studies are mainly focused on applications and the chemical analysis of the materials is often not provided. In the case of Zn_RFe phases, the results appear very disparate. The studies mostly concern compositions with Zn/Fe molar ratios close to 3 and show poorly crystalline materials[99,101] often containing impurities not always identified but recognized by us as ZnO and/or ferrihydrite[85,100,105–107,252]. Furthermore, the lack of comparative analysis of the bulk and crystalline components clearly leads to inconsistencies in the chemical compositions provided.[253]

The present study aims to develop iron-rich LDH phases, *i.e.* with a R value equal to 2. The gradual incorporation of iron into Mg_2Al-Cl and Zn_2Al-Cl LDH in substitution of aluminum was examined in detail considering both compositional and structural aspects. First, preliminary characterization using conventional techniques including powder X-ray diffraction, IR and Raman spectroscopies, ICP elemental analysis, and TGA analyses clearly shows two different behaviors. A complete series of $Mg_2Fe_yAl_{(1-y)}$-Cl LDH compositions could be synthesized between the Al and Fe end members and such results suggested that this series may represent a continuous solid solution. On the other hand, for $Zn_2Fe_yAl_{(1-y)}$-Cl compounds, iron incorporation was observed only up to $y = 0.75$ (nominal value) with the presence of $Zn(OH)_2$/ZnO impurities for $y \geq 0.5$ and the bulk chemical compositions are different from those expected.

From these preliminary results, it was clear that further thorough examination was required from both compositional and structural point of views to better understand the differences between $Mg_2Fe_yAl_{(1-y)}$-Cl and $Zn_2Fe_yAl_{(1-y)}$-Cl series. For Mg series, the crystal-

chemical plausibility of the solid solution was checked as proposed by Richardson.[244,245] By combining XRD and chemical analysis data sets, it was possible to show that for $y \geq 0.5$ the composition of LDH crystalline phase deviates from that expected by only replacing Al by Fe and is different from that of the bulk. Chemical analysis of the bulk for Mg_2Fe-Cl sample indicates a value of R equal to 2, nearly equal to the synthesis conditions, while geometrical reasoning applied on the crystalline component gives a value of 3, thus indicating the presence of an iron rich, amorphous and undetected, second phase. Interestingly, similar data treatment performed for $[Mg_3Fe_yAl_{(1-y)}(OH)_8](CO_3)_{0.5}{\cdot}2.5H_2O$ hydrotalcite-pyroaurite data in Rosoz's et al. work also reveals a deviation from ideality for $y \geq 0.6$ due to an increase of the R value.

In the case of Zn series, for *y* values higher than 0.5, the presence of 2-line ferrihydrite was demonstrated by PDF analysis. Although it has never been indicated as a probable secondary phase in the synthesis of Fe-LDH so far, its occurrence is not surprising. Indeed, 2-line FH is reported to be instantaneously formed from the Fe^{3+} ion hydrolysis[241,254]. Considering the solubility product of the isolated metallic hydroxides (Fe^{3+} < Al^{3+} < Zn^{2+} < Mg^{2+}),[230] Fe^{3+}-oxyhydroxide phases are easily precipitated. Furthermore, although thermodynamically unstable due to its low structural organization, 2-line FH transformation is inhibited in the presence of Zn cations[255]. FH can even act as a precursor for the formation of zinc hydroxides phases [256–258] and subsequent transformation into ZnO [259–261]. Finally, FH shows a solubility minimum at pH 7-8 which is consistent with the pH applied here for the synthesis of the Zn-series, *i.e.* 7.5. It has been established for LDH phases composed of only one type of divalent and trivalent cations that their stability are higher compared to single hydroxide phases, and also that Al-containing LDH phase formation is more spontaneous than Fe-LDH.[239,262] However, these trends may not necessarily apply to the preparation of multi metallic LDH with more than one type of divalent/trivalent cations. As shown here for $Zn_2Fe_yAl_{(1-y)}$ composition, at pH 7.5, when the iron content exceeds the aluminum content ($y \geq 0.5$), the precipitation of iron in FH form is found to prevail, preventing the formation of LDH layer. Comparatively, Mg series was prepared at pH 10.5 for which FH solubility is higher[254]. Therefore, it would be expected that the increase in synthetic pH could be an alternative for preparing the Zn_2Fe-Cl

composition. However, by slightly increasing the pH to 8.5, $Zn(OH)_2$/ZnO phases are formed as shown by XRD (see **Appendix B**, **Figure B.4**).

3.4. Conclusions

This study provided useful elements for better understanding and interpreting the results reported in the literature regarding iron-containing LDH phases. It was recalled that for a complete compositional and structural characterization of LDH, it is essential to differentiate the bulk to the crystalline component to identify possible contributions from amorphous components. In this sense, as shown here, PDF technique can be useful to link these different contributions together. It was shown that $Mg_2Fe_yAl_{(1-y)}$-Cl solids with $y \leq 0.5$ can be obtained as pure phases with fine control of their compositions, as requested for pharmaceutical formulations.

3.5. Acknowledgments

We would like to thank Professor Christine Taviot-Gueho for the idealization and coparticipation in this work, especially performing XRD profile refinements, PDF analysis, and contributing with data manipulation and interpretation. We are also thankfull to the *Laboratório de Espectroscopia Molecular Hans Stammreich* (*Instituto de Química – USP*) for the FT-IR spectra recording, the *Laboratório de Astrobiologia* (*Instituto de Química – USP*) for the Raman spectra recording, the *Laboratório de Materiais Híbridos* (*Instituto de Ciências Ambientais, Químicas e Farmacêuticas – UNIFESP*) for the SEM micrographs recording and also to the *Laboratório de Cristalografia* (*Instituto de Física – USP*) for the XRD patterns recording in the D8 Discover Bruker equipment.

Chapter 4: Synthesis and characterization of $Mg_2Fe_yAl_{(1-y)}$-NAP and $Zn_2Fe_yAl_{(1-y)}$-NAP LDHs: influence of Fe^{3+} content in intercalating NAP anions by ion-exchange reaction

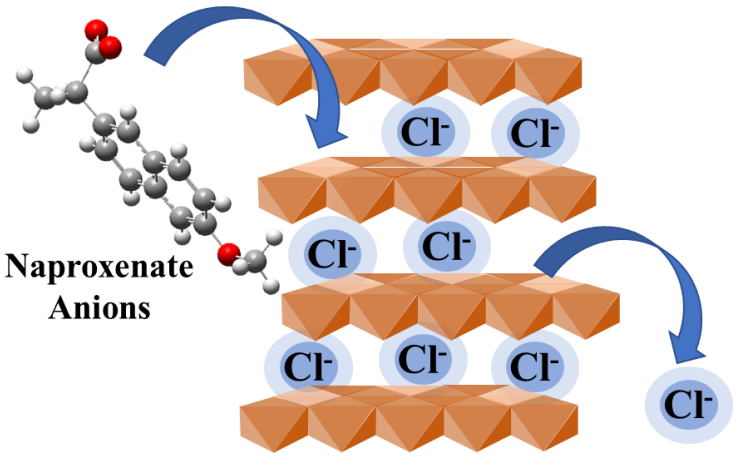

4. Abstract and data presentation

4.6. Abstract

In this chapter it is evaluated the effect of iron(III) in the intercalation of a model drug, naproxenate (NAP) anions, into two series of LDHs by ion-exchange reaction: from precursors with nominal $Mg_2Fe_yAl_{(1-y)}$-Cl and $Zn_2Fe_yAl_{(1-y)}$-Cl compositions, with nominal *y* values ranging from 0 to 1. Such study is also expected to provide additional information concerning the structure, compositions, and properties of the LDH pristine phases studied in **Chapter 3**. NAP intercalation into all LDH compositions was attested by X-ray diffractometry. The variation of the *a* cell parameters in relation to both experimental *y* and *x* indicates the exchange of chloride ion for NAP as a quite topotactic process for the Mg-LDH series. However, the composition of the layers changed after ion-exchange reaction for the Zn-LDH system. Although iron-enriched LDH samples were able to intercalate appreciable amounts of NAP, for instance with NAP representing 26.80 and 26.27 % of the mass of the bulk samples for the Mg_2Fe and $Zn_2Fe_{0.5}Al_{0.5}$ layer composition, respectively, the drug percentage tended to decrease, surpassing the expected decrease considering the increase in LDH molar mass by increasing *y*. Such behaviour could be related to the decrease in the charge density of the layers due to deviations of the experimental metals content in comparison to the nominal *x* and *y* values. Particularly for Zn-series, the decrease in NAP percentage could also be correlated to the increase in the coherent domain's lengths of LDH-Cl particles and to the presence of impurities such as $Zn(OH)_2$ and ZnO, and ferrihydrite identified for *y* above 0.5 (see **Chapter 3**) . For the Mg-series, more severe conditions, such as NAP excess and heating, were necessary to propitiate NAP intercalation into LDH from 50 % (include) of Al substituted by Fe. This study contributes to shed light on the observed difficulty to prepare hybrid organic-inorganic iron-based LDH and points out ion-exchange as a feasible method for the intercalation of organic species as NAP, mainly for magnesium-LDH phases comprising intralayer iron(III) cation.

4.7. Materials and methods

4.7.1. Reagents

Products were used as received. Magnesium chloride hexahydrate ($MgCl_2 \cdot 6H_2O$) (99 %), zinc chloride ($ZnCl_2$) (≥ 98 %), aluminum chloride hexahydrate ($AlCl_3 \cdot 6H_2O$) (99 %), ferric chloride hexahydrate ($FeCl_3 \cdot 6H_2O$) (98 %), sodium hydroxide (NaOH) (≥ 98 %), and sodium naproxenate (NaNAP) ($NaC_{14}H_{13}O_3$) (≥ 98 %) were purchased from Sigma-Aldrich. Absolute ethanol was purchased from Synth.

4.7.2. Preparation of $Mg_2Fe_yAl_{(1-y)}$ and $Zn_2Fe_yAl_{(1-y)}$ LDHs intercalated with NAP

Drug intercalation into LDHs was performed by ion-exchange reaction employing the $Mg_{(1-x)}(Fe_yAl_{(1-y)})_x$-Cl and $Zn_{(1-x)}(Fe_yAl_{(1-y)})_x$-Cl LDHs (subject of **Chapter 3)**, with nominal *x* value equal to 2 *y* values equal to 0, 0.25, 0.50, 0.75, and 1.0. For each pristine LDH, after post-synthesis aging, the remaining slurry was divided into two portions. Half was isolated and characterized and the other half was submitted to washing procedure by centrifugation with 4 cycles of 3 min each at 10000 rpm to remove excess of Cl^- ions. For the preparation of approximately 0.5 g of LDHs loading NAP, respective washed precursors were resuspended in 20 mL of an aqueous solution of NaNAP primarily in a NAP /(Fe^{3+} + Al^{3+}) molar ratio equal to 1 for all compositions and kept under stirring at room temperature for 24 h. The NAP/(Fe^{3+} + Al^{3+}) molar ratios equal to 2 and 3 and room temperature were also applied for the $Mg_2Fe_{0.5}Al_{0.5}$ composition, and equal to 3 and heating at 80 °C were applied for the $Mg_2Fe_{0.5}Al_{0.5}$, $Mg_2Fe_{0.75}Al_{0.25}$ and Mg_2Fe compositions. The suspensions were kept under N_2 atmosphere and vigorous stirring at the respective temperatures. Solids were washed with deionized water followed by washing with absolute ethanol as long as filtration under reduced pressure was performed. Solids were dried at room temperature in a desiccator. Materials were generally abbreviated by $M_2Fe_yAl_{(1-y)}$-NAP and more specifically by $M_2Fe_yAl_{(1-y)}$-nNAP_H, where M is equal to Mg or Zn, n is equal to the NAP/(Fe^{3+} + Al^{3+}) molar ratio employed for ion-exchange procedure and H indicates when applied heating.

4.7.3. Characterization

X-ray diffraction (XRD) patterns of powdered $Mg_2Fe_{0.5}Al_{0.5}$-1NAP, $Mg_2Fe_{0.5}Al_{0.5}$-2NAP, e $Mg_2Fe_{0.5}Al_{0.5}$-3NAP LDHs were obtained on a Rigaku MiniFlex equipment, using Cu anode (1.518 Å), scan range 1.5-70°(2θ), and scan step of 0.015° (2θ) / 2s. All other XRD patterns for powdered LDH were obtained on a Philips X-Pert Pro, using $CuK\alpha_1$/ $K\alpha_2$ radiation (1.5406/1.5444 Å), scan range 1.5-70°(2θ), and scan step of 0.02°(2θ)/3s.

Mass spectrometry coupled to thermogravimetric analyses (TGA-MS) were recorded on a Netzsch thermoanalyser model TGA/DSC 490 PC Luxx coupled to an Aëolos 403 C mass spectrometer, using alumina crucible and heating rate of 10 °C/min under synthetic air flow of 50 mL min^{-1}, and applying around 10 mg of sample.

Fourier transform infrared (FT-IR) spectra of powdered samples were recorded in the 4000–400 cm^{-1} range on a Bruker spectrophotometer, model alpha by ATR with acquisition step of 4 cm^{-1} and 512 scans.

Fourier transform Raman (FT-Raman) spectra were recorded in a FT-Raman Bruker FRS-100/S spectrometer using 1064 nm exciting radiation (Nd:YAG laser Coherent Compass 1064-500 N), a Ge detector, laser power of 100 mW, acquisition step of 4 cm^{-1} and 2048 scans.

ICP emission spectroscopy (ICP-AES) analysis of Mg, Zn, Fe and Al were performed in duplicate on an equipment Spectro Analytical Instruments at the Central Analítica of Instituto de Química (Universidade de São Paulo - USP).

Elemental analysis of carbon, hydrogen and nitrogen were recorded on an equipment Perkin Elmer - CHN 2400 at the Central Analítica of the *Instituto de Química* (*Universidade de São Paulo* - USP).

4.7.4. Density functional theory calculations

Computational calculations of the vibrational spectra of Naproxenate anion (in vacuum) were performed using density functional theory (DFT) implemented in Gaussian09. Geometry optimization, IR and Raman shifts were computed using BLYP/6-

311**G++. The wavelength values were adjusted by applying the correction factor equal to 0.9679.

4.8. Results and discussions

Peaks related to LDH were indexed considering the polytype 3R1, commonly observed for synthetic materials. XRD pattern of the $Mg_2Fe_yAl_{(1-y)}$-nNAP_H samples and of NaNAP are present in **Figure 4.1**. Interplanar distances, *d*(*hkl*), 2θ peak positions and correspondent Miller indexes are compiled in **Table 4.1**. XRD of the NaNAP salt reveals a mixing hydration levels of the salt[120] and no peaks related to the NAP superficial precipitation were observed in the LDH samples. For the Mg_2Al-1NAP sample, (003) plane and many (00l) harmonics peaks are visualized. Average basal spacing calculated from the (003), (006), (009) (00$\underline{12}$), and (00$\underline{18}$) peaks is equal to 22.95 Å. By increasing the iron amount, (003) and (006) peaks are progressively displaced toward higher 2θ values, consequently indicating a decrease in the interlayer distance, and the structural organization of the LDHs decreases. Peaks related to the pristine Mg_2Al-Cl phase, whose position do not change by changing iron amount, are also present and are indicated as $(003)_{Cl}$ and $(006)_{Cl}$. The visualization of the (113) peak at the same position compared to the pristine phase (see **Chapter 3**, **Figure 3.1**), dependent of the *c* cell parameter and expected to be displaced toward low angle region with the intercalation of the bulkier anion, is another indication of the presence of the residual phase, as frequently observed.[121,122,131].

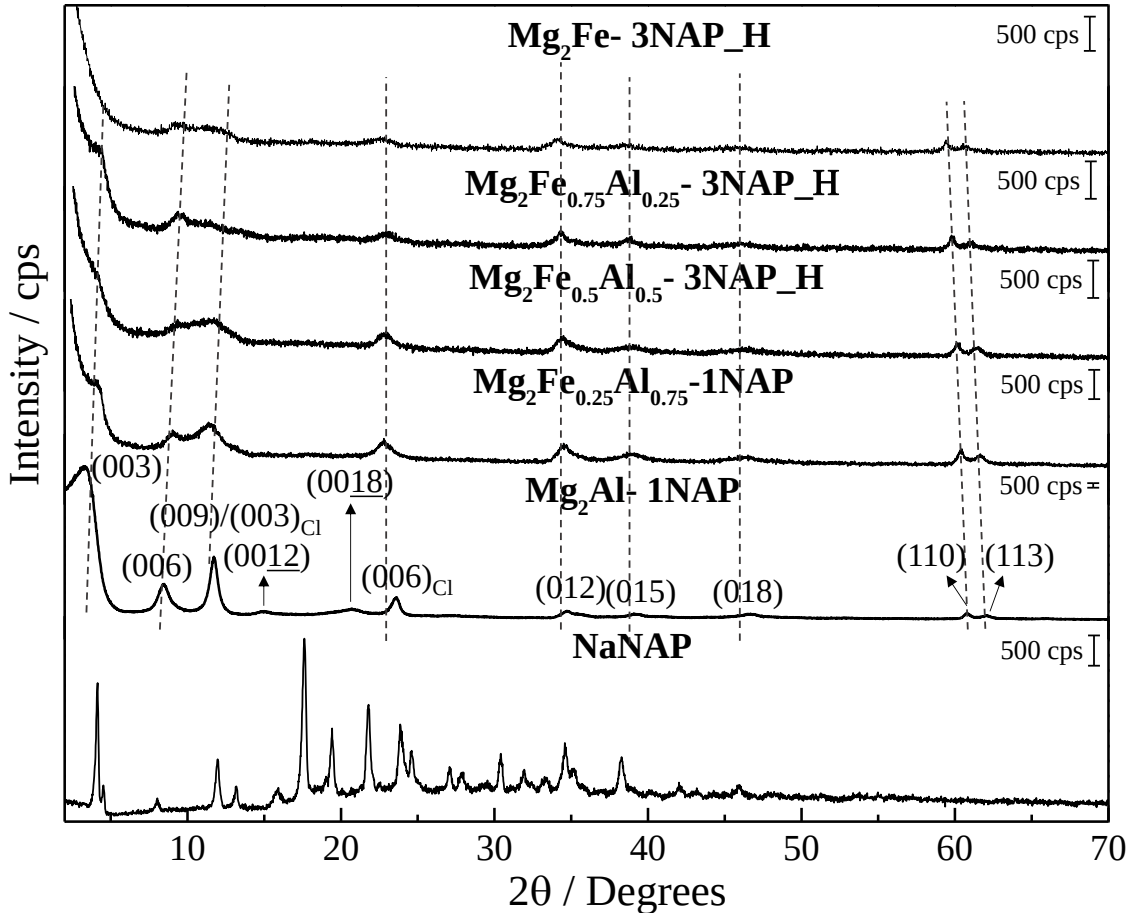

Figure 4.1. X-ray diffraction patterns of $Mg_2Fe_yAl_{(1-y)-n}$NAP_H LDHs and the NaNAP salt.

Table 4.1. LDH phases indexation: interplanar distances $d_{(hkl)}$, 2θ peak positions and correspondent Miller indexes considering $Mg_2Fe_yAl_{(1-y)-n}$NAP_H LDHs presenting the polytype 3R1.

$Mg_2Fe_yAl_{(1-y)}$-nNAP_H samples										**Miller**
***y* = 0, n = 1**		***y* = 0.25, n =1**		***y* = 0.5, n = 3, H**		***y* = 0.75, n = 3, H**		***y* = 1, n = 3, H**		**Index**
2θ	**d (Å)**	**2θ**	**d (Å)**	**2θ**	**d (Å)**	**2θ**	**d (Å)**	***2θ***	***d (Å)***	***(hkl)***
3.41	25.87	4.01	21.99	----	----	4.26	20.70	----	----	(003
8.49	10.40	9.03	9.79	9.36	9.44	9.39	9.40	9.68	9.13	(006
11.72	7.54	11.43	7.73	11.73	7.53	11.48	7.70	11.45	7.72	(009)/ $(003)_{Cl}$
14.98	5.91	15.00	5.90	----	----	----	----	----	----	(00$\underline{12}$)
20.72	4.28	----	----	----	----	----	----	----	----	00$\underline{18}$)
23.63	3.76	22.80	3.90	22.95	3.87	23.10	3.85	22.83	3.89	$(006)_{Cl}$
34.73	2.58	34.51	2.60	34.49	2.60	34.38	2.61	34.26	2.61	(012)
39.10	2.30	39.12	2.30	39.00	2.31	38.92	2.31	38.34	2,35	(015)
46.68	1.94	46.51	1.95	46.59	1.95	46.14	1.96	46.18	1.96	(018)
60.78	1.52	60.45	1.53	60.20	1.54	59.78	1.55	59.41	1.55	(110)
62.25	1.49	61.65	1.50	61.52	1.51	61.17	1.51	60.56	1.53	(113)

Table 4.2 presents the *a* and *c* cell parameters for the LDH-NAP materials. The *a* cell parameters were calculated as 2 times the interplanar distance related to the refined position of the (110) diffraction peaks ($2xd_{(110)}$) (see **Appendix C**, **Figure C.1,** for refinement results), while *c* parameters were calculated as 3 times the average basal spacing calculated as shown in **Equation 4.1**.

$$f(n) = \frac{\sum_{i=1}^{n} id_{(00(3i))}}{n} = \frac{1}{n}(d_{(003)} + 2d_{(006)} + \cdots + nd_{(00(3n))}) \quad (4.1)$$

Table 4.2. *a* and *c* cell parameters and basal space d obtained from powder X-ray diffraction data.

Sample	***a*** **(Å)**	***c*** **(Å)**
Mg_2Al-1NAP	3.04	68.84
$Mg_2Fe_{0.25}Al_{0.75}$-1NAP	3.06	66.27
$Mg_2Fe_{0.5}Al_{0.5}$-3NAP_H	3.07	62.22
$Mg_2Fe_{0.75}Al_{0.25}$-3NAP_H	3.09	62.61
Mg_2Fe-3NAP_H	3.11	62.13
Zn_2Al-1NAP	3.05	66.91
$Zn_2Fe_{0.25}Al_{0.75}$-1NAP	3.06	67.10
$Zn_2Fe_{0.5}Al_{0.5}$-1NAP	3.07	67.13
$Zn_2Fe_{0.75}Al_{0.25}$-1NAP	3.11	67.99
Zn_2Fe-1NAP	-----	69.81

X-ray patterns of $Zn_2Fe_yAl_{(1-y)}$-NAP samples are presented in **Figure 4.2**. In general, Zn-NAP LDHs show a greater structural organization in comparison to the Mg-series, resulting in more intense and narrow peaks. Interplanar distances, $d_{(hkl)}$, 2θ peak positions and correspondent Miller indexes are compiled in **Table 4.3.** The displacement of the (00l) peaks toward low angles (2θ) region in comparison with the precursor LDHs-Cl was also observed, endorsing NAP intercalation. Differently from the $Mg_2Fe_yAl_{(1-y)}$-nNAP_H LDHs, the basal spacing is not progressively decreased by increasing iron amount. For the Zn_2Al-1NAP sample, basal spacing calculated considering the (003), (006), (009), (00<u>12</u>), and (00<u>18</u>) harmonic peaks is equal to 22.30 Å. From the Zn_2Al-1NAP to the $Zn_2Fe_{0.75}Al_{0.25}$-1NAP samples, the same observations made for the Mg-series indicating the pristine LDH-Cl phases are also valid for the Zn-series. Moreover, with the increase of iron amount in the LDHs compositions, the diffractograms become more like the respective ones for the chloride phases, the intensity of the (00l) planes related

to the hybrid phase progressively decreases, which may indicate a reduction in ion-exchange yield of Cl^- by NAP ions. As observed for the precursor $Zn_2Fe_{0.75}Al_{0.25}$-Cl sample, ZnO side phase is also present for the $Zn_2Fe_{0.75}Al_{0.25}$-1NAP sample, better visualized by the zoom in the region of interest shown in **Figure 4.3**. The XRD profile of the Zn_2Fe-1NAP sample presents harmonic peaks that could be assigned to the (003), (006), and (009) peaks of the LDH-NAP, and also peaks attributed to the side ZnO phase. The characterization of the Zn_2Fe-Cl precursor indicated that LDH is not formed, either crystalline or amorphous. Instead, it is formed an amorphous ferrihydrite (2 main lines observed in XRD) (see **Chapter 3**, **Figure 3.2**) suspected to guide the formation of zinc phases (ZnO and $Zn(OH)_2$). As discussed in **Chapter 3**, the pristine Zn-LDH materials were prepared at pH equal to 7.5 in which ferrihydrite presents lower solubility. Pristine LDHs were suspended in NAP solutions in the pH range 8.5 – 8.7, where ferrihydrite solubility is higher. Thus, it is proposed that ferrihydrite solubilization have allowed the Fe^{3+} reprecipitation as a Zn_RFe LDH intercalated with NAP. Ion-exchange time (24 h) may have also propitiated side phases organization, as better visualized plotting together the XRD of the Zn_2Fe-Cl and Zn_2Fe-NAP samples (**Figure 4.4**).

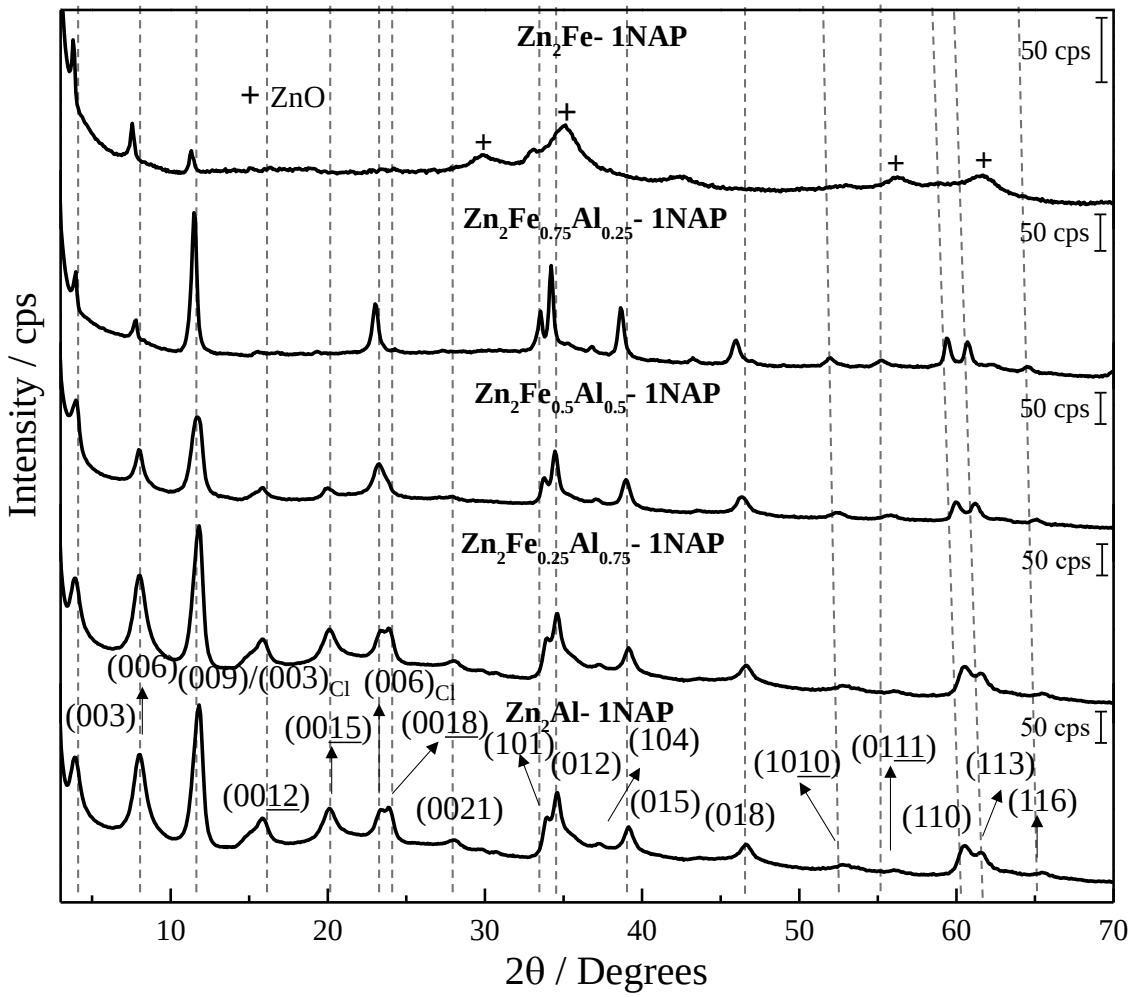

Figure 4.2. X-ray diffraction patterns of the $Zn_2Fe_yAl_{(1-y)}$-1NAP LDH samples.

Table 4.3. LDH phases indexation: interplanar distances $d_{(hkl)}$, 2θ peak positions, and correspondent Miller indexes considering $Zn_2Fe_yAl_{(1-y)}$-1NAP LDHs presenting the polytype 3R1.

$Zn_2Fe_yAl_{(1-y)}$-NAP samples										**Miller Index**
***y* = 0**		***y* = 0.25**		***y* = 0.5**		***y* = 0.75**		***y* = 1**		
2θ	**d (Å)**	**2θ**	**d (Å)**	**2θ**	**d (Å)**	**2θ**	**d (Å)**	***2θ***	***d (Å)***	***(hkl)***
3.88	22.75	3.88	22.75	3.96	22.27	3.96	22.27	3.80	22.25	(003)
8.06	10.96	8.06	10.96	7.97	11.08	7.91	11.31	7.56	11.69	(006)
11.82	7.48	11.82	7.48	11.73	7.53	11.48	7.70	11.32	7.81	$(009)/(003)_{Cl}$
15.83	5.59	15.83	5.59	15.83	5.59	15.58	5.68	----	----	(00$\underline{12}$)
20.09	4.41	20.09	4.41	20.01	4.43	19.34	4,58	----	----	(00$\underline{15}$)
23.35	3.81	23.35	3.81	23.66	23.26	3.82	23.01	----	----	$(006)_{Cl}$
23.85	3.73	23.85	3.73	----	----	----	----	----	----	(00$\underline{18}$)
28.03	3.18	28.03	3.18	27.94	3.19	----	----	----	----	(00$\underline{21}$)
33.96	2.64	33.96	2.64	33.79	2.65	33.54	2.67	----	----	(101)
34.63	2.59	34.63	2.59	34.46	2.60	34.21	2.62	----	----	(012)
37.22	2.41	31.30	2.41	37.05	2.42	36.80	2.43	----	----	(104)
36.14	2.48	39.06	2.30	38.97	2.31	38.64	2.33	----	----	(015)
46.66	1.94	46.58	1.95	46.33	1.96	45.99	1.97	----	----	(018)
52.84	1.73	52.68	1.74	52.42	1.74	52.01	1.76	----	----	(10$\underline{10}$)
56.10	1.64	55.93	1.64	55.85	1.64	55.27	1.66	----	----	(01$\underline{11}$)
60.53	1.53	60.27	1.53	59.95	1.54	59.36	1.56	----	----	(110)
61.61	1.50	61.37	1.51	61.20	1.51	60.70	1.52	----	----	(113)
65.46	1.42	65.38	1.43	65.13	1.43	64.54	1.44	----	----	(116)

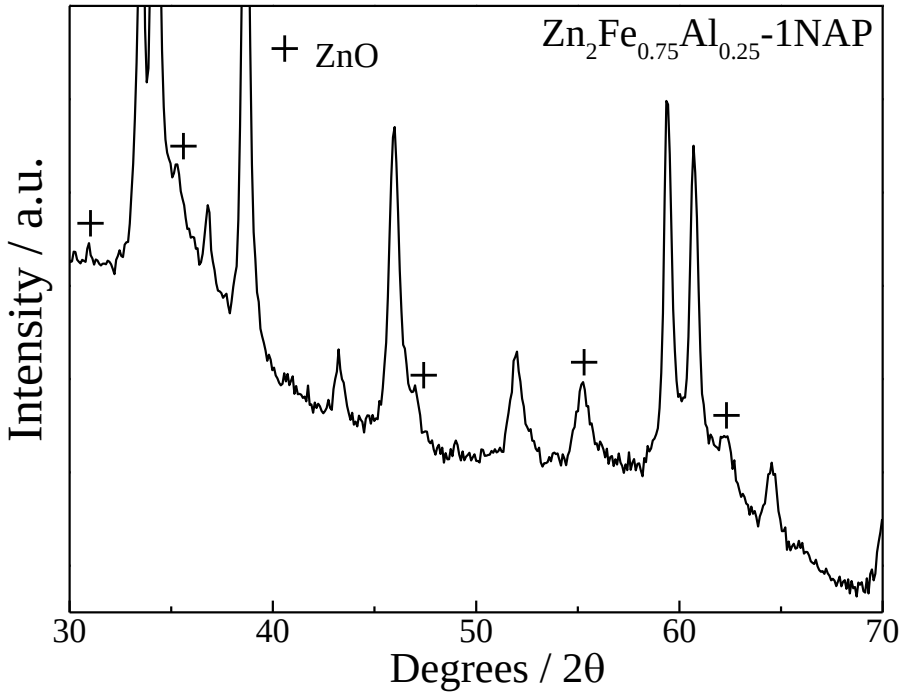

Figure 4.3. X-ray diffraction pattern of $Zn_2Fe_{0.75}Al_{0.25}$-NAP sample.

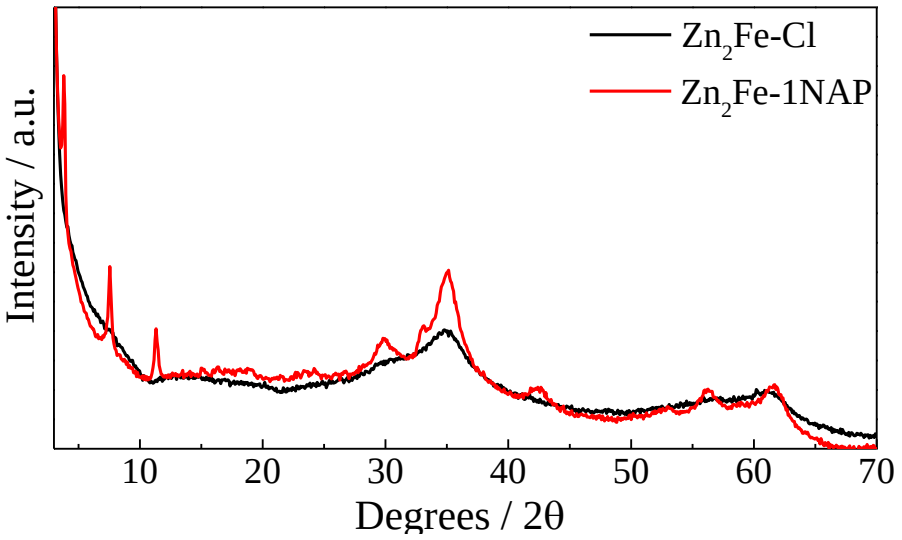

Figure 4.4. X-ray diffraction pattern of the Zn_2Fe-Cl (presented in **Chapter 3**) and Zn_2Fe-NAP samples.

Differently from the Zn-series, whose no NAP excess was needed to be employed being possible to visualize LDH-NAP phases formation by XRD, by increasing Fe^{3+} amount excess of NAP and heating were employed for iron enriched Mg-LDHs. Starting from the Mg_2Al layer composition, NAP / M^{3+} molar ratio was kept equal to 1 along the preparation of the materials by increasing the degree of substitution of Al^{3+} by Fe^{3+} cation. As can be seen in **Figure 4.5**, for the $Mg_2Fe_{0.5}Al_{0.5}$ layer composition, only peaks

related to the pristine LDH can be visualized by adding no excess of NAP or excess of 2. By adding a NAP / M^{3+} molar ratio equal to 3, a peak start being visualized below 10 ° (2θ) and close to the (003) peak related to the LDH-Cl pristine phase, indicating a possible (006) peak related to the LDH-NAP phase, indicated as $(006)_{NAP}$. Keeping the same conditions plus applying heating at 80 °C, the exchange of Cl^- by NAP anions was confirmed and such conditions were applied for the preparation of the $Mg_2Fe_{0.75}Al_{0.25}$-3NAP_H and Mg_2Fe-3NAP_H samples.

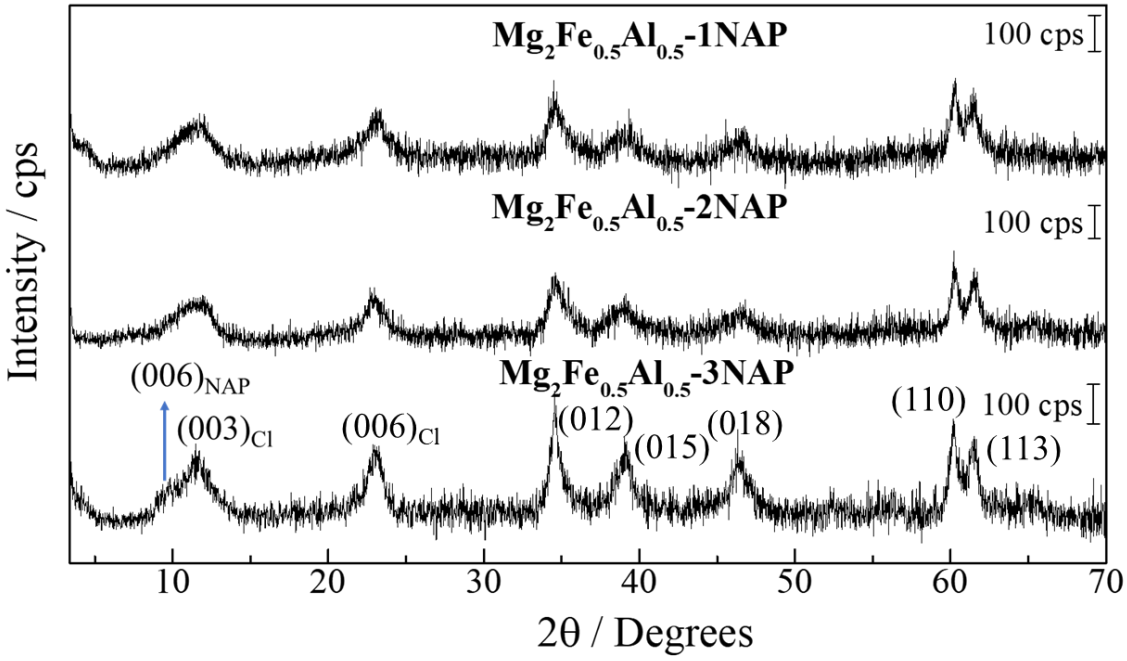

Figure 4.5. X-ray diffraction patterns of $Mg_2Fe_{0.5}Al_{0.5}$-1NAP, $Mg_2Fe_{0.5}Al_{0.5}$-2NAP, and $Mg_2Fe_{0.5}Al_{0.5}$-3NAP samples. Baseline was subtracted using Fityk software.

Table 4.4 shows the chemical analysis results for the LDH-NAP materials. The M^{2+}/M^{3+} and Fe^{3+}/Al^{3+} molar ratios of bulk materials are close to the nominal values for all samples, mainly the R values for the Mg-series, with exception of the Zn_2Fe-1NAP sample, whose Zn^{2+}/Fe^{3+} molar ratio is equal to 1.08, similarly to the value observed for the Zn_2Fe-Cl pristine sample (1.16). Only small variations are founded when compared to the elemental analysis for the pristine LDH (see **Chapter 3**, **Table 3.1**).

Table 4.4. Chemical composition for the LDH-NAP materials.

Sample	M^{2+}/Al^{3+}	M^{2+}/Fe^{3+}	y = $Fe^{3+}/(Fe^{3+}+Al^{3+})$	R = $M^{2+}/(Fe^{3+}+Al^{3+})$	%C	% NAP	% H_2O[c]
Mg_2Al-1NAP	(2.00)[a] 2.03[b]				27.23	37.30	6.0
$Mg_2Fe_{0.25}Al_{0.75}$-1NAP	(2.67) 2.78	(8.00) 8.31	(0.25) 0.27	(2.00) 2.08	18.35	25.04	6.2
$Mg_2Fe_{0.5}Al_{0.5}$-3NAP_H	(4.00) 4.21	(4.00) 4.08	(0.50) 0.51	(2.00) 2.07	20.16	27.11	3.7
$Mg_2Fe_{0.75}Al_{0.25}$-3NAP_H	(8.00) 8.32	(2.67) 2.65	(0.75) 0.76	(2.00) 2.01	22.97	31.35	3.9
Mg_2Fe-3NAP_H		(2.00) 1.93			19.64	26.80	3.9
Zn_2Al-1NAP	(2.00) 1.95				25.86	35.29	9.5
$Zn_2Fe_{0.25}Al_{0.75}$-1NAP	(2.67) 2.67	(8.00) 8.92	(0.25) 0.23	(2.00) 2.05	23.66	32.29	8.8
$Zn_2Fe_{0.5}Al_{0.5}$-1NAP	(4.00) 3.64	(4.00) 3.53	(0.50) 0.51	(2.00) 1.79	19.25	26.27	8.1
$Zn_2Fe_{0.75}Al_{0.25}$-1NAP	(8.00) 7.92	(2.67) 2.56	(0.75) 0.76	(2.00) 1.93	8.25	11.26	6.2
Zn_2Fe-1NAP		(2.00) 1.08			9.45	12.89	5.2

a) expected values according with the molar ratio of the reagents, b) experimental values and c) water amount (m/m) obtained by TGA experiments.

In **Chapter 3** it was attempted for possible mistakes in the determination of the LDH composition from analysis concerning the bulk samples only, such as the metals elemental analysis, whose results are frequently extrapolated as representing the compositions of crystallized LDHs phases identified by XRD. Recapitulating, detailed characterization of pristine LDH-Cl materials applied as precursors phases in **Chapter 3** indicated that, in general, the molar ratios between the cations for the crystalline LDH phases differ from that of the bulk samples for iron-enriched samples. It was also showed that for $Mg_2Fe_yAl_{(1-y)}$-Cl materials with y = 0, 0.25, and 0.5 the molar ratios of metals for the crystalline phases represent the values for the bulk samples, endorsing phases purity. For the $Mg_2Fe_{0.75}Al_{0.25}$-Cl and Mg_2Fe-Cl samples, however, x value of

crystalline phases showed to be lower than 0.33. For $Zn_2Fe_yAl_{(1-y)}$-Cl materials, more pronounced deviations were observed.

Figure 4.6 shows the plot of *a* cell parameters as a function of experimental *y* (obtained from elemental analysis results shown in **Table 4.4**) for the Zn and Mg series of hybrid materials. Herein, the results concerning the LDH-NAP materials are compared to the LDH-Cl pristine phases (data present in **Chapter 3**: **Table 3.2**, **Figure 3.3**) to evaluate possible changes in the composition of sample's crystalline components after the ion-exchange procedure. For the Mg materials (**Figure 4.6A**), curves are practically overlapped, indicating a possible maintenance of the M^{2+}/M^{3+} content along the exchange of Cl^- anions by NAP. The points for the $Zn_2Fe_yAl_{(1-y)}$-1NAP materials (**Figure 4.6B**) are shifted down, indicating transformations in the LDH layers along the exchange of Cl^- anions by NAP that can be explained by the decrease in the Zn^{2+} content in the case of the Zn_2Al-1NAP sample, considering its higher ionic radii (0.88 Å[263]) compared to Al^{3+} (0.675 Å[263]), or in both Zn^{2+} and Fe^{3+} (0.785 Å[263]) contents for the other samples. Moreover, a loss in the linear tendency is observed.

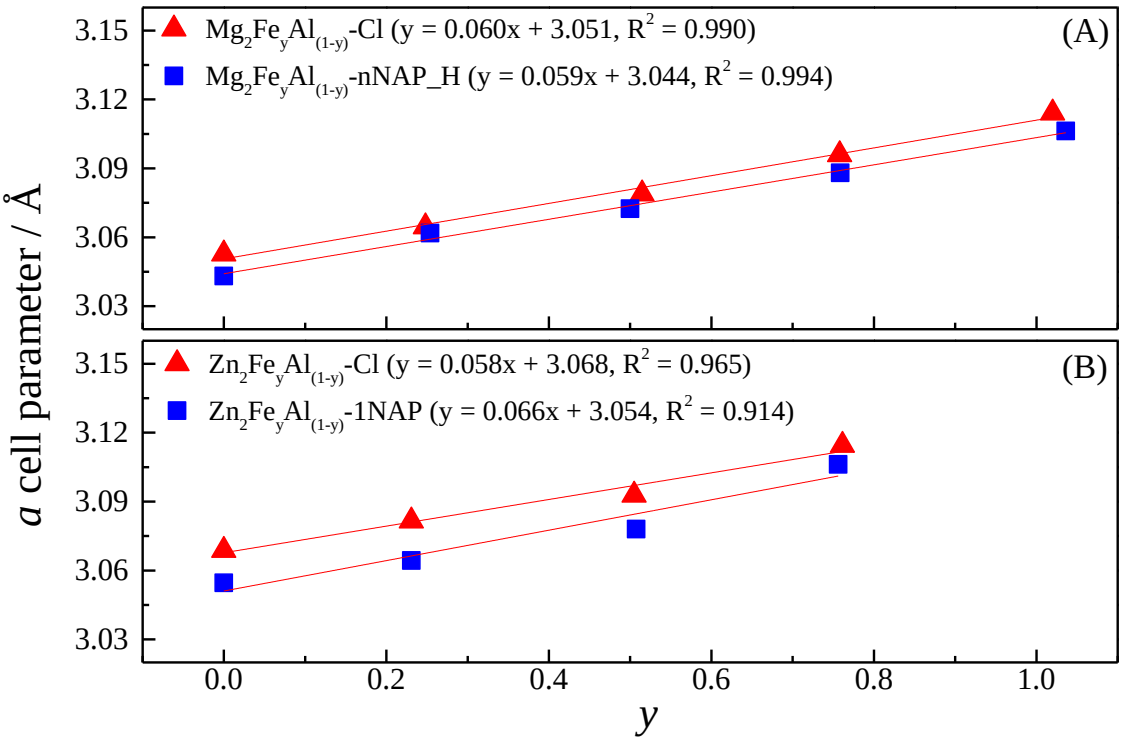

Figure 4.6. *a* cell parameter as a function of experimental *y*.

For the $Mg_2Fe_yAl_{(1-y)}$-nNAP_H series, *a* lattice parameters values were also plotted according to *x* values and compared to the results for pristine LDHs, as presented in **Figure 4.7**, where full lines represent theoretical values calculated as in **Chapter 3** (see **Figure 3.14**). $M_2Fe_yAl_{(1-y)}$-Cl and $M_2Fe_yAl_{(1-y)}$-nNAP_H data are represented by red triangles and blue squares, respectively. Points before and after ion-exchange reaction are in general overlapped, endorsing that the exchange of Cl^- by NAP comprises, in fact, a topotactic process.

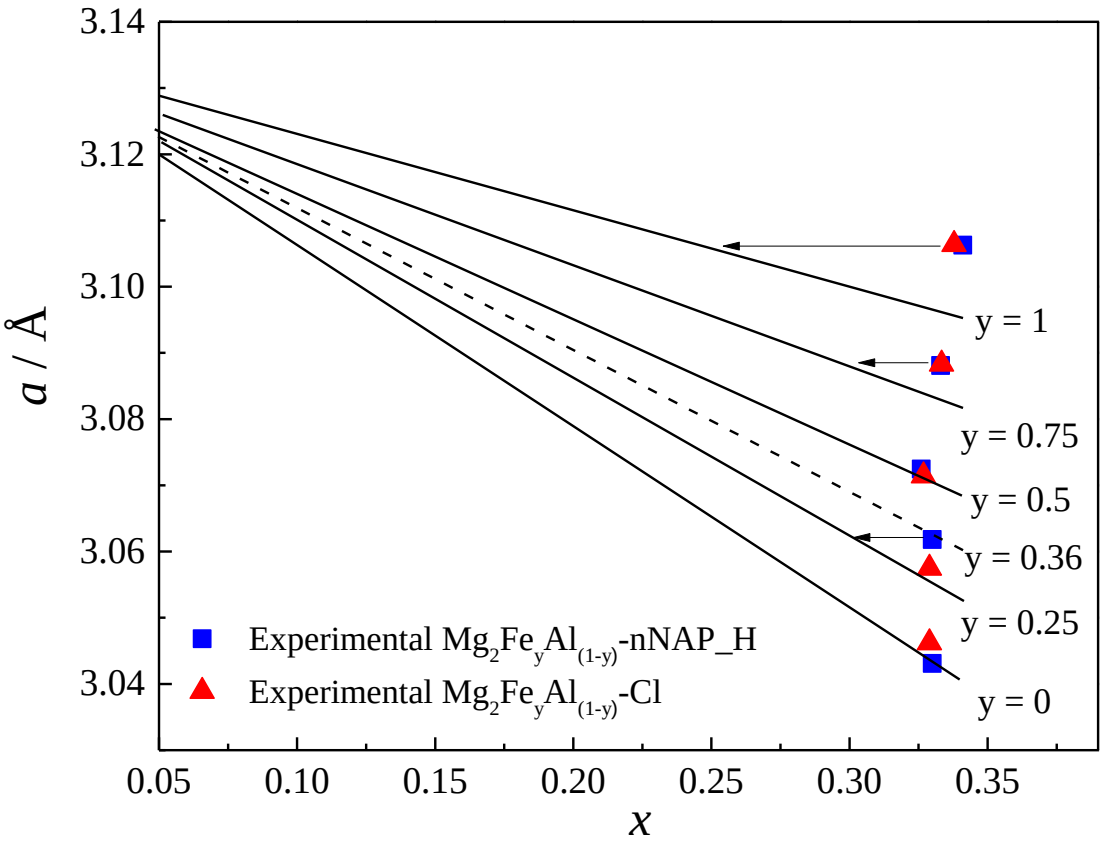

Figure 4.7. Crossed-analysis of XRD and chemical analysis data for the $Mg_2Fe_yAl_{(1-y)}$-Cl and $Mg_2Fe_yAl_{(1-y)}$-nNAP_H series: theoretical variation of the lattice parameter *a* as a function of the composition of LDH layers in terms of *x* and *y* (solid lines); filled squares and triangles represent experimental values for the LDH-Cl and LDH-NAP samples, respectively.

The shift of the point concerning the $Mg_2Fe_{0.25}Al_{0.75}$-NAP sample from the tendency can primarily be a result of the variation in both *y* or *x* values, where *y* can be equal to 0.36 instead of 0.25 or *x* can be closer than 0.30 instead of 0.33. The second hypothesis is the more reasonable, since the decrease in charge density may explain the decrease in NAP % in comparison to the Mg_2Al-NAP sample. NAP was intercalated in a high amount into the Mg_2Al-NAP LDH, representing 37.90 % of the mass of the hybrid material. By substituting 25 % of the Al content by Fe, $Mg_2Fe_{0.25}Al_{0.75}$-NAP sample, NAP percentage

downs to 25.04 wt %. It is important to point that, considering the gradual increase of *y* by 0.25 from the starting Mg_2Al-1NAP and Zn_2Al-1NAP compositions, if the same molar amount of intercalated NAP is kept constant, neglecting variations in dehydration degrees, it would be expected a decrease in NAP percentage lower than about 2 and 1 %, respectively, due to the increase in the molar mass of the LDHs. Additionally, for the further Mg- and Zn-compositions of the series, such decrease is even lower, since how higher the molar mass of the LDHs, lower is the difference caused in their molar mass by the substitution of Al for Fe. Therefore, decreases in NAP percentage higher than the values provided above can be attributed to the ion-exchange efficiency decrease and/or to the presence of impurities not able to encapsulate NAP. For the $Mg_2Fe_{0.5}Al_{0.5}$-3NAP_H sample, *x* value is close to 0.33 and layer composition matches with the expected, even so the employment of temperature and excess of NAP was necessary to observe the hybrid phase formation. Since the molar ratio between the di- and trivalent cations are comparable to those of the Mg_2Al-NAP sample, it is possible to infer that the substitution of Al^{3+} by Fe^{3+} in the LDH structure in some way hinders NAP intercalation. For the Mg_2Fe-3NAP_H sample, the decrease in intercalated NAP percentage (26.80 wt%) can be related to the *x* value lower than 0.33 (closer to 0.25), indicating a decrease in the charge density of the layers. Differently from the Mg-series, the composition of the layers for the Zn-series changes after the submission of pristine phases to ion-exchange reaction. NAP percentages progressively decreased from the Zn_2Al-NAP (35.29 wt %) to the $Zn_2Fe_{0.75}Al_{0.25}$-NAP (11.26 wt %) sample, which can be attributed to the increase in side phases with the increase in *y*. The tendency of reduction of ion-exchange efficacy may also be related to the increase in the 2D (L_{xy}) and width (L_z) coherent lengths of LDH-Cl crystals according with the increase in iron amount (see **Chapter 3**, **Table 3.4**). The higher the area of LDH layers and higher the number of pilled layers per coherent domain, the more hindered is the ion-exchange process. A reduction in both Lxy and Lz parameters is observed from the Mg_2Al-Cl to the $Mg_2Fe_{0.25}Al_{0.75}$-Cl samples, what would be expected to positively affect in exchange efficacy. However, from this composition, the lengths increase again as the iron content increases. In **Chapter 3**, the lengths of the coherent domains (**Table 3.4**) were also compared to the SEM results for the LDHs-Cl (**Figure 3.15**) that revealed micrometric sized platelets entangled each other, typical of LDH morphology. Such difference, from cents of angstroms to

micrometers indicates, as reported[246], that LDH particles observed by SEM are often polycrystalline secondary particles, resulting from the aggregation/coalescence of the primary nanoparticles as measured from peak shape analysis of XRD data. In some way, the presence of iron in the LDH structure may also affect the aggregation state of the particles, hindering the ion-exchange process. Due to the complexity of the LDH-NAP samples and the number of variables that may influence the ion-exchange process (*i.e.* the precise compositions on LDH layers and consequent charge density, the presence of crystalline and/or amorphous impurities, the size of the coherent domains and secondary polycrystalline particles) interpretations of the ion-exchange phenomena given here are only attempts and further studies are necessary.

Next, the thermal decomposition of the NaNAP and LDH-NAP samples is studied.

TGA-DSC and DTG-MS curves of NaNAP are shown in **Figure 4.8**. It was observed six mass loss events. The first event is an endothermic process occurring from 25 to 110 °C and is related to the release of adsorbed water molecules (m/z = 18). Thermal decomposition starts at 250 °C undergoing two events, with maximum signals at 400 and 470 °C, respectively, that are accompanied by the release of H_2O and CO_2 (m/z = 18), followed by three exothermic events above 700 °C, related to the formation of sodium species, with the release of CO_2.

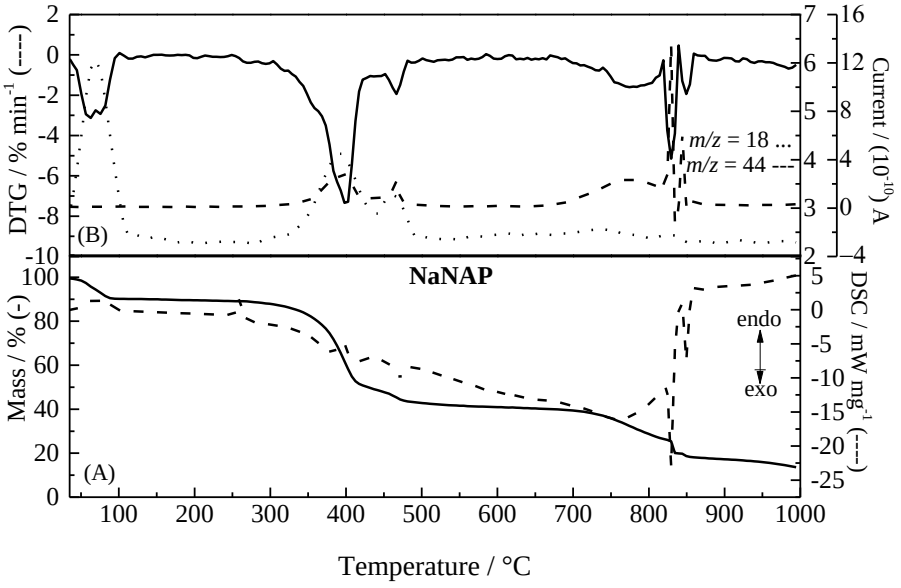

Figure 4.8. TGA-DSC (A) and DTG-MS (B) curves for the NaNAP salt.

The detailed weight loss events obtained by thermal analysis for the NaNAP sample is presented in **Table 4.5**.

Table 4.5. Thermal analysis data of naproxen sodium sample.

Sample	Temperature Range (°C)	Mass (%)	Events
NaNAP	RT – 110	9.9	Dehydration
	250 – 440	39.7	Decomposition
	440 – 500	6.2	
	500 – 820	12.8	Sodium species formation
	820 – 840	6.6	
	840 – 1000	5.6	

According to the mass loss percentages on burn of naproxen sodium, it is suggested the formation of the Na_2CO_3 phase as final product. The **Scheme 4.1** shows the chemical equations for the NaNAP decomposition and experimental and calculated released masses.

$$C_{14}H_{13}O_3Na \bullet 1.5H_2O \xrightarrow[-\,1.5\,H_2O]{\text{Dehydration (RT}-125\,^{\circ}\text{C)}} C_{14}H_{13}O_3Na$$
wt.% weight loss exp. = 9.9 %
wt.% weight loss calc. = 9.9 %

$$2\,C_{14}H_{13}O_3Na + 32O_2 \xrightarrow[-\,13\,H_2O,\,-\,27\,CO_2]{\text{Decomposition (125 - 1000 °C)}} Na_2CO_3$$
wt.% residue weight exp. = 19.2 %
wt.% residue weight calc. = 22.2 %

Scheme 4.1. Chemical decomposition of NaNAP.

TGA-DSC and DTG-MS curves for the $Mg_2Fe_yAl_{(1-y)}$-nNAP_H samples are shown in **Figures 4.9** and **4.10**, respectively. Similar to the LDH-Cl samples (**Chapter 3**), the first mass loss event (endothermic) is related to the release of superficially adsorbed water molecules (m/z = 18 MS fragment). The second mass loss event corresponds to the release of hydrated water and also to a small amount of CO_2 (m/z = 44 MS fragment) for the samples containing Fe^{3+}, corresponding to the release of adsorbed CO_3^{2+} contaminant. Following events (exothermic) are a combination of LDH dehydroxylation and NAP decomposition, followed by the concomitant release of H_2O and CO_2. Although no chloride release was verified (with m/z residues equal to 35 or 36) due to mass detector limitation, a small mass release occurs for all materials at high

temperatures and are not related to H_2O nor CO_2, thus being attributed to the dehydrochlorination process.

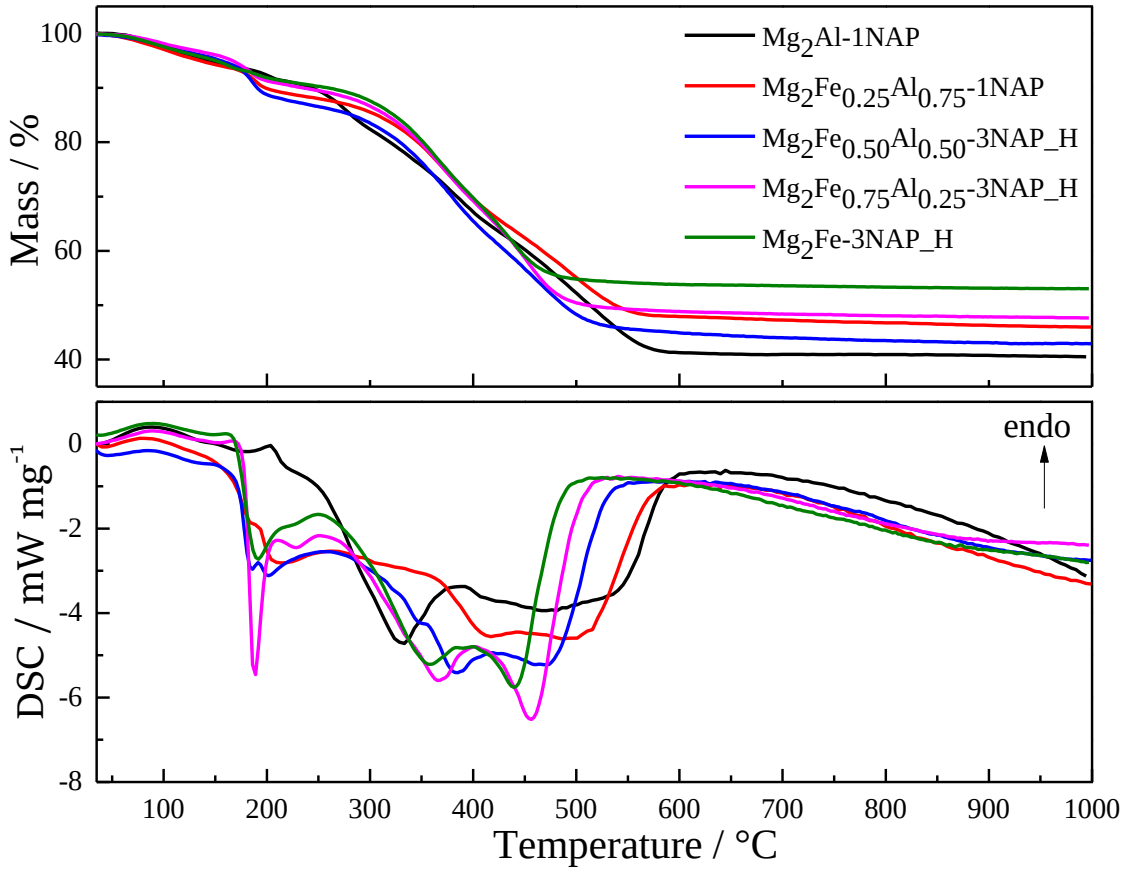

Figure 4.9. TGA and DSC curves of the $Mg_2Fe_yAl_{(1-y)}$-NAP samples.

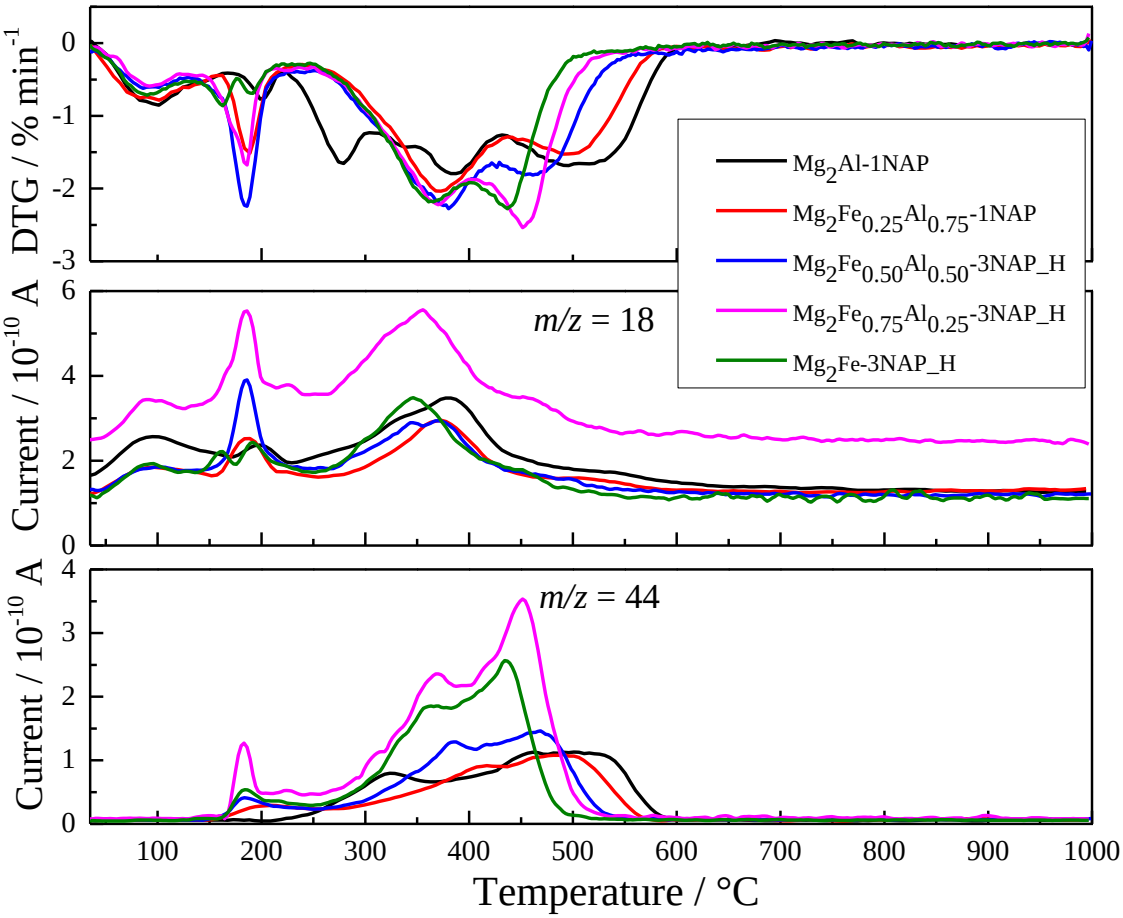

Figure 4.10. DTG and MS curves of the $Mg_2Fe_yAl_{(1-y)}$-NAP samples.

TGA-DSC and DTG-MS curves for the $Zn_2Fe_yAl_{(1-y)}$-1NAP series are shown in **Figures 4.11** and **4.12**, respectively. Differently from the Mg-LDHs, the two dehydration events overlap and NAP degradation occurs in more restricted temperature ranges.

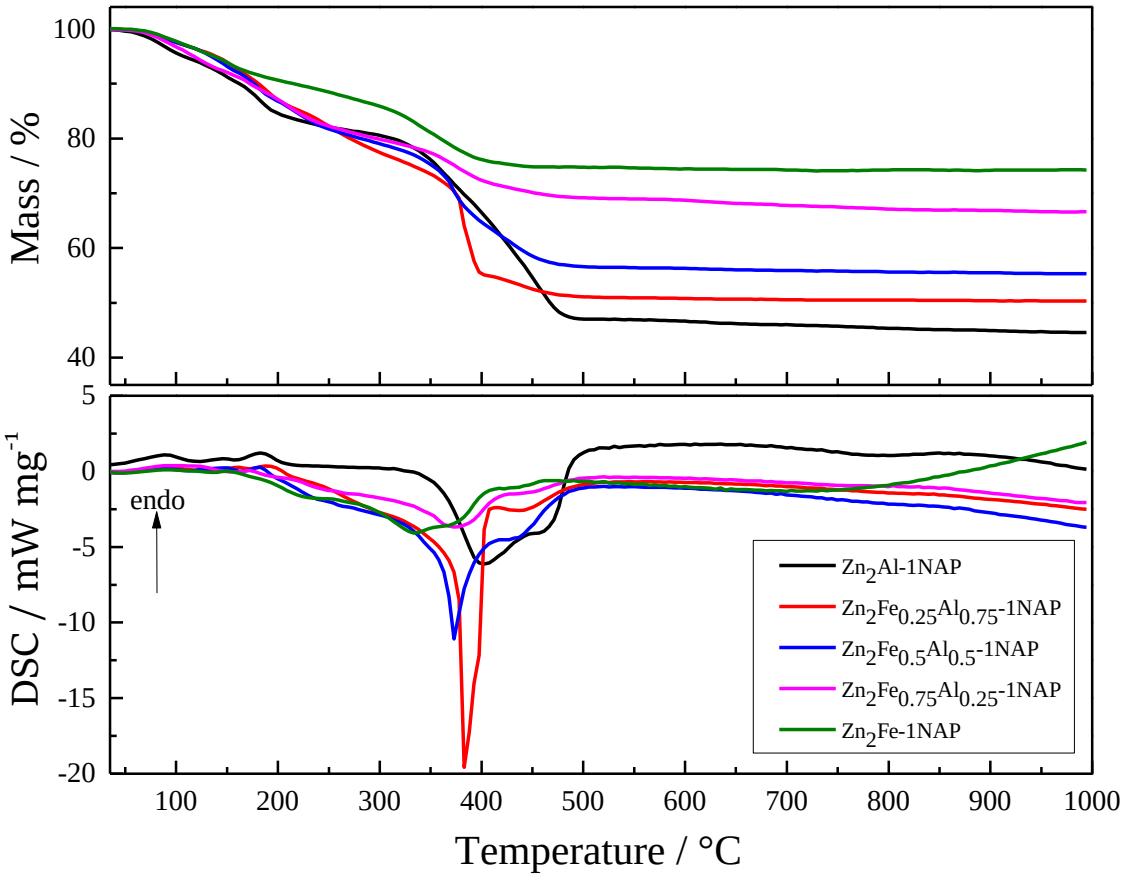

Figure 4.11. TGA and DSC curves of the $Zn_2Fe_yAl_{(1-y)}$-NAP samples.

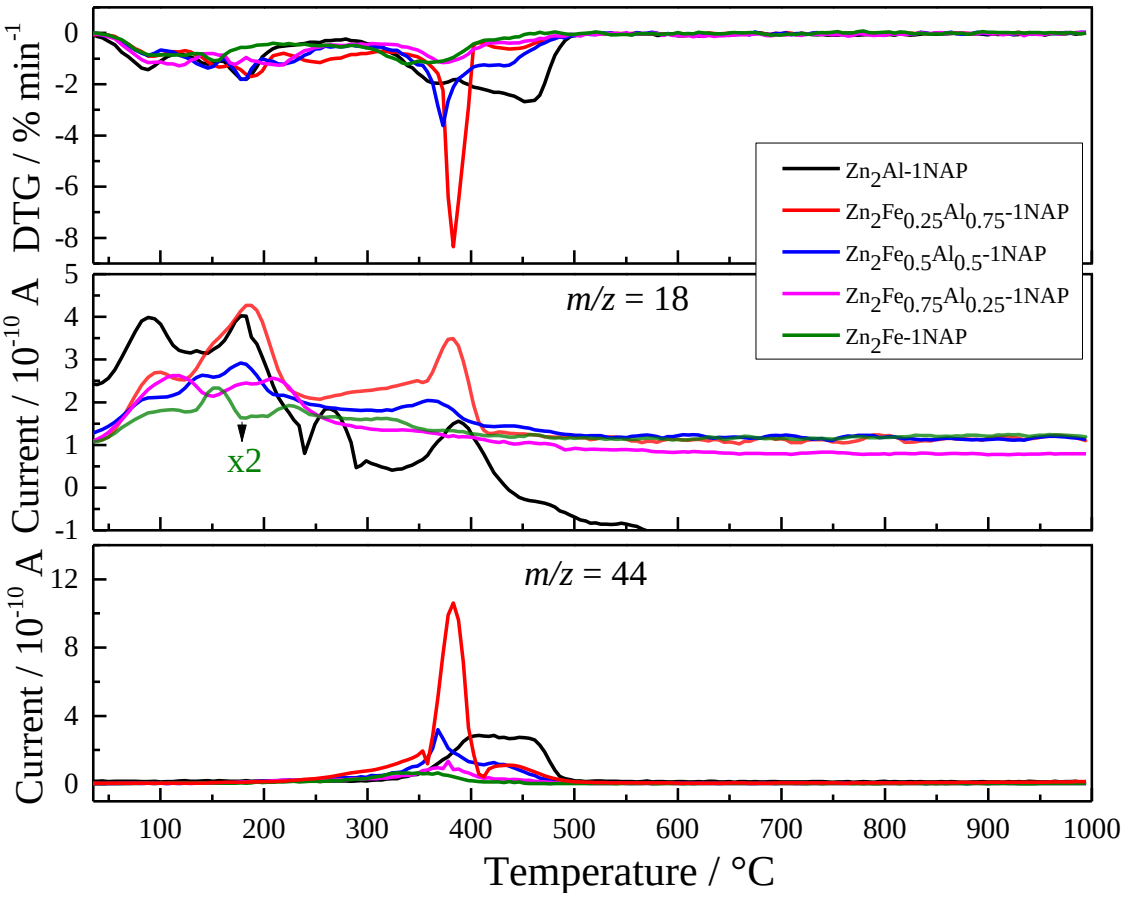

Figure 4.12. DTG and MS curves of the $Zn_2Fe_yAl_{(1-y)}$-NAP samples.

In more detail, **Figure 4.13A** shows that the starting temperatures (T) related to NAP decomposition overlapped to LDH dehydroxylation decreases according with the increase in *y* amount for both series of materials, following a linear correlation. The drug intercalated into the Zn_2Al LDH experiences an increase in its thermal stability of about 20 °C with relation to the starting NAP decompositions temperature compared to NaNAP salt (250 °C – **Figure 4.8**). On the other hand, NAP decomposition starts at around 220 °C when intercalated into the Mg_2Al LDH. Such different thermal behaviour according with the divalent cations was also observed in a previous work[115] for the $Mg_2Fe_{0.5}Al_{0.5}$-3NAP_H and $Zn_2Fe_{0.5}Al_{0.5}$-NAP LDHs, similar materials to the presented in this thesis, whose NAP starting decomposition temperature was around 165 °C and 220 °C, respectively. Additionally, NAP thermal decomposition when intercalated into LDH is a more complex process with more than 2 steps. In agreement with elemental carbon analysis, TGA residues percentages (res) (**Figure 4.13B**) increases from Mg_2Al-1NAP to $Mg_2Fe_{0.25}Al_{0.75}$-1NAP sample, indicating a decrease in the amount of NAP in the samples.

By applying NAP excess and temperature in the ion-exchange procedure along iron enrichment in the series, a decrease in the residue percentage is observed for the $Mg_2Fe_{0.5}Al_{0.5}$-3NAP_H sample. By keeping the same ion-exchange conditions and increasing *y*, a progressive increase in the amount of residues is verified. For the Zn-series, from Zn_2Al-1NAP to $Zn_2Fe_{0.75}Al_{0.25}$-1NAP the progressive increase in TGA residues agrees with the decrease in NAP encapsulation.

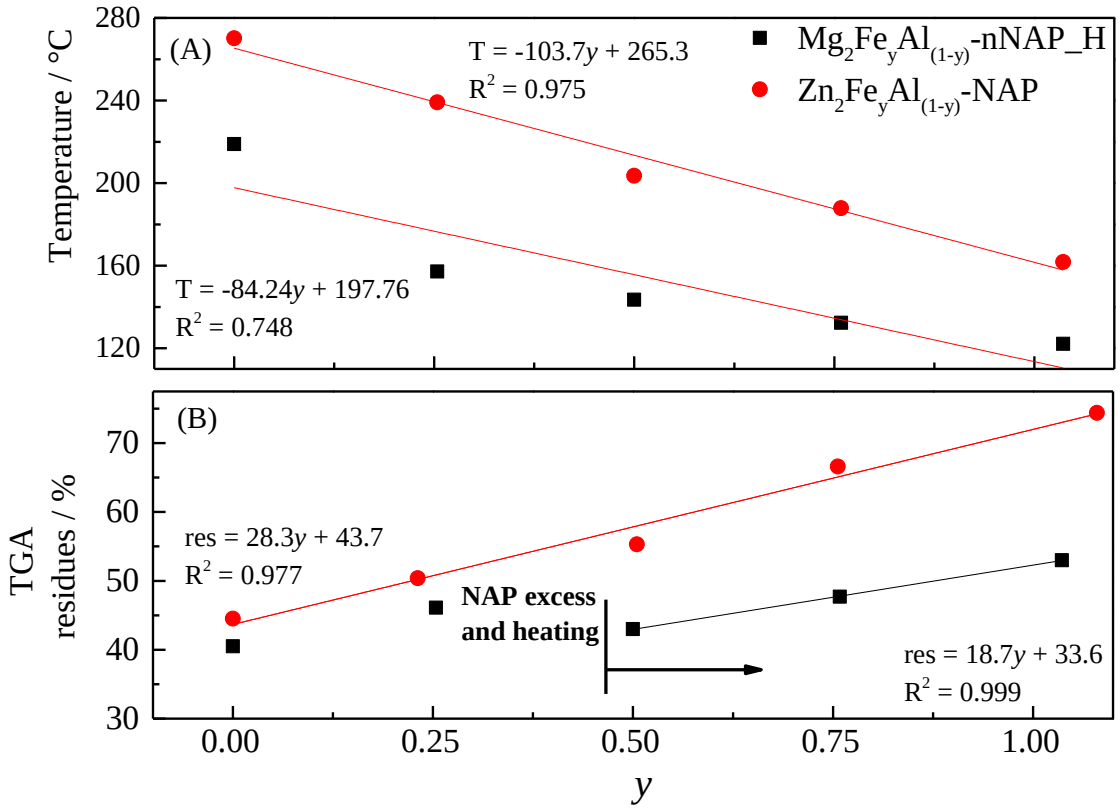

Figure 4.13. Starting temperatures of (A) NAP decomposition and LDH dehydroxylation and (B) TGA residues.

FT-IR and Raman spectra for the NaNAP and LDH-NAP samples were considered in this chapter mainly to evaluate the integrity of the organic anion after intercalation into LDH.

The attribution of Raman and IR vibrational modes was assisted by computational calculations. Raman spectra of calculated and experimental NaNAP (**Figures 4.14**) show a good concordance between data, indicating reliability in applying the calculated data to assignment the vibrations modes. FT-Raman spectra of the $Mg_2Fe_yAl_{(1-y)}$-nNAP_H samples (**Figure 4.15**) are similar. The band at 558 cm^{-1} for the Mg_2Al-1NAP sample,

related to the M^{3+}-O-M^{3+} stretching[219,221], is present at the same position observed for the pristine Mg_2Al-Cl (see **Chapter 3**, **Figure 3.7B**) and experienced a progressive shift toward lower wavenumber region according to the increase in *y*. All other bands are related to NAP[264]. Considerable band shifts are not verified compared to the experimental NaNAP spectra. **Table 4.6** shows the calculated and experimental wavenumbers for NaNAP and $M_2Fe_yAl_{(1-y)}$-nNAP_H samples, as well as the tentative attribution considering the main groups of NAP[264].

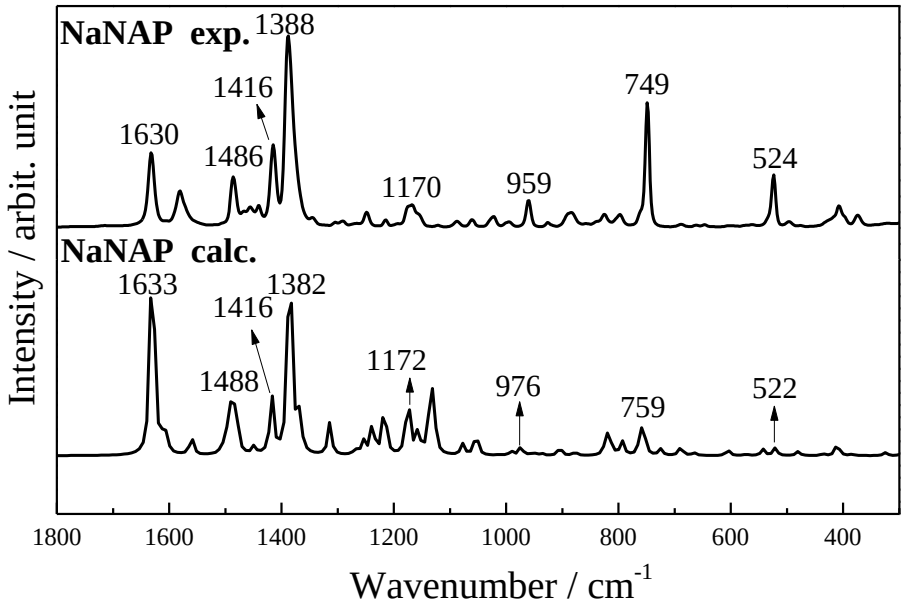

Figure 4.14. Raman spectra of calculated and experimental NaNAP.

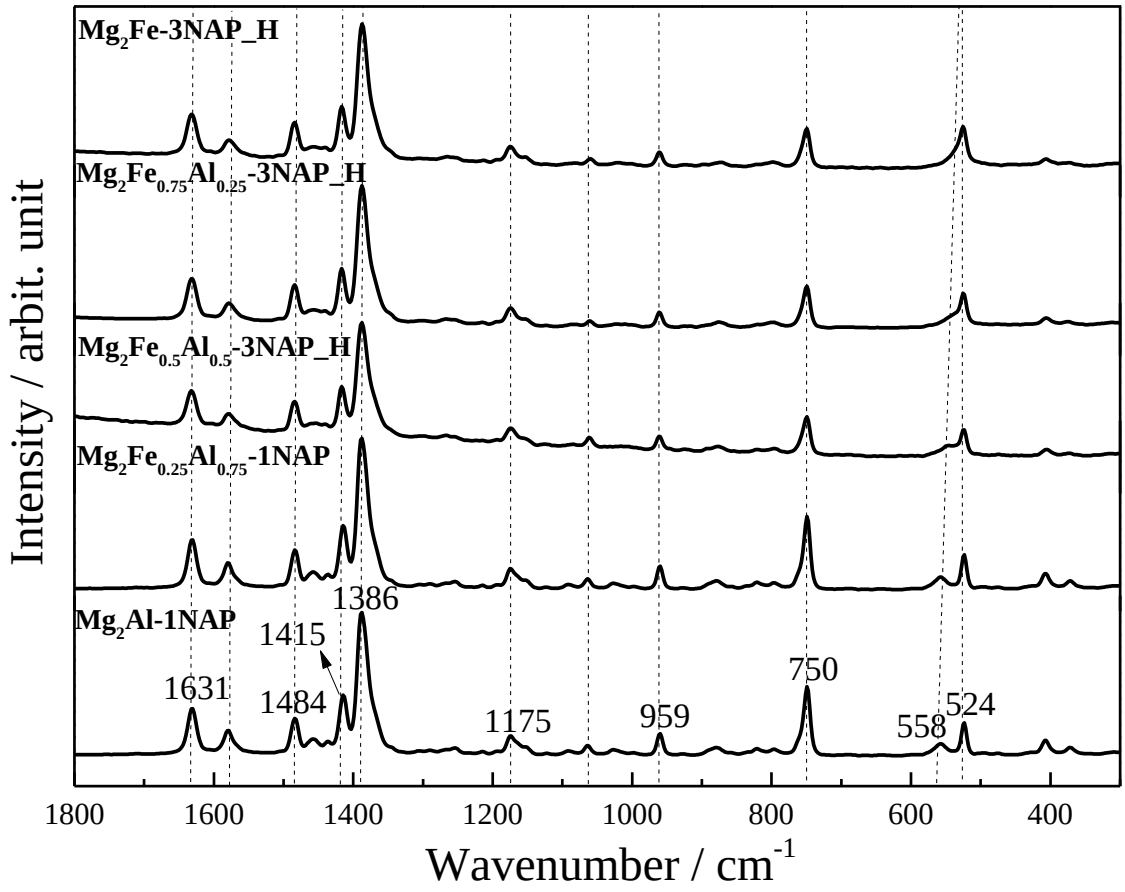

Figure 4.15. FT-Raman spectra of the $Mg_2Fe_yAl_{(1-y)}$-nNAP_H samples.

Table 4.6. Calculated and experimental Raman vibrational wavenumbers (in cm^{-1}).

Calc. NaNAP[a)]	Exp. NaNAP	$Mg_2Fe_yAl_{(1-y)}$-nNAP_H	$Zn_2Fe_yAl_{(1-y)}$-1NAP	Tentative attribution[b)]
1633	1632	1631	1631	ν_{as} C-C
1488	1486	1484	1484	w CH_3, δ C-H (naphthalene ring)
1416	1416	1415	1415	ν C-C
1382	1388	1386	1386	w CH_3, ν C-C (naphthalene ring)
1172	1170	1175	1175	δ C-H (naphthalene ring), w CH_3
976	959	959	959	γ C-H
759	749	750	749	γ C-H (naphthalene ring)
522	524	524	524	β C-C (naphthalene ring)

a) Selected values in cm^{-1} obtained by the functional/basis set BLYP/6-311**G++; b) Main groups involved in the vibration; ν = stretching, ν_{as} = antisymmetric stretching, δ = bending, w = wagging, β = bending in plane, and γ = bending out of plane.

FT-Raman spectra of the $Zn_2Fe_yAl_{(1-y)}$-NAP (**Figure 4.16**) are very similar from Zn_2Al-NAP to $Zn_2Fe_{0.75}Al_{0.25}$-NAP samples. For the Zn_2Fe-NAP sample, the spectrum is less resolved and present intense fluorescence, however the most intense bands attributed to NAP can be identified. Moreover, bands positions are practically the same compared to the Mg-samples (**Table 4.6**). The incorporation of iron is also indicated by the progressive shift of the band related to the M^{3+}-O-M^{3+} stretching, at 557 cm^{-1} for the Zn_2Al-NAP sample (same position observed for the Zn_2Al-Cl sample; see **Chapter 3**, **Figure 3.8B)**, toward lower wavenumber.

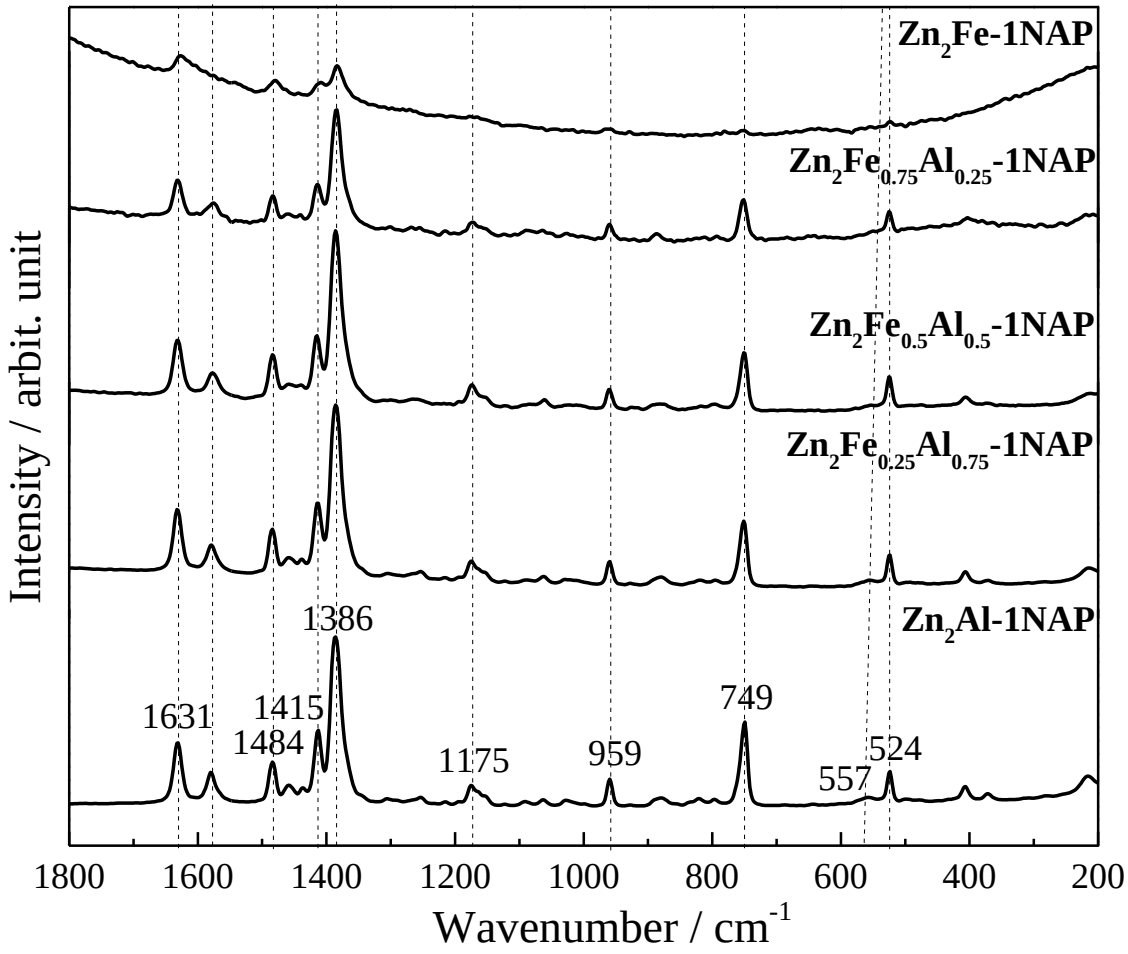

Figure 4.16. Raman spectra of the $Zn_2Fe_yAl_{(1-y)}$-1NAP samples.

The FT-IR spectra of calculated NaNAP and experimental NaNAP are present in **Figures 4.17**. The differences in spectra shape between the calculated and experimental IR data can be attributed to the contour conditions regard for the calculations, where it is considered a single molecule under vacuum. However, bands positions are quite similar.

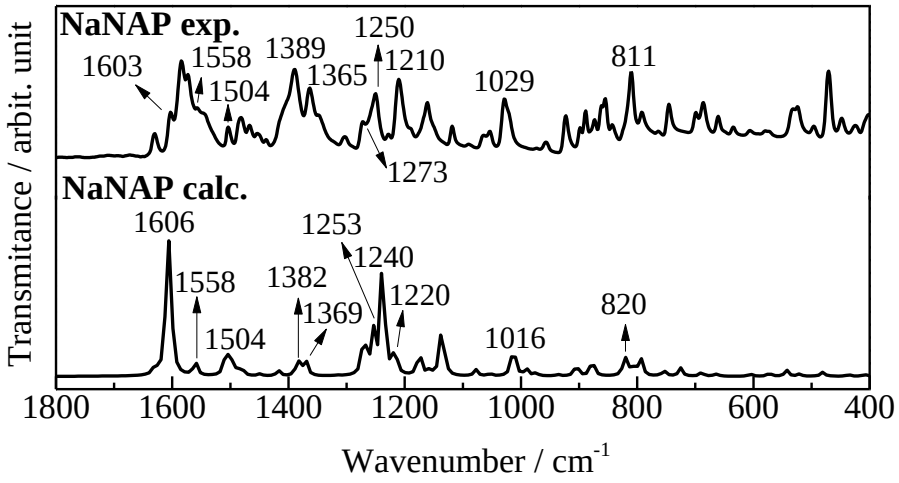

Figure 4.17. FT-IR spectra of calculated and experimental NaNAP.

The FT-IR spectra of $Mg_2Fe_yAl_{(1-y)}$-nNAP_H samples (**Figure 4.18**) are very similar. No changes in bands positions are verified with the increase of *y*. **Table 4.7** presents the calculated and experimental wavenumbers for NaNAP and $M_2Fe_yAl_{(1-y)}$-nNAP_H samples, as well as the tentative attribution considering the main groups of NAP[264]. FT-IR spectra were slightly sensitive to the intercalation process of NAP whereas four bands were shifted. Among them are the band at 1558 cm^{-1} in NaNAP shifted to 1542 cm^{-1} in LDH-NAP, assigned to the antisymmetric stretching of the C-C bonds, and the band at 1273 cm^{-1} (NaNAP) that was shifted to 1267 cm^{-1} and is related to the symmetric stretching of the carboxylate group COO^-. The other ones are the band at 1250 cm^{-1} (NaNAP) shifted to 1233 cm^{-1} (LDH-NAP) regarding the C-H bending in plane of the naphthalene ring and the band at 1210 cm^{-1} (NaNAP) shifted to 1215 cm^{-1} assigned to the C-H bending. Those shifts are an indicative of the interaction of the negative group of the molecule with the positive LDH layers, as well as, the intermolecular interaction of NAP in the arrangement of the anion between the layers.

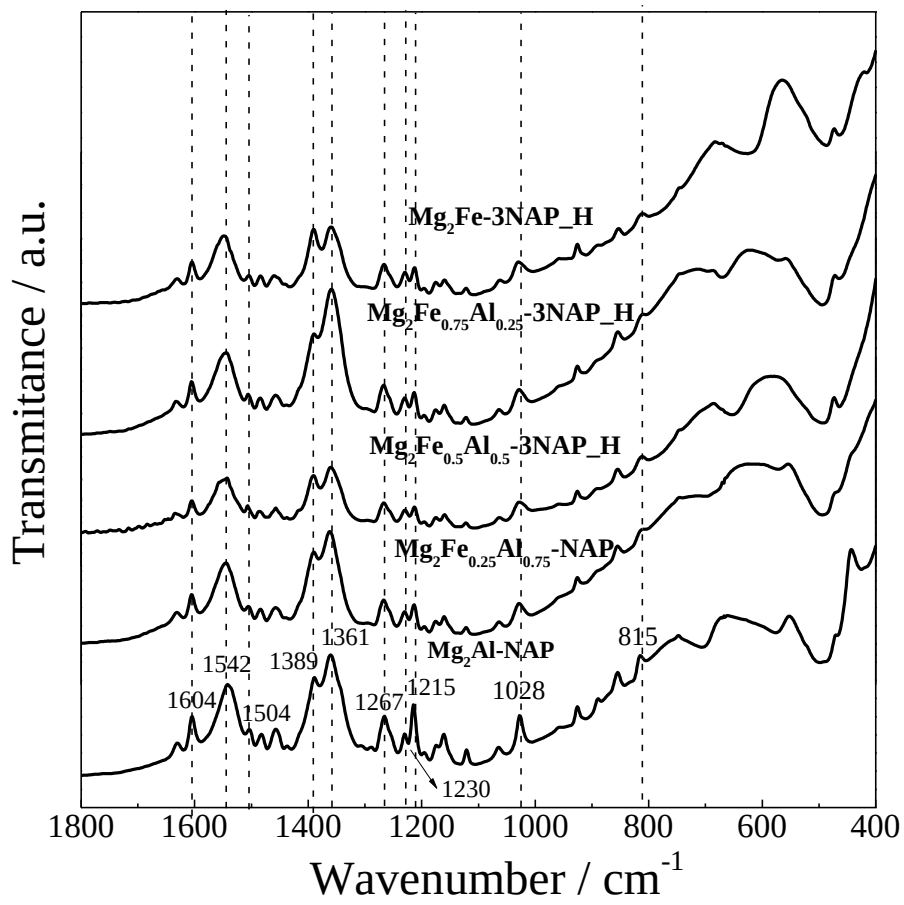

Figure 4.18. FT-IR spectra of the $Mg_2Fe_yAl_{(1-y)}$-NAP samples.

Table 4.7. Calculated and experimental vibrational IR wavenumbers.

Calc. NaNAP[a)]	**Exp. NaNAP**	**$Mg_2Fe_yAl_{(1-y)}$-nNAP_H**	**$Zn_2Fe_yAl_{(1-y)}$-1NAP**	**Tentative attribution[b)]**
1606	1606	1604	1606	ν_{as} COO^-, ν C-C
1558	1558	1542	1539	ν_{as} C-C
1504	1504	1504	1504	
1382	1389	1389	1390	w CH_3
1369	1365	1361	1361	ν C-C (naphthalene ring)
1253	1273	1267	1266	ν_s (COO^-)
1240	1250	1233	1230	β C-H (naphthalene ring)
1220	1210	1215	1215	δ C-H
1016	1029	1028	1028	ν CH_3-O
820	811	815	816	γ C-H out of phase, δ CH_3

a) Selected values in cm^{-1} obtained by the functional/basis set BLYP/6-311**G++; b) Main groups involved in the vibration; ν = stretching, ν_{as} = antisymmetric stretching, ν_s = symmetric stretching, δ = bending, w = wagging, β = bending in plane, and γ = bending out of plane.

The FT-IR spectra of $Zn_2Fe_{(1-y)}Al_x$-NAP LDHs are present in **Figure 4.19**. FT-IR spectra are very similar for all material, differing only in the intensity of the whole spectra, considerably lower for the $Zn_2Fe_{0.75}Al_{0.25}$-NAP and Zn_2Fe-NAP materials, that presented the lower NAP %. Moreover, bands positions are close to the observed for the Mg-samples (**Table 4.7**).

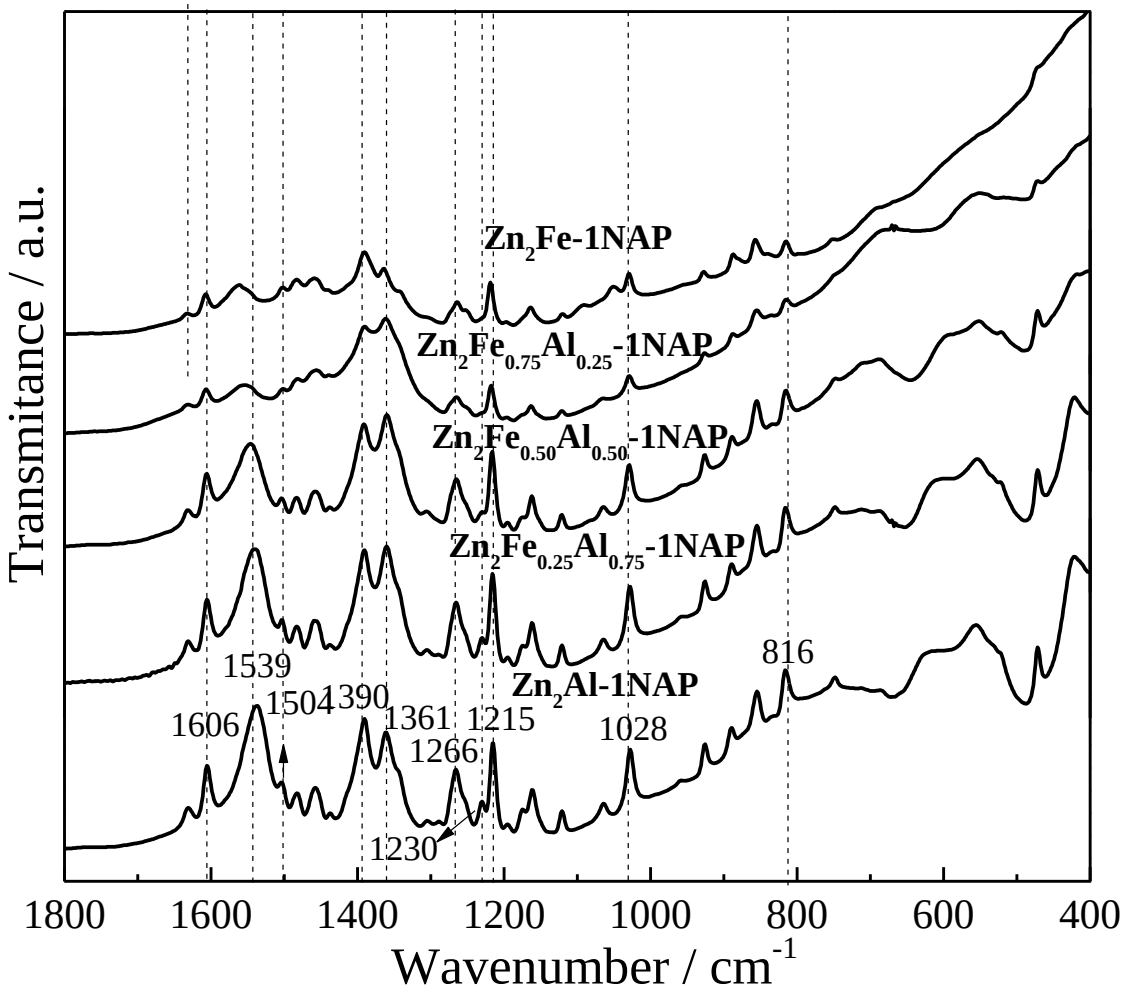

Figure 4.19. FT-IR spectra of the $Zn_2Fe_yAl_{(1-y)}$-NAP samples.

The presence of the vibrational modes related to the naphthalene ring, as well as its substituents in FT-Raman and FT-IR indicates the preservation of the NAP structure after the intercalation into Al^{3+} and Fe^{3+}-based LDHs.

4.9. Considerations about NAP incorporation into Fe^{3+}-LDHs

Literature counts with some studies concerning the intercalation of NAP into LDH. Most of these works are related to the NAP intercalation into Mg_RAl-LDHs [121,122,126,127,130,131] while only one paper could be found concerning the Zn_RAl-NAP LDH composition [123]. These works indicate coprecipitation and ion-exchange reaction as the commonly applied methods for the preparation of LDH-NAP hybrids. Also, some of them demonstrate a difficulty in obtaining pure LDH-NAP crystallographic phases, which means a mono phase consisting of LDH intercalated only with NAP (**Figure 4.20A**) or co-intercalated with NAP and the competing anions coming from the salts of the cations applied to form LDH structure or already present in the pristine LDH (**Figure 4.20B**), when the hybrid materials are prepared by the coprecipitation method or ion-exchange reaction, respectively. On the other hand, crystallographic impurities can be interpreted as phases other than LDH-NAP, which can be represented by non LDH or LDH phases intercalated only with NAP competing anions (**Figure 4.20C**), coming from the salts source of the cations for the LDH structure formation or consisting of the pristine LDH applied in the ion-exchange procedure, *i.e.* as a mixture of the structures shown in **Figures 4.20A** and/or **4.20B**, and **4.20C**.

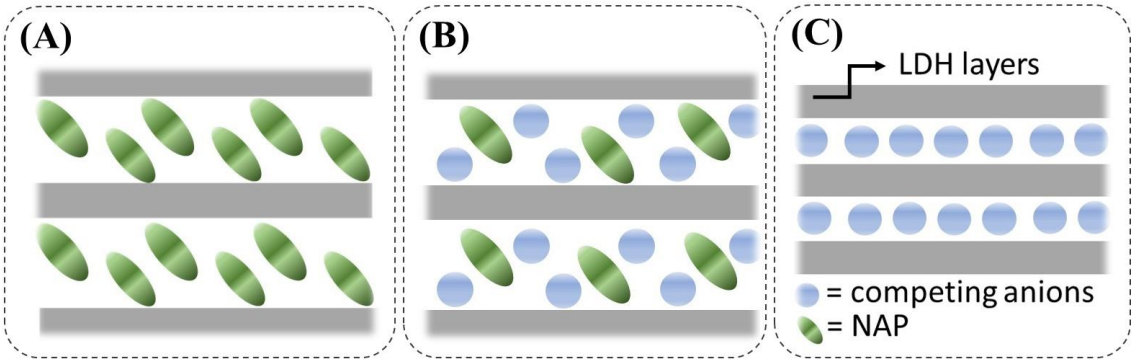

Figure 4.20. Schematic representation of LDH intercalated with NAP anions (A), both competing anions and NAP (B), and only competing anions (C).

As observed in this chapter, the formation of a mixture of LDH phases is also frequently noticed in the literature. For instance, in the work of Wei *et al.* [122] the Mg_2Al-NAP LDH was prepared by ion-exchange starting from the Mg_2Al-NO_3 material, where the nitrate anions are more susceptible to participate in anion-exchange reactions compared to other inorganic anions, such as, for instance, chloride or carbonate [53].

Then, the XRD pattern of the Mg_2Al-NAP material clearly presented the (113) peak as in this thesis. Thus, the final sample actually contained the pristine phase, indicating that not all NO_3^- could be exchanged by NAP [122]. The presence of the pristine LDH phase after the isolation of the $Mg_2Fe_{0.1}Al_{0.9}$-NAP material (nominal formula), prepared by ion-exchange reaction for 7 days and starting from the LDH-Cl, was also observed in the work of Del-Arco *et al*. [131] The peak attributed to the (009) harmonic plane for the LDH-NAP phase, whose intensity is drastically higher than the intensity of (006) plane, matches with the (003) peak related to the precursor phase. Moreover, a high intensity peak and not attributed to any phase is present and matches with the (006) harmonic peak related to the pristine LDH. The (113) plane is also observed at the same position compared to the XRD pattern of the precursor, endorsing the limitation in performing a complete ion-exchange reaction. The difficulty in isolating pure crystallographic LDH intercalated with NAP anions can be a consequence of the synthetic method performed for the drug intercalation. By ion-exchange reaction, the LDH structure is formed previously and then the anionic exchange takes place, maintaining the layer's structure minimally, which explains the presence of two types of particles: one containing Cl^- and the other containing NAP anions. However, in the work of Del Arco *et al*. [131], the LDH with the same composition prepared by coprecipitation reaction, whose layers are formed in the presence of the organic anions, showed by XRD indications of the presence of more than one type of particles. Therefore, it seems that there is a particular difficulty in stabilizing the LDH-NAP phase.

Considering the NAP dimensions (11.00 x 6.50 x 5.00 Å), as shown in **Figure 4.21**, and the interlayer space equal to the basal space minus the thickness of the hydrated LDH layers as around 4.8 Å[265], for all LDH-NAP materials it is possible to propose a bilayer disposition of NAP between the LDH's layers, as previously proposed.[115,121,127] **Figure 4.22** presents an estimation of the disposition of intercalated NAP (chloride anions were omitted) for the Mg_2Al-1NAP sample.

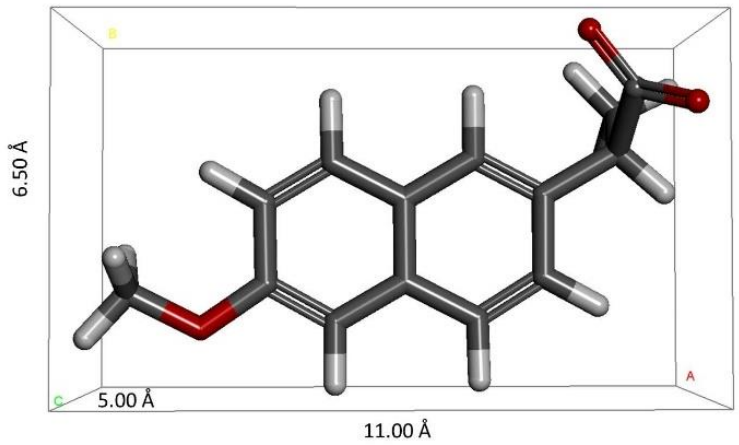

Figure 4.21. Dimensions of NAP structure obtained from Discovery Studio Visualizer software.

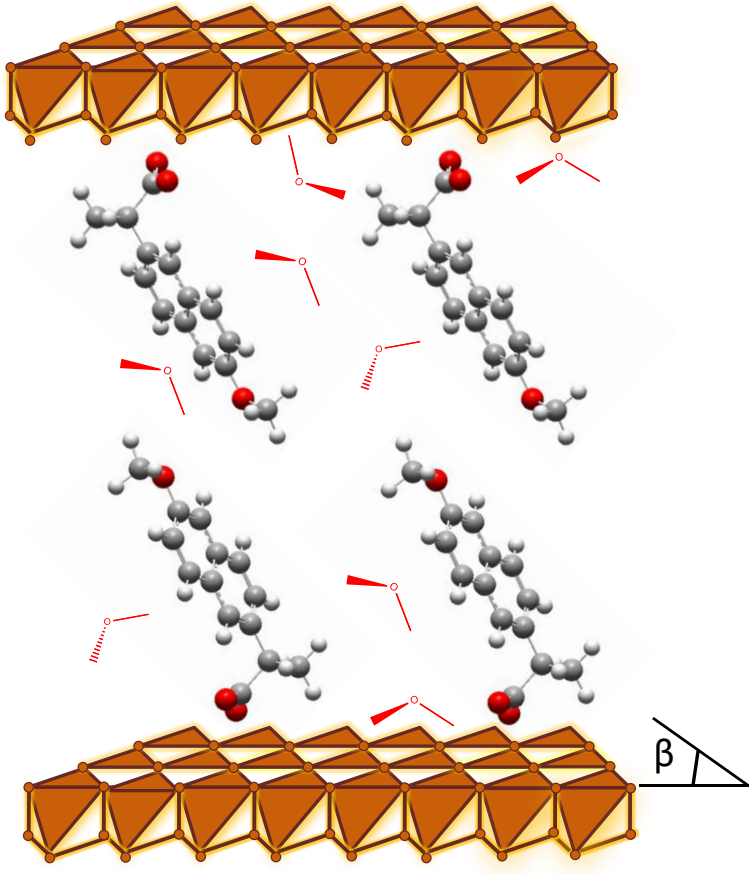

Figure 4.22. Estimation of the disposition of intercalated NAP for the Mg_2Al-1NAP sample (chloride anions were not represented).

For the Mg-series, from Mg_2Al-1NAP to Mg_2Fe-3NAP_H sample it is observed the progressive decrease in the *c* cell parameter from 68.84 to 62.13 Å, respectively (**Table 4.2**). Such tendency may be related to the decrease in the hydration percentage along the series (**Table 4.4**), from 6.0 to 3.9 wt%. However, it is important to consider the

difficulties in distinguish the different TGA events (*i.e.* dehydration, NAP thermal decompositions, dehydroxylation) conferring limitations to the estimation of the hydration percentage. Moreover, an increase in the amount of interparticle water, for instance, would contribute to the increase in the general hydration percentage, however not a variation in the interlayer space. Considering a constant layer charge density, for instance for the Mg_2Al-1NAP, $Mg_2Fe_{0.25}Al_{0.75}$-1NAP, and $Mg_2Fe_{0.5}Al_{0.5}$-1NAP samples, the substitution of Al^{3+} by Fe^{3+} cations may conduct to the increase of the *a* cell parameter, expanding the layer's length and deconcentrating the positive charge, allowing the decrease in the β angle (see **Figure 4.22**). Comparatively, Mg_2Fe-3NAP_H sample presented a smaller charge density (thus lower β angle) due to *x* lower than 0.33. Also, the decrease of intercalated NAP anions in the compositions can mean less LDH-Cl crystallites performing ion-exchange or also the increase in the amount of co-intercalated Cl^- anions, which also leads to the decrease in the basal space. For the Zn-series, no tendency is observed in the *c* cell parameters (**Table 4.2**), whose values fluctuate around 67.87 Å (average). The presence of impurities, deviations from the expected compositions together with lack of precise materials compositions do not allow further data interpretation.

4.10. Conclusions

This chapter presented a detailed study concerning the effect of Fe^{3+} cations amount (*y*) in the ion-exchange capacity of a series of $Mg_2Fe_yAl_{(1-y)}$-Cl and $Zn_2Fe_yAl_{(1-y)}$-Cl LDHs. XRD analysis indicated NAP intercalation for all samples, despite the presence of residual pristine phases. By increasing *y*, NAP excess (NAP / (Fe^{3+} + Al^{3+}) equal to 3 and heating were necessary to attest the formation of crystalline $Mg_2Fe_yAl_{(1-y)}$-NAP LDHs, for *y* equal or greater than 0.5. No NAP excess was necessary for the Zn-series, although the relative intensity of the peaks related to the pristine phases progressively increased by increasing *y*. The plot of the *a* cell parameter versus *y* and *x* shows that the exchange of Cl^- by NAP is characterized by a practically topotatic process for the Mg-LDHs. On the other hand, layer compositions considerably change after ion-exchange for the Zn-series. Mg_2Al-1NAP and Zn_2Al-1NAP samples were able to encapsulate an appreciable amount of the drug, with NAP representing 37.30 and 35.29 wt % of the samples mass,

respectively. Although NAP % decreased with the increase in *y*, iron-enriched samples were still able to considerably encapsulate NAP, for instance 26.80 and 26.27 NAP % were verified for the Mg_2Fe-3NAP_H and $Zn_2Fe_{0.5}Al_{0.5}$-1NAP samples, respectively. For the Mg-series, such tendency could be attributed to the increase in the M^{2+}/M^{3+} molar ratio, resulting in a lower charge density, but also intrinsically due to Fe^{3+}. For the Zn-series, besides variations in the layer compositions related to the nominal values, more variables can be pointed as responsible for the decrease in NAP %, such as the increase in the lengths of the coherent domains and the presence of impurities (verified for the iron enriched $Zn_2Fe_{0.25}$-$Al_{0.75}$-1NAP and Zn_2Fe-1NAP samples). The linear decrease of the dehydroxylation, NAP decomposition and dehydrochlorination temperatures with the increase in *y* reinforces the maintenance of iron into the samples. Vibrational FT-IR and Raman bands related to intercalated NAP were attributed based on the calculated NaNAP spectrum. Experimental FT-IR and Raman spectra of NaNAP were also record for validation of the computational calculations. For all samples, NAP integrity after intercalation was attested. Ion-exchange reaction can be, in fact, useful for the intercalation of organic anions into Fe^{3+}-based LDHs. The maintenance of LDH layer composition after the ion-exchange procedure offers an advantage for Mg,Fe-LDHs to be applied as drug carriers in comparison to Zn,Fe-LDHs.

4.11. Acknowledgments

We would like to thank Philippe Alexandre Divina Petersen for the DFT simulation of the IR and Raman spectra of NaNAP and Vanessa Roberta Rodrigues da Cunha for the contribution to bands tentative attribution. We are also thankfull to the *Laboratório de Espectroscopia Molecular Hans Stammreich* (*Instituto de Química – USP*) for the FT-IR and Raman spectra recording and also to Professor Christine Taviot-Gueho for conducting the XRD patterns recording in the Institute of Chemistry of Clermont-Ferrand.

Chapter 5: Synthesis and characterization of $Mg_2Fe_yAl_{(1-y)}$-ABI and $Zn_2Fe_yAl_{(1-y)}$-ABI LDHs: the role of Fe^{3+} in ABI anions intercalation by the coprecipitation method

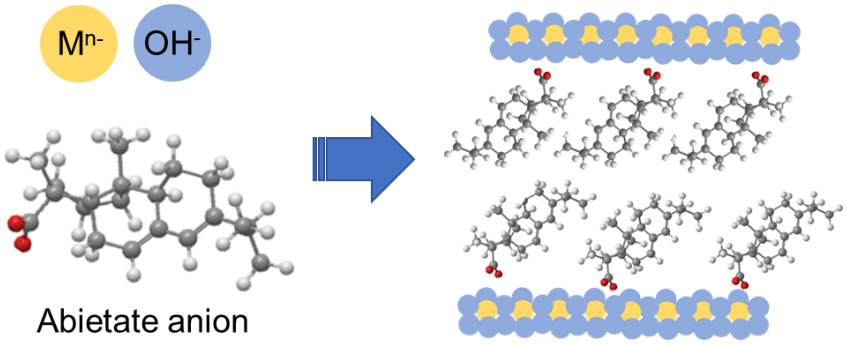

5. Abstract and data presentation

5.1. Abstract

In general, this chapter is concerned with the investigation of the capacity of Fe^{3+}-LDHs to intercalate organic anions by the coprecipitation (one-pot) method. More specifically, there is also the interest in developing Fe^{3+}-LDH host carriers for natural bioactive species. Due to their multiple biological properties, the natural diterpenoid abietic acid was evaluated to comprise organic-inorganic hybrid systems; its anion (ABI) was for the first time intercalated into the LDH structure. Two series of LDH systems with $M_2Fe_yAl_{(1-y)}$-ABI nominal compositions (M = Mg^{2+} or Zn^{2+}; y = 0, 0.25, 0.5, 0.75, or 1) were prepared by the coprecipitation method. Abietic acid and isolated sodium abietate (NaABI) were also studied for comparison. The progressive substitution of Al^{3+} for Fe^{3+} into the LDH layers produced non-pure LDH-ABI phases, containing either LDH-Cl for the Mg-series, or also amorphous phases for the Zn-series. Crystallographic pure hybrid Mg-LDH materials were observed for a substitution ratio of up to half of the Al^{3+} content ($y \leq 0.5$), associated with a satisfactory amount of intercalated ABI, representing from 48.57% to 41.14% of the mass of the Mg_2Al-ABI and $Mg_2Fe_{0.5}Al_{0.5}$-ABI samples, respectively. Scarcely reported, such Fe^{3+} cation substitution was scrutinized to better understand the integrity of the host structure when intercalated with organic species as well as to address possibilities of biological applications of these hybrid LDH phases. More specifically, pure LDH-ABI assemblies may inspire the design of high technological pharmaceutical formulations.

5.2. Materials and methods

5.2.1. Reagents

Magnesium chloride hexahydrate ($MgCl_2 \cdot 6H_2O$, purity ≥ 99 %), aluminium chloride hexahydrate ($AlCl_3 \cdot 6H_2O$, 99 %), zinc chloride (Zn_2Cl, ≥ 98 %), iron(III) chloride hexahydrate ($FeCl_3 \cdot 6H_2O$) (≥ 98%), sodium hydroxide (NaOH) (≥ 98 %), and abietic acid (HABI) ($C_{20}H_{30}O_{23}$) (≥ 75 %) were purchased from Sigma-Aldrich. Absolute ethanol was purchased from Synth. All products were used as received.

5.2.2. Synthesis of the LDHs intercalated with ABI

LDH materials were prepared directly from HABI reagent. Initially, HABI was deprotonated by dropwise addition of a 0.2 mol L^{-1} NaOH solution under stirring until complete dissolution due to deprotonation. LDH with expected layer compositions $M_2Fe_yAl_{(1-y)}$, with M = Mg or Zn and *y* values equal to 0, 0.25, 0.5, 0.75, or 1, were prepared by the coprecipitation method. Hence, a 0.05 mol L^{-1} solution with appropriate amounts of $MgCl_2{\cdot}6H_2O$ (or $ZnCl_2$) and $AlCl_3{\cdot}6H_2O$ (and/or $FeCl_3{\cdot}6H_2O$) was added concomitantly with a 0.2 mol L^{-1} NaOH solution into the abietate anions (ABI) solution, containing no excess of ABI in relation to M^{3+} amount; to keep the pH value constant and equal to 10.5 or 7.5 along the synthesis of Mg-LDH or Zn-LDH materials, respectively, the NaOH solution was added to the ABI solution. ABI solution was submitted to a mechanical stirring at 900 rpm, kept at room temperature and under a dynamic N_2 atmosphere. After the metal solution addition, the materials dispersions were aged at room temperature for 24 h under nitrogen gas. The solids were isolated by filtration under reduced pressure, washed with deionized water followed by washing with absolute ethanol, and dried at room temperature in a desiccator.

5.2.3. Sodium abietate preparation

Starting from while-yellowish HABI solid, sodium abietate salt (NaABI) was prepared by the dropwise slow addition of a stoichiometric amount of a 0.1 mol L^{-1} NaOH solution (about 1 drop / 3 s) under vigorous stirring. The NaABI solution was filtrated in a glass Büchner funnel for removal of non-dissolved solids, frozen and lyophilized for 24 h at 200 mbar and – 50 °C in a Thermo Savant ModulyoD equipment. After lyophilization, the also white-yellowish solid was transferred to a glass Büchner funnel and washed with cold water followed by cold absolute ethanol. The remaining slurry was frozen and lyophilized at the same conditions described above.

5.2.4. Characterization

X-ray diffraction patterns (XRD) of powdered LDH were recorded on a Philips X-Pert Pro equipment, using $CuK\alpha_1/K\alpha_2$ radiation (1.5406/1.5444 Å), scan range 1.5-70°(2θ) and

scan step of 0.02°(2θ)/3s. XRD pattern of powdered NaABI salt was obtained on a Rigaku MiniFlex equipment using CuKα radiation (1.5406 Å), Ni filter, scan range 1.5-70°(2θ) and scan step of 0.02°(2θ)/3s. Single or double XRD peaks deconvolution was performed using the FullProf Studio program version 2.0.

Mass coupled thermal analyses (TGA-MS) were recorded on a Netzsch thermoanalyser model TGA/DSC 490 PC Luxx coupled to an Aëolos 403 C mass spectrometer, using alumina crucible, and applying a constant heating rate of 10°C/min, under synthetic air flow of 50 mL/min, in the 35-1000°C range, and applying around 10 mg of sample.

Fourier transform infrared (FT-IR) spectra of powdered samples were recorded in the 4000–400 cm^{-1} range on a Bruker spectrophotometer, model alpha by attenuation total reflectance (ATR) mode, with acquisition step of 4 cm^{-1} and 512 scans.

Fourier transform Raman (Raman) spectra were recorded in a FT-Raman Bruker FRS-100/S spectrometer using 1064 nm exciting radiation (Nd:YAG laser Coherent Compass 1064-500 N), a Ge detector, laser power of 100 mW, acquisition step of 4 cm^{-1} and 2048 scans.

Inductively coupled plasma atomic emission spectroscopy (ICP-AES) analysis of Mg, Zn, Fe, and Al were performed on Spectro Analytical Instrument. Elemental analysis of carbon, hydrogen and nitrogen were recorded on Perkin Elmer – CHN 240. Both analyses were obtained at the *Central Analítica* of the *Instituto de Química* (*Universidade de São Paulo – USP*).

High Performance Liquid Chromatograph (HPLC) analysis of HABI was performed at the *Central Analítica* of the *Instituto de Química* (*Universidade de São Paulo – USP*) and carried on a Shimadzu equipment with a CBM-20A controller, LC-20AD pumps, SPD-20A detector, CTO-20A heater and a SIL 20 AC autoinjector. It was used a Spelco Ascentis C-18 column (250 x 4.6 mm – 5 µm), at 35°C and a solvents flux of 1.0 mL min^{-1}. Solvent A was composed of aqueous solution containing 0.05 wt% of formic acid. Solvent B was composed of methanol solution containing 0.05 wt% formic acid. It was applied a mixture of solvents A and B at specified times as follows (time – B%): 0 min – 50%, 5 min – 50%, 40 min – 100%, 45 min – 100%, 50 min – 50%.

Mass spectrometry (MS) of HABI was performed at the *Central Analítica* of the *Instituto de Química* (*Universidade de São Paulo – USP*) in an Amazon Speed ETD Bruker equipment, with nebulizer at 27 psi, a dry gas flux of 12 L min^{-1}, 325°C and 4500 V of voltage.

^{13}C nuclear magnetic resonance (NMR) spectra was recorded in a 300 Bruker spectrometer operating at 75.47 MHz for ^{13}C spin resonance and using magic angle spinning (MAS) condition at 10 kHz with a 4 mm diameter size zirconia rotor. ^{13}C spectra were obtained by proton enhanced cross-polarization method (CP, contact time of 1 ms, recycling time of 5 s) and referenced to the carbonyl of glycine calibrated at 176.03 ppm. To get a proper signal to noise ratio, over 1,000 CPMAS scans were accumulated for both NaABI and Mg_2Al-ABI (ABI). Component analysis of ^{13}C spectra of NaABI was performed using OriginPro® 9 software, applying Voigt function on baseline discounted curves. It was considered the minimum number of component bands as possible in the fitting process and results with R-Squared values greater than 0.998.

Mechanic stirring was performed using a Fisatom homogenizer model 713D.

5.2.5. Density functional theory calculations

Computational calculations of the vibrational spectra of HABI and NaABI anion (in vacuum) were perform using density functional theory (DFT) implemented in Gaussian09. Geometry optimization, IR/Raman shifts were computed using BLYP/6-311**G++. The wavelength values were adjusted by applying the correction factor equal to 0.973.

5.3. Results and discussion

As described in the experimental section, the synthesis of LDHs intercalated with ABI were performed by direct deprotonation of HABI reagent applied with no further purification. **Appendix D** contains the characterization of HABI reagent (**Figures D.1 – D.17**), whose results combined with the LDH characterization presented and discussed below indicate that HABI reagent impurities are not intercalated into LDH and are removed by materials washing and isolation processes.

XRD patterns of $Mg_2Fe_yAl_{(1-y)}$-ABI and NaABI salt, and $Zn_2Fe_yAl_{(1-y)}$ and NaABI salt are shown in **Figure 5.1** and **5.2, respectively**. NaABI salt diffractogram presents a well-defined peak at 4.23 ° (2θ) and two broader peaks at 15.23 and 29.10 ° (2θ). The NaABI diffraction pattern suggests a layered structure in which the isopropyl associated with diterpene backbone is defined as an alkyl chain while the carboxylic group is hydrophilic. Such dual presence in a same molecule leads to a hydrophilic and hydrophobic balance, thus forming double layer arrangement according to the medium. Such bilayer is structurally well organized as observed by the sharp peak at low 2θ value, while larger peaks are occurring from the intra alkyl chain organization and repetition. Peaks related to the salt are not visualized in the XRD pattern of the LDH, thus indicating that ABI intercalation prevails to the superficial adsorption. For both $Mg_2Fe_yAl_{(1-y)}$ and $Zn_2Fe_yAl_{(1-y)}$ series it is clear the decrease in the structural organization of the materials with the increase in iron amount. The Zn_2Fe-ABI sample consisted of a material with a high degree of amorphization and probably a mixture with amorphous side phase(s).

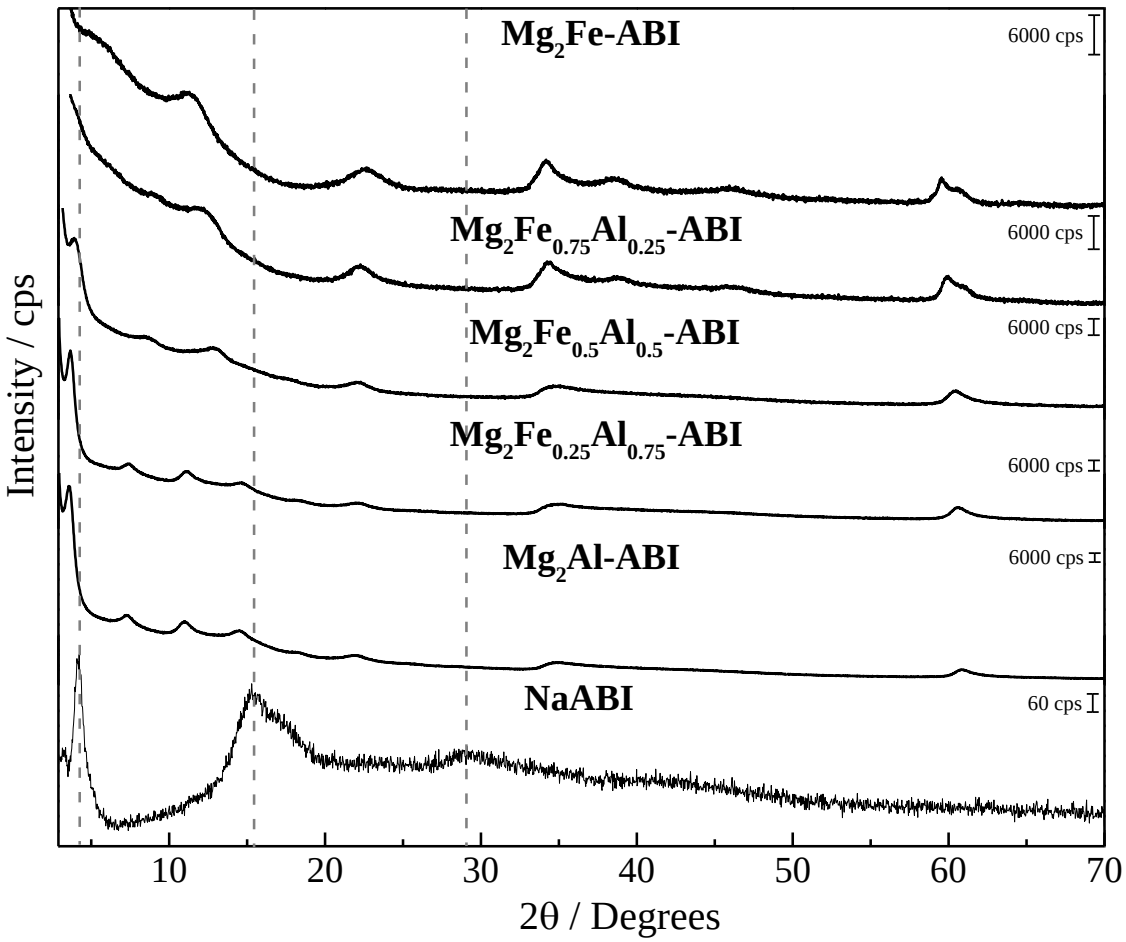

Figure 5.1. XRD patterns of $Mg_2Fe_yAl_{(1-y)}$-ABI and the NaABI samples.

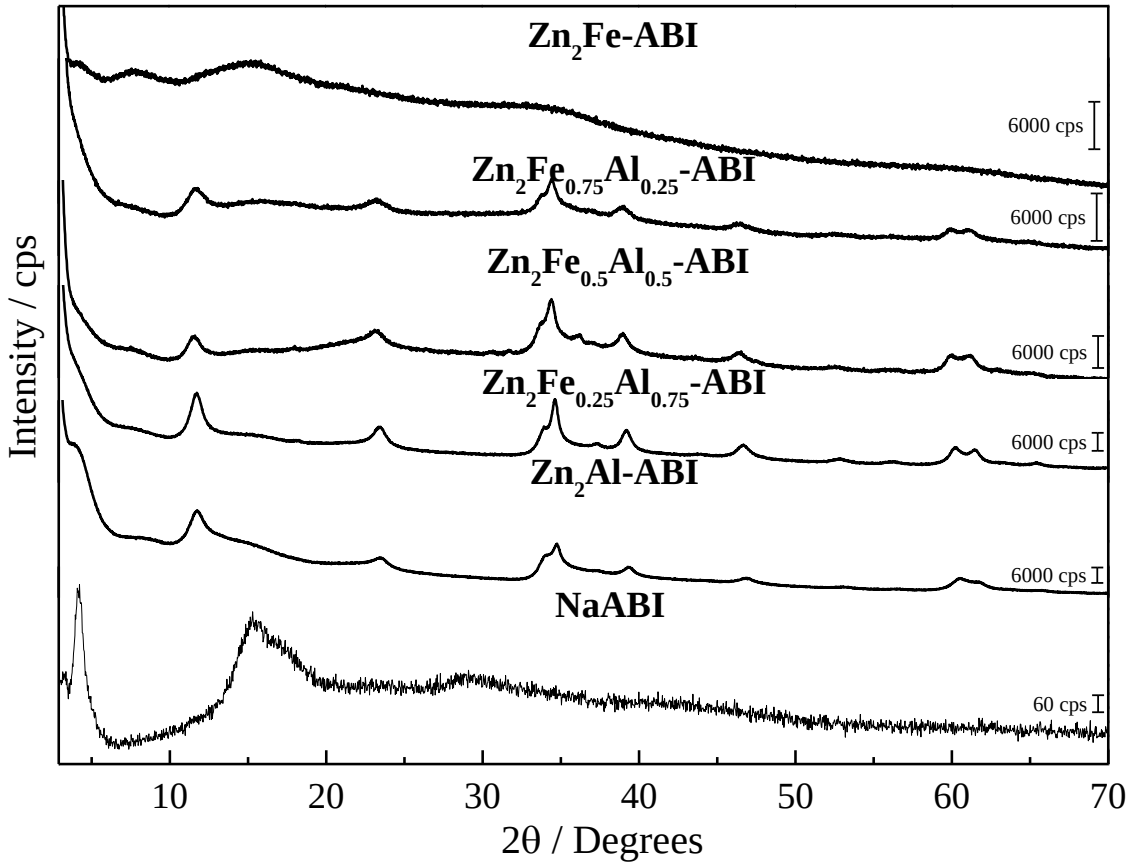

Figure 5.2. XRD patterns of $Zn_2Fe_yAl_{(1-y)}$-ABI and the NaABI samples.

For the aluminium enriched samples, the high intense peak below 5 ° (2θ) makes difficult the analysis of the other less intense peaks. Therefore, **Figures 5.3** and **5.4** presents the XRD patterns fragmented by regions, privileging the visualization of each peaks set. Miller index *hkl* were attributed to each peak considering the common arrangement of LDH as the 3R1 polytype. The peaks' position (2θ), the correspondent interplanar distances (d_{hkl}-values), and the related Miller indexes for the $Mg_2Fe_yAl_{(1-y)}$-ABI and $Zn_2Fe_yAl_{(1-y)}$-ABI series are compiled in **Tables 5.1** and **5.2**, respectively.

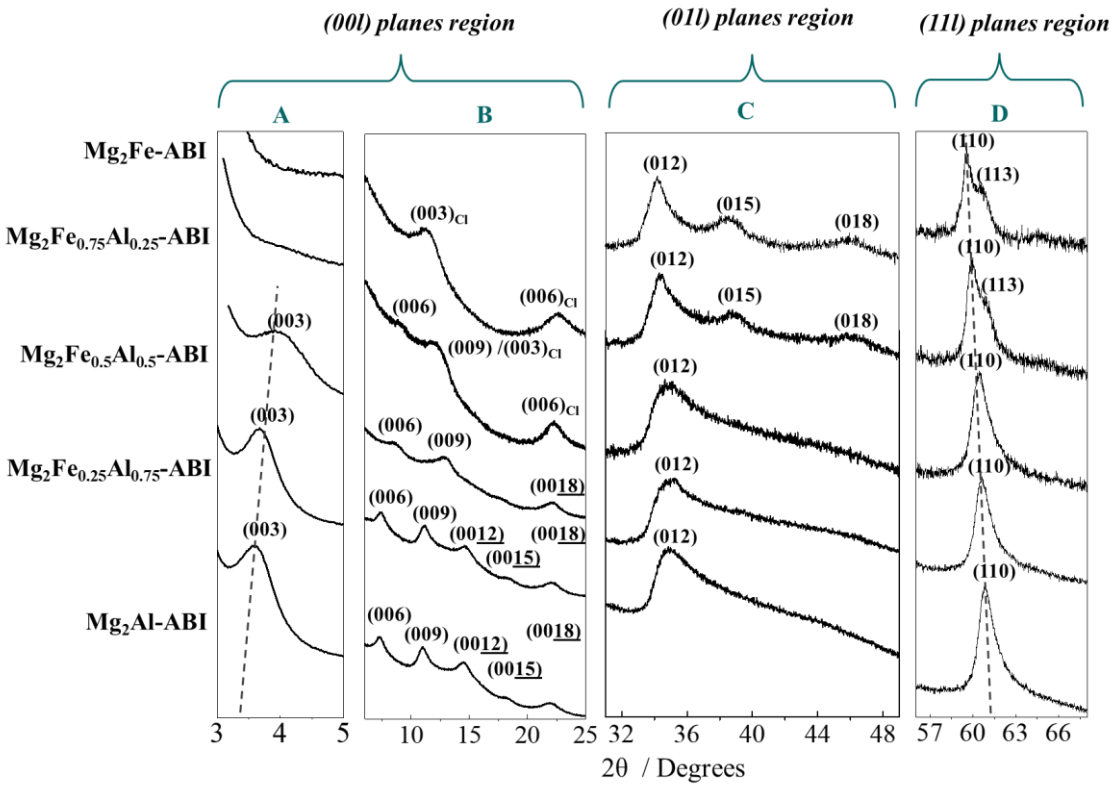

Figure 5.3. XRD patterns of the $Mg_2Fe_yAl_{(1-y)}$-ABI samples fragmented by regions. A and B: (00l) planes region, C: (01l) planes region, and D: (11l) planes regions.

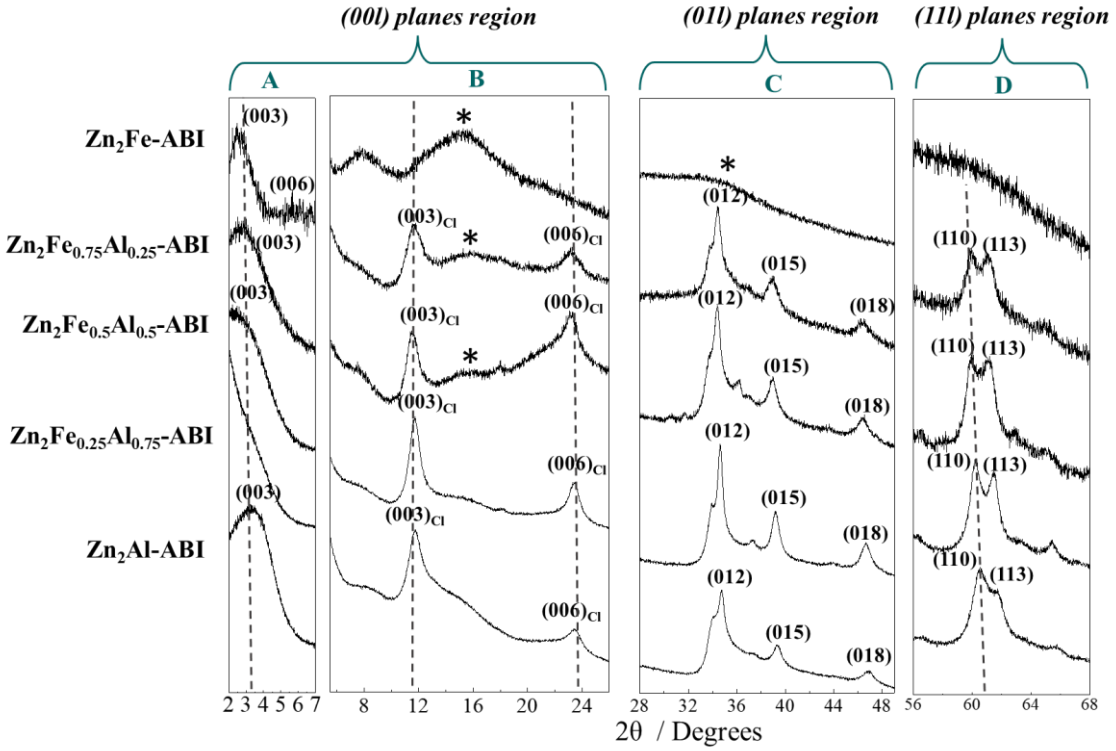

Figure 5.4. XRD patterns of the $Zn_2Fe_yAl_{(1-y)}$-ABI samples fragmented by regions. A and B: (00l) planes region, C: (01l) planes region, and D: (11l) planes regions. (*) indicates amorphous component's contribution.

Table 5.1. Interplanar distances (d_{hkl}-values), 2θ peak positions and correspondent Miller indexes considering $Mg_2Fe_yAl_{(1-y)}$-ABI LDH phases presenting the polytype 3R1

***y* = 0**		***y* = 0.25**		***y* = 0.50**		***y* = 0.75**		***y* = 1.0**		**Miller Index**
2θ	***d* (Å)**	**2θ**	***d* (Å)**	**2θ**	***d* (Å)**	**2θ**	***d* (Å)**	**2θ**	***d* (Å)**	***(hkl)***
3.55	24.83	3.67	24.04	3.92	22.50	----	----	----	----	(003)
----	----	----	----	----	----	11.69	7.56	11.33	7.80	$(003)_{Cl}$
7.25	12.18	7.46	11.83	8.52	10.37	9.05	9.76	----	----	(006)
----	----	----	----	----	----	22.27	9.99	22.47	3.95	$(006)_{Cl}$
10.96	8.06	11.21	7.88	12.81	6.90	----	----	----	----	(009)
14.52	6.09	14.57	6.07	----	----	----	----	----	----	(00<u>12</u>)
18.57	4.910	18.19	4.87	----	----	----	----	----	----	(00<u>15</u>)
21.85	4.06	22.10	4.02	22.29	3.98	----	----	----	----	(00<u>18</u>)
----	----	----	----	----	----	----	----	----	----	(101)
35.85	2.57	34.94	2.57	34.93	2.57	34.25	2.61	34.19	2.62	(012)
----	----	----	----	----	----	38.73	2.32	38.53	2.33	(015)
---	----	----	----	----	----	45.82	1.98	45.93	1.97	(018)
60.82	1.52	60.64	1.53	60.47	1.53	59.99	1.54	59.55	1.55	(110)
----	----	----	----	----	----	60.92	1.52	60.57	1.53	(113)

Table 5.2. Interplanar distances (d_{hkl}-values), 2θ peak positions and correspondent Miller indexes considering $Zn_2Fe_yAl_{(1-y)}$-ABI LDH phases presenting the polytype 3R1.

***y* = 0**		***y* = 0.25**		***y* = 0.50**		***y* = 0.75**		***y* = 1.0**		**Miller Index**
2θ	***d* (Å)**	**2θ**	***d* (Å)**	**2θ**	***d* (Å)**	**2θ**	***d* (Å)**	***2θ***	***d (Å)***	***(hkl)***
3.35	26.38	----	----	----	----	2.80	31.49	2.72	32.43	(003)
----	----	----	----	----	----	----	----	5.66	15.60	(006)
11.74	7.53	11.73	7.54	11.59	7.62	11.78	7.51	----	----	$(003)_{Cl}$
23.46	3.79	23.36	3.80	23.09	3.85	23.27	3.82	----	----	$(006)_{Cl}$
34.75	2.58	34.62	2.51	34.40	2.60	34.37	2.61	----	----	(012)
39.43	2.28	39.20	2.30	38.67	2.31	39.93	2.31	----	----	(015)
46.92	1.93	46.67	1.94	46.54	1.95	46.47	1.95	----	----	(018)
60.54	1.44	60.24	1.53	60.01	1.54	59.97	1.54	----	----	(110)
61.71	1.50	61.46	1.51	61.19	1.51	60.02	1.52	----	----	(113)

In **Figure 5.3A**, it is observed (003) peaks with corresponding d_{hkl} values equal to 25.37, 25.01, and 23.78 Å for the Mg_2Al-ABI, $Mg_2Fe_{0.25}Al_{0.75}$-ABI, and $Mg_2Fe_{0.5}Al_{0.5}$-ABI samples, respectively, indicating the intercalation of the bulk ABI anion. **Figure 5.3B** shows five harmonics of the (003) peaks for the Mg_2Al-ABI and $Mg_2Fe_{0.25}Al_{0.75}$-ABI samples, indicating an elevated structural organization when Al^{3+} cations are present in higher amounts than iron(III) in the LDH composition. Though the (003) peak could not be visualized due to the lower structural organization of iron-enriched $Mg_2Fe_{0.75}Al_{0.25}$-ABI composition, the (006) and (009) harmonic peaks indicate ABI intercalation. For the Mg_2Fe-ABI sample, peaks at (2θ) 11.08 and 22.71 ° present corresponding interplanar distances values equal to 7.97 and 3.91 Å respectively, in agreement with the (003) and (006) peaks observed for LDH intercalated with Cl^- anions[115]. **Figure 5.3C** shows, for the $Mg_2Fe_{0.75}Al_{0.25}$-ABI and Mg_2Fe-ABI samples, peaks at very similar positions and satisfying the –h + k +l = 3n condition, thus indicating that samples present similar stacking pattern arranging in a typical rhombohedral symmetry. The incorporation of Fe^{3+} into LDH conducted to the displacement of 110 peaks, corresponding to the X-ray diffraction occurring only in atoms of the layers, to smaller angles region, due to the higher ionic radius [38] of Fe^{3+} (0.645 Å) in comparison

to Al^{3+} (0.535 Å) cations (**Figure 5.3D**). For the Mg_2Al-ABI, $Mg_2Fe_{0.25}Al_{0.75}$-ABI, and $Mg_2Fe_{0.5}Al_{0.5}$-ABI samples, the absence of the 113 peaks, dependent of *c* cell parameter and normally displaced to small angle when bulky anions are intercalated in contrast with smaller inorganic anions, indicates the formation of a single LDH phase with crystallographic purity. Increasing the iron amount in the compositions, the 113 peaks presence indicates a mixture of phases. The intercalation of Cl^- anions instead of ABI seems to prevail for the Mg_2Fe-ABI sample.

From Zn_2Al-ABI to Zn_2Fe-ABI samples, the 003 peaks are displaced towards smaller angles region, with d_{003} value ranging from 26.38 to 33.67 Å, respectively, an opposite tendency in comparison with the Mg-series. A mixture of phases is verified by the presence of the (003) and (006) peaks corresponding to the LDH phases intercalated with Cl^- anions (**Figure 5.4B**) and of the (113) peaks (**Figure 5.4D** and **5.4E**). The 110 peaks were also displaced to small angles region with the increase in iron amount, indicating the Fe^{3+} ion incorporation into LDH layers. Differently from the $Mg_2Fe_yAl_{(1-y)}$-ABI samples, despite the ABI intercalation, a mixture of phases is observed for all samples. For the Zn_2Fe-ABI sample, although not observed the narrow peaks at (2θ) 4.23 degrees corresponding to NaABI, a broad peak is observed at (2θ) 15.23 degrees. Contributions of amorphous phases are indicated by (*) symbol. **Figure 5.4C** shows very well defined 01l peaks at similar positions for all samples, with exception of the Zn_2Fe-ABI sample, less structurally organized.

Table 5.3 presents the *a* and *c* cell parameters for the LDH-ABI materials. The *a* cell parameters were calculated as 2 times the interplanar distance related to the refined position of the (110) diffraction peaks ($2xd_{(110)}$) (see **Appendix D**, **Figure D18**, for peaks refinement results), while the *c* parameters were calculated as 3 times the average basal spacing calculated by the **Equation 5.1**.

$$f(n) = \frac{\sum_{i=1}^{n} i d_{(00(3i))}}{n} = \frac{1}{n}(d_{(003)} + 2d_{(006)} + \cdots + nd_{(00(3n))}) \quad (5.1)$$

Table 5.3. *a* and *c* cell parameters obtained from powder X-ray diffraction data.

Sample	*a* (Å)	*c* (Å)
Mg_2Al-ABI	3.043	73.32
$Mg_2Fe_{0.25}Al_{0.75}$- ABI	3.052	72.06
$Mg_2Fe_{0.5}Al_{0.5}$- ABI	3.061	65.88
$Mg_2Fe_{0.75}Al_{0.25}$- ABI	3.082	58.56
Mg_2Fe- ABI	3.098	-----
Zn_2Al- ABI	3.056	79.14
$Zn_2Fe_{0.25}Al_{0.75}$-ABI	3.068	-----
$Zn_2Fe_{0.5}Al_{0.5}$- ABI	3.080	-----
$Zn_2Fe_{0.75}Al_{0.25}$-ABI	3.082	94.47
Zn_2Fe- ABI	-----	95.45

Chemical analysis results are shown in **Table 5.4**. For the Mg-series, the Mg^{2+} / (Fe^{3+} + Al^{3+}) molar ratio is higher than 2 for the Mg_2Al-ABI and $Mg_2Fe_{0.25}Al_{0.75}$-ABI samples, however for the other samples the molar ratios among cations are very close to the nominal values. ABI was encapsulated in appreciable amount even for the most iron-enriched sample, whose preferential (or co-intercalation) of Cl^- anions was verified by XRD analysis, representing 48.57 wt % (m/m) of ABI in the LDH system for the Mg_2Al-ABI sample and 41.14 w % for the $Mg_2Fe_{0.5}Al_{0.50}$-ABI material. However, a progressive decrease in the amount of ABI is verified from increasing of the iron amount, surpassing the expected decrease in organic mass percentage, since Al^{3+} cation is being substituted for Fe^{3+} which elevates the molar mass of the LDH. For the Zn-series, Fe^{3+}/Al^{3+} molar ratios are close to the nominal values. However, the Zn^{2+} / (Fe^{3+} + Al^{3+}) molar ratios are lower than 2. Considering that a M^{2+}/M^{3+} ratio lower than 2 is not plausible because three octahedra containing Al^{3+} would be adjacent and repel each other [266], the presence of amorphous impurities is indicated for all materials of the Zn-series. Curiously, Zn_2Fe-ABI material presented the higher ABI percentage (45.19 wt%) among the $Zn_2Fe_yAl_{(1-y)}$-ABI samples. The precipitation of NaABI salt on particles surface could have contributed to the higher level of organic species.

Table 5.4. Chemical composition, molar ratios, and mass/mass percentages for the $Mg_2Fe_yAl_{(1-y)}$-ABI and $Zn_2Fe_yAl_{(1-y)}$-ABI series.

Samples	M/Al	M/Fe	y = $Fe^{3+}/(Fe^{3+}+Al^{3+})$	R = M /(Fe + Al)	wt% C	wt% ABI	% H_2O
Mg_2Al-ABI	(2.00)[a] 2.23[b]				38.67	48.57	4.8
$Mg_2Fe_{0.25}Al_{0.75}$-ABI	(2.67) 2.71	(8.00) 8.25	(0.25) 0.25	(2.00) 2.36	36.78	46.20	7.4
$Mg_2Fe_{0.5}Al_{0.5}$-ABI	(4.00) 4.23	(4.00) 4.06	(0.50) 0.51	(2.00) 2.07	32.75	41.14	8.2
$Mg_2Fe_{0.75}Al_{0.25}$-ABI	(8.00) 7.98	(2.67) 2.65	(0.75) 0.75	(2.00) 1.99	26.34	33.08	6.3
Mg_2Fe-ABI		(2.00) 1.96			17.45	21.92	11.5
Zn_2Al-ABI	(2.00) 1.66				34.49	43.32	6.6
$Zn_2Fe_{0.25}Al_{0.75}$-ABI	(2.67) 2.26	(8.00) 7.83	(0.25) 0.22	(2.00) 1.75	30.35	38.12	8.9
$Zn_2Fe_{0.5}Al_{0.5}$-ABI	(4.00) 3.13	(4.00) 3.29	(0.50) 0.49	(2.00) 1.60	33.00	41.45	6.4
$Zn_2Fe_{0.75}Al_{0.25}$-ABI	(8.00) 4.30	(2.67) 1.44	(0.75) 0.75	(2.00) 1.08	27.17	34.13	9.0
Zn_2Fe-ABI		(2.00) 1.26			35.98	45.19	5.8

a) expected values according with the molar ratio of the reagents, b) experimental values, and c) water amount (m/m) obtained by TGA experiments.

Figure 5.5 shows the plot of the *a* cell parameters, calculated as $2xd_{(110)}$ from (110) refined XRD peak positions, versus the experimental amount of iron (*y*) for the Mg- and Zn-series (with exception of the Zn_2Fe-ABI sample). A satisfactory linear correlation is observed for the Mg-series. For the Zn-series, iron was incorporated in a lower extension compared to the $Mg_2Fe_yAl_{(1-y)}$-ABI materials. Non incorporated iron into LDH probably originates amorphous iron phases, in agreement with the elemental analysis of the bulk samples.

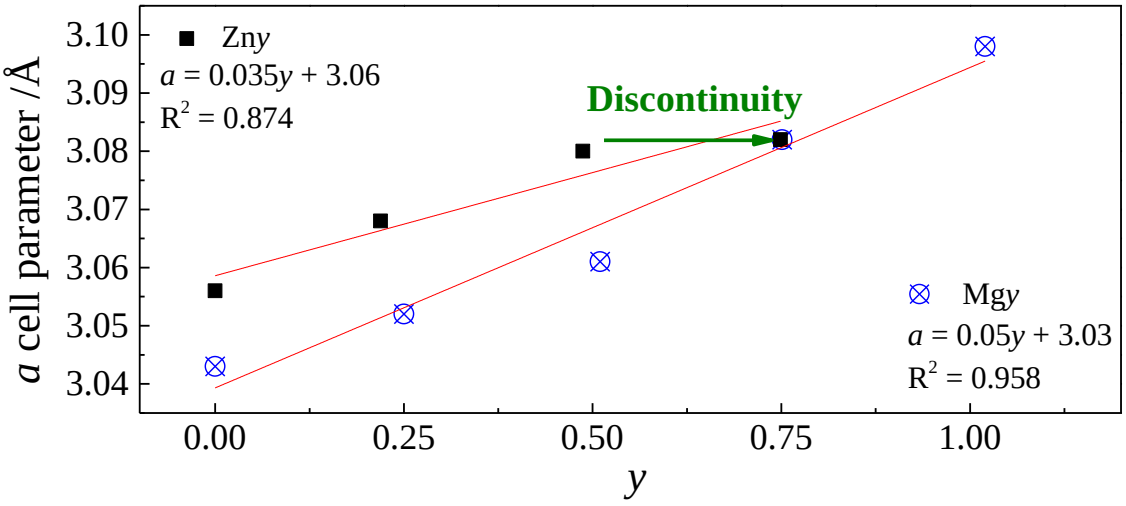

Figure 5.5. Plot of the calculated *a* cell parameter as a function of the experimental y value for the $Mg_2Fe_yAl_{(1-y)}$-ABI and $Zn_2Fe_yAl_{(1-y)}$-ABI series.

Figure D.19 (**Appendix D**) shows the refined (see refinement results in **Figure D.18**) and calculated *a* cell parameter plotted as a function of *x*. Unfortunately, it was not possible to apply the same geometrical reasoning for the LDH-ABI series as performed for the LDHs in **Chapters 3** and **4**. Experimental points for the Mg_2Al-ABI, $Mg_2Fe_{0.25}Al_{0.5}$-ABI, and $Mg_2Fe_{0.5}Al_{0.5}$-ABI samples are clearly way lower than the experimental ones. However, for the $Mg_2Fe_{0.75}Al_{0.25}$-ABI and Mg_2Fe-ABI samples, which consist of the mixture of LDH-ABI and LDH-Cl phases, theoretical and experimental points coincide. Clearly, there is a limitation in the estimation of the 110-peak position, not only by the low structural organization of the LDH-ABI LDHs but also by the influence of the 113-peak, shifted towards a small angle when ABI is intercalated in comparison to chloride anions, in the 110-peak position. For $Mg_2Fe_{0.75}Al_{0.25}$-ABI and Mg_2Fe-ABI samples, the 110 peaks observed are the majority due to the LDH-Cl phase.

Next, the thermal degradation of the NaABI and LDH-ABI samples is studied.

TGA-DTG and DSC-MS curves of $Mg_2Fe_yAl_{(1-y)}$-ABI samples are shown in **Figures 5.6** and **5.7**, respectively. The endothermic dehydration event, accompanied by the release of adsorbed and/or intercalated water molecules (see MS curves, $m/z = 18$), occurs from room temperature to 160°C and to 170°C for the Mg_2Al-ABI and $Mg_2Fe_{0.25}Al_{0.75}$-ABI LDH, respectively. For the Mg_2Al-ABI sample, the dehydroxylation and ABI decomposition combined exothermic processes, occur in two steps in the temperature ranges 160 – 470 and 470 – 600°C, and are accompanied by the release of water ($m/z = 18$) and CO_2 (m/z

= 44) molecules. For the $Mg_2Fe_{0.25}Al_{0.75}$-ABI LDH sample, these events take place in three steps in the temperature ranges 170 – 325, 325 – 420 and 420 – 600°C. For the LDH with Fe/Al molar ratio equal and higher than 1 the release of adsorbed and intercalated water molecules occurs at higher temperatures. ABI decomposition and dehydroxylation of the matrices resulted in exothermic events described by three mass loss events for the $Mg_2Fe_{0.5}Al_{0.5}$-ABI sample, in the temperature range 180 – 310, 310 – 420 and 420 – 600°C.

For the $Mg_2Fe_{0.75}Al_{0.25}$-ABI and Mg_2Fe-ABI samples, three decomposition events can also be seen. Prolonged mass loss for these two samples can be related to dehydrochlorination due to the presence of LDH-Cl phase, verified by XRD. Residues percentages are much higher for the iron-enriched $Mg_2Fe_{0.75}Al_{0.25}$-ABI and Mg_2Fe-ABI samples, indicating lower amounts of ABI, as verified by elemental analysis. Intercalated ABI thermal stability increased for the most iron-enriched samples; however, was similar compared to the NaABI salt (**Figure 5.8**), whose ABI decomposition started around 170°C.

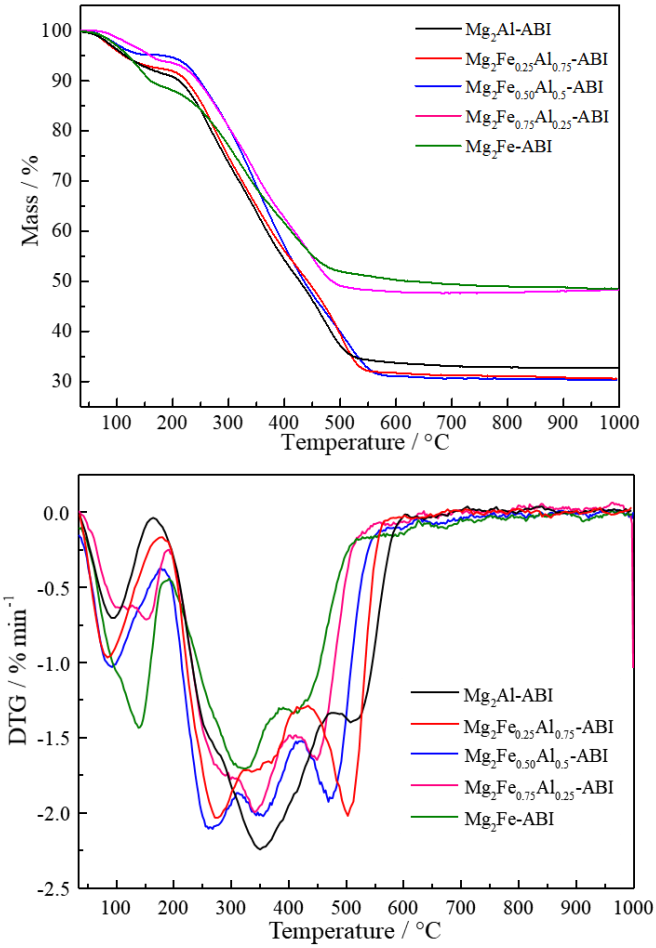

Figure 5.6. TGA (top) and DTG (bottom) curves for the $Mg_2Fe_yAl_{(1-y)}$-ABI samples.

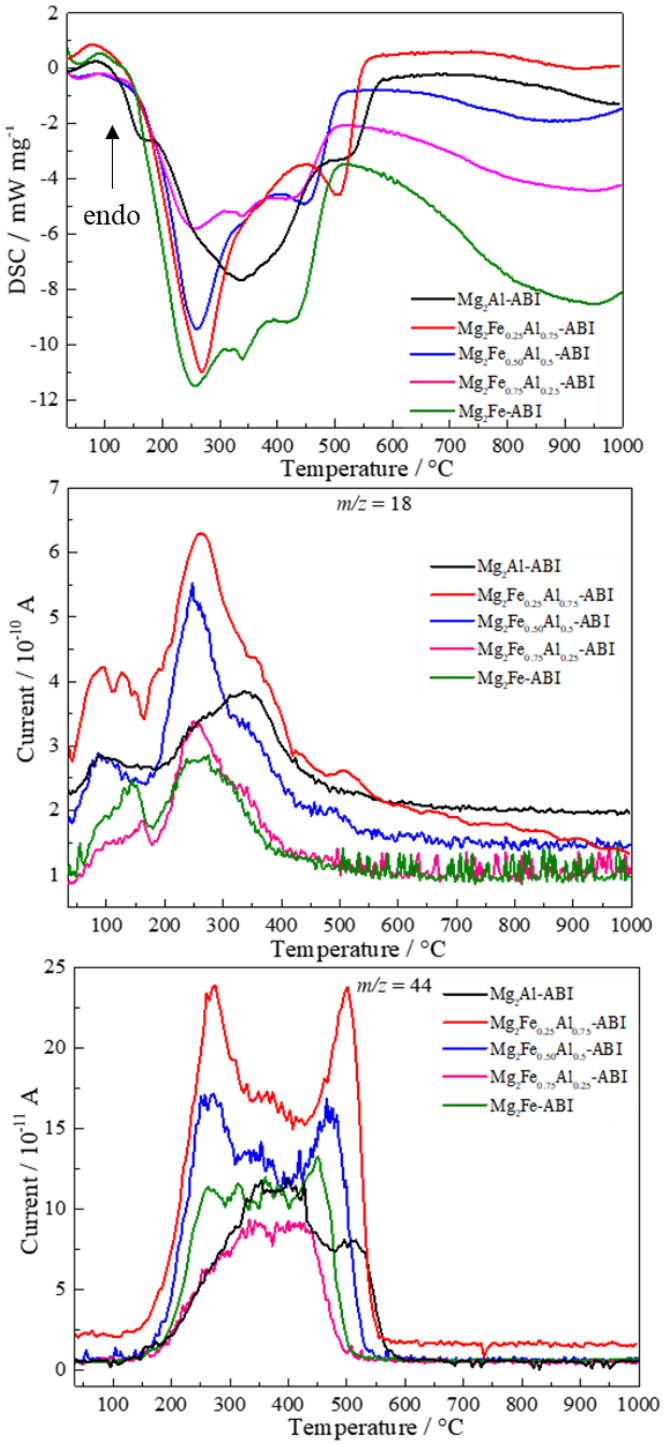

Figure 5.7. DSC (top) and MS curves (middle and bottom) for the $Mg_2Fe_yAl_{(1-y)}$-ABI samples.

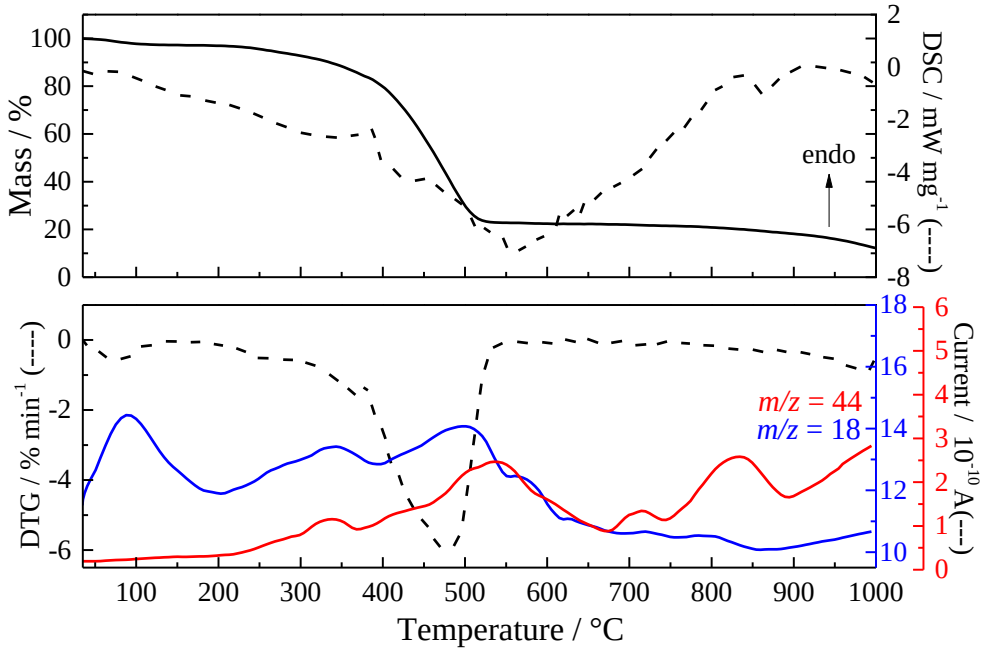

Figure 5.8. TGA-DSC (top) and DTG-MS (bottom) curves for the NaABI salt.

TGA-DTG and DSC-MS curves for the $Zn_2Fe_yAl_{(1-y)}$-ABI samples are shown in **Figures 5.9** and **5.10**, respectively. Dehydration endothermic event occurs from room temperature until 170°C for the Zn_2Fe-ABI sample and 160°C for the other materials. Differently from the Mg-LDH materials, ABI decomposition (exothermic) occurred in a shorter temperature range and just one main mass low loss event is visualized (see MS curves, m/z = 44) and was slightly shifted to smaller temperature values from Zn_2Al-ABI to Zn_2Fe-ABI samples. Matrix dehydroxylation and ABI thermal decomposition combined processes occurred until 500 – 550°C for all samples. Focusing on the thermal behaviour of the Zn_2Fe-ABI sample, TGA curve presents two abrupt loss mass at around 240 and 360°C, clearly visualized in the DSC curve and not observed for the other samples. This sample differed from the behaviour of the others in the complementary characterization technics probably due to the presence of amorphous impurities. No tendency was observed among the calcination residues percentages and amount of intercalated ABI amount once M^{2+}/M^{3+} ratios differ considerably among the samples.

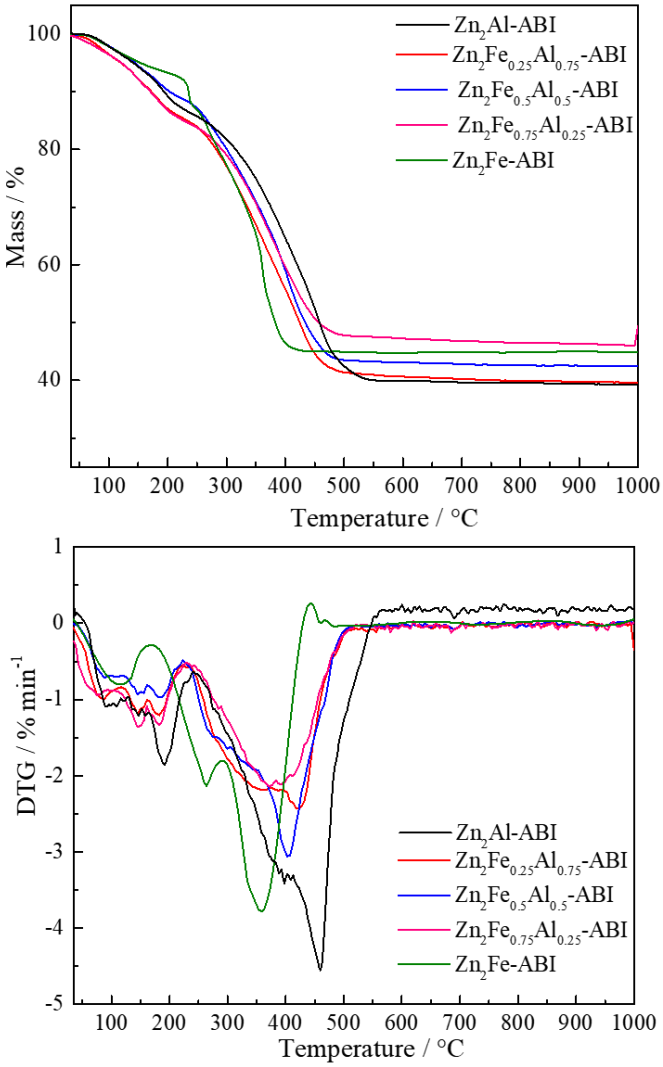

Figure 5.9. TGA (top) and DTG (bottom) curves of the $Zn_2Fe_yAl_{(1-y)}$-ABI samples.

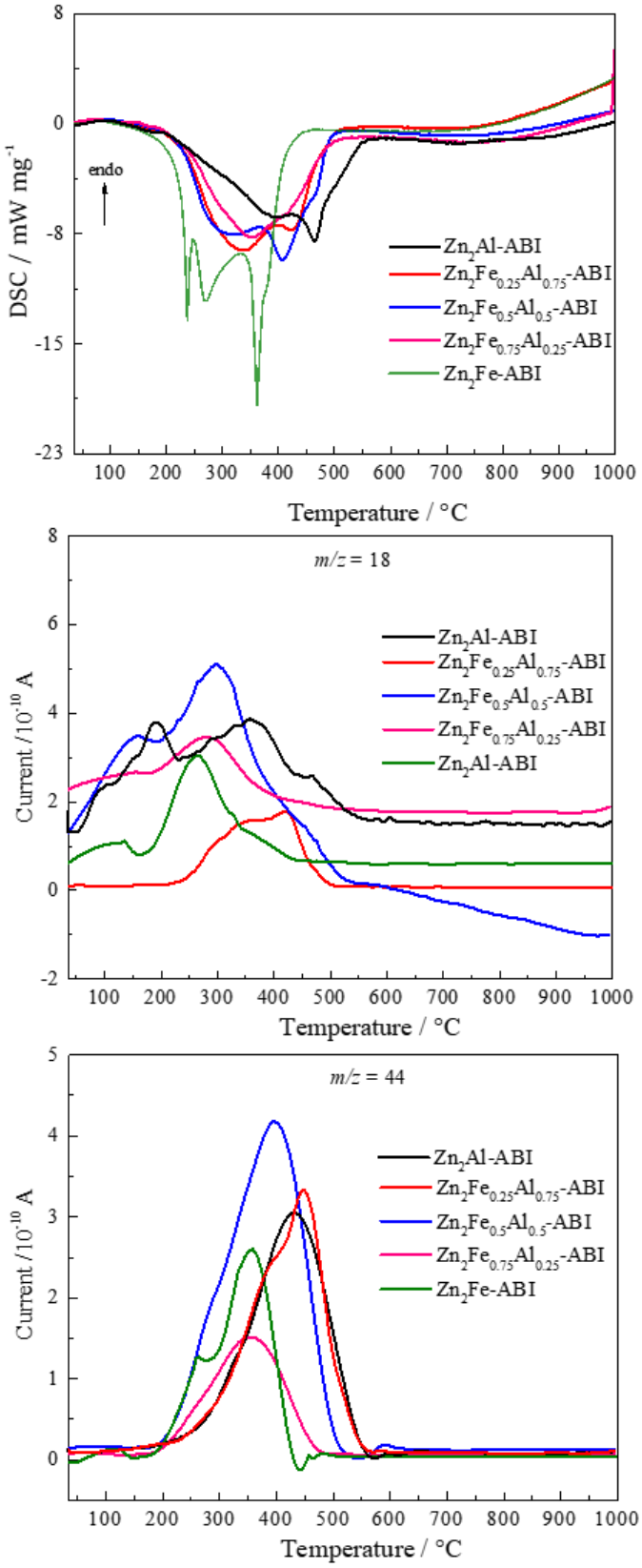

Figure 5.10. DSC (top) and MS curves (middle and bottom) of the $Zn_2Fe_yAl_{(1-y)}$-ABI samples.

As in **Chapter 4**, FT-IR and FT-Raman spectra for the NaABI and LDH-ABI samples were considered in this chapter mainly to evaluate the integrity of the organic anion after intercalation into LDH.

It is verified a great agreement between calculated and experimental Raman spectra of NaABI (**Figure 5.11**), indicating reliability in applying the calculated data to assignment the vibrations modes.

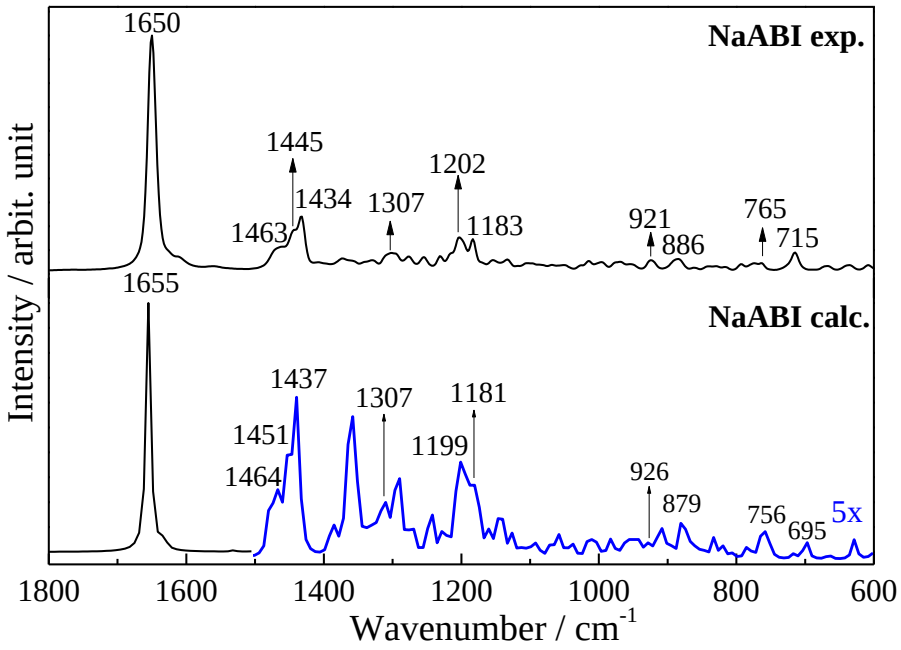

Figure 5.11. Raman spectra of calculated and experimental NaABI.

Raman spectra of the $Mg_2Fe_yAl_{(1-y)}$-ABI and $Zn_2Fe_yAl_{(1-y)}$-ABI samples are present in **Figures 5.12** and **5.13**, respectively. The main vibrational modes contributing to the most intense bands of the spectra are assigned according to the simulated NaABI spectrum, in agreement with the literature.[267] The band at 1650 cm^{-1} (experimental) is attributed to the conjugated C=C stretching. The bands from 1463 to 886 cm^{-1} are mainly related to the C-C stretching and vibrational models of the CH, CH_2, and CH_3 groups. The band at 765 cm^{-1} is assigned to the COO^- bending. M-OH translation in the LDH layers are assigned to the bands in the 500-600 cm^{-1} range [218].

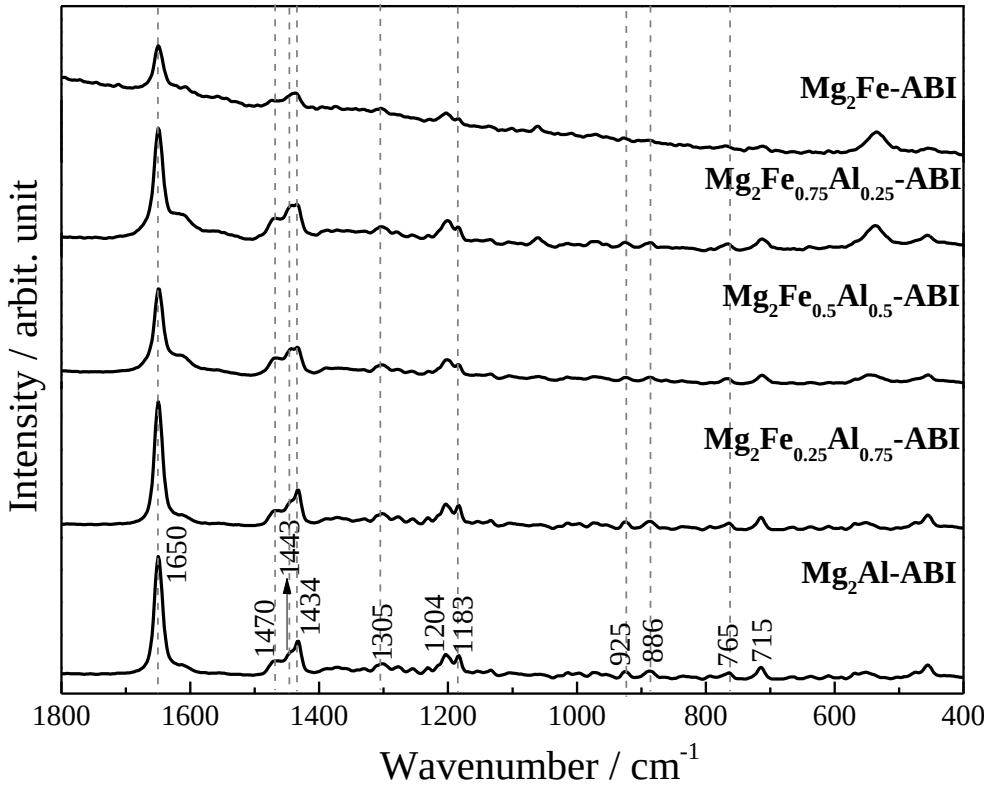

Figure 5.12. Raman spectra of the $Mg_2Fe_yAl_{(1-y)}$-ABI samples.

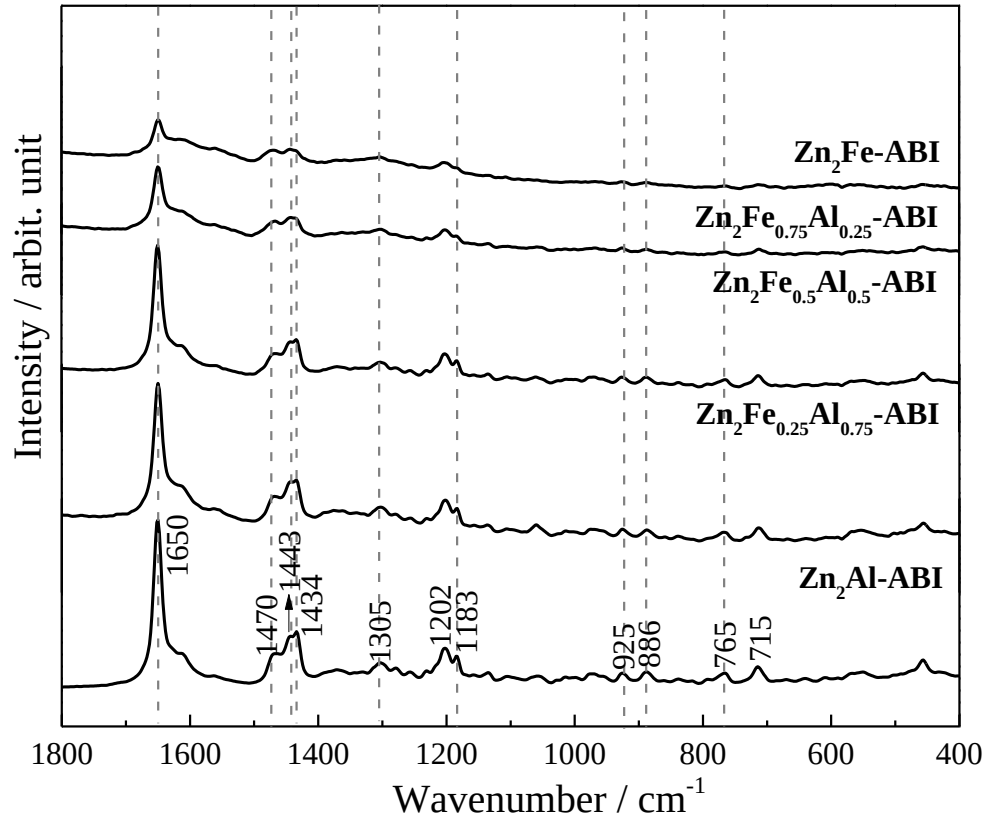

Figure 5.13. Raman spectra of the $Zn_2Fe_yAl_{(1-y)}$-ABI samples.

Table 5.5 shows the calculated and experimental Raman wavenumbers for NaABI and $M_2Fe_yAl_{(1-y)}$-ABI samples, as well as the tentative attribution considering the main groups of ABI. For the best of our knowledge, it is the first time that sodium abietate vibrational FT-IR bands are assigned.

Table 5.5. Calculated and experimental vibrational Raman wavenumbers (in cm^{-1}).

Calc. NaABI[a)]	**Exp. NaABI**	**$Mg_2Fe_yAl_{(1-y)}$-ABI**	**$Zn_2Fe_yAl_{(1-y)}$-1NAP**	**Tentative attribution**[b)]
1655	1650	1650	1650	ν C=C
1464	1463	1470	1470	δ CH_3, δ CH_2
1451	1445	1443	1443	
1437	1434	1434	1434	
1307	1307	1305	1305	δ CH_2, CH_3, CH, ν C-C
1199	1202	1204	1202	δ CH_2, CH_3, CH, ν C-C, tw CH_2
1181	1183	1183	1183	
926	926	925	925	
879	886	886	886	δ CH_2, CH_3 and CH
756	765	765	765	δ COO^-, δ CH_2 and CH_3
695	715	715	715	δ C-C, δ CH_2 and CH_3

a) Selected values in cm^{-1} obtained by the functional/basis set BLYP/6-311**G++; b) Main groups involved in the vibration; ν = stretching, δ = bending, and tw = twisting.

Calculated and experimental IR spectra of NaABI are present in **Figure 5.14.** Experimental bands are broader compared to the calculated ones. Bands positions and general spectrum share are quite similar among these samples.

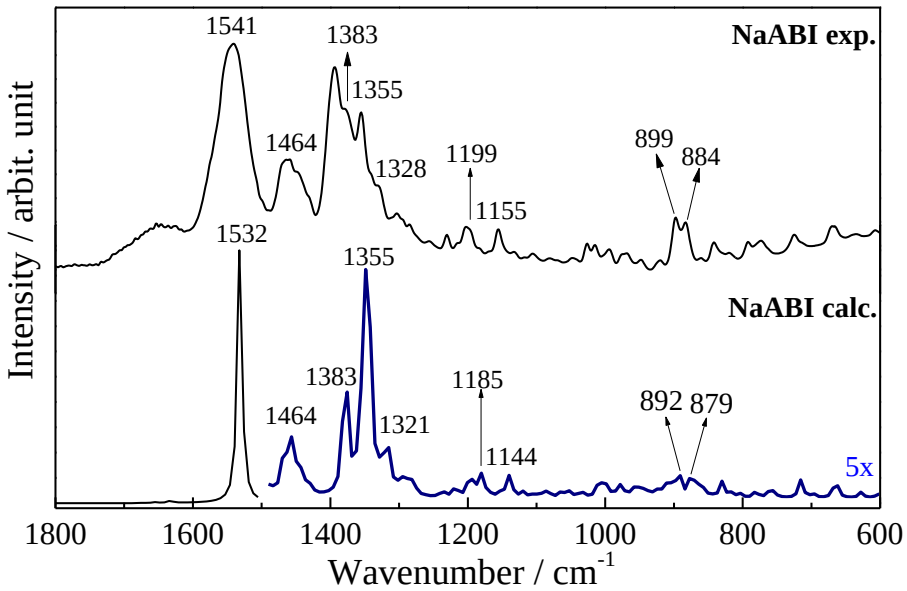

Figure 5.14. FT-IR spectra of calculated and experimental NaABI.

FT-IR spectra of the Mg- and Zn-series are shown in **Figures 5.15** and **5.16**, respectively, and are very similar to the NaABI spectrum. No considerable bands shifts are observed among the samples. The main vibrational modes contributing to the most intense bands of the spectra are assigned according to the simulated NaABI spectrum and the literature.[268] Besides C-H bending modes (CH, CH_2 groups) in the diterpenoid ring and CH_3 substituted group, asymmetric and symmetric stretching of the COO^- group are related to the bands at 1541 and 1328 cm^{-1} (experimental NaABI), respectively. **Table 5.6** shows the calculated and experimental IR wavenumbers for NaABI and $M_2Fe_yAl_{(1-y)}$-ABI samples, as well as the tentative attribution considering the main groups of ABI.

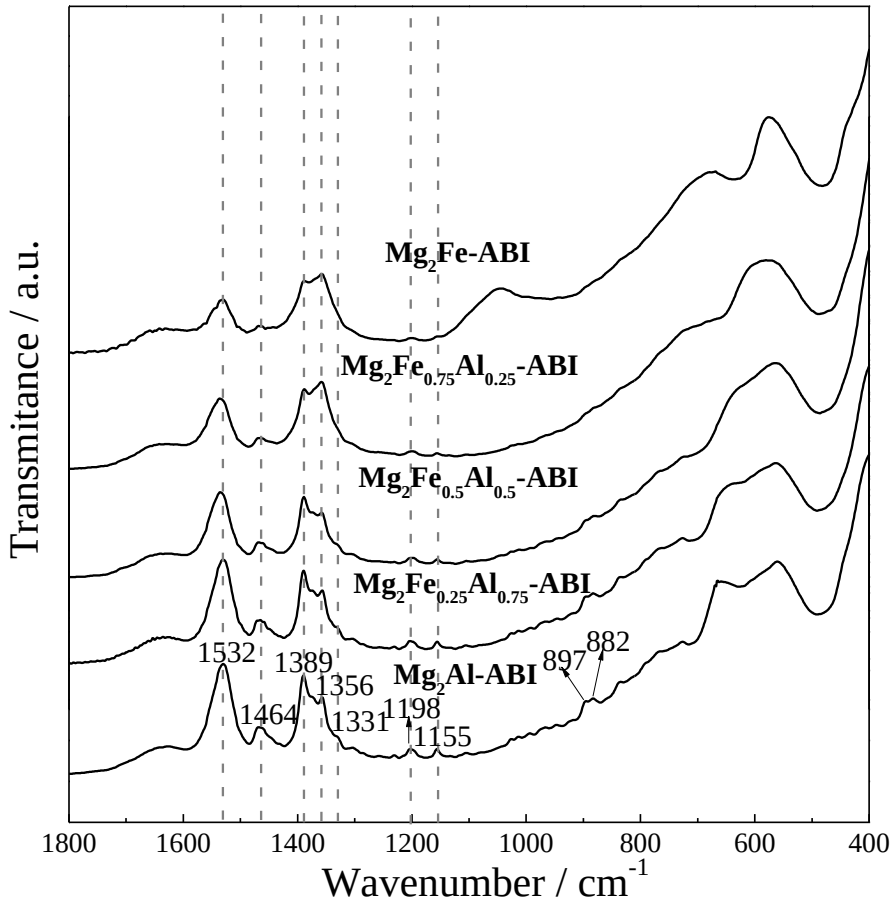

Figure 5.15. FT-IR spectra of the $Mg_2Fe_yAl_{(1-y)}$-ABI samples.

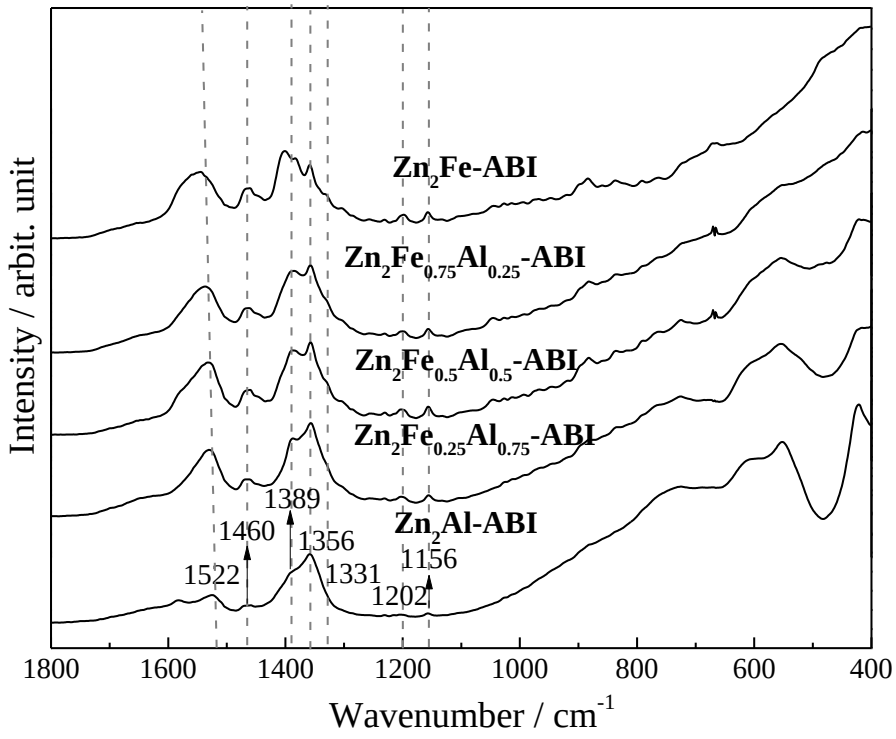

Figure 5.16. FT-IR spectra of the $Zn_2Fe_yAl_{(1-y)}$-ABI samples.

Table 5.6. Vibrational FT-IR calculated and experimental wavenumbers.

Calc. NaABI[a)]	**Exp. NaABI**	**$Mg_2Fe_yAl_{(1-y)}$-ABI**	**$Zn_2Fe_yAl_{(1-y)}$-ABI**	**Tentative attribution[b)]**
1532	1541	1532	1522	ν_{as} COO^-
1464	1464	1464	1460	δ CH_2, δ CH_3
1383	1383	1389	1389	ν C-C, δ CH_2, δ CH and CH_3
1355	1355	1356	1356	
1321	1328	1331	1331	ν_s COO^-, tw CH_2, ν C-C, δ CH_3
1185	1199	1198	1202	tw CH_2, ν C-C, δ CH, CH_2 and CH_3
1144	1155	1155	1156	
892	899	897	-----	ν C-C, δ CH, CH_2, CH_3,
879	884	882	-----	δ CH, CH_2 and CH_3

a) Selected values in cm^{-1} obtained by the functional/basis set BLYP/6-311**G++; **b)** Main groups involved in the vibration; ν = stretching, ν_{as} = antisymmetric stretching, ν_s = symmetric stretching, and δ = bending, and tw = twisting.

To validate the integrity of the molecular backbone after intercalation, ^{13}C-NMR spectrum of Mg_2Al-ABI sample was compared to the spectrum of the NaABI salt (**Figure 5.17**). The resonance peaks were assigned according to Landucci *et al.*[269] and Nong *et al.* [268], and some peaks were decomposed for better indexation. It is observed that both Mg_2Al-ABI and NaABI spectra are quite superimposed.

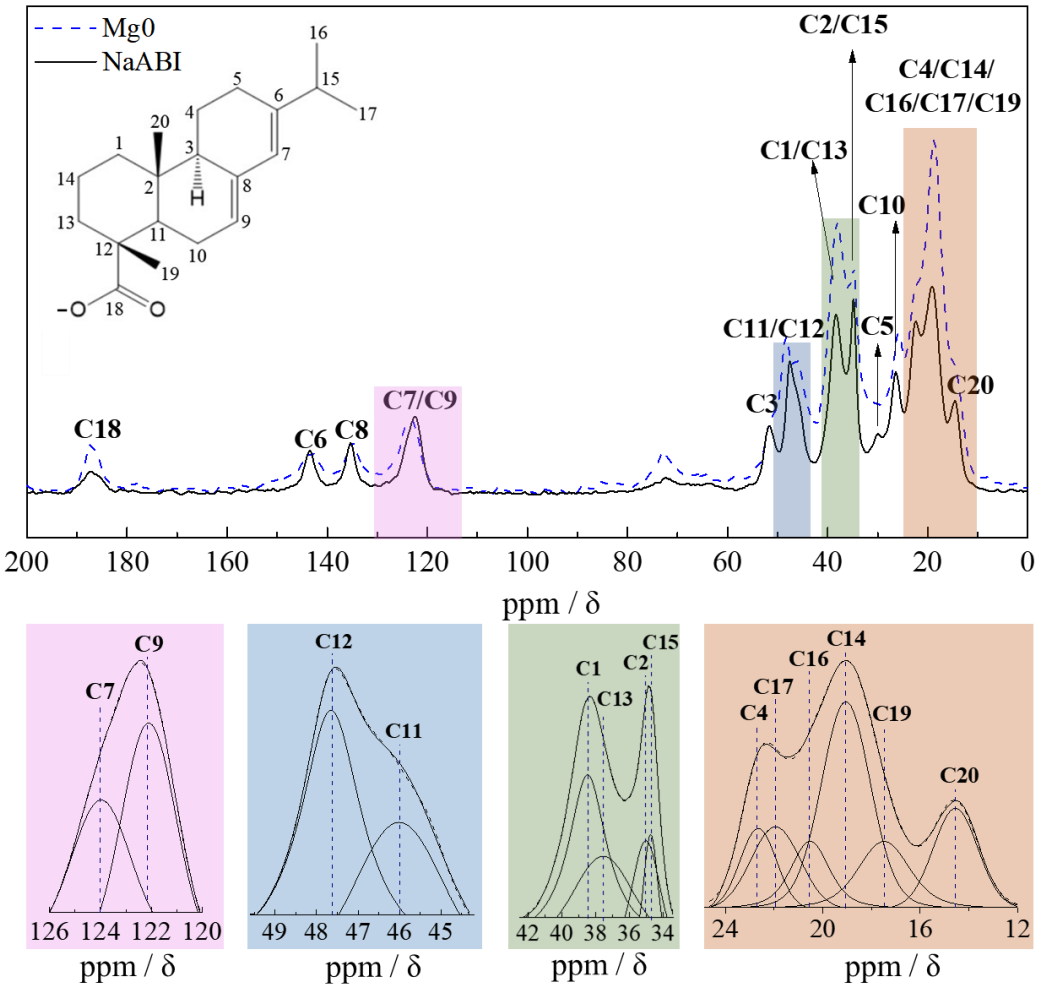

Figure 5.17. Solid state ^{13}C-NMR spectra of Mg_2Al-ABI sample and NaABI salt.

Chemical shifts related to the unsaturations, terpene ring, and carboxylate group together with spectroscopic vibrational data, Raman and IR, that present bands related to the deprotonated carboxylate group, the terpene ring and ring substituents, indicate that the molecule is deprotonated into the LDH structure while keeping its integrity after intercalation.

5.4. Considerations about Fe^{3+} incorporation ABI intercalation into LDH

Materials composed by Mg^{2+} as divalent cations and containing a high degree of Al^{3+} substitution for Fe^{3+} were able to form pure crystallographic phases (Mg_2Al-ABI, $Mg_2Fe_{0.25}Al_{0.75}$-ABI, and $Mg_2Fe_{0.5}Al_{0.5}$-ABI samples). Even showing evidences of the formation of a mixture of phases, that is LDH-Cl and LDH-ABI, the $Mg_2Fe_{0.75}Al_{0.25}$-ABI and Mg_2Fe-ABI samples were able to encapsulate a high ABI amount. Iron incorporation into LDH was indicated considering the XRD data. No phases other than LDH were verified by the applied characterization techniques. On the other hand, for all $Zn_2Fe_yAl_{(1-y)}$-ABI samples a mixture of crystalline LDH-Cl and LDH-ABI phases were formed. Besides, amorphous impurities were considered to be present, from by XRD data, and since the Zn^{2+}/M^{3+} molar ratios were considerably lower than 2. For the Zn_2Fe-ABI sample, even presenting a low crystallinity, the XRD profile, the general thermal behaviour, and the vibrational analyses pointed to the formation of the LDH phase. ^{13}C-NMR and vibrational FT-Raman and FT-IR analyses indicated the integrity of ABI after intercalation.

From ABI dimensions (6.86 x 8.42 x 11.01 Å), obtained with ChemDraw Ultra 12.0, from minimized structure energy, and considering the interlayer distance as equal to the basal space minus the layer thickness (4.8 Å)[265], a bilayer disposition between the layers can be proposed, as exemplified in **Figure 5.18** for the Mg_2Al-ABI sample. As for the $Mg_2Fe_yAl_{(1-y)}$-nNAP_H LDHs (**Chapter 4**: discussions in the **item 4.9**), it was also observed the decrease in the *c* cell parameter according to the increase in *y* for the $Mg_2Fe_yAl_{(1-y)}$-ABI samples (**Table 5.3**) which could not be related to dehydration degree of the materials and can be a consequence of the incorporation on Fe^{3+} into LDH structure, as previously discussed.

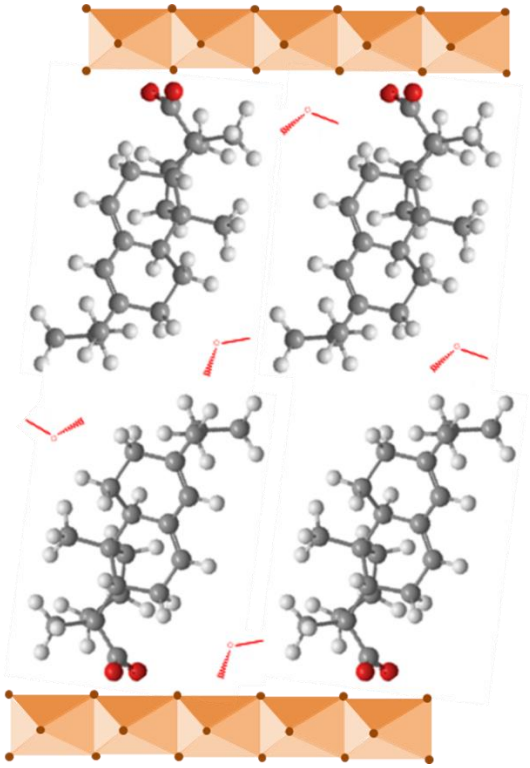

Figure 5.18. Schematic representation of the LDH structure containing ABI anions in the interlayer region distributed as a bilayer.

5.5. Conclusions

This chapter described the intercalation of an organic anion (ABI) into several Fe^{3+}-LDHs and by one-pot method. It was presented a detailed structural description of the materials. Through XRD analyses, it was possible to analyse different aspects such as LDH formation, crystallographic phase purity, and structural evolutions when increasing the amount of Fe^{3+} cations within the intra-sheet compositions. In general, all materials were able to load a satisfactory amount of ABI (representing from 22 to 49 wt % of the hybrid mass). This study may inspire future works not only in medicinal field but in different research areas.

5.6. Acknowledgments

We would like to thank Eduardo Diaz Suarez and Professor Helena Petrilli for the DFT simulation of the IR and Raman spectra of NaABI. We are also thankfull to the *Laboratório de Espectroscopia Molecular Hans Stammreich* (*Instituto de Química – USP*) and Victor Vindruscolo for the FT-IR and Raman spectra recording. Professor Christine

Taviot-Gueho is also acknowledged for conducting the XRD patterns recording in the Institute of Chemistry of Clermont-Ferrand.

Selected Compositions for Application in the Part II of the Thesis

From the results presented in **Chapters 3**, **4**, and **5,** one composition of each $M_2Fe_yAl_{(1-y)}$-A series (with M equal to Mg^{2+} or Zn^{2+} and A equal to Cl^-, NAP, or ABI, with exception of the Zn-LDH-ABI system) was selected as components of the polymeric devices approached in the second part of this thesis. The substitution of Al^{3+} by Fe^{3+} resulting in pure or crystallographic pure materials, and whose the nominal composition could be translated to the LDH phase, was limited to half of the aluminium content. Although the geometric reasoning could not be performed for the $Zn_2Fe_yAl_{(1-y)}Cl$ LDHs, the $Zn_2Fe_{0.5}Al_{0.5}$-Cl composition presented crystallographic purity and no indication of the formation of crystalline nor amorphous side phases. The $Mg_2Fe_{0.5}Al_{0.5}$-Cl sample was proven that the composition of the bulk sample represents the one of the crystalline LDH component and that this phase is the unique precipitated. The exchange process was considered practically topotatic for the $Mg_2Fe_{0.5}Al_{0.5}$ composition, thus the $Mg_2Fe_{0.5}Al_{0.5}$-3NAP_H material was selected fort application in the further studies. Small variation in the compositions of the crystalline LDH phase was observed after ion-exchange procedure compared to the pristine phase for the $Zn_2Fe_{0.5}Al_{0.5}$-NAP and no side phases could be identified; thus, this phase was also selected. Differently from the $Mg_2Fe_yAl_{(1-y)}$-ABI series, for the $Zn_2Fe_yAl_{(1-y)}$-ABI series the composition of the bulk samples differed from the nominal values and no material was selected. The $Mg_2Fe_{0.5}Al_{0.5}$-ABI composition was also selected due to the absence of LDH-Cl competitive phase.

Chapter 6: Development of 3D Multi-Layered Electrospun Membranes Embedding $Mg_2Fe_{0.5}Al_{0.5}$ LDH particles for Drug Storage and Release Modulation

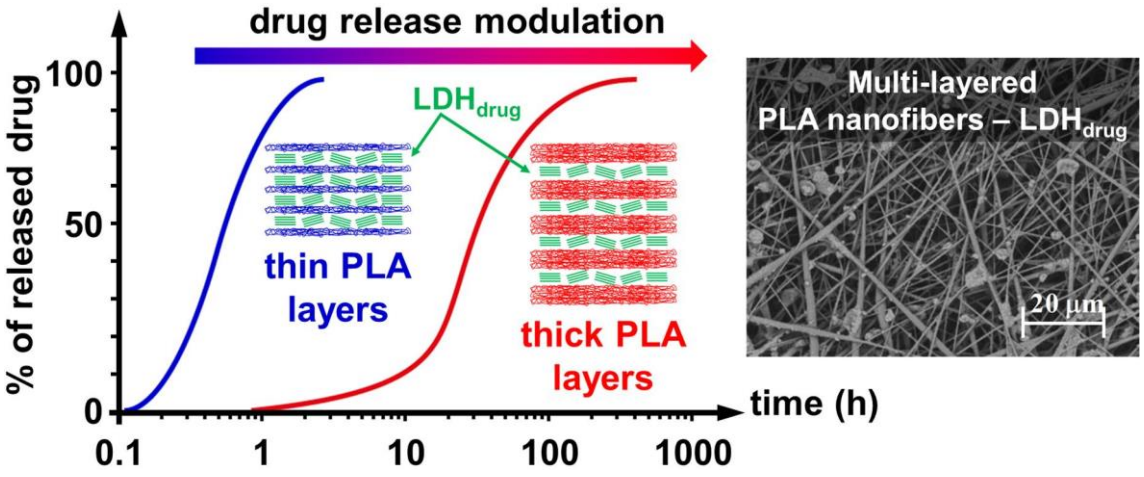

6. Abstract and data presentation

6.7. Abstract

In this chapter it is presented the design of PLA membranes containing $Mg_2Fe_{0.5}Al_{0.5}$ iron-based LDH particles intercalated with NAP anions aiming multifunctional dressings. Membranes were engineered to overcome the incompatibility between hydrophilic drugs and hydrophobic polymers observed to hinder drug release modulation and a long-term release achievement. Pristine LDH with composition $Mg_2Fe_{0.5}Al_{0.5}$-Cl was also employed to study the effect of NAP in the interaction between LDH particles and polymer. Nanofibrous membranes were prepared by the combination of electrospun PLA and electrosprayed LDH as alternated layers (approach A) and also by both technics performed at the same time (approach B). In approach A, by varying the thickness of the PLA fibrous layers, it was possible to easily modulate the drug release rate. Half of the drug content was released after 1, 4, and 17 days for the membranes containing the thinnest, the intermediate and the thicker PLA layers, respectively, and after 56 hours for the membrane prepared by the approach B. Naproxen release was kept for 18 days for the thinnest membrane, 59 days for the membrane prepared by the approach B, and 66 days for the thicker membranes. Results shown in this chapter are published as an article in the *European Polymer Journal*, 131 (15) (2020) 109675, Copyright Elsevier (please, see https://doi.org/10.1016/j.eurpolymj.2020.109675 and the original abstract in **Appendix E**).

6.8. Materials and methods

6.8.1. Reagents

Poly(D,L-lactide) (PLA) (MW 180 kDa, L = 95%, NatureWorks 7000D). N,N-dimethylformamide (DMF) (≥ 99.8%), dichloromethane (DCM) (≥ 99.8%), magnesium chloride hexahydrate ($MgCl_2{\cdot}6H_2O$) (99 %), aluminum chloride hexahydrate ($AlCl_3{\cdot}6H_2O$) (99 %), ferric chloride hexahydrate ($FeCl_3{\cdot}6H_2O$) (98 %), sodium chloride (NaCl) (99.5 %), sodium hydroxide (NaOH), and sodium naproxenate (NaNAP) ($NaC_{14}H_{13}O_3$) with purity ≥ 98 %, were purchased from Sigma-Aldrich. Absolute ethanol was purchased from Carlo Erba. All products were used as received.

6.8.2. LDH preparation

$Mg_2Fe_{0.5}Al_{0.5}$-Cl and $Mg_2Fe_{0.5}Al_{0.5}$-3NAP_H LDH phases were prepared exactly as described in sections 3.2.1 (**Chapter 3**) and 4.2.1 (**Chapter 4**), with exception that solids were then dried by freeze drying instead of in desiccator. Freeze-drying application was important to avoid particles coalescence, an important characteristic to be considered for further LDH-polymer composites preparation.

6.8.3. Preparation of suspensions and solution

6.8.3.1. Preparation of LDH suspension to be electrosprayed

The LDH suspension used to prepare the LDH-PLA membranes has been optimized for efficient electrospraying of the smallest aggregates (see **Appendix E**, **Figures E.1 – E.3** and discussions). LDH-ethanol suspensions (1 % wt) were previously submitted to ultrasonication (Branson Digital Sonifier equipment) at 40 % amplitude for 30 min (2 seconds on / 2 seconds off) just before the electrospraying procedure.

6.8.3.2. Preparation of PLA solution to be electrospun

A 10 % wt PLA solution was prepared by dissolving the beads in a mixture of DCM and DMF in a weight ratio equal to 3 : 2 overnight under slow stirring with a magnetic stirring bar.

6.8.4. Preparation of the composite membranes

Two approaches are proposed for the preparation of composite membranes (**Figure 6.1.**). The approach A consists in the fabrication of multi-layered membranes by alternating electrospinning PLA fibers and electrospraying LDHs particles. In approach B LDHs electrosprayed particles are regularly dispersed in the PLA electrospun fibrous scaffold.

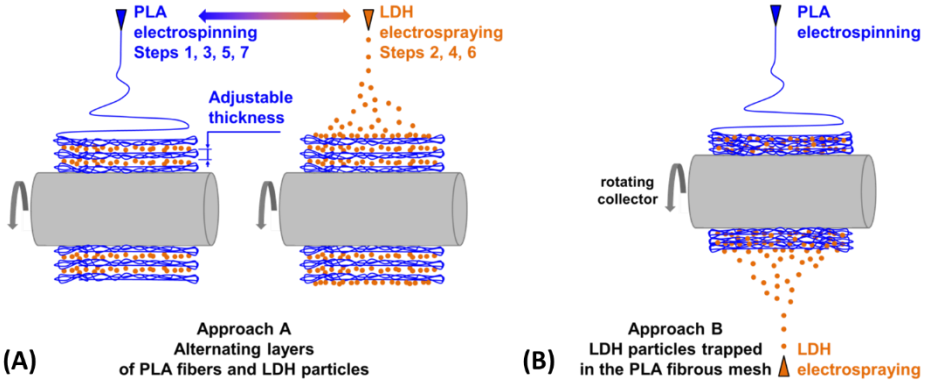

Figure 6.1. Preparation of the composite membranes in the case of a) approach A with variable and adjustable thickness of the PLA fibrous layers and b) approach B with simultaneous PLA electrospinning and LDH electrospraying.

6.8.4.1. Electrospun PLA and electrosprayed LDH: building up a delivery membrane (Approach A)

Electrospinning and electrospraying experiments were conducted with a home-made setup previously described[270] and allowing the deposition on a drum collector rotating at 125 rpm. All solutions or suspensions were electrospun or electrosprayed at a temperature T = 22 +/-1°C and a relative humidity RH = 40 +/- 5%. Working distance between needle and collector was equal to 16 cm for all samples.

In approach A, the membranes contain 7 layers made from the deposition of 4 PLA electrospun fibers taking in sandwich 3 LDHs electrosprayed particles (**Figure 6.1A**). Three different PLA layer thicknesses were prepared by changing the production time of the electrospun layers. Applied voltages, flow rates, and production times are given in **Table 6.1**. Membranes containing electrosprayed $Mg_2Fe_{0.5}Al_{0.5}$-NAP particles are called NAP-A_{thin}, NAP-A_{med}, and NAP-A_{thick} and the membranes with electrosprayed $Mg_2Fe_{0.5}Al_{0.5}$-Cl are called Cl-A_{thin}, Cl-A_{med}, and Cl-A_{thick}. To compare the samples, the total electrospraying time was the same for each membrane and equal to 78 minutes.

Table 6.1. Applied parameters for preparation of the membranes.

Approach	Method	Voltage on the needle (kV)	Voltage on the collector (kV)	Flow rates ($mL.h^{-1}$)	Production Time (min)
A_{thin}, A_{med}, A_{thick}	Electrospraying Layers 2, 4, 6	25	0	6	3 layers 26 min/layer
A_{thin}	Electrospinning Layers 1, 3, 5, 7	16	-5	2.8	4 layers 15 min/layer
A_{med}	Electrospinning Layers 1, 3, 5, 7	16	-5	2.8	4 layers 22 min/layer
A_{thick}	Electrospinning Layers 1, 3, 5, 7	16	-5	2.8	4 layers 30 min/layer
B	Electrospinning Electrospraying	16 28	0	2.8 6	78 in

6.8.4.2. Simultaneous PLA electrospinning and LDH electrospraying (Approach B)

In approach B (**Figure 6.1B**, **Table 6.1**), the membranes were prepared by simultaneous deposition of electrospun PLA and electrosprayed LDH aiming to contain the same total amount of LDH as applied in approaches A (total electrospraying time equal to 78 min). Samples were abbreviated as Cl-B and NAP-B, indicating the application of B approach and LDHs particles containing Cl^- and NAP anions, respectively.

6.8.4.3. Pristine PLA membrane

As a control, the pristine PLA membrane was electrospun for 2 hours. Therefore, it contained the same polymer amount as in the membranes prepared according to approach A_{thick}.

6.8.5. NAP release tests

Naproxen release experiments were conducted in triplicate from 3 cm x 10 cm membranes. The membranes were accommodated into closed glass flasks containing 70 mL of saline aqueous solution (0.9 % wt NaCl) and the pH value was equal to 5.55 ± 0.01. The release media was magnetically stirred at 130 rpm and the assays were performed in a climatized room at 22 °C. At specified times, 3 mL of saline solution were collected and replaced with an equivalent amount of dissolution medium. NAP concentration was determined by UV–visible absorption spectrophotometry at a maximum absorption (λ_{max}) equal to 230 nm. After the first released NAP aliquot measured, accumulative NAP weight ($m^{NAP}{}_i$) released was corrected through the **Equation 6.1**, where *Ci* is the NAP concentration (mL L^{-1}) in such a time *i*, considering the removed aliquots (3 mL) for measurement in anterior times *k* and then replaced by the same volume of saline solution to maintain the volume of the flasks equal to 70 mL.

$$m^{NAP}{}_i = 0.07C_i + 0.003 \sum_{k=1}^{k=i-1} C_k \quad (6.1)$$

6.8.6. Characterization

X-ray diffraction (XRD) patterns of powdered LDHs were obtained on a Bruker D8 Advance A25 equipment with variable slits mode, using Cu anode (λ = 1.518 Å), scan range 1.5-70°(2θ) and scan step of 0.02° (2θ) / s.

Fourier transform infrared (FT-IR) spectra of powdered LDHs samples and of the composites were recorded in the 4000–400 cm^{-1} range on a Bruker spectrophotometer, model α, by attenuation total reflection (ATR) mode with acquisition step of 4 cm^{-1} and 512 scans.

Fourier transform Raman (FT-Raman) spectra of the LDHs were recorded in na FTRaman Bruker FRS-100/S spectrometer using 1064 nm exciting radiation (Nd:YAG laser Coherent Compass 1064–500 N), a Ge detector, laser power of 100 mW, acquisition step of 4 cm^{-1}, and 2048 scans.

Chemical elemental analyses of carbon, hydrogen, and nitrogen were recorded on Perkin Elmer-CHN 2400.

Inductively coupled plasma atomic emission spectroscopy (ICP-OES) analyses of metals were performed in duplicate on Spectro Analytical Instrument.

Images by scanning electron microscopy (SEM) of the membranes were obtained in a VEGA3SEM equipment using samples deposited on a copper tape and coated with gold using a Q150RS Quorum equipment. The LDHs micrographs were obtained in a XL30 FEG Philips equipment depositing the powders in a copper tape and covering samples with carbon.

Mechanical tensile measurements were performed with a TA Instruments Discovery HR-3 hybrid rheometer at room temperature and applying a velocity of 50 μm s^{-1}. The normal force sensor of the rheometer was used to record the tensile force. Samples were analysed in quintuplicate and were prepared cutting 3 x 1.5 cm rectangles. The mechanical tests were carried out at room temperature (T = 21 ± 2°C) and humidity (RH = 50 ± 20%) without environmental control.

Thermal analyses (TGA) were recorded on TA instrument, Q5000 model, using platinum crucible and a heating rate of 10 °C min^{-1}, from room temperature to 1000 °C, under synthetic air flow of 25 mL min^{-1}.

Membranes thicknesses were determined using a Schut digital micrometre. Six measurements in different points were performed in samples with 3 cm x10 cm area.

Contact angle measurements were performed with static deionized water drop on the membranes using a DSA 25 tensiometer.

Absorbance in the ultraviolet–visible region was measured on a Shimadzu UV-2600 spectrometer.

6.9. Results and Discussions

6.9.1. $Mg_2Fe_{0.5}Al_{0.5}$-Cl and $Mg_2Fe_{0.5}Al_{0.5}$-3NAP_H LDHs characterization

The characterization of LDHs intercalated with Cl^- anions or NAP is shown in **Appendix E** (see **Figures E.4– E.9**, **Table E.1**, and discussions). XRD, TGA, elemental analysis (ICP-OES and CHN), and vibrational (FT-IR and Raman) spectroscopies

indicate no discrepancies in comparison to the characterization of the first batch of $Mg_2Fe_{0.5}Al_{0.5}$-Cl and $Mg_2Fe_{0.5}Al_{0.5}$-3NAP_H materials presented in **Chapters 3** and **4**, respectively.

6.9.2. 3D Composite membranes prepared by PLA electrospinning and LDH electrospraying

Membrane's micrographs are presented in **Figure 6.2**. Regarding the multi-layered membranes obtained from approach A, some LDHs particles are exposed on the surface of the membranes containing the thinnest PLA layers (Cl-A_{thin} and NAP-A_{thin}). Increasing the PLA thickness, fewer particles are visualized on Cl-A_{med} and NAP-A_{med} surfaces and no particles are observed for the Cl-A_{thick} and NAP-A_{thick} samples. The surface aspects of the Cl-A_{thick} and NAP-A_{thick} samples are similar to the one of the pristine PLA membrane, indicating that 30 min of PLA electrospinning is enough to completely cover the last layers containing LDHs particles. Less particles aggregation is observed for the membranes prepared from approach B by simultaneous PLA electrospinning and LDH electrospraying (Cl-B and NAP-B samples) compared to the distribution of on the surface of the thinnest membranes and the aspect of the surfaces of the last deposited LDH layers (L), abbreviated by Cl-A_{thick}L and NAP-A_{thick}L samples. Indeed, in the approach A, a large number of particles is electrospun at the same time, favouring the formation of aggregates on the mat, as was seen when electrospraying on a flat collector (see **Figure E.1, Appendix E**) whereas in approach B, only few particles are electrosprayed before new fibers land on the mat and hide them, hindering the formation of aggregates.

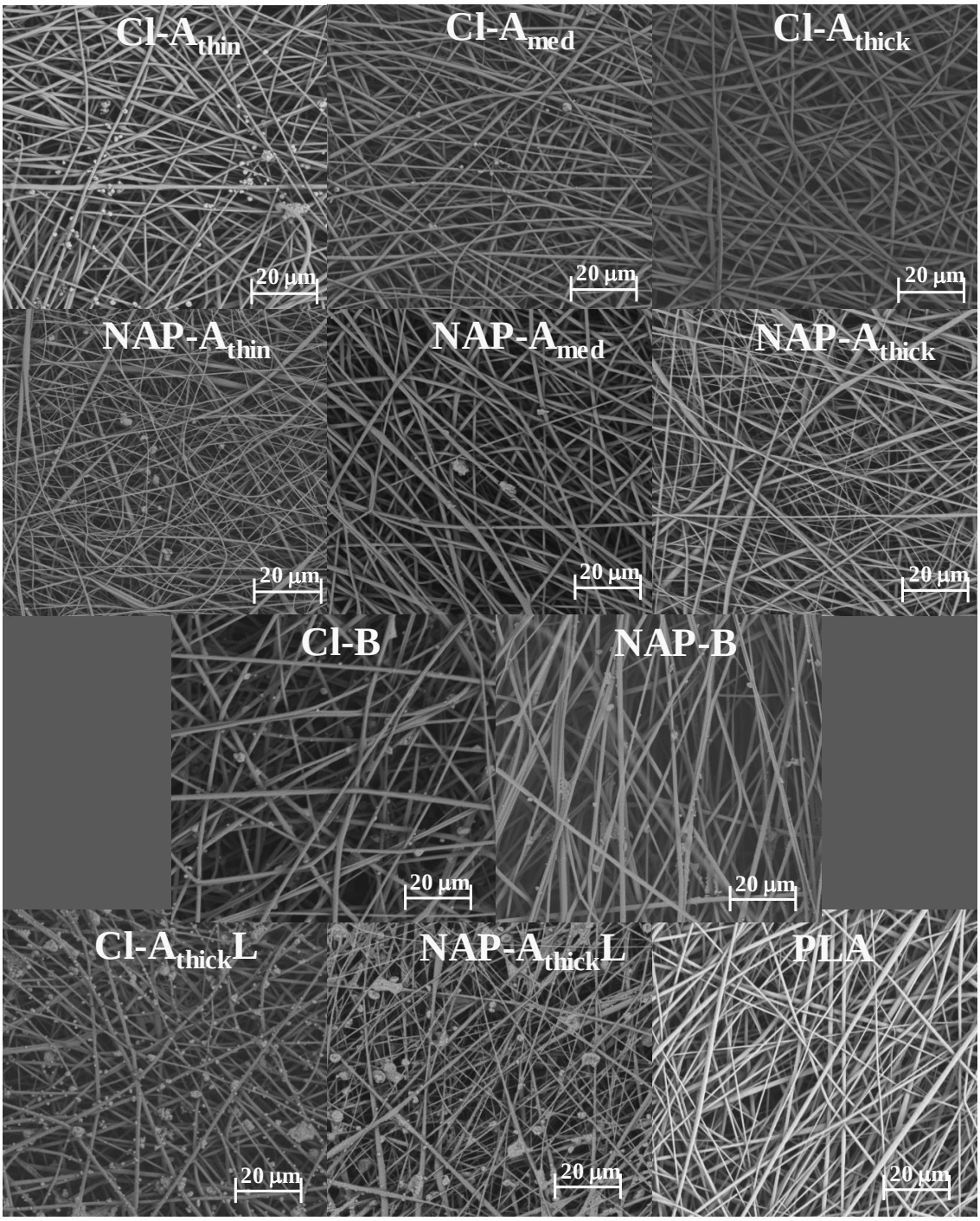

Figure 6.2. SEM micrographs of pristine PLA membrane and PLA membranes containing $Mg_2Fe_{0.5}Al_{0.5}$ LDHs intercalated with Cl^- and NAP anions, prepared by alternating 4 electrospun PLA layers with 3 electrosprayed LDH layers (Approach A) with different PLA thickness (A_{thin} – electrospinning of each layer performed for 15 min, A_{med}- 22 min and A_{thick} – 30 min) and prepared by both electrospinning and electrospraying at the same time (Approach B). Samples were analyzed applying BSE detector, 5 kV and work distance around 10 mm.

Figures 6.3 and **6.4** show the FT-IR spectra of the membranes containing LDH-Cl and LDH-NAP particles, respectively. All bands observed for the pristine PLA (**Figure 6.5**) are present in the spectra related to the composites, whose assignment was made as follows.[271] The bands at 2994 and 2945 cm^{-1} are attributed to the antisymmetric and symmetric stretching of the $-CH_3$ group, respectively. The band at 1751 cm^{-1} is assigned to the stretching of the -C=O group. Antisymmetric $-CH_3$ bending frequency is observed at 1452 cm^{-1}, while the corresponding symmetrical mode appears at 1361 cm^{-1}. The bands at 1261, 1184, 1129, 1084, and 1043 cm^{-1} are related to vibrational modes of the C-O-C group. Finally, the band at 867 cm^{-1} is related to the stretching of the O-CH-CH_3 portion and the band at 753 cm^{-1} to the wagging of the α-CH_3 group. For the membranes whose SEM images show higher levels of exposed particles, the bands at 3430 cm^{-1}, in the spectra for Cl-A_{thick}L and Cl-B, and at 3433 cm^{-1}, for the NAP-A_{thick}L and NAP-B samples, respectively, are attributed to the stretching of the -OH group presented in the LDH layers and in intercalated and adsorbed water molecules. Bands below 700 cm^{-1}, attributed to the metal-OH stretching, are also present in the spectra of the A_{thick}L and B samples. Additionally, for the NAP-A_{thick}L sample, the bands at 1547 and 926 cm^{-1} are assigned to vibration modes of NAP the anions.[115]

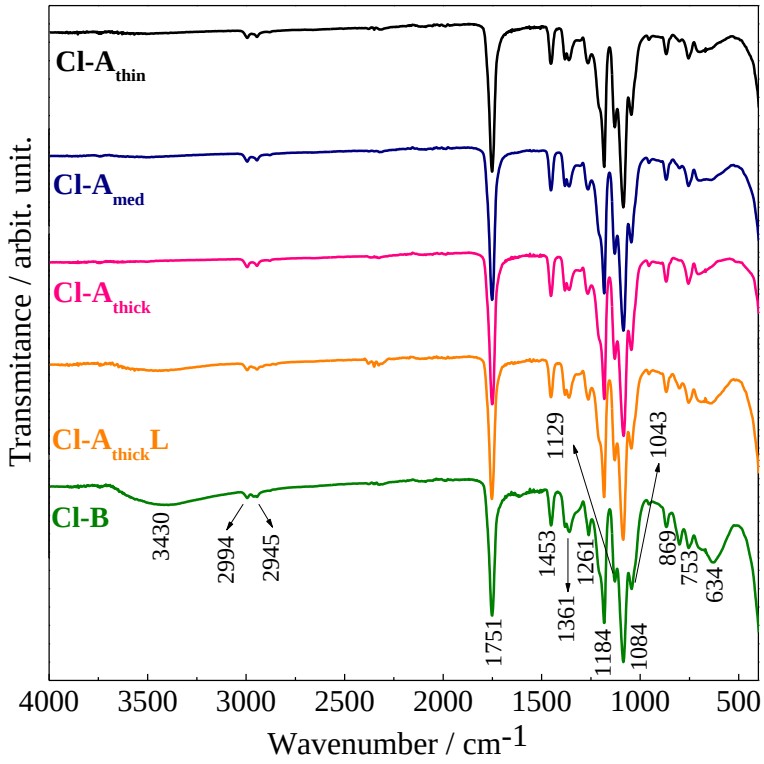

Figure 6.3. FT-IR spectra of membranes containing LDH-Cl particles.

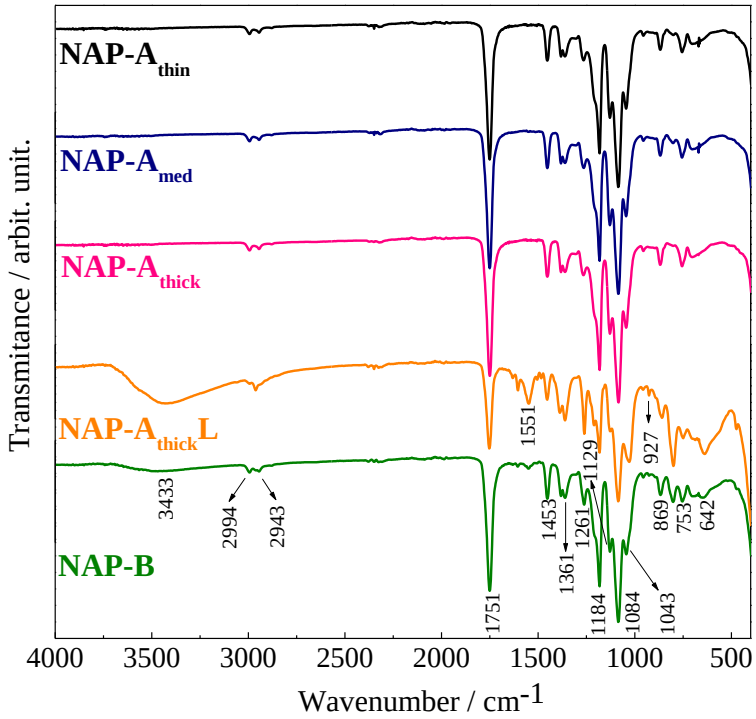

Figure 6.4. FT-IR spectra of membranes containing LDH-NAP particles.

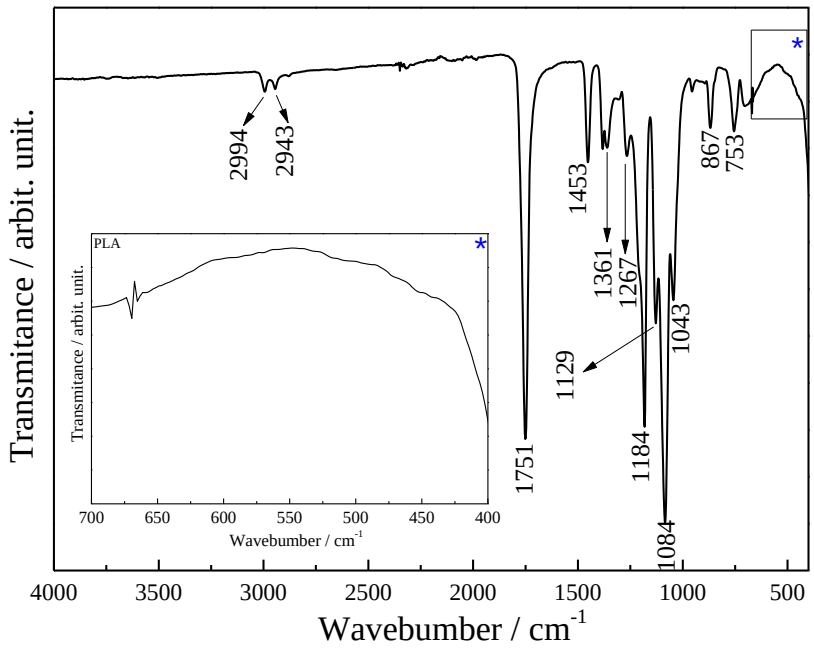

Figure 6.5. FT-IR spectra of pristine PLA. The region between 700 – 400 cm-1 is highlighted and shows the absence of bands.

Table 6.2 presents the membranes thickness. A non-significant difference was observed for the membranes prepared by the same approach, differing by the presence of LDH-Cl or LDH-NAP particles, indicating a similarity in particles disposition during

electrospraying method, independent of the nature of the LDH. In agreement with the architecture of the membranes, according with the consecutive increase in PLA layers thickness from A_{thin} to A_{thick}, it was observed the corresponding increase in thickness, from 61 ± 24 μm for Cl-A_{thin} and 53 ± 21 μm for NAP-A_{thin} to 116 ± 14 μm for Cl-A_{thick} and 120 ± 16 μm for NAP-A_{thick}, respectively. Comparing the membranes prepared by the B approach (78 min of PLA deposition) with the ones prepared by A_{med} approach, in which the PLA fibbers content is slightly higher (88 min of PLA deposition as compared to 78 min for B), a decrease in thickness is observed for Cl-B and NAP-B samples. It may indicate a better particles-PLA fibers accommodation when electrospinning and electrospraying are performed at the same time.

Table 6.2. Membranes average thickness, static water contact angle and mechanical properties obtained by tensile tests for PLA membrane and PLA_LDH composites.

Sample	Membranes Thickness (μm)	Contact Angle (°)	Yield stress (MPa)	Yield strain (%)	Stress at break (MPa)	Strain at break (%)	Young modulus (MPa)
PLA	148 ± 22	128.6 ± 5.1	1.82 ± 0.20	2.75 ± 0.21	2.92 ± 0.37	69.7 ± 1.0	98.5 ± 4.9
Cl-A_{thin}	61 ± 24	120.9 ± 4.8	1.53 ± 0.10	3.35 ± 0.30	2.06 ± 0.16	82.1 ± 3.6	74.0 ± 6.2
Cl-A_{med}	102 ± 22	121.5 ± 4.9	1.46 ± 0.19	2.85 ± 0.61	2.47 ± 0.19	81.5 ± 5.6	81.9 ± 7.1
Cl-A_{thick}	116 ± 14	123.8 ± 5.0	2.12 ± 0.13	2.98 ± 0.31	3.95 ± 0.18	99.9 ± 3.2	109.0 ± 6.2
Cl-B	86 ± 26	121.3 ± 4.9	1.46 ± 0.23	2.75 ± 0.92	2.77 ± 0.27	79.0 ± 6.4	76 ± 13
Cl-A_{thick}L	--------	121.4 ± 4.9	--------	--------	--------	--------	--------
NAP-A_{thin}	53 ± 21	125.5 ± 5.0	0.68 ± 0.44	2.60 ± 0.78	1.41 ± 0.96	42.2 ± 4.8	39 ± 29
NAP-A_{med}	92 ± 19	127.4 ± 5.1	1.83 ± 0.07	4.60 ± 0.51	2.41 ± 0.97	99.9 ± 2.4	84.9 ± 2.0
NAP-A_{thick}	120 ± 16	123.8 ± 5.0	2.04 ± 0.15	2.65 ± 0.68	3.56 ± 0.10	51.9 ± 1.8	96.3 ± 5.4
NAP-B	99 ± 33	124.5 ± 5.0	1.73 ± 0.08	3.05 ± 0.10	2.46 ± 0.07	80.7 ± 2.7	84.2 ± 1.2
NAP-A_{thick}L	--------	127.3 ± 5.1	--------	--------	--------	--------	--------

Table 6.2 presents mechanical properties (Young modulus, yield stress and strain, and stress and strain at break) of the membranes obtained by tensile measurements. Stress-strain curves can also be seen in **Figure 6.6**. Yield stress and yield strain are the limit point on the stress *versus* strain curves in which the elastic behavior is visualized. Above this point, membranes deform inelastically until reaching the rupture point. Young modulus values represent the angular coefficient of the stress *versus* strain curve in the elastic region. For membranes containing both LDH-Cl or LDH-NAP particles,

Young modulus progressively increased with the increase in the PLA thickness from A_{thin} to A_{tick}. Membranes prepared by the approach B presented a rheological performance comparable to the performance of the membranes with intermediate PLA thickness (A_{med}).

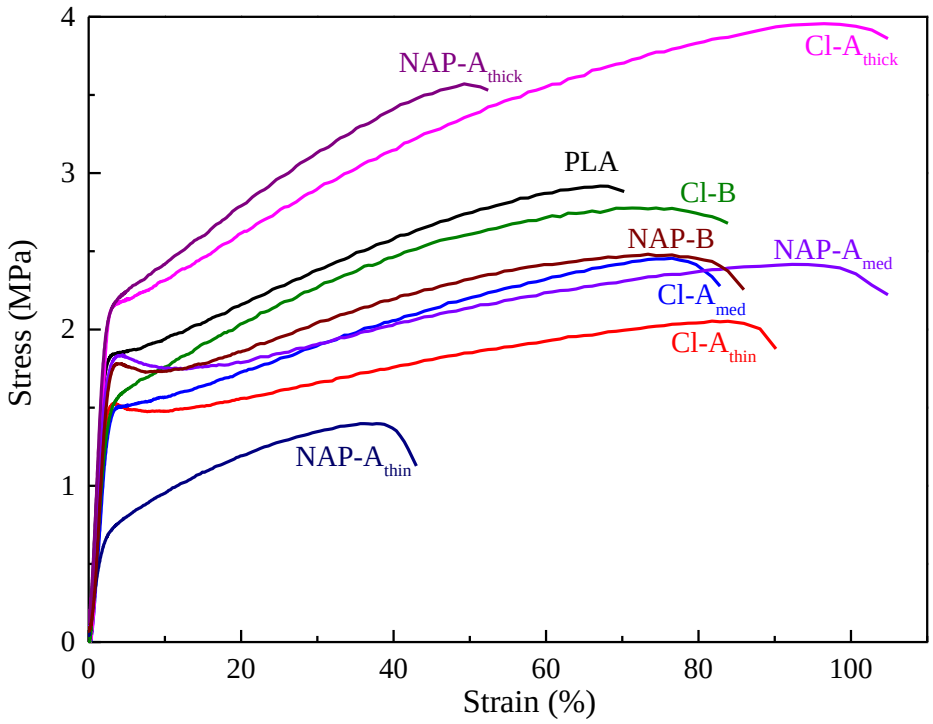

Figure 6.6. Examples of representative stress-strain curves of pristine PLA and composite membranes.

Static water contact angles (SCA) for the pristine PLA and LDH-PLA membranes, as well as for the last LDH electrosprayed layer of the A_{thick} samples (Cl-A_{thick}L and NAP-A_{thick}L) are compiled in **Table 6.2** (see also **Figure 6.7**). Comparing the SCA value of the pristine electrospun PLA (128.6 ° ± 5.1 °) with the values for the Cl-LDH-PLA samples, it is observed a decrease in the hydrophobicity to 123.8° ± 5.0 ° for the Cl-A_{thick} sample and a more pronounced decrease for the other Cl-LDH-PLA samples. When LDH-NAP particles are present in the composites, the decrease in hydrophobicity compared to the pristine electrospun PLA membrane is less pronounced, showing the property of NAP anions in conferring higher hydrophobicity to the LDHs.

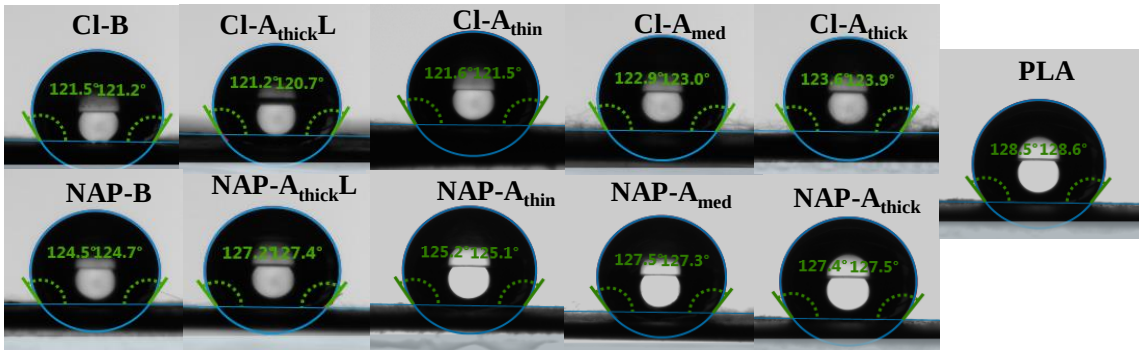

Figure 6.7. Examples of water static contact angle pictures for pristine PLA and devices.

Technological medical devices, such as multifunctional dressings, require a detailed understanding of the structure of the materials to tune materials properties and explain their behaviour once applied. LDHs were previously fully characterized and a high drug load was verified. Physicochemical properties of the nanofiber membranes were investigated. The interaction degree among PLA nanofibers and LDH particles responded to the applied approach and resulted in mechanical properties improvements. The different membranes presented a particular superficial morphology, in which modifications in the thickness of the polymeric diffusional barrier are expected to affect the drug release profile, as discussed below.

6.9.3. Kinetic of NAP release: effect of the morphology of the membranes

Released drug amount was calculated from the calibration curve shown in **Figure E.10**. Initial release, highlighted in **Figure 6.8**, shows that after 5 min more than 5 % of NAP was quantified and probably LDHs particles present in the membrane's surface were responsible for the initial release, with exception of the NAP-A_{thick} sample, whose initial drug release was delayed for about 2 hours. Later release profile, better visualized in **Figure 6.9**, shows a considerable release rate difference among the samples. Half of NAP amount was released after 24, 56, 96, and 408 h (17 days) of experiment for the NAP-A_{thin}, NAP-B, NAP-A_{med}, and NAP-A_{thick} composites, respectively. The release rate can be correlated with the degree of LDHs particles exposure to the saline solution media. Moreover, to reach the LDH particles inside the structure, the aqueous media

has to penetrate through the PLA layers, which are hydrophobic. From A_{thin} to A_{thick}, the thickness of the PLA layer increases, increasing the penetration time inside the membrane and slowing the drug release. Naproxen was released over 18 days for the NAP-A_{thin} sample and for longer time for the other samples: 59 days for the membrane prepared by the approach B and 66 days for both NAP-A_{med} and NAP-A_{thick}, after which it reached a plateau.

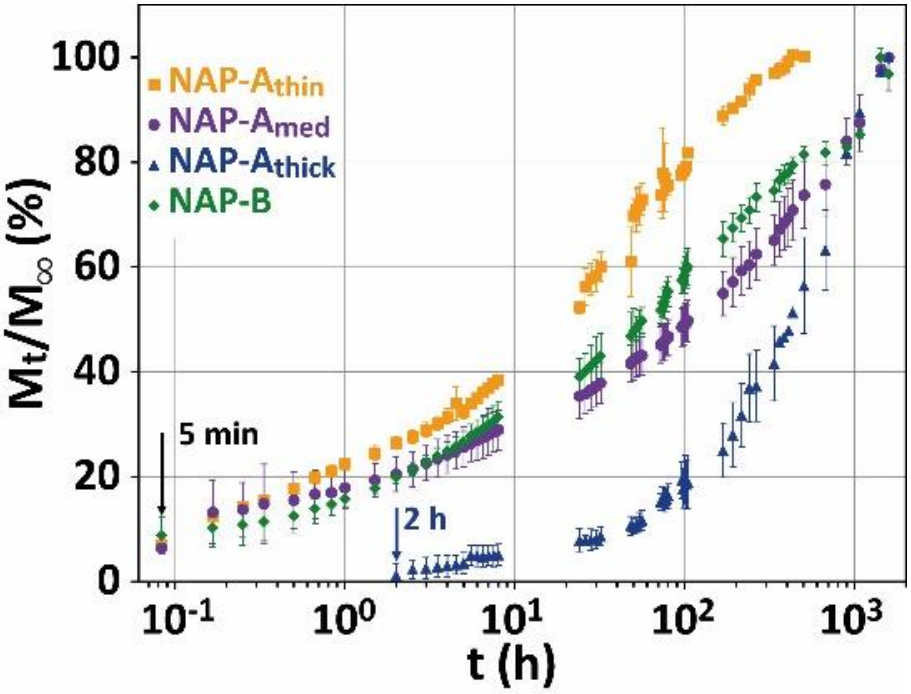

Figure 6.8. Drug release profile: naproxen release percentage as a function of time, in semi-log scale, for the different composites.

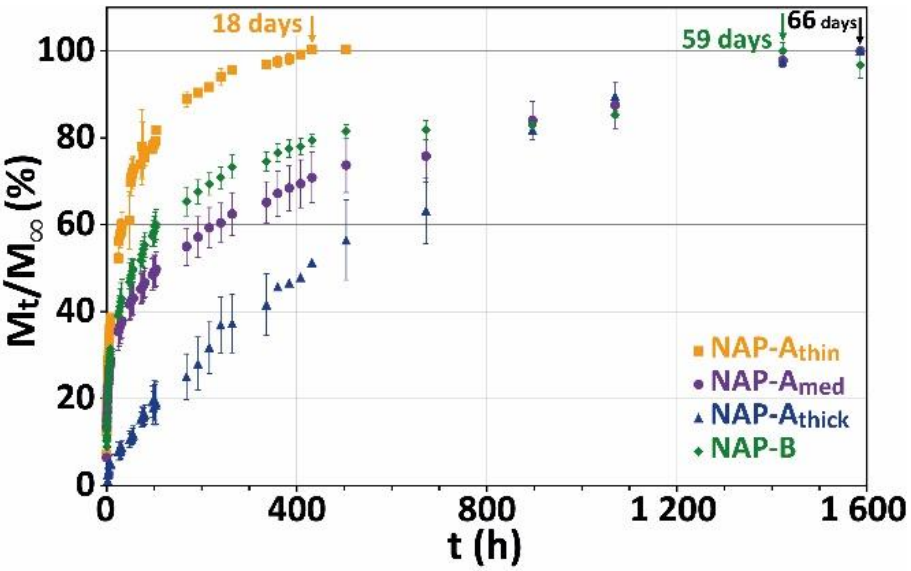

Figure 6.9. Drug release profile: naproxen release percentage as a function of time, in linear scale, for the different composites.

Naproxen kinetic release mechanisms from the different membranes were studied by the application of the Power Law Ritger-Peppas model (also called Power Law model)[272] (**Equations 6.2**) (with M_t equal to the drug amount released after a time t and M_∞ equal to the drug amount at the equilibrium state) which is currently used to describe the drug release process from matrices in general and polymeric systems. **Figure 6.10** presents the curves of the model as well as the obtained kinetic parameters (constant K and release exponent n) and linear correlation coefficients (R^2). Drug release from all devices was well fitted by the Power Law model, with R^2 values greater than 0.98. The low n values obtained for NAP-A_{thin}, NAP-A_{med}, and NAP-B membranes (respectively 0.28, 0.23, and 0.26), smaller than 0.45, suggest a Fickian type release with a dominant diffusion process.[272–274] In the case of NAP-A_{thick} membranes, n is much larger and equal to 0.59, characterizing an anomalous transport. It must be mentioned that such model gives only an overall behavior of the membrane rendering difficult an exact description of the drug release mechanisms and especially the lag-time observed for the NAP-A_{thick} membranes. LDH alone are well-known for their Fickian diffusion release behavior which is based on ion-exchange process.[275,276] However, in the case of this study, the multilayer structure of the membranes induces a complex sequential flow through the PLA nanofibrous layers and then, through the internal LDH layers being the reservoirs of the drug. Considering the architecture of the NAP-A_{thick} membranes, it is possible to propose that initially the release medium permeates the pores of the PLA hydrophobic mesh of the external layer. Then, after this first step, the exchange of NAP by Cl^- saturating the LDH layers allows the release of the drug through the porous layer of PLA towards the external medium. The drug release delay was not evidenced for all other membranes because some LDH particles were immediately exposed to the release medium as shown in **Figure 6.8** for the membranes containing the thinnest PLA layers (*i.e.* NAP-A_{thin}, NAP-A_{med}, and NAP-B).

$$\frac{M_t}{M_\infty} = Kt^n \qquad (6.2)$$

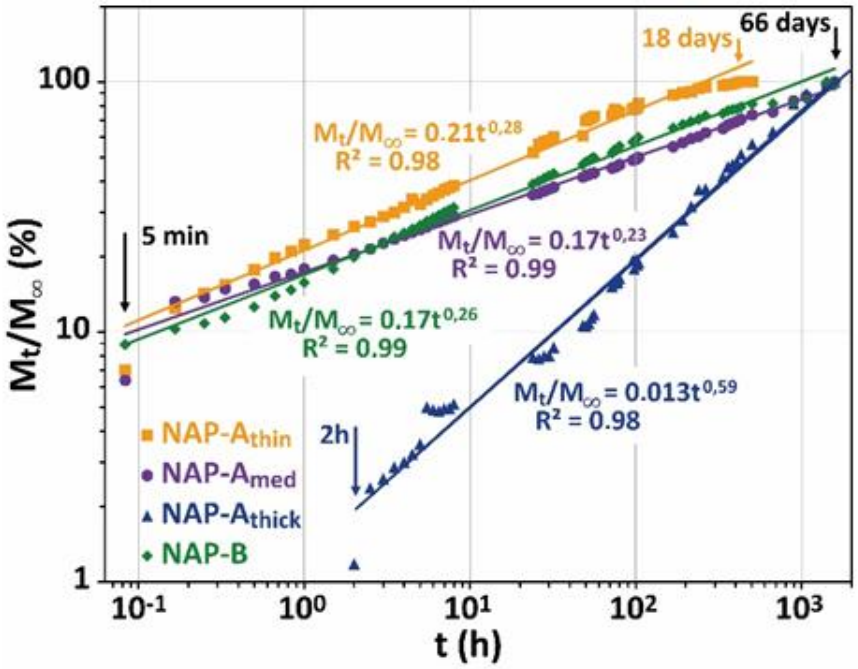

Figure 6.10. Experimental points and Power Law (solid lines) of Naproxen release percentage as a function of time for the different composites in log-log scale.

To better understand the dissimilarity among the dissolution profiles for the membranes prepared by the different approaches, the "difference factor" (f_1) and the "similarity factor" (f_2), described by **Equations 6.3** and **6.4**, respectively, were calculated and are indicated by the *Agência Nacional de Vigilância Sanitária* (The Brazilian Health Regulatory Agency)[277] and by the FDA[278] to compare tested and reference formulations. Where, N is the number of dissolution time points and R_t and T_t are the dissolution values (percentages in our case) for the reference and the tested system at a time t, respectively. The factor values are shown in **Table 6.3**. Dissolutions profiles are considered equivalents if f_1 is between 0 and 15 and if f_2 is between 50 and 100, as observed among the NAP-A_{med} and NAP-B membranes, while all other membranes show a different profile, compared two by two.

$$f_1 = 100\left(\frac{\sum_{t=1}^{N}|R_t - T_t|}{\sum_{t=1}^{N} R_t}\right) \quad (6.3)$$

$$f_2 = 50\log\left[100\left[1 + \frac{1}{N}\sum_{t=1}^{N}(R_t - T_t)^2\right]^{-0.5}\right] \quad (6.4)$$

Table 6.3. "Difference" (f_1) and "similarity" (f_2) factors calculated for the composites compared two by two.

Rt	**NAP-A$_{thin}$**	**NAP-A$_{med}$**	**NAP-B**	**NAP-B**	**NAP-B**
Tt	**NAP-A$_{med}$**	**NAP-A$_{thick}$**	**NAP-A$_{thin}$**	**NAP-A$_{med}$**	**NAP-A$_{thick}$**
f_1	28.4	44.7	27.7	10.0	49.5
f_2	33.2	32.1	39.9	60.4	27.7

6.10. Conclusions

The development of 3D multi-layered electrospun membranes containing drug loaded iron-based LDHs particles was achieved with the aim of forming multifunctional dressings by different approaches. In approach A, a faster, an intermediate, and a slower NAP release were observed for the thin, medium, and thick PLA layer thickness, respectively. Therefore, drug release could be modulated by simply varying one preparation parameter. Compared to the membranes prepared by the approach A, approach B involved only one step preparation and the membrane presented an intermediate NAP release profile. The developed membranes fulfilled important characteristics expected for a technological drug delivery device, since drug delivery composites prepared were able to modulate and keep NAP release for more than two months. Besides, membranes architecture can inspire the development of even more interesting and functional devices based on electrospinning and electrospraying technics.

6.11. Acknowledgments

Professor Guy Schlatter is acknowledged for the supervision and idealization of the architectures of the membranes. Professors Jocelyne Brendle, Anne Hébraud, and Lionel Limousy are also acknowledged by supervision and facilities. We are also thankful to Doctor Géraldine Layrac by the contribution in investigation and membranes

characterization. Céline Piras and Saeel Momin are acknowledged for the technical support. *Laboratório de Espectroscopia Molecular Hans Stammreich* (LEM, *Instituto de Química–USP*) is also acknowledged for the Raman and FT-IR spectra recording.

Chapter 7: Polymer/iron-based layered double hydroxides ($Mg_2Fe_{0.5}Al_{0.5}$ and $Zn_2Fe_{0.5}Al_{0.5}$) particles aiming multifunctional wound dressings

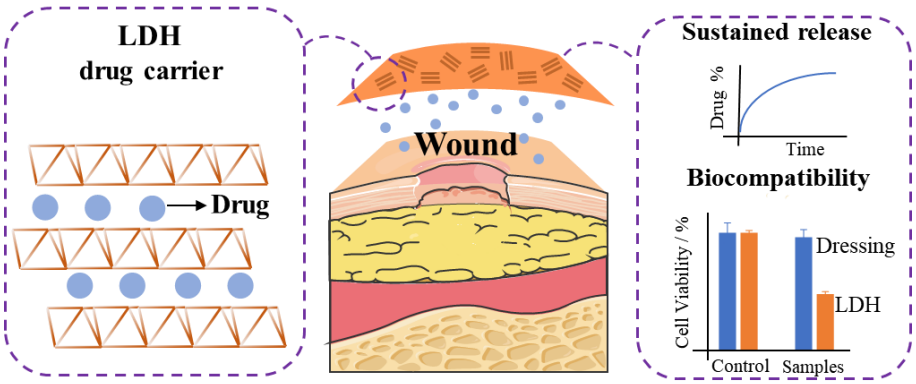

7. Abstract and data presentation

7.1. Abstract

In this chapter it is presented the development of multifunctional therapeutic membranes based on a PEBA high-performance block copolymer scaffold and LDHs biomaterials, aiming their uses as wound dressings. Two LDH layer compositions were employed containing Mg^{2+} or Zn^{2+}, Fe^{3+} and Al^{3+} cations, intercalated with chloride anions, abbreviated as Mg-Cl or Zn-Cl, or intercalated with NAP, abbreviated as Mg-NAP or Zn-NAP. Membranes were structurally and physically characterized, and the *in vitro* drug release kinetics and biocompatibility were assessed. PEBA loading NaNAP salt particles was also prepared for comparison. Intercalated NAP anions improved LDH-polymer interaction resulting in membranes with greater mechanical performance compared to the pristine polymer membrane or to the membranes containing the LDHs-Cl. Drug release (in saline solution) was sustained for at least 8 h for all samples and release kinetics could be modulated: a slower, an intermediate, and a faster NAP release were observed from membranes containing Zn-NAP, NaNAP, and Mg-NAP particles, respectively. In general, cell viability was higher in the presence of Mg-LDH and the membranes presented improved biocompatibility in comparison with the powdered samples. PEBA containing Mg-NAP sample stood out among all membranes in all the evaluated aspects, thus being considered a great candidate for application as multifunctional therapeutic dressings. Results shown in this chapter are published as an article in the *Pharmaceutics* Journal, 12 (11) (2020) 12111130 (please, see https://doi.org/10.3390/pharmaceutics12111130 and the original abstract in **Appendix F**).

7.2. Materials and methods

7.2.1. Reagents

PEBAX®2533 (PEBA) containing 80 % of poly(tetramethylene oxide) and 20 % of poly(amide 12) portions was obtained from Arkema Inc., France. Magnesium chloride hexahydrate ($MgCl_2{\cdot}6H_2O$) (99 %), aluminum chloride hexahydrate ($AlCl_3{\cdot}6H_2O$) (99

%), iron(III) chloride hexahydrate ($FeCl_3 \cdot 6H_2O$) (98 %), sodium hydroxide (NaOH) (≥ 98 %), sodium naproxenate (NaNAP) ($NaC_{14}H_{13}O_3$) (≥ 98 %), thiazolyl blue tetrazolium bromide (MTT) (98 %) and fetal bovine serum (PBS) (cod. F2442) were purchased from Sigma-Aldrich. Sodium chloride (NaCl) (99 %) was purchased from iqa analítica and 2-propanol PA was purchased from Synth. DMEM High Glucose (4500 mg L^{-1} glucose, L-glutamine, sodium bicarbonate, and without sodium pyruvate) was purchased from Microtech®. Solution containing 1% amphotericin/streptomycin/penicillin solution was purchased from EuroClone®. Normal Human Dermal Fibroblasts (NHDF) juvenile foreskin (cod. C-12300) were purchased from Promocell®. All products were used as received.

7.2.2. Synthesis of $Mg_2Fe_{0.5}Al_{0.5}$ and $Zn_2Fe_{0.5}Al_{0.5}$ LDHs intercalated with Cl^- or NAP anions

$Mg_2Fe_{0.5}Al_{0.5}$-Cl, $Zn_2Fe_{0.5}Al_{0.5}$-Cl, $Zn_2Fe_{0.5}Al_{0.5}$-1NAP, and $Mg_2Fe_{0.5}Al_{0.5}$-3NAP_H LDH phases were prepared as described in sections 3.2.1 (**Chapter 3**) and 4.2.1 (**Chapter 4**) and are abbreviated by Mg-Cl, Zn-Cl, Mg-NAP, and Zn-NAP, respectively. Solids washing and drying procedures were the same applied in **Chapter 6**.

7.2.3. Preparation of pristine PEBA and PEBA composite membranes

Composites were designed to have a LDH percentage as higher as possible but maintaining visual homogeneity and resistance to handling. As shown in **Table 7.1**, membranes containing NAP, as sodium salt, or loaded into LDH were prepared as reported[279], aiming to have approximately the same drug amount (about 4 wt %). For each layer composition, it was applied the same weight percentage for pristine and hybrid LDH to favor comparison.

Table 7.1. Weight percentages of LDH and NAP in the membranes.

Components of the membranes	LDH wt %	NAP wt %
NaNAP	-----	4
Mg-Cl	10	-----
Mg-NAP	10	4
Zn-Cl	13	-----
Zn-NAP	13	4

7.2.4. Preparation of pristine PEBA membrane

PEBA membrane was prepared by casting method, dissolving polymer beads in 2-propanol in a 3 wt % concentration under stirring at 80 °C for 2 hours. Polymer solution was transferred to a Teflon sample holder with a cylindrical internal cavity with 2 cm of diameter and 0.7 cm of height. Solvent evaporation was performed in a fume hood for at least 8 h.

7.2.5. Preparation of PEBA membranes impregnated with the NaNAP salt

First of all, it was performed the polymer dissolution as described above. Then, the amount of NaNAP necessary to obtain the NAP percentage mentioned in **Table 7.1** was dispersed in the polymer solution under stirring. Solvent evaporation was carried out as applied for the PEBA membrane. Sample was abbreviated as PEBA_NaNAP.

7.2.6. Preparation of PEBA membranes containing LDHs particles

LDHs were previously treated to improve suspensions stability and homogeneity of particles distribution. The respective amounts of LDHs to reach the same drug percentage encapsulated in the composites, shown in **Table 7.1**, were suspended in 5 mL of 2-propanol. Suspensions were submitted to Ultra-Turrax® disperser at 7000 rpm for 5 min. Solids were isolated through centrifugation at 10000 rpm for 3 min, resuspended in the 3 wt % PEBA solution and manually homogenized. Suspensions were transferred to Teflon plates and the solvent evaporation was carried out as previously described.

Samples were abbreviated as PEBA_LDH or more specifically, according to the composition of the LDH, as follows: PEBA_Mg-Cl, PEBA_Mg-NAP, PEBA_Zn-Cl, and PEBA_Zn-NAP. **Figure 7.1** presents a schematic representation of PEBA membranes preparation.

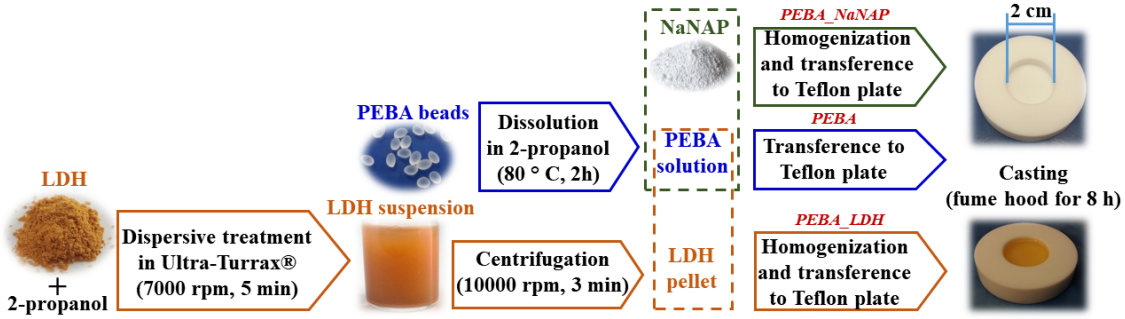

Figure 7.1. Schematic representation of PEBA membrane and composites preparation processes.

7.2.7. *In vitro* NAP release assays

Naproxen release experiments were conducted in quintuplicates using 2 cm diameter circular membranes. Membranes were directly accommodated in Franz's cells with no additional membrane since it is intended to mimic wound. Franz receptor chambers were filled with 6.4 mL of saline solution (0.9 wt % NaCl), pH value equal to 7.22 +/- 0.01, simulating human plasma. The release media was constantly homogenized with stir-bar. At predefined times, 0.8 mL of the media was collected and immediately replenished with fresh saline medium. NAP concentration was determined by UV–visible absorption spectrophotometry at a maximum absorption (λ_{max}) equal to 230 nm. Quantification was made using a calibration curve (R^2 = 0.999) build with minimal and maximal NaNAP solutions concentration equal to 0.971 and 2.200 ppm, respectively. After the first released NAP aliquot removal, accumulative NAP weight released at each time was corrected taking in account the NAP amount present in each subsequent aliquot removed for the measurements. Metals were quantified at the end of the assay by ICP-OES.

7.2.8. Biocompatibility evaluation: MTT assay

In vitro biocompatibility of the membranes was assessed by MTT test in 96-well plates (Cellstar 96 Well Culture Plate, Greiner Bio-One). Membranes were cut as circles with the correspondent well's area (0.32 cm^2). For comparison, the biocompatibility of the equivalent amount of LDH and NaNAP samples in powder present in the composites (**Table 7.1**) were also evaluated, as well as pristine PEBA membrane. NHDF were seeded onto membranes in well plates ($0.35 \cdot 10^5$ cell/well in 200 µL/well) and incubated for 24 h at 37 °C in a humidified atmosphere containing 5% CO_2 (CO_2 Incubator, PBI International, Milano, I). Powdered samples were added after cell confluence and then, the same MTT procedure was applied for all the samples. Briefly, medium was removed after 24 h of treatment, cells were washed with PBS (10 % v/v, 200 µL/well), exposed to 50 µL MTT solution (2.5 mg ml^{-1} solubilized in DMEM w/o red phenol) diluted in 100 µL of DMEM (w/o red Phenol), and incubated for 3 h at 37 °C. Next, the MTT reagent was removed and 100 µL of DMSO were added in each well to lyse cells. Finally, the absorbance was read at 570 nm with 690 nm as wavelength reference using a ELISA plate reader (Imark Absorbance Reader, Biorad, Milan, Italy). Cell viability was calculated as the percentage ratio between the absorbance of each sample and the absorbance of controls (cell substrates in growth medium).

7.2.9. Characterization

Carbon percentage was determined on a Perkin Elmer-CHN 2400 equipment at the *Central Analítica* of *Instituto de Química* of the *Universidade de São Paulo* (USP).

Inductively coupled plasma atomic emission spectroscopy (ICP-AES) analysis was applied for metals quantification in synthesized LDHs, in a Spectro Analytical Instrument at the *Central Analítica* of *Instituto de Química* of *USP*. The quantification of metal cations from the release media after *in vitro* drug release assay was performed in a Perkin-Elmer optima 8300 instrument at the *Centro de Instrumentación Científica* of UGR.

X-ray diffraction (XRD) patterns were obtained on a Rigaku Ultima Plus equipment, with Bragg-Brentan geometry and graphite crystal monochromator, using Cu-Kα

radiation (1.5406 Å), 30 kV, 15 mA, Ni filter, scan range 1.5-70°(2θ) and scan step of 0.05°(2θ)/2s.

Average particles size determination was conducted in 2-propanol through low angle laser light scattering in a Mastersize 200 Malvern equipment.

Differential scanning calorimetry (DSC) was carried out at the *Central Analítica* of *Instituto de Química* of USP using a TA instruments – Q10 equipment under 50 mL min^{-1} N_2 flow, a heating/cooling rate of (±) 10 °C/min, using alumina hermetic and close crucible. Samples were first equilibrated at -70 °C and then submitted to a heating cycle until 100 °C (to erase information coming from the preparation procedure), a cooling cycle until -70 °C and a second heating cycle until 100 °C.

Mass spectrometry coupled to thermogravimetric analyses (TGA-MS) were recorded on a Netzsch thermoanalyser model TGA/DSC 490 PC Luxx coupled to an Aëolos 403 C mass spectrometer, using alumina crucible and heating rate of 10 °C min^{-1} under synthetic air flow of 50 mL min^{-1}.

Fourier transform infrared (FT-IR) spectra were recorded in the 4000–400 cm^{-1} range on a Bruker spectrophotometer, model alpha by ATR with acquisition step of 4 cm^{-1} and 512 scans.

Images by optic microscopy were registered in an Optic microscope Oleman DN-107T.

Images from scanning electron microscopy (SEM) were obtained at the *Central Analítica* of *Instituto de Química* of USP in an FE-SEM Jeol JSM 7401F (FREG) equipment applying membranes deposited on a copper tape covered with gold. Energy-dispersive X-ray spectroscopy (EDS) spectra from membrane's surface were also obtained.

Dynamo-mechanical analysis (DMA) were performed at the *Central Analítica* of *Instituto de Química* of USP on a DMA Q800 TA instruments equipment. Each PEBA membrane was cut into 5 rectangles with 3 x 0.5 cm and the analysis were performed at 70 °C.

Membranes thicknesses was determined using a Mitutoyo analogical micrometer. Five measurements in different points were performed in 2 cm diameter circular membranes.

Static water contact angle measurements were performed in triplicate with static deionized water drop on the membranes using a SEO portable equipment.

Absorbance in the ultraviolet–visible region was measured on a Perkin Elmer Lambda 25 spectrophotometer.

NAP release experiments were conducted on a BioScientific Inc Franz diffusion cells system (FDC40020FF, Phoenix, AZ, USA) with contact area equal to 0.63 cm^2.

7.3. Results

7.3.1. Samples Characterization

Table 7.2 presents the chemical composition of the LDHs. The molar ratios between the metals are close to the expected values according to the salt's concentration in the mother solution. Appreciable amount of carbon is verified for both Mg-NAP and Zn-NAP LDHs, corresponding to 36.35 and 26.64 % of the materials mass, respectively.

Table 7.2. Elemental chemical composition of $M_2Fe_{0.5}Al_{0.5}$-Cl and $M_2Fe_{0.5}Al_{0.5}$-3NAP_H LDHs (M = Mg^{2+} or Zn^{2+}).

Sample	M/Al	M/Fe	Fe/Al	M / (Fe + Al)	wt % C	wt % NAP
Mg-Cl	4.32	4.09	1.06	2.10	----	----
Mg-NAP	4.29	4.10	1.05	2.10	26.64	36.35
Zn-Cl	3.53	3.47	1.02	1.75	----	----
Zn-NAP	3.64	3.53	1.03	1.79	19.41	26.48

Figure 7.2 presents surface aspects of the polymeric samples in different scales. Samples are disposed in the columns. In line A, showing macroscopic images, it is possible to verify that membranes are visually homogeneous. Pristine PEBA is translucent while PEBA_NaNAP is cloudy. Membranes turn opaque and acquire an orange color when LDH particles are present.

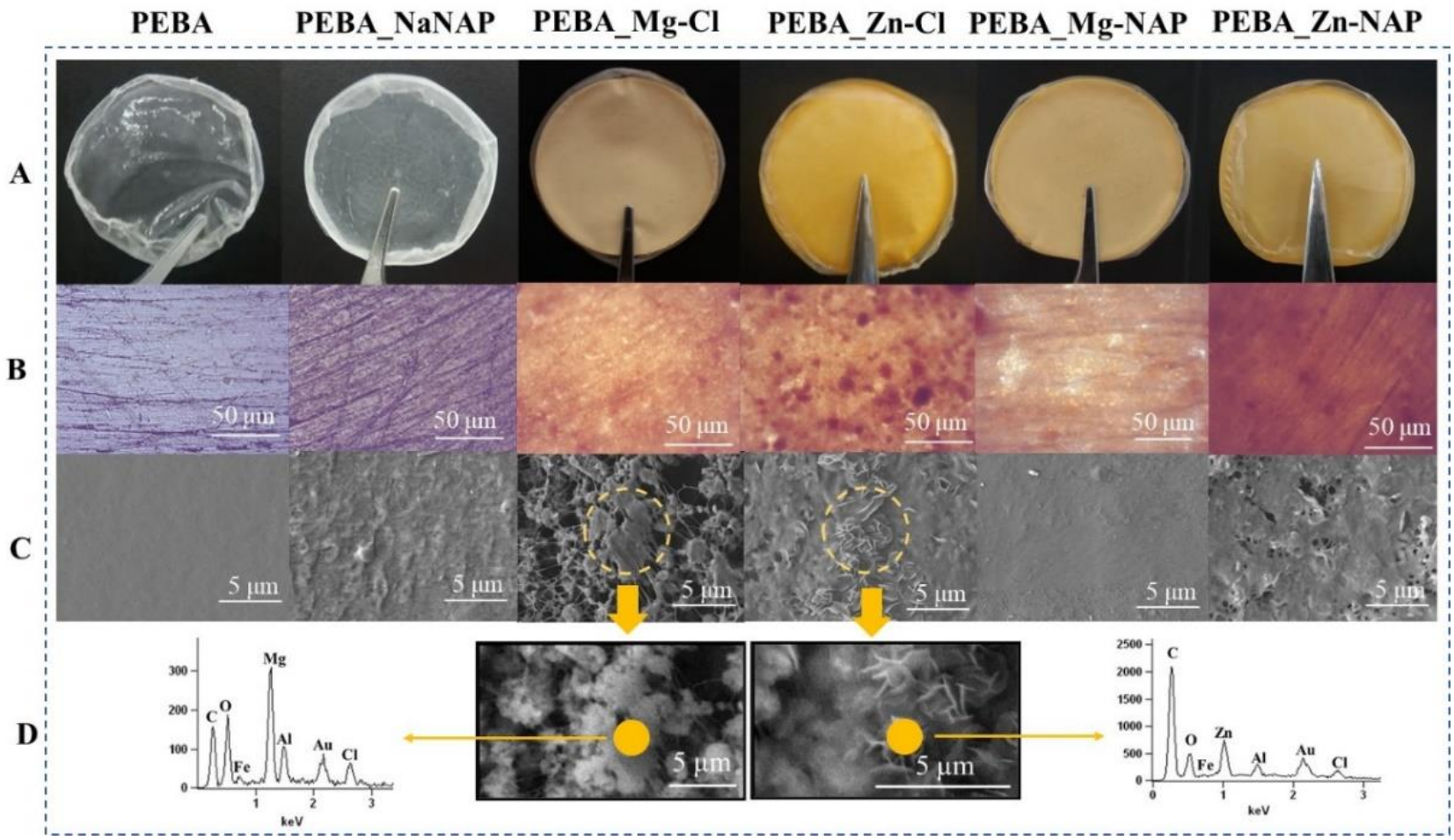

Figure 7.2. Samples are disposed in the columns. Line A: macroscopic aspects, line B: optical microscopy images, C: SEM micrographs and D: EDS spectra.

In line B (optical microscopy images), Teflon-plates surface originates the wrinkles clearly visualized for PEBA and PEBA_NaNAP samples. For PEBA_Mg-Cl, PEBA_Mg-NAP and PEBA_Zn-NAP membranes, particles are more homogeneously dispersed into the polymer compared to the PEBA_Zn-Cl sample, in which it is possible to clearly see darker points of particles aggregation. Line C (SEM micrographs) shows a smooth surface for pristine PEBA and a rough surface for PEBA_NaNAP sample, due to NaNAP particles aggregation. For PEBA_Mg-Cl sample, LDHs particles are surrounded by polymer fibers. Instead, for the PEBA_Zn-Cl sample, plates-like association of LDH particles is visualized and are similar to the morphology observed for powder LDHs [115,280]. For PEBA_Zn-NAP sample, surface fill failures are observed and LDH particles aggregation are no longer visualized. PEBA_Mg-NAP sample is compared to that of pristine PEBA. For the Peaks in EDS spectra (line D) of the indicated yellow points match with the composition of the LDH layers (Mg^{2+} or Zn^{2+}, Fe^{3+} and Al^{3+} cations), the intercalated anion (Cl^{-}) and the composition of the polymer (C and O). Characteristic emission of Au refers to samples recover.

Table 7.3 presents the average thicknesses of the membranes. Composite membranes are thicker than pristine PEBA (82 ± 14 μm). PEBA_NaNAP sample experienced a lightly increase in thickness (90 ± 10 μm). Compared to the PEBA_Mg-Cl (103.3 ± 1.3 μm) and PEBA_Zn-Cl (103.3 ± 5.0 μm) samples, the presence of LDHs particles intercalated with NAP resulted in thinner membranes (thicknesses equal to 85.6 ± 5.6 and 96.3 ± 5.6 μm for the PEBA_Mg-NAP and PEBA_Zn-NAP samples, respectively).

Static water contact angle (SWCA) values for pristine PEBA and composites (see also **Figure 7.3**) are shown in **Table 7.3**. SWCA for pristine PEBA (78.1 ± 0.9°) is close to the value reported for a PEBAX®2533 membrane also prepared by casting method (81 ± 2 ° [281]). PEBA_LDH membranes presented lower SWCA values indicating an increase in surfaces hydrophilicity. PEBA_NaNAP membranes presented the lowest SWCA value (60.1 ± 5.3 °), an expected behavior due to the presence of particles of an organic salt relatively soluble in water (0.5504 ± 0.0012 mol dm^{-3} at 293.15 K[282]).

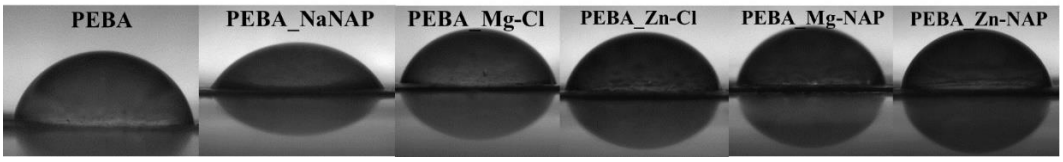

Figure 7.3. Representative pictures of water static drop deposited on the surface of PEBA and PEBA composite membranes.

Table 7.3. Thickness, water static contact angle, stress and strain at break and Young modulus of pristine PEBA membrane and PEBA composites.

Sample	Thickness (μm)	Contact Angle (°)	Stress at break (kPa)	Strain at break (%)	Young Modulus (MPa)
PEBA	82 ± 14	78.1 ± 0.9	479 ± 27	22.2 ± 7.3	3.47 ± 0.92
PEBA_NaNAP	90 ± 10	60.1 ± 5.3	550 ± 14	15.4 ± 6.5	7.40 ± 0.82
PEBA_Mg-Cl	100.3 ± 1.3	73.3 ± 0.9	535 ± 49	43.2 ± 6.9	3.94 ± 0.50
PEBA_Mg-NAP	85.6 ± 5.6	74.3 ± 1.1	829 ± 45	55 ± 16	5.25 ± 0.71
PEBA_Zn-Cl	103.3 ± 5.0	74.7 ± 2.3	379 ± 120[a)]	22.0 ± 7.8	3.43 ± 0.43
PEBA_Zn-NAP	96.3 ± 5.6	75.2 ± 1.4	632 ± 129[a)]	25.6 ± 1.8	5.18 ± 0.66

Mass percentage of LDHs in the membranes are comparable, 10 wt % for LDHs composed by Mg^{2+} and 13 wt % for LDHs composed by Zn^{2+} cations. Thus, to better understand the effect of macroscopic characteristics related to the different materials compositions in the homogeneity of the composite membranes, LDHs particle size distribution was evaluated in the same solvent applied in previous particles dispersive treatment and for composites preparation (**Figure 7.4**).

Mg-Cl

d(0.1)= 6.273 µm d(0.5)= 16.093 µm d(0.9)= 36.719 µm

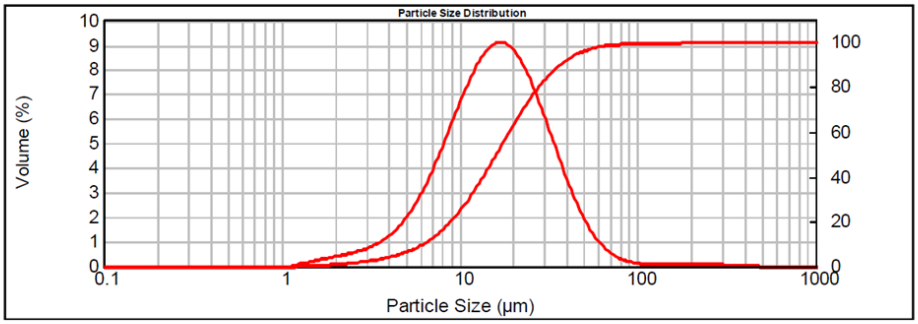

Mg-NAP

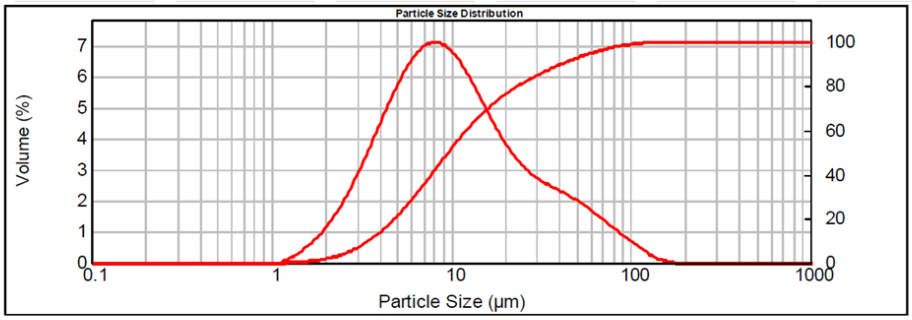

Zn-Cl

d(0.1)= 4.414 µm d(0.5)= 25.617 µm d(0.9)= 86.357 µm

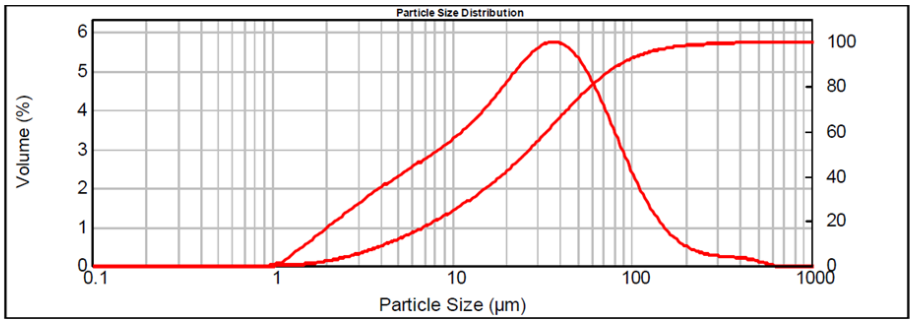

Zn-NAP

d(0.1)= 2.566 µm d(0.5)= 6.928 µm d(0.9)= 35.830 µm

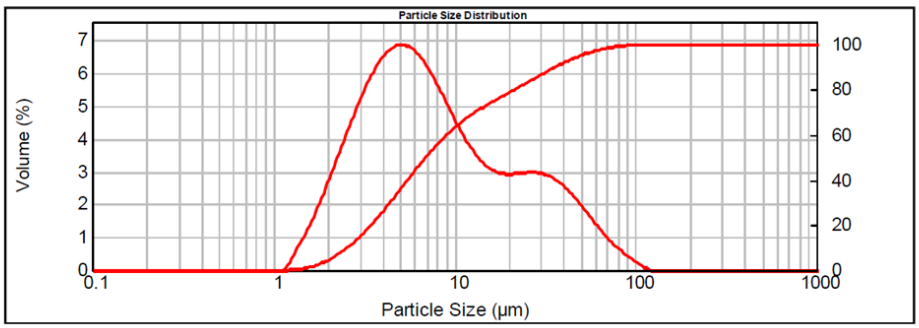

Figure 7.4. Particles size distribution of powdered LDHs dispersed in the solvent used for the preparation of the membranes (2-propanol). The relation among LDHs particles size and composition with cells viability can be seen in **Figure 7.12**.

Zn-Cl LDH average particles size is higher than that of the Mg-Cl LDH. Pristine LDHs present higher average particles size compared to LDHs intercalated with NAP. Although 50 % of the particles have a size up to 6.928 ± 0.001 μm for the Zn-NAP, against 9.631 ± 0.001 μm for the Mg-NAP sample, the polydispersity of the Zn-NAP sample compared to the other LDHs compositions is higher, where the presence of two curves of particles distribution with well-defined maximums is clear.

Figure 7.5A shows the XRD patterns of pristine PEBA and PEBA composites plus pristine LDHs, while **Figure 7.5B** exhibits the profiles of composites containing the NaNAP salt and hybrid organic-inorganic LDHs. In **Figure 7.5A**, pristine PEBA possess a semi-crystalline structure presenting a high intense and broad peak at 20 °(2θ), similarly to the literature [283] and to the XRD pattern of poly(amide 12) [284]. The indexation of diffraction peaks of LDHs was made considering the 3R1 polytype, mostly observed for synthetic LDHs. Basal spacing related to the (003) plane for both Mg-Cl and Zn-Cl materials is equal to 7.8 Å. As usually observed, Zn^{2+} cations promoted a higher structural organization of the LDH structure then the magnesium ions [115,242]. Most intense LDH peaks are present in the XRD pattern of the PEBA_LDH composites. According to **Figure 7.5B**, PEBA_NaNAP sample presents intense and narrow peaks assigned to the sodic salt. Compared to the LDHs-Cl, NAP intercalation shifts the (00l) peaks to smaller angle (2θ) region, indicating larger interlayer distances. Basal spacing related the (003) plane is equal to 21.0 and 21.8 Å for the Mg-NAP and Zn-NAP LDHs, respectively. For both hybrid LDHs, the (003) and (006) harmonic peaks attributed to the LDH-Cl phases are also present. The permanence of the (113) peak, dependent on the c axis and, therefore, expected to be dislocated to small angle region with the intercalation of a much more bulk anion, is another indication of the presence of a mixture of phases. These characteristics have also being observed for NAP loaded into LDH with different layer compositions and prepared by other methods besides ion-exchange reaction (such as coprecipitation[131] or reconstruction[121]), therefore being considered a peculiarity of the NAP-LDH system. Differently from the PEBA_Zn-NAP membrane, whose peaks associated with the Zn-NAP LDH are clearly observed, XRD pattern of PEBA_Mg-NAP sample shows only the broad peaks of the organic polymer.

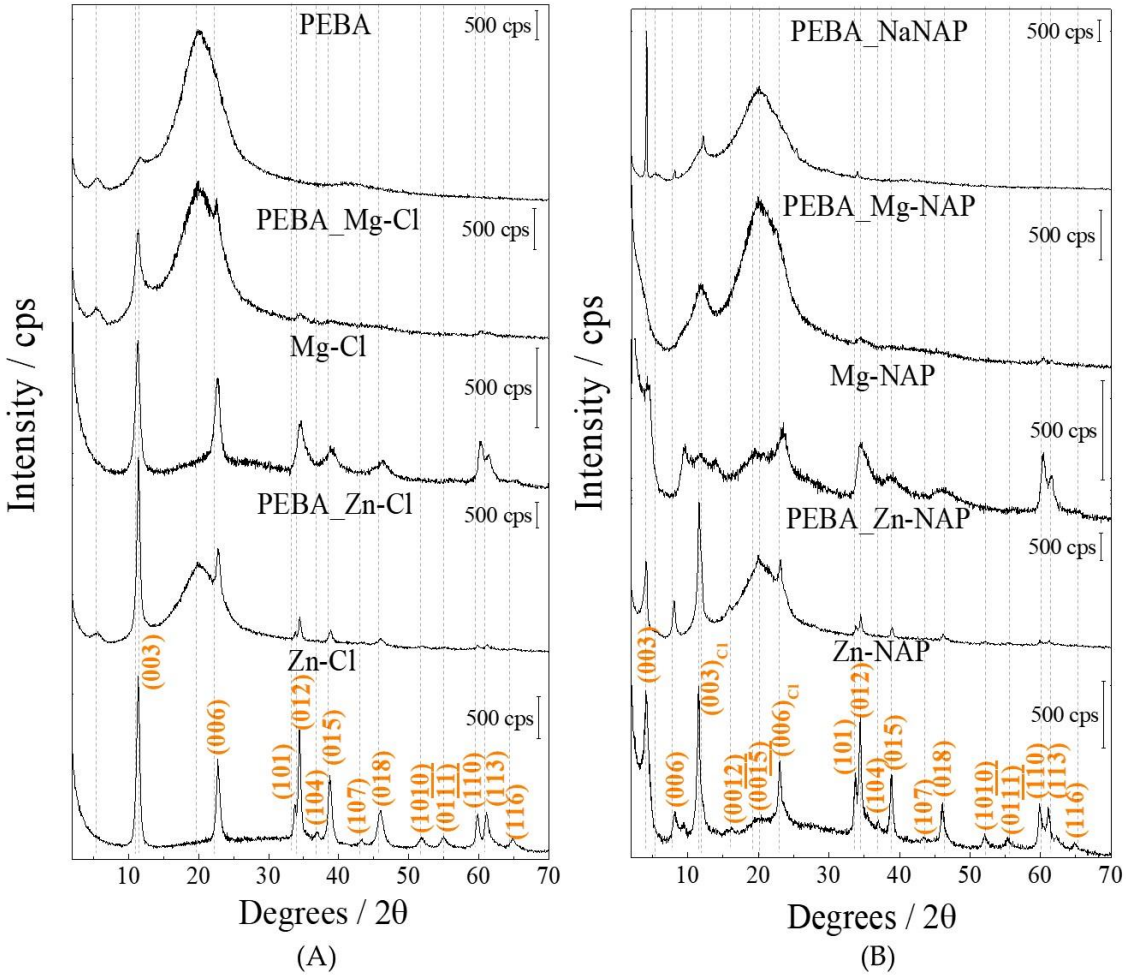

Figure 7.5. XRD patterns of pristine PEBA and PEBA composites containing Cl-LDHs (A) and composites containing the NaNAP salt and NAP-LDHs (B).

Stress at break, strain at break, and Young modulus of membranes submitted to tensile tests are shown in **Table 7.3**. With exception of the Zn-Cl LDH, all particles improved the stress at break of the composites. PEBA_Mg-NAP sample (829 ± 45 kPa) can be highlighted for having approximately twice the average tension at break in relation to pristine PEBA (479 ± 27 kPa). PEBA_Mg-NAP membrane also presented, as well, the higher elongation value (55 ± 16 %) among all samples. Pristine PEBA membrane and membranes containing Mg-Cl or Zn-Cl LDH particles presented a similar rigidity, with Young modulus values equal to 3.47 ± 0.92, 3.94 ± 0.50, and 3.43 ± 0.43 MPa, respectively. On the other hand, NaNAP particles conferred a considerable stiffening to the membrane, with Young modulus equal to 7.40 ± 0.82 MPa. PEBA_Mg-NAP and PEBA_Zn-NAP samples presented an intermediate stiffness, with Young modulus values equal to 5.25 ± 0.71 and 5.18 ± 0.66 MPa, respectively.

FT-IR spectra of pristine PEBA and PEBA composites containing LDHs-Cl and the composites containing the NaNAP salt and LDHs-NAP are shown in **Figure 7.6A** and **7.6B**, respectively; the bands tentative assignment is compiled in **Table 7.4**. For PEBA (wavenumbers indicated in blue), PA portion originates the bands at 3300, 1638, 1541, and 1242 cm^{-1}, attributed to hydrogen bonded amide group, and also the band at 720 cm^{-1} assigned to the CH_2 bending of the alkyl portion[196,197,281,283,285–287]. The strong band at 1104 cm^{-1} is assigned to the C–O–C stretching of ether group (PE portion). The bands at 2920, 2850, 1467, and 1447 cm^{-1} are attributed, respectively, to the asymmetric stretching, symmetric stretching, bending, and scissoring of the CH_2 group of both hard and soft segments. The band at 1368 cm^{-1} is assigned to the bending of the C–C–H group while the band at 1735 cm^{-1} is related to the ester linking group. The bands at 3400, 1360, and bellow 700 cm^{-1} (orange wavenumbers indicated in the spectra of Zn-Cl and Zn-NAP samples) are attributed to the O–H stretching of the hydroxyl groups in the LDH layers and of superficially adsorbed and intercalated water molecules, to the antisymmetric stretching of CO_3^{-2} (υ_3), and to M–OH translations, respectively[36]. The band at 1624 cm^{-1} is assigned to angular deformation of water molecules[288]**.** The spectrum of the PEBA_NaNAP sample is very similar to that of pristine PEBA. The bands at 1393, 1162, 925, and 815 cm^{-1} are related to the vibrational modes of NAP (shown in green)**.**

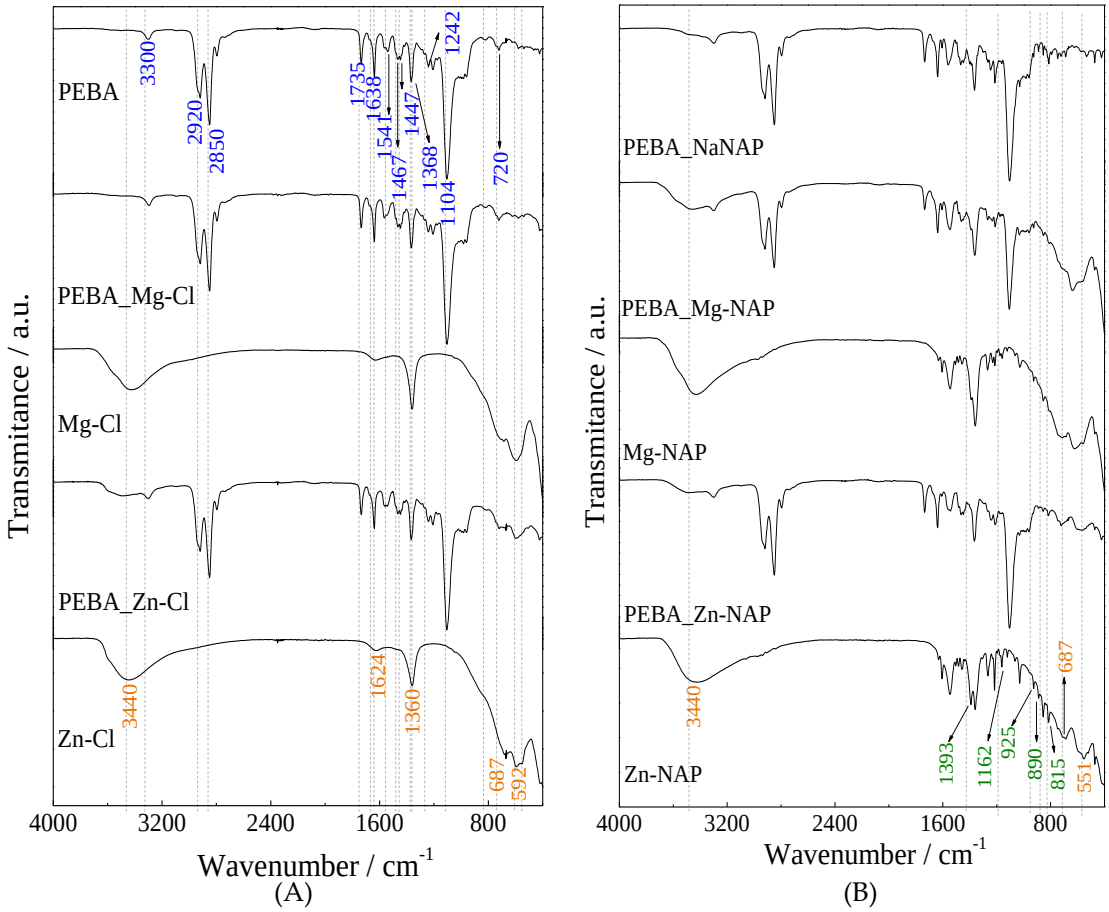

Figure 7.6. FT-IR spectra of pristine PEBA and PEBA composites containing Cl-LDHs (a) and composites containing the NaNAP salt and hybrid organic-inorganic LDHs (b).

Table 7.4. IR wavenumbers (in cm^{-1}) indicated in the spectra of PEBA membrane and PEBA composites and tentative assignments.

Wavenumber	Assignment	Wavenumber	Assignment[1]
3440	υ O–H	1393	υ C–C (naphthalene), ω CH_3
3300	υ N–H	1368	δ C–C–H
2920	υ_a CH_2	1360	υ_3 CO_3^{2-}
2850	υ_s CH_2	1242	υ C–N–H
1735	υ C=O (O–C=O)	1162	υ C–O
1638	υ C=O (H–N–C=O)	1104	υ_a C–O–C
1631	υ C–C=C	925	υ =C–H
1541	υ C–N	815	υ =C–H
1467	δ CH_2	721	δ CH_2 group $(-(CH_2)_n-, n > 4)$
1447	sc CH_2	< 700	Mg-OH or Zn-OH translations

[1]υ = stretching, υ_a = antisymmetric stretching, υ_s = symmetric stretching, δ = bending, and ω = wagging.

Figure 7.7 shows the cooling (top) and second heating (bottom) DSC scans for pristine PEBA and PEBA composites, whose peak temperature values related to the thermal events are gathered in **Table 7.5**. The temperature of glass-transition for PE portion (Tg PE), varied for all samples between -59 and -60 °C, as reported[289]. Crystallization peak temperature values of PE ($T_{c\ PE}$) portion ranged from -14 to -16 °C, also consistent with the literature[289], and slightly decreased with the presence of particles. Peak melting temperature value for PE (T_m PE) is normally observed around 0 and 20 °C[290]. No considerable variation in T_m PE was also verified among the samples, ranging from 19 to 21 °C. Upper temperature for DSC analysis was carefully limited to ensure that no particles degradation would take place. Therefore, it was only possible to obtain information about thermal events occurring in the PE portion (portion present in much greater quantity in PEBAX®2533), since the peak melting temperature (T_m) of PA is expected at around 140 °C or above[290]. Additionally, the endothermic event appearing around -72 °C for the PEBA_NaNAP sample is related to the release of water from salt particles[291].

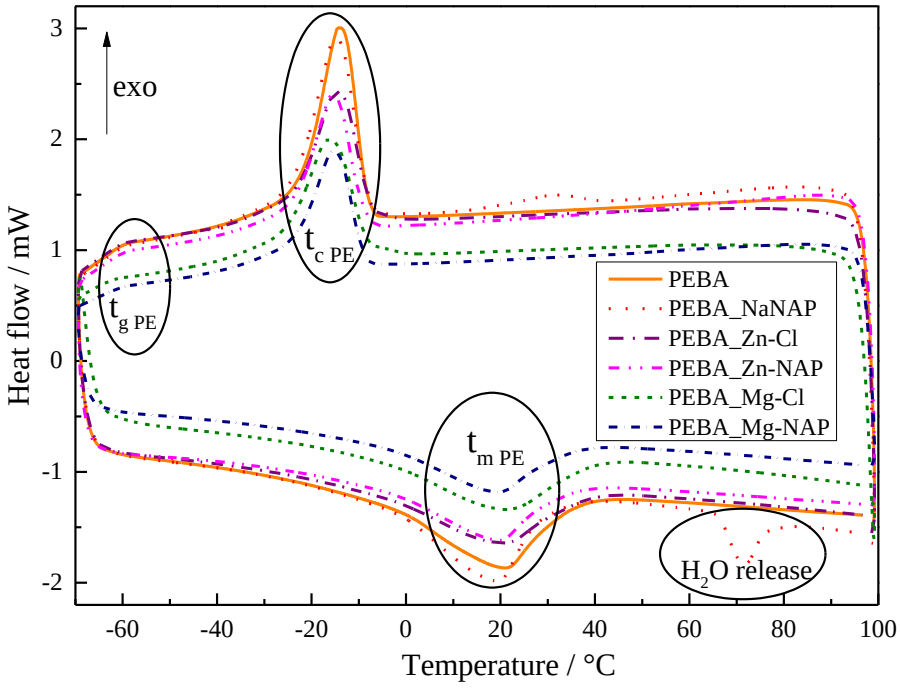

Figure 7.7. Cooling (top) and second heating (bottom) DSC scans for pristine PEBA and PEBA composites. $T_{g\ PE}$ – glass transition temperature of PE portion, $T_{c\ PE}$ – crystallization temperature of PE portion, $T_{m\ PE}$– melting temperature of PE portion.

Table 7.5. Peak glass transition ($T_{g\,PE}$), crystallization ($T_{C\,PE}$), and melting ($T_{m\,PE}$) temperatures obtained from DSC analyses of pristine PEBA and PEBA composites.[a)]

Material	$T_{g\,PE}$ (°C)	$T_{c\,PE}$ (°C)	$T_{m\,PE}$ (°C)
PEBA	-60	-14	21
PEBA_NaNAP	-59	-15	20
PEBA_Zn-Cl	-59	-15	20
PEBA_Zn-NAP	-59	-16	20
PEBA_Mg-Cl	-59	-16	21
PEBA_Mg-NAP	-60	-16	19

[a)] $T_{g\,PE}$ – glass transition temperature of PE portion, $T_{c\,PE}$ – crystallization temperature of PE portion, $T_{m\,PE}$– melting temperature of PE portion.

Considering the application of dressings on wound and the importance of materials toxicity, residual solvent fixation on PEBA chain after pristine membrane preparation was investigated by TGA-DTG-MS analyses (**Figure 7.8**). If present, the release of residual solvent is expected at low temperatures region, around 2-propanol boiling point (82 °C [292]). However, until approximately 200 °C, no weight loss occurs. From 200 °C, a release of a fragment with *m*/*z* ratio equal to 60 is observed. To confirm that the *m*/*z* = 60 signal is not associated with 2-propanol release, possibly delayed due to the interaction with the polymer chains (and/or to a decomposition fragment), pristine PEBA pellets were also analyzed (**Figure 7.9**). In this case, a *m*/*z* = 60 signal was in fact observed, being associated with the polymer not to the solvent. The different shapes of the samples could plausibly explain the temperature shift due to differential heat transfer.

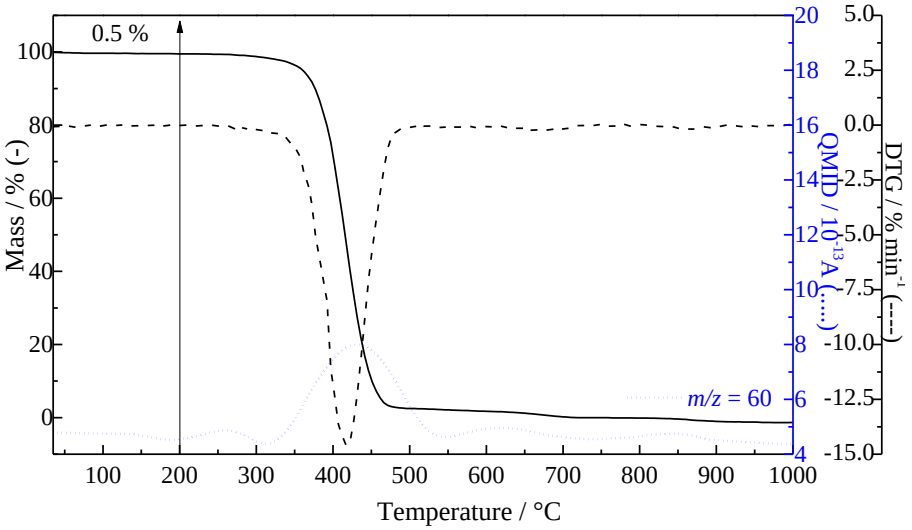

Figure 7.8. TGA and MS curves of pristine PEBA membrane.

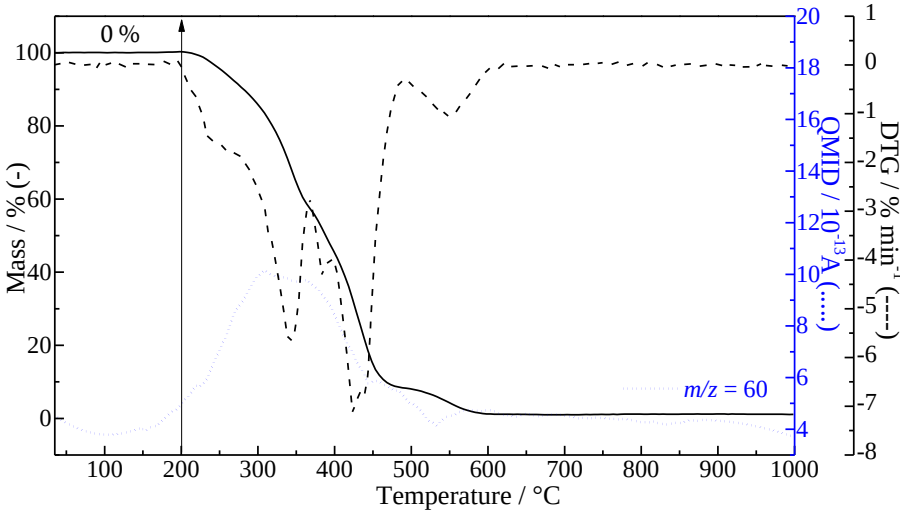

Figure 7.9. TGA and MS curves of PEBA reagent (beads).

The design of multifunctional dressings requires the understanding of the structure and properties of the final materials, as well as of each component separately. It was shown above the structural and compositional characterization of the applied LDHs, and the structural, compositional, textural, and thermal characterization of pristine PEBA and PEBA composite membranes. Next it will be shown the *in vitro* drug performance and *in vitro* biological response of the multifunctional dressings.

7.3.2. *In vitro* NAP release profile and kinetics

Figure 7.10A presents the profiles of NAP released from the PEBA_Mg-NAP, PEBA_Zn-NAP, and PEBA_NaNAP samples in saline solution. After 10 hours, 47 and 16 % of NAP were released from PEBA_Mg-NAP and PEBA_Zn-NAP samples, respectively. PEBA_NaNAP sample shows an intermediate behavior in which 29 % of NAP was released after 10 h. The release of leached metals after the end of the tests (10 h) was observed: the amount of Mg and Zn were 2.2 and 0.9 mg L^{-1}, corresponding to 12.2 and 2.0 % of the metal content in the membranes, respectively. The amount of trivalent cations was below the limit of detection.

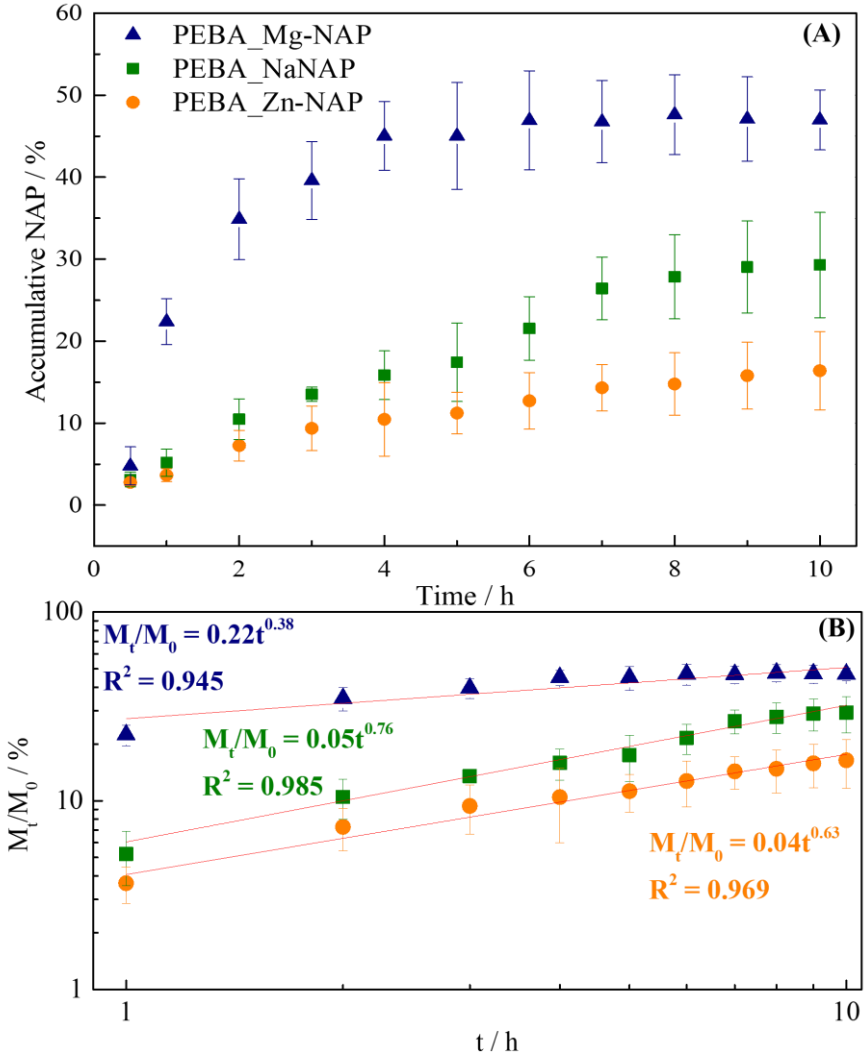

Figure 7.10. (A) Release profile of PEBA_NaNAP, PEBA_Mg-NAP, and PEBA_Zn-NAP samples and (B) application of Power Law model of Naproxen release percentage as a function of time for the different composites in log-log scale.

Power law kinetic model was also applied here and model's equation is refreshed in **Equation 7.1**, where M_t is equal to the released drug at a certain time (t) and M_o the total loaded drug. **Figure 7.10B** shows the plot of Power Law kinetic model that resulted in a satisfactory linear correlation (R^2 values close to 1) for all samples. The lower n value obtained for the PEBA_Mg-NAP sample indicates a Fickian type release in which drug release is governed by diffusion, event more notable than polymeric chain relaxation. For the PEBA_Zn-NAP and PEBA_NaNAP samples, $0.5 < n < 1.0$ and the drug release is characterized by a non-Fickian or anomalous transport, and both solvent diffusion and polymeric chain relaxations are relevant events.

$$M_t / M_o = kt^n, \quad (7.1)$$

7.3.3. *In vitro* biocompatibility evaluations: MTT assay

Cell viability percentages for PEBA membranes and powdered samples on NHDF cells are shown in **Figure 7.11**. LDHs and their composites containing Mg^{2+} presented higher cellular viability percentages compared to the materials composed by Zn^{2+}, whose tendency is supported by previous works[202,293]. For powdered LDHs, cell viability was also higher when intercalated with Cl^- anions. The relation among LDH particle sizes and composition with cell viability can be seen in **Figure 12**.

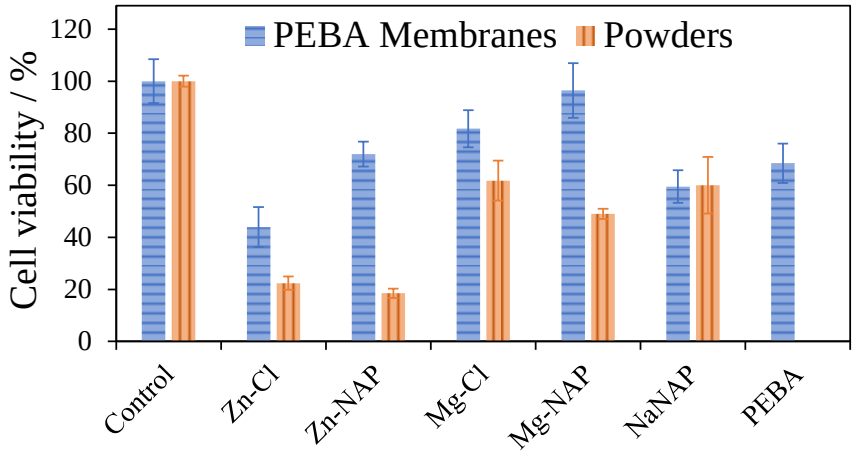

Figure 7.11. MTT test for NHDF cells in contact with pristine PEBA and PEBA composite membranes containing Zn-Cl, Zn-NAP, Mg-Cl, Mg-NAP, or NaNAP particles (in blue – horizontal lines) and powdered samples of Zn-Cl, Zn-NAP, Mg-Cl, Mg-NAP, and NaNAP (in orange – vertical lines) for 3 h. Error bars represent standard error (n = 6).

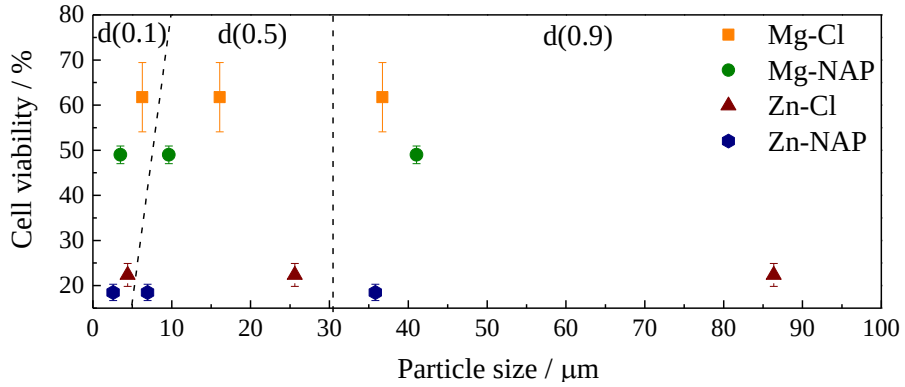

Figure 7.12. Cell viability percentage of LDHs powder samples (from **Figure 7.11**) according to particles size expressed by d(0.1), d(0.5), and d(0.9) values (from **Figure 7.4**), related to the percentage of particles that present up to the corresponding sizes.

All LDH-PEBA membranes presented higher cellular viability compared to the respective powdered LDHs samples. The viability of PEBA_NaNAP membrane and powder NaNAP are comparable. PEBA_Zn-NAP, PEBA_Mg-Cl, and PEBA_Mg-NAP samples display an improved biological response in comparison to pristine PEBA, even more pronounced for hybrid LDHs, which can be related to the favored particles dispersion into PEBA when NAP is intercalated, as earlier discussed. Once more, PEBA_Mg-NAP sample stands out exhibiting the higher viability percentage among all samples (96 %). NAP intercalated into the Mg-LDH dispersed in the polymeric decreased the cytotoxicity of the drug in comparison with NaNAP powder and to the PEBA_NaNAP composite. Moreover, a synergistic effect was observed, since PEBA_Mg-NAP biocompatibility was higher than the ones observed for pristine PEBA, NaNAP salt, or Mg-NAP LDH.

7.4. Discussion

Hybrid organic-inorganic LDHs experienced an improved interaction with PEBA. Such improvement was reflected on membranes thicknesses, lower for the PEBA_Mg-NAP and PEBA_Zn-NAP compared to the Mg-Cl and Zn-Cl samples. The gain in particles-polymer chains interaction compared to the LDH-Cl materials is in consonance with the superficial morphology analyzed by SEM. Although surface fill failures are observed for the PEBA_Zn-NAP sample, LDH particles aggregation are not visualized, differently from the PEBA_Mg-Cl and PEBA_Zn-Cl membranes. As normally observed[115,242], Zn^{2+} cations conferred a higher structural organization to the LDH

structure, which possibly contributed to the visualization of the characteristic plate-like morphology of Zn-Cl particles in the SEM image of the PEBA_Zn-Cl membrane. The smoothness of the PEBA_Mg-NAP sample is compared to that of pristine PEBA. Lower average particles size, verified for NAP-LDHs, resulted in a better particle distribution. However, the lower polydispersity of the Mg-LDH helps to explain its unpaired performance. Though Zn-NAP LDH presents a higher structural organization than the Mg-NAP LDH, verified by XRD, the absence of peaks related to LDH phase could also indicate a more effective dispersion of particles in the PEBA_Mg-NAP membrane, which is consonant with its improved homogeneity and surface smoothness verified by SEM. The superior Mg-NAP interaction with PEBA is once again reinforced by the greater mechanical performance of the PEBA_Mg-NAP membrane. This inference is also supported by the opposite behavior of the PEBA_Zn-Cl sample that experienced an inferior mechanical performance and showed an elevated Zn-Cl particles aggregation, verified by optical microscopy and SEM, and suggested by XRD data. Independently of the homogeneity of particles distribution into PEBA or particles nature, LDH or NaNAP salt, the very close T_g values show that particles didn't cause a disorder in the polymer chains, frequently observed for polymer composites by the decrease in T_g values in relation to pristine polymer[285].

Concerning the *in vitro* NAP release profiles, NAP release rate could be modulated by changing the nature of the divalent cation in the LDH composition. Retarded NAP release from $Zn_2Fe_{0.5}Al_{0.5}$-NAP LDH in comparison to the $Mg_2Fe_{0.5}Al_{0.5}$-3NAP_H, same compositions applied in this thesis, was also observed in our previous work[115], whose *in vitro* NAP release was performed from tablets and the assay conducted in a dissolution tester in phosphate buffer solution (pH equal to 7.4). In such work, after 10 h, 30 and 59 % of NAP release were observed for Zn-LDH and Mg-LDH, respectively. Differently from the results shown herein, NaNAP dissolution lasted for only 30 min. Therefore, PEBA can be a good support for NaNAP particles to sustain drug release. As discussed earlier, PEBA_Mg-NAP sample characterization indicates a more homogeneous distribution of particles in the polymeric matrix. Therefore, related to the other samples, it is expected an improvement in the contact area of the particles with the release medium, which can explain its higher k value. On the other hand, higher Zn-NAP and NaNAP particles

aggregation lead to small k values. As observed in another works [115,242], the lower amount of released M^{3+} (Fe^{3+} or Al^{+3}) cations is out of the limit of detection from the same quantitative method. The higher solubility of Mg^{2+} in comparison with Zn^{2+} are directly related to the solubility product (Kps) values of the isolated hydroxides, as follows: $Mg(OH)_2 > Zn(OH)_2 > Al(OH)_3 > Fe(OH)_3$[294].

For both powdered LDHs and LDHs membranes, cell viability was higher in the presence of LDH intercalated with Cl^- anions. Despite the nature of the intercalated anion, in the case of suspensions, toxicity has shown a dependence on surface area. Small particle sizes with high superficial areas tend to overload cells [202]**.** In fact, LDHs intercalated with NAP presented lower average particle sizes and lower cell viabilities. Several papers report the biocompatibility of LDHs by MTT method. Some of these papers are briefly discussed hereafter. Kura *et al.*[295] analyzed the cytotoxicity of the Zn/Al-NO_3 LDH and the same layer composition intercalated with levodopa, an anti-Parkinsonian compound. Concentrations of levodopa, pristine, and hybrid-LDH equal to 5, 10 50, 100 and 150 μg mL^{-1} were applied to mouse embryonic fibroblasts (3T3 cells). Cell viability decreased progressively with the increase in levodopa and LDH materials concentration. Although the hybrid LDH has reached the highest cell viability percentage for the higher tested concentration compared to non-loaded levodopa and the pristine LDH, the value was reduced for about 40 % compared to the lower applied concentration. Saifullah *et al.*[296] studied the biocompatibility of the Mg/Al-NO_3 LDH and the corresponding LDH intercalated with izoniazid, a drug used for the treatment of tuberculosis, in contact with normal human lung fibroblast and 3T3 cells. Increasing materials concentration from 0.781 to 50 μg mL^{-1}, it is noted a reduction of about 20 % in cells viability of both materials. Mohsin *et al.*[297] evaluated the cytotoxicity of the Zn/Al LDH intercalated with NO_3^- anions and with a mixture of two ultraviolet-ray absorbers benzophenone 4 and Eusolex®232, applying dermal fibroblast cells. Pristine and hybrid LDHs do not presented significant toxicity up to 25 μg mL^{-1}, however, cell viabilities decreased for about 50 % by doubling materials concentration. Pagano *et al.* [293] studied the intercalation of folate into Zn/Al and Mg/Al LDHs aiming topical applications for treatment of aged and photo-damaged skin. Cytotoxicity essays were carried on human keratinocytes and human primary dermal fibroblasts. Zn-LDH was

more toxic than Mg-LDH, as observed in this work. For the Mg-LDH, cell viability percentage varied from about 60 % to 30 % by increasing materials concentration (related to the content of loaded folate) from 215 to 1529 μg mL^{-1}. Moreover, at the tested condition, intercalation into LDH didn't show an advantage concerning the cytotoxicity, once cells treated with folic acid presented cells viability of about 80 % or more for all concentrations and, once again, such results are in agreement with the ones presented here. NAP concentration applied in this thesis for verification of the *in vitro* cytotoxicity when present in the NaNAP salt, loaded on LDHs or in the respective PEBA composites is around 1000 μg mL^{-1} and cell viability was below 70 % for samples in powder. The statement of the biocompatibility depends on the material's concentration and, as discussed above, the biocompatibility of LDHs is restricted to concentrations in the order of tenths or hundredths μg mL^{-1}. As shown in this thesis, this limitation can be overcome by embedding LDHs particles in a polymeric matrix, reducing the dependence of particles size and concentration in the materials cytotoxicity.

PEBA_Mg-NAP membrane presented a sufficient or greater performance in all aspects evaluated in here. As proposed, a multifunctional membrane was designed based on a polymeric support whose mechanical performance was improved, containing LDHs particles aiming adequate LDHs compositions for biological application (containing a larger content of essential metals in the compositions). The engendered material was able to sustain the release of a bioactive organic species and also Mg^{2+} cations as well as a great *in vitro* biocompatibility. This study is expected to advance the application of iron-based LDHs and PEBA composites in general devices to support tissues regeneration.

7.5. Conclusions

The intercalation of NAP into LDH improved the polymer-LDH interaction, considerably enhancing the mechanical performance of PEBA. Drug release could be modulated and sustained for at least 8 hours by all formulations. A slower, an intermediate, and a faster NAP release was achieved from the PEBA_Zn-NAP, PEBA_NaNAP, and PEBA_Mg-NAP samples, respectively. Developed PEBA_Mg-NAP composite was considered the ideal among the tested formulations to act as therapeutic

dressing, once it was able to sustain drug release, originated PEBA composites with greater mechanical resistance, and improved the biocompatibility of PEBA, NAP, and LDH.

7.6. Acknowledgments

We are thankful to Professors Fernanda Ferraz Camilo and Marcos Bizeto for providing PEBAX®2533. Professor César Viseras is acknowledged for the supervision and data validation, and Ana Borrego-Sánchez and Fátima García-Villén by technical supports, investigation, and data revision. We are grateful to the *Laboratório de Espectroscopia Molecular Hans Stammreich* (*Instituto de Química* – USP) for the FT-IR spectra recording, the *Laboratório de Interações entre Macromoléculas e Superfícies* (*Instituto de Química* – USP) for the contact angle measurements and the *Laboratório de Cristalografia of the Instituto de Física* of the *Universidade de São Paulo* for the XRD recording. The graphical abstract includes images obtained from https://smart.servier.com/ under Creative Commons attribution unported (CC BY 3.0).

Chapter 8: Development of an innovative membrane containing layered double hydroxide particles intercalated with natural abietate-type diterpenoid aiming wound dressing

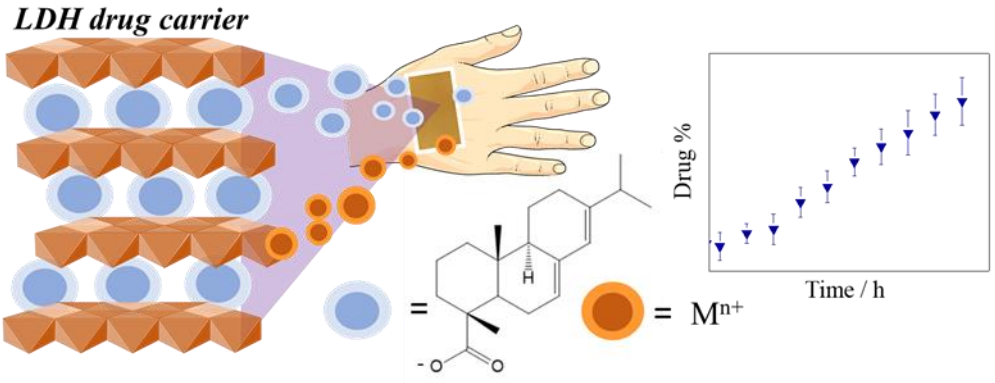

8. Abstract and data presentation

8.1. Abstract

This chapter presents the development of an innovative wound dressing with potential to assist tissues regeneration process. The dressing consists of a composite based on the high-performance PEBAX®2533 (PEBA) block copolymer and particles of iron-based layered double hydroxide (LDH) drug carrier ($Mg_2Fe_{0.5}Al_{0.5}$ layer composition) intercalated with abietate anions (ABI) (abbreviated by LDH-ABI). The PEBA_LDH-ABI composite membrane was prepared by simple casting method. To evaluate the effect of LDH in the formulations, the sodium abietate (NaABI) salt and the PEBA_NaABI membrane were also studied. ABI could be successfully intercalated into LDH, with ABI representing around 38 % of the hybrid weight. Vibrational FT-IR and Raman analyses indicated the intercalation of the deprotonate ABI species and the structure preservation after the LDH synthesis process. *In vitro* release assays performed on powdered samples and membranes showed that, after 10 hours, around 5 and 3 % of the ABI content were dissolved and release from the powdered NaABI and LDH-ABI samples, respectively. On the other hand, the dispersion of NaABI or LDH particles into the polymer propitiated a sustained and approximately constant ABI release, improved to 20 and 22 %, respectively. The improvement in ABI release profile from the membranes could be related to the decrease in particles aggregation and improved media permeation. Although both membranes presented a similar ABI release profile, PEBA_LDH-ABI showed promising to compose wound dressings, additionally providing bioactive Mg^{2+} cations to the media and improving the mechanical resistance of the membrane, *c.a.* doubling the vertical tension resistance and increasing the strain by 1.3 in comparison to the PEBA_NaABI membrane.

8.2. Materials and methods

8.2.1. Reagents

Magnesium chloride hexahydrate ($MgCl_2{\cdot}6H_2O$, purity ≥ 99 %), aluminum chloride hexahydrate ($AlCl_3{\cdot}6H_2O$, 99 %), zinc chloride ($ZnCl_2$, ≥ 98 %), ferric chloride hexahydrate ($FeCl_3{\cdot}6H_2O$) (≥ 98 %), sodium hydroxide (NaOH) (≥ 98 %), abietic acid

(HABI) ($C_{20}H_{30}O_{23}$) (≥ 75 %), and absolute ethanol (≥ 99.8 %) were purchased from Sigma-Aldrich. PEBAX®2533 (PEBA), obtained from Arkema group, is composed by 80 % of poly(tetramethylene oxide) and 20 % of polyamide 12. Isopropanol PA was purchased from Synth and sodium chloride (NaCl) (99 %) from *iqa analítica*. All products were used as received.

8.2.2. NaABI salt preparation

Sodium abietate (NaABI) salt was prepared from HABI as described in **Chapter 5**.

8.2.3. Synthesis of the $Mg_2Fe_{0.5}Al_{0.5}$-ABI LDH

The LDH with layer composition $Mg_2Fe_{0.5}Al_{0.5}$ intercalated with ABI anions (abbreviated as LDH-ABI) was prepared as reported in **Chapter 5**. The drying condition was the same as reported in **Chapters 6** and **7**.

8.2.4. Preparation of PEBA membranes

PEBA membranes containing NaABI or $Mg_2Fe_{0.5}Al_{0.5}$-ABI particles, abbreviated by PEBA_NaABI and PEBA_LDH -ABI, respectively, were prepared by casting method, as the membranes presented in **Chapter 7**, containing 11 wt% of LDH or 4.5 wt% of NaABI, thus with both membranes carrying an equivalent amount of ABI anions.

8.2.5. ABI calibration curve

Three stock solutions were prepared by adding 100 µL of absolute ethanol into around 4 mg of NaABI in an Eppendorf® tube followed by manually homogenization. After, it was added 400 µL of saline solution (0.9 % w/w NaCl) and the tube was manually homogenized resulting in a translucid solution. Then, this solution was transferred to a 100 mL volumetric flask and its volume was completed with saline solution resulting in around 40 ppm solution. Calibration curve was built through UV-Vis spectrophotometry measurements in triplicate into the 0.2 – 0.8 range.

8.2.6. NaABI solubility in the dissolution media

NaABI solubility in the dissolution media was determined to adequately set the ABI release experiment avoiding solution saturation and NaABI precipitation. The assay was performed in sextuplicate. Around 11 mg of NaABI, accurately weighed, was added into a Medicall International Ltd dialysis membrane (size 10, 1 ¼", 31.7 mm and 12 – 14000 Daltons range). Dialysis membranes were accommodated into 50 mL Falcon tubes and filled with 40 mL of saline solution. Tubes were sealed and accommodated into a water batch at 32 °C and shaking speed of 130 strokes per minute. After specific periods of time, three tubes were removed from the batch, ABI concentration was measured by UV-Vis spectrophotometry and NaABI dissolution percentage was calculated. The assay was conducted until reaching the equilibrium (confirmed by the curve plateau).

8.2.7. In vitro ABI release assays

ABI release assay was performed in sextuplicate applying Franz cell using saline solution as dissolution media. PEBA membranes had 2 cm diameter and around 3.9 mg of NaABI or 9.3 mg of $Mg_2Fe_{0.5}Al_{0.5}$-ABI particles. Considering an ideal thus perfectly homogeneous distribution of particles in the membranes, the total amount of NaABI and $Mg_2Fe_{0.5}Al_{0.5}$-ABI in contact with the dissolution media was considered the content in the area of the orifice of the Franz cell, equal to around to 0.37 and 0.89 mg, respectively. To evaluate the effect of dispersed NaABI or LDH particles into the polymer in the ABI release profile, the release experiment with the powdered samples was also performed as follows. Around 1.5 mg or 5 mg of NaABI or $Mg_2Fe_{0.5}Al_{0.5}$-ABI powered samples, respectively, were sandwiched between MF-MilliporeTM 0.45 µm (HAPO2500) support membranes. The release media was magnetically stirred and ABI amount was spectrophotometrically quantified. After the measurement of the first released ABI aliquot, accumulative ABI weight released was corrected by the same equation applied in **Chapter 7**, refreshed in **Equation 8.1**, where m^{ABI}_i is the ABI weight released in a time i, C_i is the ABI concentration (mg L^{-1}) in time i, considering the removed aliquots (0.8 mL) for measurement in anterior times k and then replaced by the same volume of saline solution to maintain the volume of the flasks equal to 6.4 mL.

$$m^{ABI}{}_i = 0.0064C_i + 0.0008\sum_{k=1}^{k=i-1} C_k \quad (8.1)$$

8.2.8. Materials Characterization

High performance Liquid Chromatograph analysis of HABI was performed at the *Central Analítica of the Instituto de Química* (*Universidade de São Paulo* - USP) and carried on a Shimadzu equipment with a CBM-20A controller, LC-20AD pumps, SPD-20A detector, CTO-20A heater and a SIL 20 AC autoinjector. It was used a Spelco Ascentis C-18 column (250 x 4.6 mm – 5 μm), at 35°C and a solvents flux of 1.0 mL min-1. Solvent A was composed of water solution containing 0.05 wt% of formic acid. Solvent B was composed of methanol solution containing 0.05 wt% formic acid. It was applied a mixture of solvents A and B at specified times as follows (time – B%): 0 min – 50%, 5 min – 50%, 40 min – 100%, 45 min – 100%, 50 min – 50%.

Mass spectrometry of HABI was performed at the *Central Analítica of the Instituto de Química* (*Universidade de São Pa*ulo - USP) in an Amazon Speed ETD Bruker equipment, with nebulizer at 27 psi, dry gas flux of 12 L min-1, 325°C and 4500 V of voltage.

X-ray diffraction (XRD) patterns were obtained at the *Instituto de Cristalografia* of the *Universidade de São Paulo* on a Rigaku Ultima Plus equipment, with Bragg-Brentan geometry and graphite crystal monochromator, using Cu-Kα radiation (1.5406 Å), 30 kV, 15 mA, Ni filter, scan range 1.5-70°(2θ) and scan step of 0.05°(2θ)/2s.

Inductively coupled plasma atomic emission spectroscopy (ICP-AES) analyses of Mg, Fe and Al for the $Mg_2Fe_{0.5}Al_{0.5}$-ABI sample was performed in Spectro Analytical Instrument at the Central Analítica of the Instituto de Química of USP. Metals quantification from the release media after in vitro ABI release assay was performed in a Perkin-Elmer optima 8300 instrument at the Centro de Instrumentación Científica of the University of UGR.

Elemental analysis of carbon, hydrogen and nitrogen were recorded on an equipment Perkin Elmer - CHN 240. Both analyses were obtained at the Central Analítica of the *Instituto de Química* of USP.

Mass spectrometry coupled to thermogravimetric analyses (TGA–MS) were recorded in a Netzsch thermoanalyzer model TGA/DSC 490 PC Luxx coupled to an Aëolos 403 C mass spectrometer using alumina crucible and heating rate of 10 °C min^{-1} under a synthetic air flow of 50 mL min^{-1}.

Differential scanning calorimetry (DSC) was carried out at the *Central Analítica* of *Instituto de Química* of USP using a TA instruments – Q10 equipment under 50 mL min^{-1} N_2 flow, a heating/cooling rate of (±) 10 °C/min, using alumina hermetic and close crucible. Samples were first equilibrated at -70 °C and then submitted to a heating cycle until 100 °C (to erase information coming from the preparation procedure), a cooling cycle until -70 °C and a second heating cycle until 100 °C.

FT-IR spectra of powdered samples were recorded in the 4000–400 cm^{-1} range on a Bruker spectrophotometer, model alpha by attenuation total reflectance (ATR) mode, with acquisition step of 4 cm^{-1} and 512 scans.

FT-Raman spectra (Raman) were recorded in a FT-Raman Bruker FRS-100/S spectrometer using 1064 nm exciting radiation (Nd:YAG laser Coherent Compass 1064-500 N), a Ge detector, laser power of 100 mW, acquisition step of 4 cm^{-1} and 2048 scans.

Average particles size measurements were performed in 2-propanol through low angle laser light scattering in a Mastersize 200 Malvern equipment.

Images by optic microscopy were registered in an Optic microscope Oleman DN-107T.

Images from scanning electron microscopy (SEM) were obtained in a Phenom™ G2 pro desktop Scanning Electron Microscope (voltage 5 kV; High-sensitivity backscattered electron detector). The samples were deposited on a double-sided carbon tab.

Membranes thicknesses was determined using a Mitutoyo analogical micrometre. Five measurements in different points were performed in 2 cm diameter circular membranes.

Dynamo-mechanical analysis (DMA) tests were performed at the *Central Analítica* of *Instituto de Química* of USP on a DMA Q800 TA instruments equipment. Each PEBA

membrane was cut into 5 rectangles with 3 x 0.5 cm and the analysis were performed at 70 °C.

Static water contact angle measurements were performed in triplicate with static deionized water drop on the membranes using a SEO portable equipment.

Absorbance in the ultraviolet–visible region was measured on a spectrophotometer Perkin Elmer Lambda 35.

Memmert water bath (WNB 22) was used to provide agitation and to provide a constant temperature for the test of the chemical stability of NaABI in the dissolution media, for the NaABI solubility assay and for the ABI release from the Mg-ABI and Zn-ABI samples.

Perme Gear Franz cell of 6.4 mL capacity and orifice area equal to 0.64 cm^2 coupled to a Bunsen immersion thermostat were applied for the ABI dissolution test from LDH powdered samples and membrane LDH composites.

8.3. Results and Discussions

8.3.1. NaABI solubility in the dissolution media

Figure G.1 (**Appendix G**) shows an example of full-scan electronic spectra of ABI in physiological solution (NaCl 0.9 wt %) obtained from a 13.33 ppm NaABI solution. The band of maximum absorbance was verified at 243 nm. **Figure G.2** (**Appendix G**) presents the calibration curve for ABI obtained at 243 nm. A great linearity was obtained, with R^2 = 0.994. The equation of the linear regression curve (y = 0.045x-0.080) was applied for ABI concentration calculation from absorbance measurements.

Results from NaABI solubility study are shown in **Figure 8.1**. After 2.5 h, NaABI dissolution curve reached a plateau, due to the saturation of the solution, in a dissolved ABI concentration of approximately 2.3×10^{-4} mol L^{-1} (68.5 mg L^{-1}), at 32 °C. As a comparison, abietic acid presents a solubility in water equal to 1.4×10^{-5} mol L^{-1} (at 20 °C). Estimation of NaABI solubility in saline solution is important to preclude its precipitation in the conditions in which the *in vitro* ABI release assays were conducted.

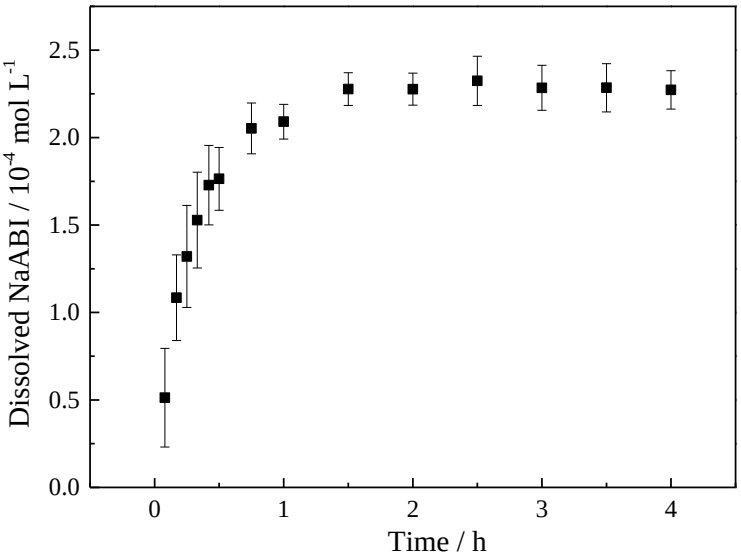

Figure 8.1. NaABI dissolution along time in saline solution (0.9 % w/w) at 32 °C (n=6).

8.3.2. Materials Characterization

8.3.2.1. NaABI salt and LDH-ABI samples

Appendix G presents the characterization of the NaABI and LDH-ABI sample. No discrepancies are observed comparing these results with those related to the first batch of NaABI and $Mg_2Fe_{0.5}Al_{0.5}$-ABI materials presented in **Chapter 5**.

8.3.2.2. Membrane's characterization

XRD patterns of PEBA_NaABI and PEBA_$Mg_2Fe_{0.5}Al_{0.5}$-ABI samples (**Figure 8.2**) show the profile observed for PEBA: a semi-crystalline structure presenting a high intense and broad peak at 20 ° (2θ)[283,298] and to the XRD pattern of poly(amide 12) [284]. The absence of peaks related to the crystalline LDH phase may indicate a satisfactory dispersion of the particles into polymer chains.[298]

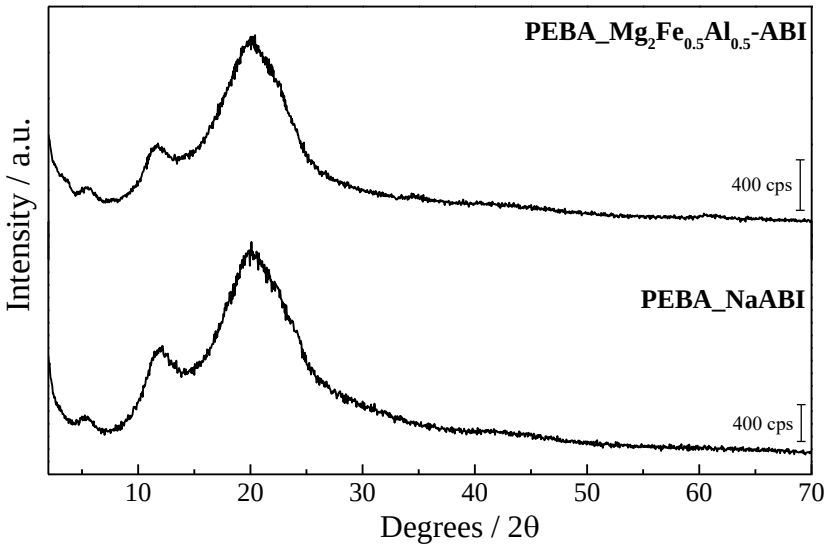

Figure 8.2. XRD patterns of the PEBA-NaABI and PEBA_$Mg_2Fe_{0.5}Al_{0.5}$-ABI membranes.

Figure 8.3 presents surface aspects of the membranes in different scales: (**A**) macroscopic images, (**B**) optical microscopy images, and (**C**) SEM micrographs. **Figure 8.3A** shows that PEBA_NaABI membrane is slightly opaque and PEBA_$Mg_2Fe_{0.5}Al_{0.5}$-ABI membrane is completely covered by the orange brown LDH particles, homogeneously distributed by visual inspection. **Figure 8.3B,** for the PEBA_NaABI sample, shows wrinkles due to Teflon-plate's surface. $Mg_2Fe_{0.5}Al_{0.5}$-ABI particles could fill relatively well the membrane surface, although some darker regions indicate points of particles concentration. In **Figure 8.3C**, PEBA_NaABI membrane presents points of salt concentration. While for the PEBA_ $Mg_2Fe_{0.5}Al_{0.5}$-ABI sample, a rough morphology is observed with aggregates of LDH particles.

Figure 8.3D shows representative images of water drops on the surface of the membranes for determination of static water contact angles (SWCA). Static water contact angle for the PEBA_$Mg_2Fe_{0.5}Al_{0.5}$-ABI membrane is equal to 81 ± 2°, the same value reported by Vatani *et al.*[299] and close to the value reported in **Chapter 7** (**Table 7.3**) for PEBAX®2533 membranes prepared by casting method. PEBA_NaABI membrane presented a lower SWCA value (62 ± 3 °); an expected behavior due to the presence of particles of a salt.

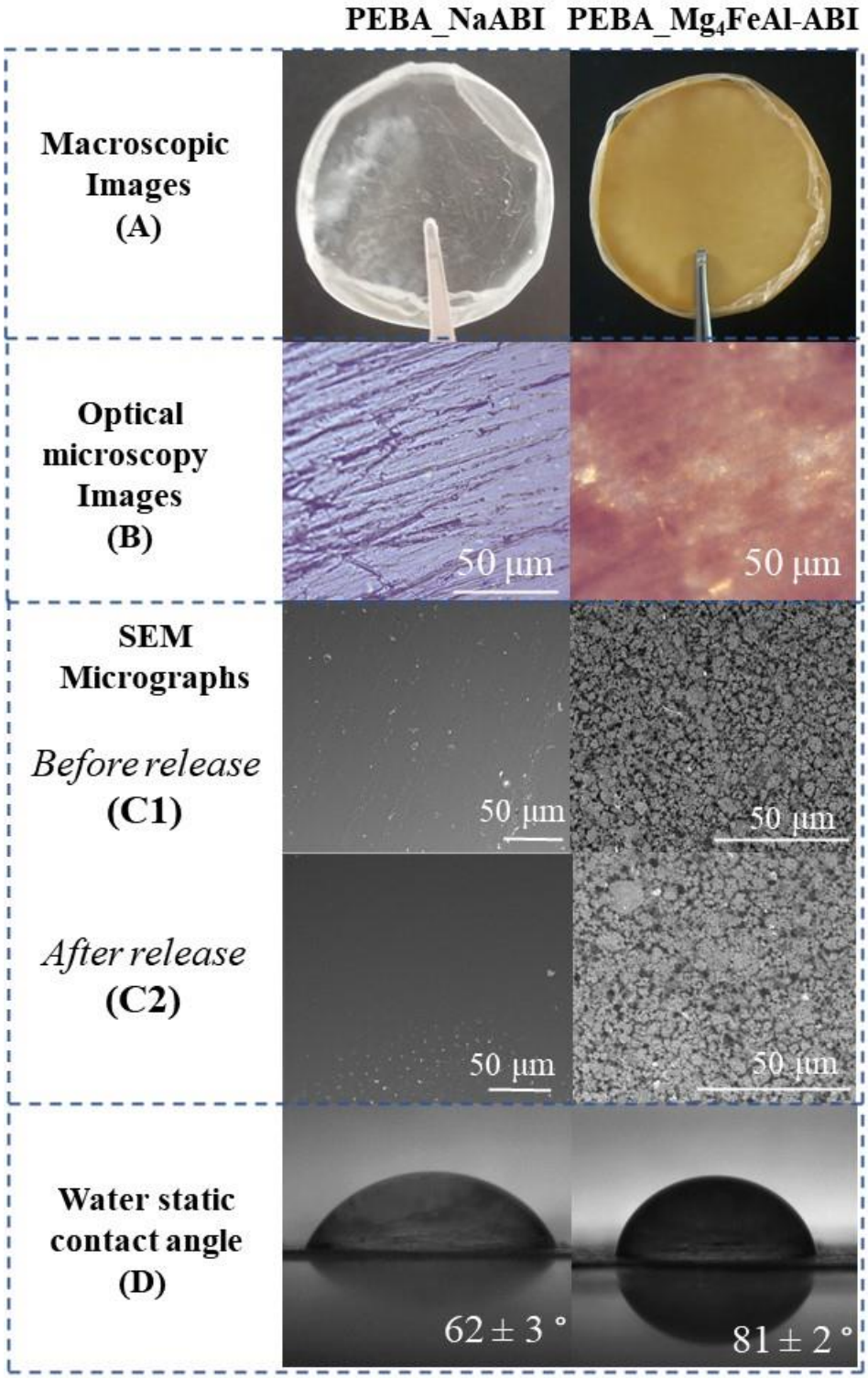

Figure 8.3. Visual aspect (A), optical microscopy images (B), SEM micrographs (C1 and C2), a representation of the static water contact angle (D) of the PEBA_NaABI and PEBA_$Mg_2Fe_{0.5}Al_{0.5}$-ABI membranes.

As can be seen in **Table 8.1**, the thickness values of the membranes are close: 85 ± 4 and 88 ± 3 µm for the PEBA_NaABI and PEBA_$Mg_2Fe_{0.5}Al_{0.5}$-ABI samples, respectively. Stress at break, strain at break, and Young modulus of membranes submitted to tensile

tests are also shown in **Table 8.1**. The presence of NaABI particles decreased the stress at break, although the elongation has increased, in comparison with pristine PEBA (stress at break equal to 479 ± 27 kPa and elongation equal to 22 ± 7 %) (see **Chapter 7**, **Table 7.3**), having a Young modulus equal to 3.9 ± 0.8 MPa. On the other hand, $Mg_2Fe_{0.5}Al_{0.5}$-ABI particles improved the mechanical resistance of the PEBA membrane, resulting in a stress at break of 790 ± 118 kPa and elongation of 81 ± 2 %, and a Young modulus equal to 6.6 ± 0.9 MPa.

Table 8.1. For PEBA composites: Thickness, stress and strain at break, and Young modulus; peak glass transition ($T_{g\ PE}$), crystallization ($T_{C\ PE}$) and melting ($T_{m\ PE}$) temperature values (obtained from DSC analyses).

Sample	Thickness (µm)	Stress at break (kPa)	Strain at break (%)	Young modulus (MPa)	$T_{g\ PE}$ (°C)	$T_{c\ PE}$ (°C)	$T_{m\ PE}$ (°C)
PEBA_NaABI	84.5 ± 4.4	415 ± 23	16.9 ± 2.7	3.53 ± 0.15	-59	-15	19
PEBA_$Mg_2Fe_{0.5}Al_{0.5}$-ABI	88.0 ± 3.0	767 ± 32	32.1 ± 1.8	6.24 ± 0.47	-59	-15	19

Tg PE – glass transition temperature of PE portion, Tc PE – crystallization temperature of PE portion, and Tm PE– melting temperature of PE portion.

Figure 8.4 shows the cooling (top) and second heating (bottom) DSC scans for PEBA_NaABI and PEBA_$Mg_2Fe_{0.5}Al_{0.5}$-ABI membranes, whose temperature values related to the thermal events are gathered in **Table 8.1**. The temperatures of glass-transition for PE portion ($T_{g\ PE}$) (-59 °C), crystallization peak temperature ($T_{c\ PE}$) values of PE portion (-15 °C), and melting peak temperatures ($T_{m\ PE}$) (19 °C) were equal for both samples. The presence of NaABI or LDH particles have not caused a disorder in the polymer chains, frequently observed for polymer composites by the decrease in T_g values in relation to pristine polymer.[190] Upper temperature for DSC analysis was carefully limited to ensure that no particles degradation would take place.

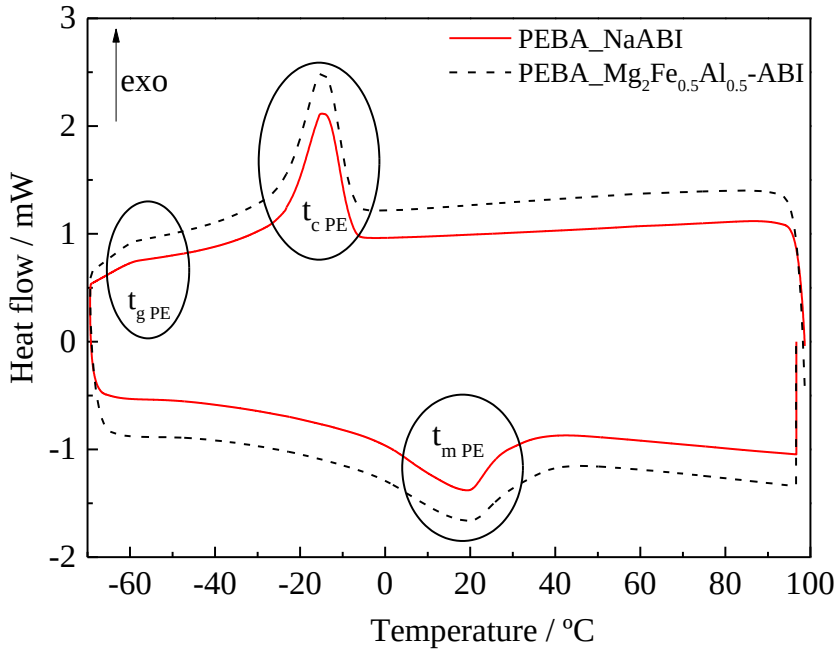

Figure 8.4. Cooling (top) and second heating (bottom) DSC scans for PEBA_NaABI and PEBA_Mg-ABI membranes. $T_{g\,PE}$ – glass transition temperature of PE portion, $T_{c\,PE}$ – crystallization temperature of PE portion, $T_{m\,PE}$– melting temperature of PE portion.

Figure 8.5 presents the profiles of ABI dissolution from the NaABI salt and release from the $Mg_2Fe_{0.5}Al_{0.5}$-ABI, PEBA_NaABI, and PEBA_ $Mg_2Fe_{0.5}Al_{0.5}$-ABI samples in saline solution at 32 °C. For the calculation of released ABI percentage from the polymeric composites, it was considered the amount of ABI in the membrane's area in contact with the solution in the Franz's cell, assuming a homogeneous distribution of particles. ABI release from powdered samples was much slower in comparison with the PEBA composites. After 10 hours, around 3, 5, 20, and 22 % of ABI were released (or dissolved) from $Mg_2Fe_{0.5}Al_{0.5}$-ABI, NaABI, PEBA_$Mg_2Fe_{0.5}Al_{0.5}$-ABI, and PEBA_NaABI samples, respectively. For both types of samples, powdered or membranes, the intercalation into LDH slightly retarded ABI release.

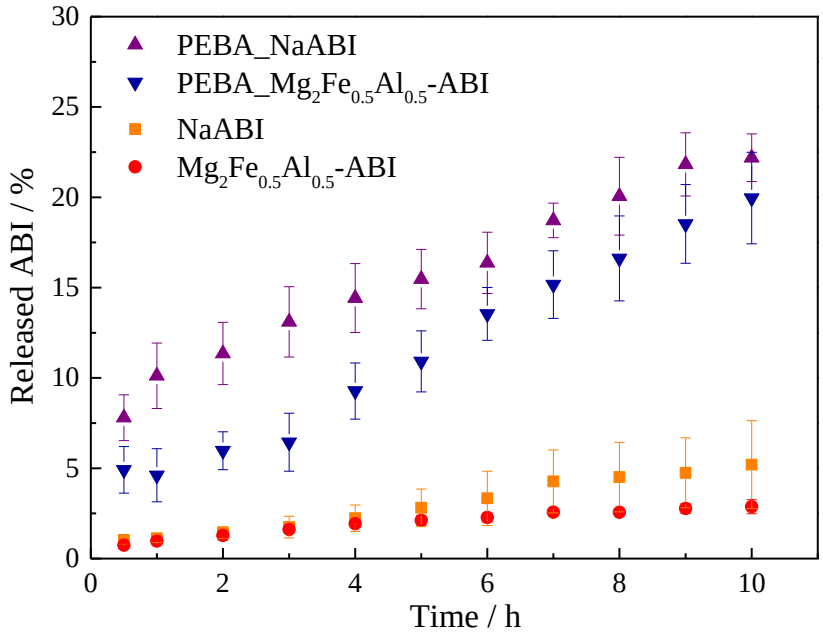

Figure 8.5. Release (or dissolution) profile of NaABI, $Mg_2Fe_{0.5}Al_{0.5}$-ABI, PEBA_NaABI, and PEBA_$Mg_2Fe_{0.5}Al_{0.5}$-ABI samples. Saline solution at 32 °C.

Figure 8.6A shows the SEM images of the $Mg_2Fe_{0.5}Al_{0.5}$-ABI LDH that displays a high level of particles aggregation, whose distribution fitted by a Lorentzian curve presents mode equal to 7.377 µm. As shown in **Figure 8.6B,** compared to the powdered samples, particles size distribution for the PEBA_LDH-ABI sample is shifted towards lower values and the mode is equal 2.634 µm. Thus, LDH-ABI can consist of polycrystalline secondary particles that disaggregate into smaller particles during the preparation of the membranes. The dispersion of LDH into PEBA improved particles surface area and the release media permeation. The higher dissolution rate observed for the NaABI and PEBA_NaABI samples can be related to the lower hydrophobicity of the salt compared to ABI intercalated into LDH (**Figure 8.3D**).

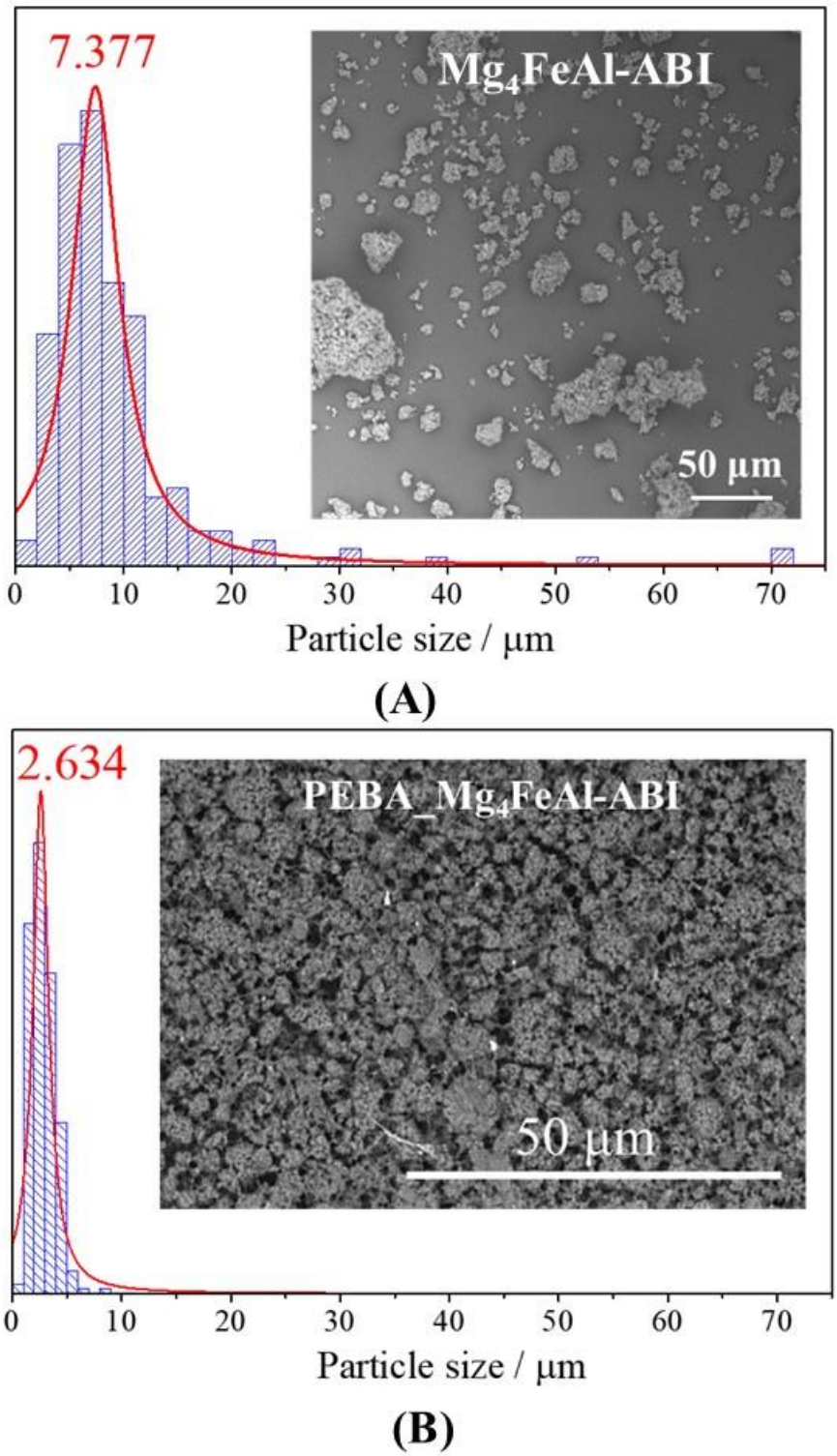

Figure 8.6. Particle**s** size estimation from SEM images for the $Mg_2Fe_{0.5}Al_{0.5}$-ABI powdered (A) and PEBA_ $Mg_2Fe_{0.5}Al_{0.5}$-ABI (B) samples.

After ABI release experiment, membranes were dried in desiccator and reanalysed by SEM. No previous washing process was employed to do not affect their appearance just after the end of the assay. Comparing **Figures 8.3C1** (before release) and **8.3C2** (after release), no signal of polymer degradation or LDH particles detachment are verified. However, after release the surface of the PEBA_NaABI membrane is smoother due to NaABI particles dissolution, indicating a poor interaction between the NaABI and the polymer; small and white particles present can be related to precipitated NaCl from saline solution, since membranes were not washed.

Metals were quantified from the release media after the end of the assay for the PEBA_LDH-ABI sample. After 10 h, Mg^{2+} concentration was equal to 2.5 mg/L, corresponding to 16.3 % of the metal content in the LDH. Fe^{3+} or Al^{3+} cations were not detectable. LDH leaching was a little bit higher for the PEBA_LDH-ABI in comparison to the PEBA membranes containing particles of the $Mg_2Fe_{0.5}Al_{0.5}$ LDH intercalated with naproxenate anions (12.2 %) (**Chapter 7**), evaluated in the same conditions (*i.e.* release apparatus, release media, and time).

8.4. Conclusions

In this chapter, a PEBA_LDH-ABI composite was successfully prepared and characterized, and its usefulness as wound dressing demonstrated concerning mechanical and pharmacological points of view. ABI anions were effectively intercalated into LDH by one-pot method and comprising 37.77 % of ABI in the LDH carrier, an appreciable amount considering common drug delivery systems. Both NaABI and LDH-ABI particles were satisfactorily dispersed into PEBA polymer chains originating membranes visually homogeneous and resistant to handling. However, unlike NaABI, LDH-ABI particles improved the mechanical performance of PEBA membrane. The dispersion of NaABI or $Mg_2Fe_{0.5}Al_{0.5}$-ABI particles into PEBA membrane have shown to enhance the hindered ABI release from powdered samples due to the increase in particles' surface area and consequent improvement in release media permeation. The higher dissolution rate observed for NaABI and PEBA_NaABI samples could be related to the lower hydrophobicity of the salt compared to the intercalated ABI. This study

encourages to advance the development of the PEBA_$Mg_2Fe_{0.5}Al_{0.5}$-ABI compositions to act as therapeutic dressings.

8.5. Acknowledgments

We acknowledge Brenda Lini for the great contribution to development of this work. Professor César Viseras is acknowledged by supervision and data validation, and Ana Borrego-Sánchez and Fátima García-Villén by technical supports, investigation, and data revision. We are also thankful to Fernanda F. Camilo and Marcos A. Bizeto for providing PEBAX®2533. We are thankful to the the *Laboratório de Interações entre Macromoléculas e Superfícies* (*Instituto de Química – USP*) for the contact angle measurements and the *Laboratório de Cristalografia* of the *Instituto de Física* of the *Universidade de São Paulo* for the XRD recording. The graphical abstract contains an image obtained from https://smart.servier.com/ under Creative Commons attribution unported (CC BY 3.0).

Chapter 9: Reproducibility of the synthesis of the $M_2Fe_{0.5}Al_{0.5}$-A LDHs (with M = Mg^{2+} or Zn^{2+} and A = Cl^-, NAP, or ABI)

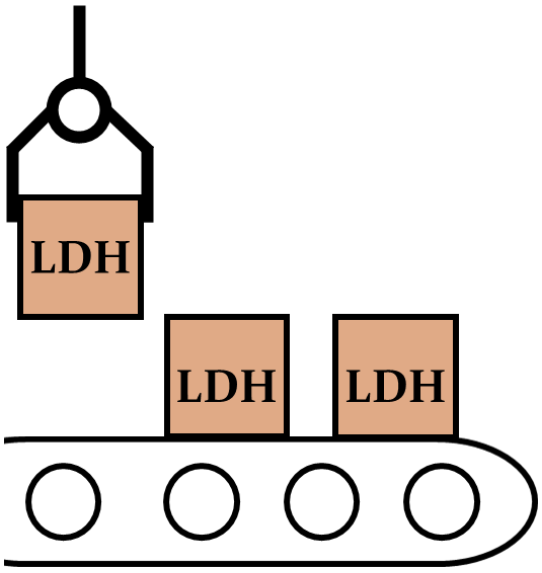

Tables 9.1 compiles average values and related standard deviations (SD) concerning the composition (metals and also carbon for hybrid organic-inorganic phases) of the LDHs presented in this thesis and applied in its second part, including one additional batch prepared for the $Mg_2Fe_{0.5}Al_{0.5}$-ABI composition. Metals and carbon quantifications were performed in the same equipment. Standard deviations concerning the molar ratio between the metals are lower than 2 % of the average values and indicate that shifts in *y* or *x* values from experimental values in comparison to the theoretical ones (see geometrical reasoning approach applied in **Chapters 3** and **4**) attributed to differences between the metallic composition of the bulk samples and the crystalline LDH phase do not come from analytical errors. Deviations on carbon percentage are more pronounced and can be related not only to limitation in the reproducibility of the production of the hybrid organic-inorganic LDHs but also to the way the analysis is performed. While metals are quantified from acidic solution of dissolved or digested LDH samples, carbon percentage is estimated from flash combustion of powdered samples whose molar mass is considerably influenced by the hydration degree of LDH, which in its turn is dependent on storage conditions and the ambient humidity.

Table 9.1. Average molar ratio between the metals and carbon percentage and standard deviation for $M_2Fe_{0.5}Al_{0.5}$-A LDH (with M = Mg^{2+} or Zn^{2+} and A = Cl^-, NAP, or ABI) replicas.

Samples	M^{2+}/Al^{3+} ± SD	M^{2+}/Fe^{3+} ± SD	Fe^{3+}/Al^{3+} ± SD	M^{2+} / (Fe^{3+} + Al^{3+})	% C
$Mg_2Fe_{0.5}Al_{0.5}$-Cl	4.29 ± 0.05	4.060 ± 0.044	1.057 ± 0.006	2.087 ± 0.023	-----
$Zn_2Fe_{0.5}Al_{0.5}$-Cl	3.53 ± 0.07	3.47 ± 0.07	1.010 ± 0.020	1.750 ± 0.035	------
$Mg_2Fe_{0.5}Al_{0.5}$-3NAP_H	4.29 ± 0.08	4.12 ± 0.05	1.040 ± 0.010	2.103 ± 0.035	24 ± 4
$Zn_2Fe_{0.5}Al_{0.5}$-NAP	3.64 ± 0.07	3.53 ± 0.07	1.030 ± 0.021	1.790 ± 0.036	19. 33 ± 0.11
$Mg_2Fe_{0.5}Al_{0.5}$-ABI	4.21 ± 0.03	4.067 ± 0.006	1.037 ± 0.006	2.067 ± 0.006	31.6 ± 1.4

CONCLUSIONS

Concerning the first aim of this thesis, structural and compositional aspects of $M_2Fe_yAl_{(1-y)}(OH)_6$-A LDHs as long as Al^{3+} is substituted by Fe^{3+} cations were lightened from **Chapter 3** to **5**. In general, it was verified that the preparation of pure (or crystallographic pure) Fe^{3+}-LDHs is restricted to *y* value equal to 0.5, for materials intercalated with Cl^- or more complex organic anions. For the $M_2Fe_yAl_{(1-y)}$-Cl compositions addressed in **Chapter 3**, the combination of crystal-chemical reasoning and PDF revealed the presence of amorphous impurities of difficult identification by the most frequent characterization techniques (*e.g.* XRD, vibrational spectroscopies, thermal, and elemental analyses) applied in the literature to attest the precipitation of LDH phase and also for the determination of LDH chemical formula, possibility resulting in mistakes or neglected inconsistencies. From PDF results, amorphous 2-line ferrihydrite was observed for the $Zn_2Fe_yAl_{(1-y)}$-Cl compositions with *y* above 0.5. It was also rationalized why it is difficult to obtain Zn_RFe-Cl LDHs. In general, the incorporation of Fe^{3+} into the LDH structure, since synthesis are normally conducted in aqueous solution, is hindered by its hydrolysis even at low pH values, allowing the precipitation of M^{2+} cations with low solubility product, such as Zn^{2+}, as isolated phases. For the $Mg_2Fe_yAl_{(1-y)}$-Cl series, *y* values above 0.5 also led the formation of amorphous phase(s) (not identified) other than ferrihydrite.

Focussing on the interest in preparing pure LDH phases to act as carriers for organic bioactive species, in **Chapter 4**, the exchange of Cl^- by NAP in the $Mg_2Fe_yAl_{(1-y)}$-Cl LDHs showed to be practically topotatic. NAP could be intercalated in appreciable amounts for the selected $Mg_2Fe_{0.5}Al_{0.5}$ and $Zn_2Al_{0.5}Fe_{0.5}$ layers compositions for application in the second part of the thesis, with NAP corresponding to 30 and 26 % of the weight of the hybrid LDH-NAP materials, respectively. In **Chapter 5**, the intercalation of ABI anions into LDH was reported for the first time. Also, iron-based LDH-ABI phases could be successfully prepared by the coprecipitation (one-pot) method. The characterization of abietic acid, NaABI salt, and LDH-ABI material indicated that ABI is present in its deprotonated form between the LDH layers and kept its structural integrity after intercalations. Although more detailed compositional inferences concerning the LDH-ABI materials were limited, mainly due to their low structural organization, results

indicated that $Mg_2Fe_yAl_{(1-y)}$-ABI LDHs with $y \leq 0.5$ present crystallographic phase purity and were also able to encapsulate a high amount of ABI, representing from around 49 and 40 % (average) of the hybrids samples weight for the Mg_2Al-ABI and $Mg_2Fe_{0.5}Al_{0.5}$-ABI compositions, respectively.

The five intermediate $Mg_2Fe_{0.5}Al_{0.5}$-Cl, $Zn_2Fe_{0.5}Al_{0.5}$-Cl, $Mg_2Fe_{0.5}Al_{0.5}$-3NAP_H, $Zn_2Fe_{0.5}Al_{0.5}$-NAP, and $Mg_2Fe_{0.5}Al_{0.5}$-ABI compositions were chosen to compose the developed polymeric membranes shown in the second part of the thesis (from **Chapter 6** to **8**) due to their high amount of Fe^{3+} together with purity (or crystallographic phase purity) and high amount of intercalated bioactive species. The presence of LDH particles in the polymeric membranes offered physical, pharmaceutical, and biological advantages. As presented in **Chapter 6**, alternating polymer electrospun and LDH electrosprayed layers, innovative architectures were produced allowing the easy and effective drug release modulation by varying just one synthetic parameter: the thickness of the polymer layers. The composition of LDHs (*i.e.* Mg^{2+} or Zn^{2+}) have also shown to influence the drug release kinetics (**Chapter 7**). As shown in **Chapters 7** and **8**, from the physical point of view, LDH particles considerably improved the mechanical performance of the membranes prepared by casting method, mainly when intercalated with organic anions. The dispersion of $Mg_2Fe_{0.5}Al_{0.5}$-ABI particles into PEBAX®2533 membrane (**Chapter 8**) showed to surpass the hindered ABI release from the powdered sample. When dispersed into PEBAX®2533 polymer, a higher amount of drug intercalated into LDH could be support by cells. Also, $Mg_2Fe_{0.5}Al_{0.5}$-3NAP_H LDH showed to improve PEBAX®2533 polymer cytotoxicity and presented a satisfactory cell compatibility (**Chapter 7**).

FUTURE PERSPECTIVES

In a general way, this thesis indicated pure ternary Fe^{3+}-LDH compositions as promising to compose advanced pharmaceutical formulation and presented the methodology for their preparation, as well as strategies for their proper characterization. LDH-polymer composites, promising for application as multifunctional implantable devices or wound dressings, were also developed and tested from different perspectives. Thus, this thesis is intended to inspire the development of new and advanced LDH biomaterials. The establishment that half of the aluminium content in the $M_2Fe_yAl_{(1-y)}$ LDH compositions could be isomorphically substituted by Fe^{3+} cations is intended here to provide not a limiting but a new starting point for researchers working in the field of LDH materials. However, it is clear that the capacity to propose new synthetic routes to reach pure LDHs composed only by Fe^{3+} walks together with a deep structural understanding of the synthesis products, where amorphous phases have to be considered. It is also fundamental to assess thermodynamic and kinetic aspects of the crystallization-dissolution dynamic process occurring during cations precipitation to better set synthesis parameters such as pH, temperature, cations concentration, and synthesis time. How deeper the comprehension of the structure and composition of biomaterials, more paths are open for creating compounds and materials able to interact in an intimist and precise way with the living entities, and more powerful technologies are possible to be created to effectively cure and to provide better life conditions.

Specifically, additional chemical, pharmaceutical, and biological assays on pristine abietate anions and its formulations, as for instance concerning chemical stability, half-life, and bioactivities, are necessary. For powdered LDH-drug and polymer/LDH-drug membranes, *in vivo* drug release and biocompatibility assays are indispensable. Assays concerning the reproducibility of the membranes preparation and scale up processes are also indicated.

Appendix A. Supplementary data related to Chapter 1

Table A.1. Papers about Mg_RFe and Zn_RFe LDHs: LDH composition and molar ratio between the metals, synthetic method applied, synthetic pH, aging conditions, and obtained phase(s).

Expected LDH composition		**Synthetic method**	**Synthetic pH**	**Stirring aging time and temperature (if applied)**	**Obtained phase(s) according to XRD**	**Ref.**
Nominal M^{2+}/M^{3+} molar ratio	**Anion**					
Mg^{2+}/Fe^{3+}= 2	Cl^-	Coprecipitation	10.0	2 h	LDH	[300]
Mg^{2+}/Fe^{3+}= 3						
Mg^{2+}/Fe^{3+}= 4						
Mg^{2+}/Fe^{3+}= 2	NO_3^-					
Mg^{2+}/Fe^{3+}= 3						
Mg^{2+}/Fe^{3+}= 4						
Mg^{2+}/Fe^{3+}= 2	NO_3^-	Coprecipitation	10.0	24 h	LDH	[301]
Mg^{2+}/Fe^{3+}= 3						
Mg^{2+}/Fe^{3+}= 2	HPO_4^{2-} (From pristine LDH-NO_3^-)	Ion-exchange	7.4	24 h	LDH and side phase(s)	
Mg^{2+}/Fe^{3+}= 3	HPO_4^{2-} (From pristine LDH-NO_3^-)					
Mg^{2+}/Fe^{3+}= 2	Cl^-	Coprecipitation	10.0	24 h	LDH	
Mg^{2+}/Fe^{3+}= 3						
Mg^{2+}/Fe^{3+}= 2	HPO_4^{2-} (From pristine LDH-NO_3^-)	Ion-exchange	7.4	24 h	LDH and side phase(s)	
Mg^{2+}/Fe^{3+}= 3	HPO_4^{2-} (From pristine LDH-NO_3^-)					

Mg^{2+}/Fe^{3+}= 4	CO_3^{2-}	Coprecipitation	9.0 – 10.0	65 °C for 18 h	LDH	[78]
Mg^{2+}/Fe^{3+}= 1	CO_3^{2-}	Coprecipitation	10.0	72 h	LDH	[302]
Mg^{2+}/Fe^{3+}= 2						
Mg^{2+}/Fe^{3+}= 3						
Mg^{2+}/Fe^{3+}= 4						
Mg^{2+}/Fe^{3+}= 2	Cl^-	Coprecipitation	13.0	24 h	Side phase(s)	[303]
Mg^{2+}/Fe^{3+}= 2	NO_3^-	Coprecipitation	10.0	120 °C for 24 h	LDH	[304]
Mg^{2+}/Fe^{3+}= 3	CO_3^{2-}	Coprecipitation	8.0 – 10.0	Not applied	Side phase(s)	[305]
Mg^{2+}/Fe^{3+}= 3	CO_3^{2-}	Coprecipitatio (40 °C)	10.0 – 11.0	65 °C for 18 h	LDH	[306]
Mg^{2+}/Fe^{3+}= 3	CO_3^{2-}	Coprecipitation	11.0	65 °C for 48 h	LDH	[307]
Mg^{2+}/Fe^{3+}= 2	CO_3^{2-}	Coprecipitation	10.0	80 °C for 24 h	LDH	[308]
Mg^{2+}/Fe^{3+}= 3						
Mg^{2+}/Fe^{3+}= 2	Cl^-	Coprecipitation	13.0	4 h	LDH and side phase(s)	[309]
Mg^{2+}/Fe^{3+}= 2	Cl^-	Coprecipitation (40 °C)	9.5 – 10.5	85 °C for 18 h	LDH	[310]
Mg^{2+}/Fe^{3+}= 2	NO_3^-					
Mg^{2+}/Fe^{3+}= 2	CO_3^{2-}	Coprecipitation	13.0	Not applied	LDH	[311]
Mg^{2+}/Fe^{3+}= 1.5	Cl^-	Coprecipitation	13.0	24 h	Side phase(s)	[312]
Mg^{2+}/Fe^{3+}= 4	Cl^-	Coprecipitation	9.5	100 °C for 6 h	LDH	[313]
	CO_3^{2-}	Coprecipitation				
	NO_3^-	Coprecipitation				
	SO_4^{2}	Ion-exchange	-----		LDH and side phase(s)	
	$S_2O_3^{2-}$	Ion-exchange	-----		LDH and side phase(s)	
	Tartrate	Ion-exchange	-----		LDH and side phase(s)	
	vinylbenzenesulfonate	Ion-exchange	-----		LDH	

$Mg^{2+}/Fe^{3+} = 3$	CO_3^{2-}	Coprecipitation	10.0	Boiling for 5 h	LDH	[113]
	L-ascorbate	Coprecipitation	9.0	1h	LDH	
$Mg^{2+}/Fe^{3+} = 2$	Cl^-	Coprecipitation	10.0	Not applied	LDH	[83]
$Mg^{2+}/Fe^{3+} = 2$	CO_3^{2-}	Coprecipitation	10.0	80 °C for 24 h	LDH	[84]
$Mg^{2+}/Fe^{3+} = 3$					LDH and side phase(s)	
$Mg^{2+}/Fe^{3+} = 4$						
$Mg^{2+}/Fe^{3+} = 5$					LDH	
$Mg^{2+}/Fe^{3+} = 3$	CO_3^{2-}	Coprecipitation	10.0	80 °C for 24 h	LDH	[51]
$Mg^{2+}/Fe^{3+} = 3$	Cl^-	Coprecipitation (80 °C)	10.0	70 °C for 24 h	LDH	[87]
$Mg^{2+}/Fe^{3+} = 4$						
$Mg^{2+}/Fe^{3+} = 3$	CO_3^{2-}	Coprecipitation (80 °C)	9.0 - 10.0	80 °C for 24 h	LDH and side phase(s)	[88]
$Mg^{2+}/Fe^{3+} = 2$	Cl^-	Coprecipitation	12.6 - 13	85 °C for 2 h	Side phase(s)	[91]
$Mg^{2+}/Fe^{3+} = 2$	Cl^-	Coprecipitation (20 °C)	10.0	20 °C for 24 h	LDH	[93]
$Mg^{2+}/Fe^{3+} = 2$	CO_3^{2-}	Coprecipitation (40 °C)	9.3	65 °C for 18 h	LDH	[103]
$Mg^{2+}/Fe^{3+} = 3$					LDH and side phase(s)	
$Mg^{2+}/Fe^{3+} = 4$						
$Mg^{2+}/Fe^{3+} = 3$	CO_3^{2-}	Coprecipitation	10	65 °C for 24 h	LDH	[314]
$Mg^{2+}/Fe^{3+} = 3$	CO_3^{2-}	Coprecipitation	10.0 – 11.0	80 °C for 18 h	Side phase(s)	[315]
$Mg^{2+}/Fe^{3+} = 3$	Cl^-	Coprecipitation	9.0	80 °C for 2 h	LDH	[99]
			10.0			
			11.0			
			12.0			
$Mg^{2+}/Fe^{3+} = 3$	NO_3^-	Coprecipitation	10.0	24 h	Side phase(s)	[316]
$Mg^{2+}/Fe^{3+} = 2$	Cl^-	Coprecipitation	9.0 - 10.0	24 h	LDH	[317]
$Mg^{2+}/Fe^{3+} = 3$	CO_3^{2-}	Coprecipitation	11.0	80 °C for 18 h	LDH	[100]
$Mg^{2+}/Fe^{3+} = 2$	NO_3^-	Coprecipitation	9.5 -10.5	85 °C for 18 h	LDH	[310]

	Cl^-	(40 °C)				
$Mg^{2+}/Fe^{3+} = 2$ $Mg^{2+}/Fe^{3+} = 3$ $Mg^{2+}/Fe^{3+} = 4$	Cl^-	Coprecipitation	10	80 °C for 4 h	LDH	[318]
$Mg^{2+}/Fe^{3+} = 2.8$ $Mg^{2+}/Fe^{3+} = 4.1$ $Mg^{2+}/Fe^{3+} = 5.5$	Cl^-	Coprecipitation (50 °C)	9.5	50 °C for 2 h	LDH	[110]
$Mg^{2+}/Fe^{3+} = 2$	Cl^-	Coprecipitation	10.0	25 °C for 48 h	LDH	[109]
				50 °C for 48 h	LDH	
				75 °C for 48 h	LDH	
				100 °C for 48 h	LDH	
				125 °C for 48 h	LDH and side phase(s)	
				150 °C for 48 h	LDH and side phase(s)	
$Mg^{2+}/Fe^{3+} = 3$	Cl^-	Coprecipitation	10.0	25 °C for 48 h	LDH	
				50 °C for 48 h	LDH	
				75 °C for 48 h	LDH	
				100 °C for 48 h	LDH	
				125 °C for 48 h	LDH	
				150 °C for 48 h	LDH and side phase(s)	
$Mg^{2+}/Fe^{3+} = 4$	Cl^-	Coprecipitation	10.0	25 °C for 48 h	LDH	
				50 °C for 48 h	LDH	
				75 °C for 48 h	LDH	
				100 °C for 48 h	LDH	
				125 °C for 48 h	LDH	
				150 °C for 48 h	LDH	
$Zn^{2+}/Fe^{3+} = 2$	NO_3^-	Coprecipitation	7.0	85 °C for 18 h	Side phase(s)	[310]

	Cl^-	(40 °C)				
Zn^{2+}/Fe^{3+} = 0,33 Zn^{2+}/Fe^{3+} = 1 Zn^{2+}/Fe^{3+} = 3	Cl^-	Coprecipitation	10.0	24 h	Side phase(s)	[252]
Zn^{2+}/Fe^{3+} = 3	CO_3^{2-}	Coprecipitation	10.0	70 °C overnight	LDH	[319]
Zn^{2+}/Fe^{3+} = 3	CO_3^{2-} Cl^- NO_3^-	Coprecipitation	10.0	Not applied	LDH	[253]
Zn^{2+}/Fe^{3+} = 3	NO_3^-	Coprecipitation	8.5	65 °C for 24 h	LDH and side phase(s)	[105]
Zn^{2+}/Fe^{3+} = 1 Zn^{2+}/Fe^{3+} = 2 Zn^{2+}/Fe^{3+} = 3 Zn^{2+}/Fe^{3+} = 4	CO_3^{2-}	Coprecipitation	8.0	70 °C for 18 h	LDH and side phase(s)	[85]
Zn^{2+}/Fe^{3+} = 3	Cl^-	Coprecipitation	9.0 10.0 11.0 12.0	80 °C for 2 h	Side phase(s)	[99]
Zn^{2+}/Fe^{3+} = 3	CO_3^{2-}	Coprecipitation	11.0	80 °C for 18 h	Side phase(s)	[100]
Zn^{2+}/Fe^{3+} = 2	SO_4^{2-}	Modified coprecipitation method	7.0	40 °C for 24 h	LDH and side phase(s)	[108]
Zn^{2+}/Fe^{3+} = 3	Cl^-	Coprecipitation	8.5 - 9.5	16 h	Side phase(s)	[107]
Zn^{2+}/Fe^{3+} = 2	Citrate	coprecipitation method (sono-assisted)	10.0	Sonication of 2 h at 70 °C	LDH	[320]
Zn^{2+}/Fe^{3+}~ 1	Cl^-	Coprecipitation	9.5 - 10.0	70 °C for 12 h	Side phases	[321]
Zn^{2+}/Fe^{3+} = 2	CO_3^{2-}	Coprecipitation	8.0	4 h	LDH and side phase(s)	[322]

Zn^{2+}/Fe^{3+} = 4	NO_3^-	Coprecipitation	10.0	50 °C for 12 h	LDH and side phase(s)	[323]
Zn^{2+}/Fe^{3+}= 3	CO_3^{2-}	Coprecipitation	8.0 – 10.0	Not applied	Side phase(s)	[305]
Zn^{2+}/Fe^{3+}= 2	CO_3^{2-}	Coprecipitation	10.0	70 °C for 15 h	LDH and side phase(s)	[324]
Zn^{2+}/Fe^{3+}= 4	NO_3^-	Coprecipitation	9.0	Overnight	Side phas(s)	[325]
Zn^{2+}/Fe^{3+}= 4	NO_3^-	Coprecipitation	9.0	Overnight	Side phas(s)	[326]
Zn^{2+}/Fe^{3+}= 4	CO_3^{2-}	Coprecipitation	8.0	Not applied	LDH and Side phases	[327]
Zn^{2+}/Fe^{3+}= 4	NO_3^-	Coprecipitation	8.0	24 h	LDH and Side phases	[328]
Zn^{2+}/Fe^{3+}= 2	Cl^-	Coprecipitation	7.0 - 8.0	85 °C for 18 h	Side phas(s)	[310]
Zn^{2+}/Fe^{3+}= 2	NO_3^-					

Appendix B. Supplementary data related to Chapter 3

Published paper related to the results shown in Chapter 3

Title: Investigation about iron(III) incorporation into layered double hydroxides: Compositional and structural properties of $Mg_2Fe_yAl_{(1-y)}(OH)_6$-Cl and $Zn_2Fe_yAl_{(1-y)}(OH)_6$-Cl

Abstract: Layered Double Hydroxides (LDH) and related nanocomposites have attracted much attention for biomedical applications and the development of LDH drug carriers composed by endogenous metals such as iron is of obvious interest. However, most of the studies reported so far on iron-containing LDH, mainly focusing on the applications, suffer from insufficient data about the synthesis and the characterization of these materials. In this study, it is addressed compositional and structural properties of two series of LDH materials, $Mg_2Fe_yAl_{(1-y)}$-Cl and $Zn_2Fe_yAl_{(1-y)}$-Cl with a M^{2+}/M^{3+} molar ratio (R) equal to 2 and $0 \leq y \leq 1$. By combining crystal-chemical reasoning, Rietveld refinements and pair distribution function analysis (PDF), it was possible to differentiate between contributions from crystalline and amorphous components. Concerning Mg-series, for $y > 0.5$, the compositions were found to slightly deviate from those expected with an increase in the value of R tending to 3. For Zn-series, more heterogeneous samples were obtained with the presence of amorphous 2-line ferrihydrite clearly demonstrated by PDF analysis. As well as providing a reliable approach to the characterization of Fe-LDH, this study gives useful elements for better understanding and interpreting the results reported in the literature regarding these phases.

DOI link: https://doi.org/10.1016/j.jallcom.2021.161184

Optimization of the synthesis of the $Mg_2Fe_yAl_{(1-y)}$-Cl and $Zn_2Fe_yAl_{(y-1)}$-Cl LDH materials

Aiming at improve Fe-based LDH structural organization to auxiliate materials characterization, several synthetic parameters were optimized (**Table B.1**). The $Mg_2Fe_{0.5}Al_{0.5}$-Cl nominal composition was chosen as a model for the optimization. All experiments were conducted at pH constant and equal to 10.5.

Table B.1. Synthetic parameters studied for preparation of the $Mg_2Fe_{0.5}Al_{0.5}$-Cl sample, whose optimized parameters were applied for the synthesis of the Mg and Zn-series of LDH.

Material	Stirring Device	Salts solution concentration / mol L^{-1}	Temperature	Sample's abbreviation
1	Magnetic mediated (Stir bar)	0.1	Room temperature	Stir bar_0.1_RT
2	Mechanical (*Pitch Blade* type impeller)	0.1	Room temperature	Impeller _0.1_RT
3	Mechanical (*Pitch Blade* type impeller)	0.05	Room temperature	Impeller _0.05_RT
4	Mechanical (*Pitch Blade* type impeller)	0.05	50 °C	Impeller_0.05_50

Figure B.1 shows the XRD patterns for 1 – 4 samples (**Table B.1**). All materials present only peaks related to LDH phase. Although the increase of the (00l) peak width at half height ($l_{h1/2}$) is observed by modifying the mode and the stirring speed, from magnetic (400 rpm) to mechanical (900 rpm), the diffractograms of the material stirred with the impeller show, in general, more intense, and defined peaks, being possible to well distinguish the (110) and (113) peaks. Changing from the Impeller_0.05_RT sample to the Impeller_0.05_50, a narrow (00l) peak and more intense peaks are verified.

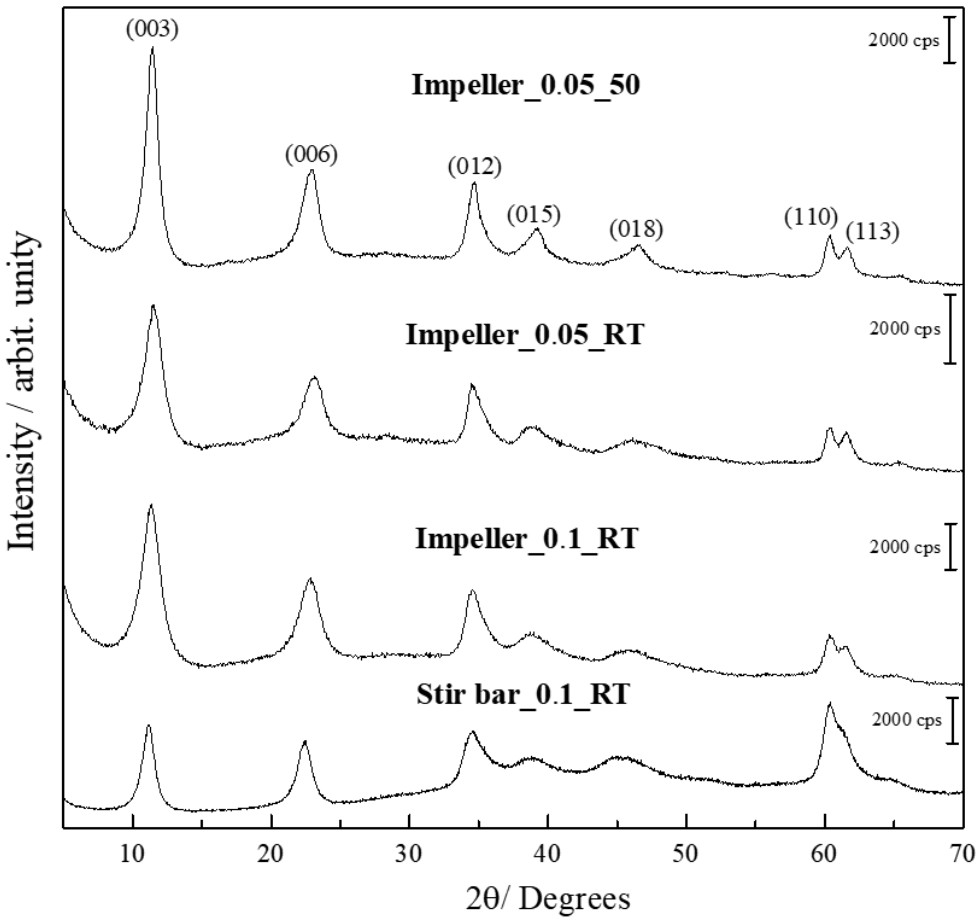

Figure B.1. X-ray diffraction patterns for the $Mg_2Fe_{0.5}Al_{0.5}$-Cl composition obtained by different synthesis conditions (see **Table B.1**).

Figures B.2 shows the SEM micrographs of 1 – 4 samples. For the Stir bar_0.1_RT sample, it is verified a morphology similar to sheets with low organization. By changing the stirring method from magnetic to mechanical, well-defined sets of particles can be visualized and aggregate's dimension is around 300 nm. With the decrease in salts solution concentration, the dimension of aggregates seems to be reduced. Increasing the temperature value, it is possible to verify an intermediate morphology between the material 1 and the materials 2 and 3.

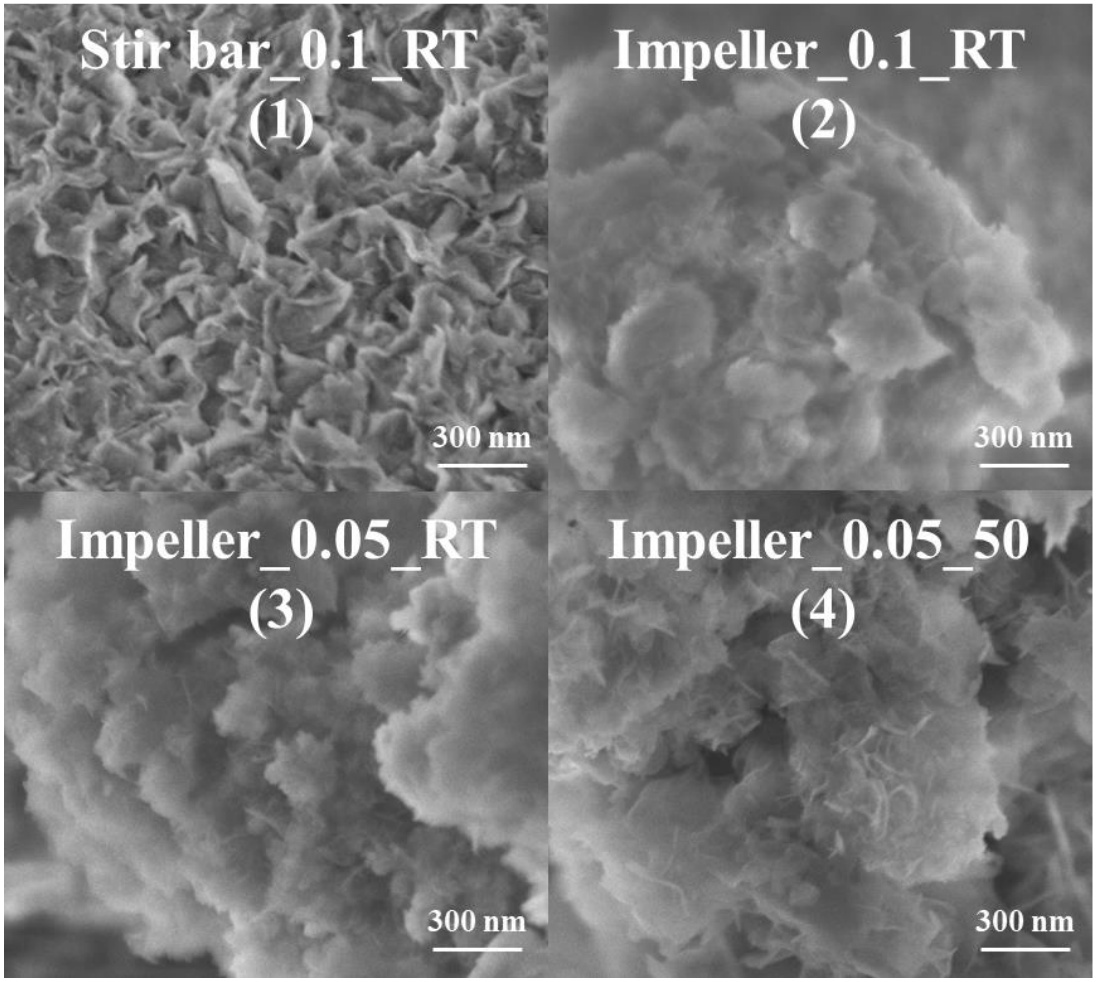

Figure B.2. Scanning electron micrographs of the 1 – 4 materials.

Figure B.3 presents hydrodynamic particle size distribution of the 1 – 4 materials. For sample 1, two distributions centered in 825 and 5560 nm (in the equipment reading limit) are observed. By changing the mode of stirring, from magnetic to mechanic, and applying a diluted salts solution, once again two size particle distributions are observed, with maximums at 275 and 1718 nm for the Impeller_0.1_RT sample and at 275 and 1106 nm for the Impeller_0.05_RT sample; however, the average hydrodynamic diameter was dislocated to low values. Considering the synthesis temperature value, a small increase in particles size to 1281 nm was observed when the material was prepared at 50 °C, but the distribution curve is more homogeneous.

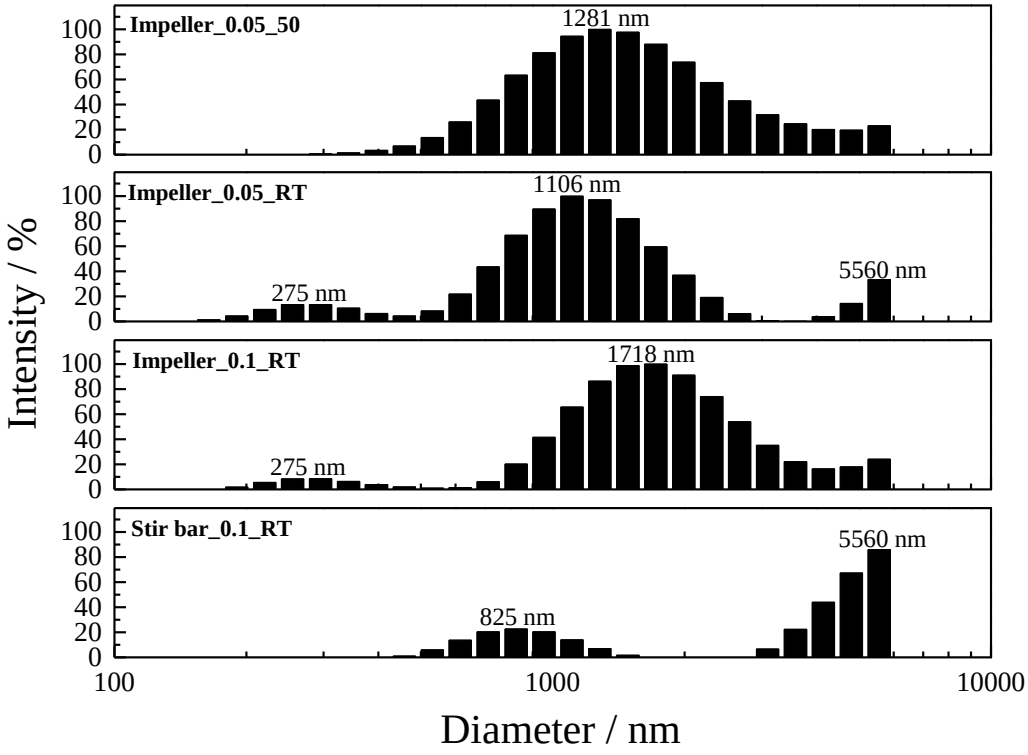

Figure B.3. Hydrodynamic particle size distribution measurements of the 1 - 4 materials showing the occurrences as a function of the diameters of the particles.

The formation of LDH samples prepared by the coprecipitation method may be understood as a sequence of three steps. First, dissociated salts are mixed with OH^- anions. Second, the homogeneous nucleation due to saturation is obtained. Finally, it occurs the guided growth of the nucleus. These steps overlap, resulting in more than one particle size distribution, also a contribution of particles agglomeration. The decrease in ion concentration leads to higher nucleus population with low particle size. On other hand, elevated synthetic temperature not only leads to larger nucleus, in detriment to small nuclei solubility, but also leads to crystal growth via oriented reprecipitation on larger formed seeds.[329]

According to the results above discussed, the application of the following parameters to the synthesis of the series of iron-based LDH containing Mg as divalent cation shows to be more plausible: mechanical stirring, low concentrated salts solution (0.05 mol L^{-1}), which decreased the degree of particle aggregation, and synthesis temperature value equal to 50 °C, due to the improvement in the XRD data quality. By simplification, the same parameters were applied for the materials composed by zinc,

but without heating to avoid the formation of undesired zinc phases, such as $Zn(OH)_2$ and/or ZnO.[85,252]

Also, synthetic pH for the Zn-series was lowered to 7.5, since even an increase in one pH unity from this value conducted to the formation of only $Zn(OH)_2$ and ZnO side phases for the material with Zn_2Fe-Cl nominal composition, as shown in **Figure B.4**.

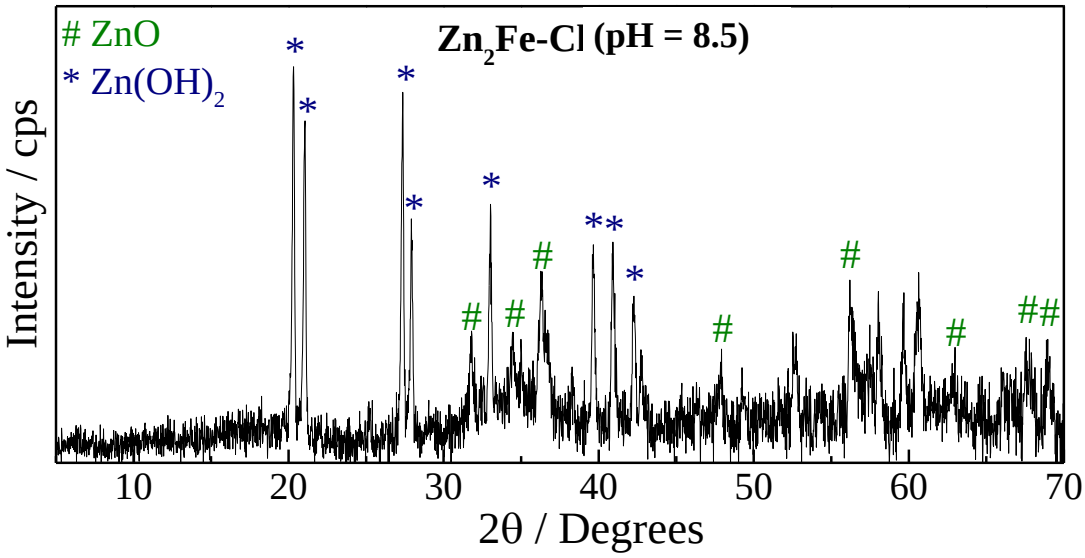

Figure B.4. XRD pattern of the Zn_2Fe-Cl material prepared at pH equal to 8.5.

Le Bail refinement of X-ray diffraction data

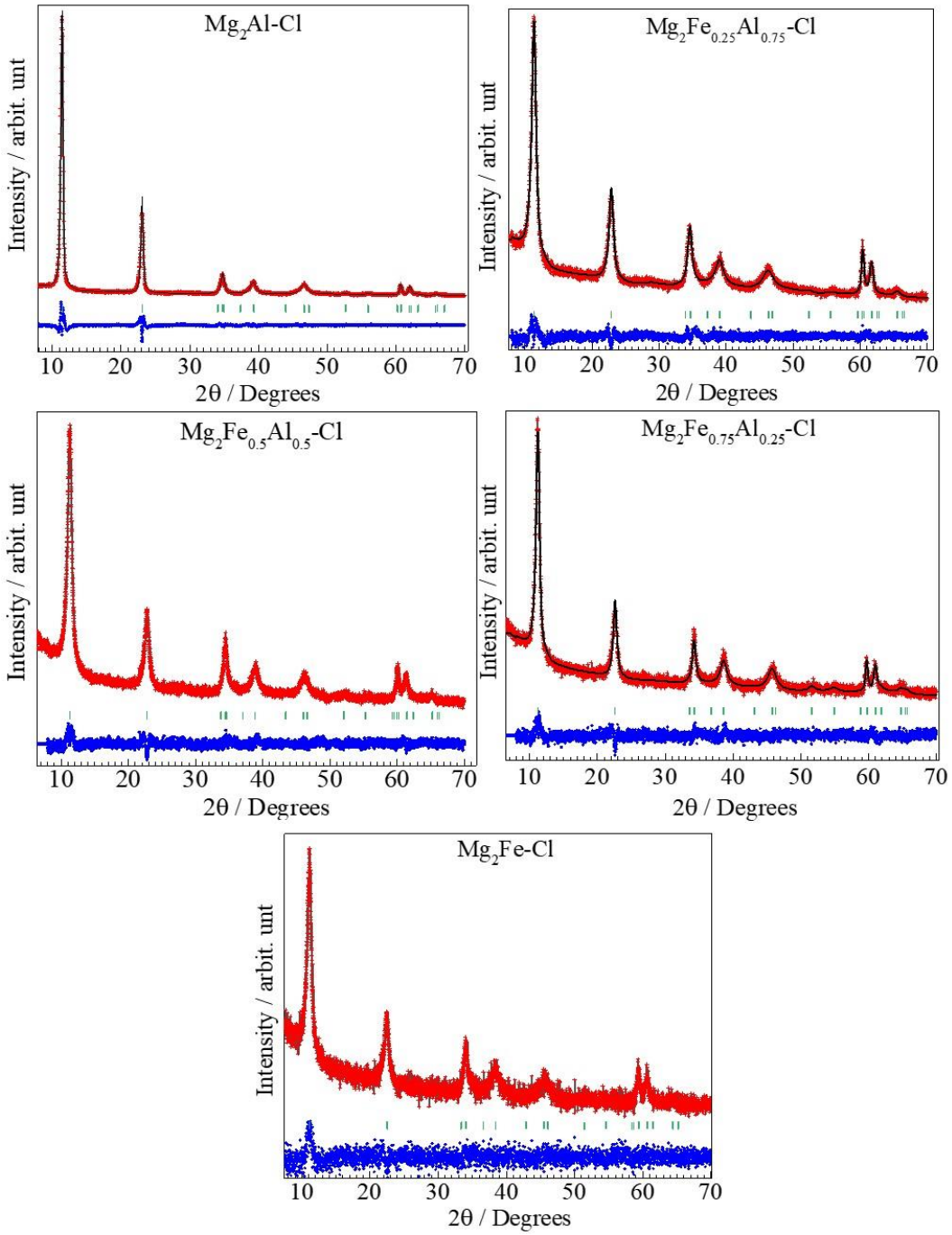

Figure B.5. Graphical presentation of the full profile refinements of XRD patterns for $Mg_2Fe_yAl_{(1-y)}$-Cl series: experimental X-ray diffraction pattern (red cross), calculated pattern (solid black line), Bragg peaks (green ticks), and difference profiles (solid blue line).

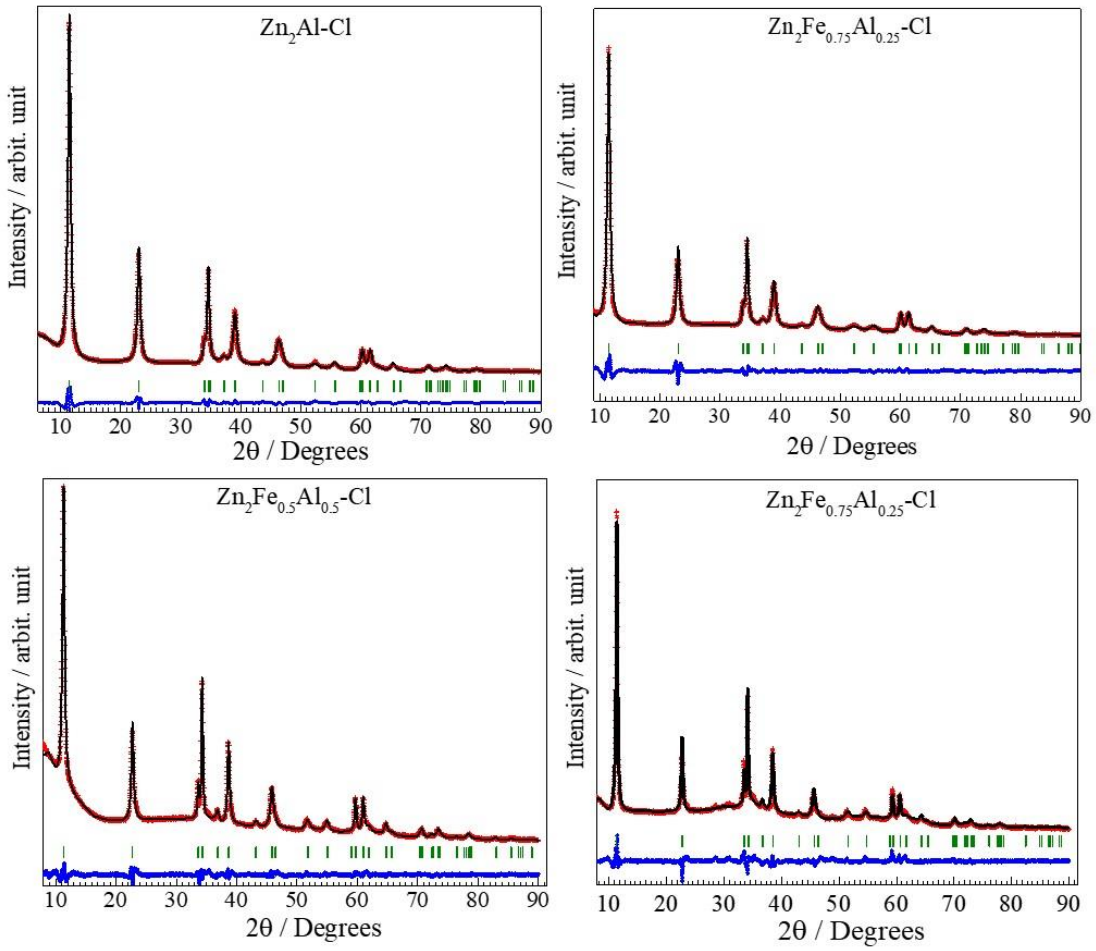

Figure B.6. Graphical presentation of the full profile refinements of XRD patterns for $Zn_2Fe_yAl_{(1-y)}$-Cl series (with exception of the Zn_2Fe-Cl amorphous phase): experimental X-ray diffraction pattern (red cross), calculated pattern (solid black line), Bragg peaks (green ticks), and difference profiles (solid blue line).

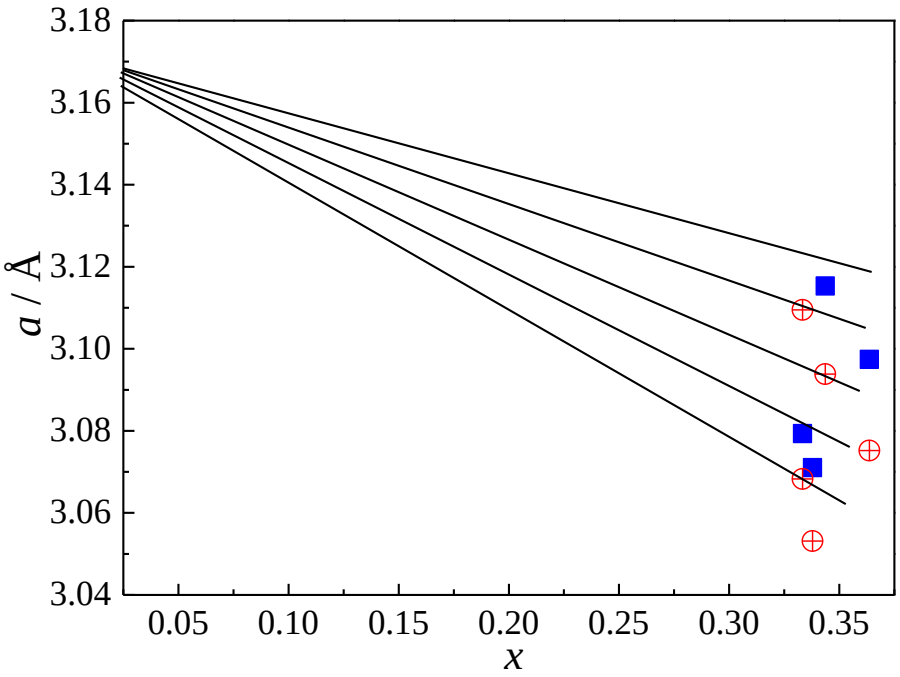

Figure B.7. Crossed-analysis of XRD and chemical analysis data for the $Zn_{1-x}Fe_yAl_{(1-y)}$-Cl series: theoretical variation of the lattice parameter *a* as a function of the composition of LDH layers in terms of *x* and *y* (solid lines); experimental (filled squares) and expected (open circles) values of the cell parameters *a* for each experimental composition.

Appendix C. Supplementary data related to Chapter 4

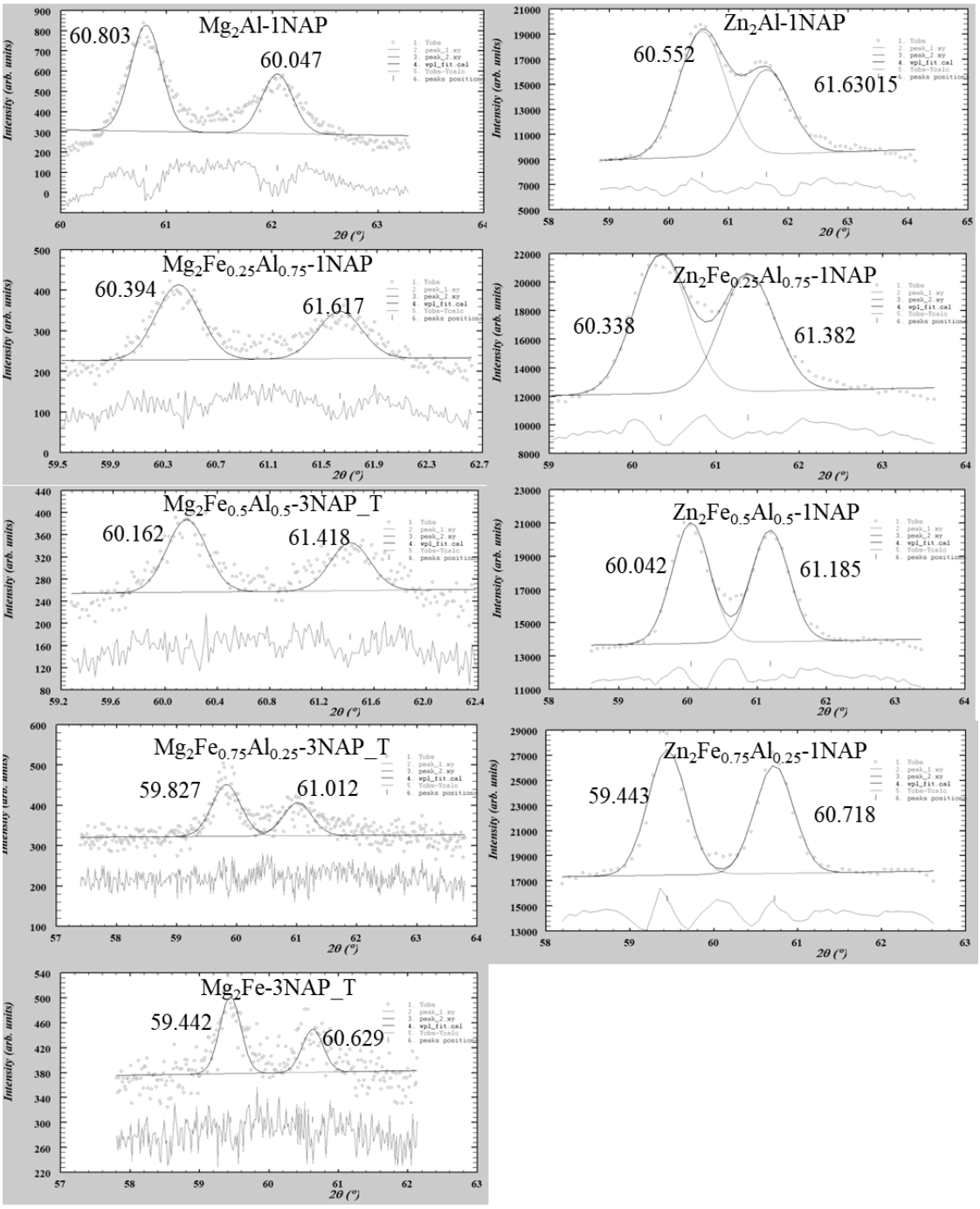

Figure C.1. Refined 110 and 113 peaks from XRD patterns of the $Mg_2Fe_yAl_{(1-y)}$-NAP and $Zn_2Fe_yAl_{(1-y)}$-NAP samples (with exception of the Zn_2Fe-1NAP sample) using FullProf Studio program.

Appendix D. Supplementary data related to Chapter 5

Characterization of Abietic Acid reagent

Figure D.1. presents the TGA-DTG-DSC (A) and MS (B) curves for HABI. DTG curve shows two main mass loss events. The first event, with onset temperature at 120 °C, is a combination of the release of hydration water molecules (see MS curve, m/z = 18), HABI melting (about 170 °C[268]), both endothermic, and an additional event not associated with the release of high amount of CO_2 that contributed to an overall exothermic event. Considering the MS curves, CO_2 release due to HABI decomposition, an exothermic process, initiates at 225°C. Therefore, hydration water is released from room temperature until the start of CO_2 release and corresponds at least to 5 wt% of the reagent mass. HABI decomposition onset temperature is 305 °C and extends until around 800°C.

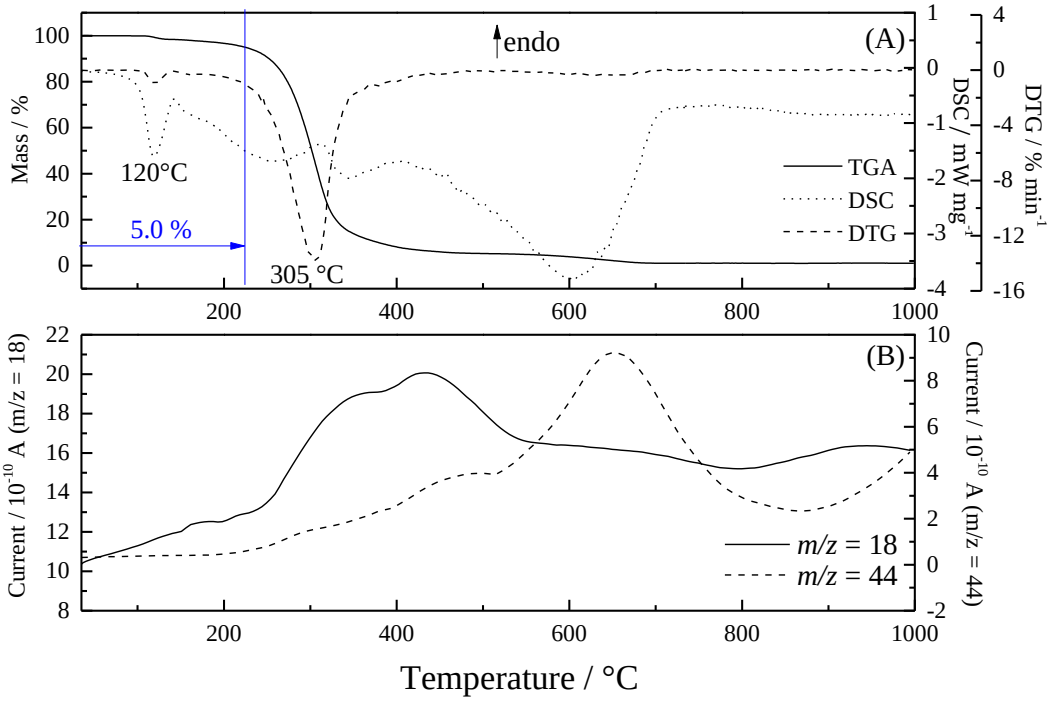

Figure D.1. Thermal analysis data of HABI: (A) TGA, DTG, and DSC curves; (B) MS curves.

Calculated and experimental Raman spectra of HABI (**Figure D.2**) are very similar and agrees with the literature.[267] Other products could not be identified.

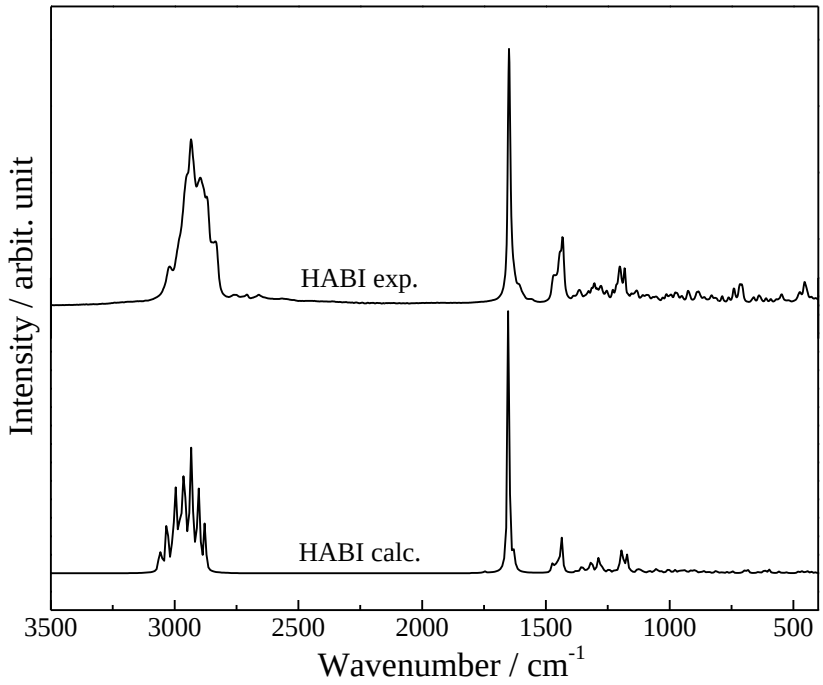

Figure D.2. Calculated and experimental FT-Raman spectra of HABI.

Figure D.3 presents the experimental and calculated IR spectra of HABI. All bands observed in the spectrum of NaABI salt are also noticed in the spectrum of the acid form. The bands at 2650 and 2531 cm^{-1} are attributed to the overtone stretching of the carboxyl group.[330] The bands at 1711 and 1270 cm^{-1}, absent in the spectra of NaABI or LDH (**Figures 5.14**, **5.15**, or **5.16**), are assigned to the C=O and C—O stretching.

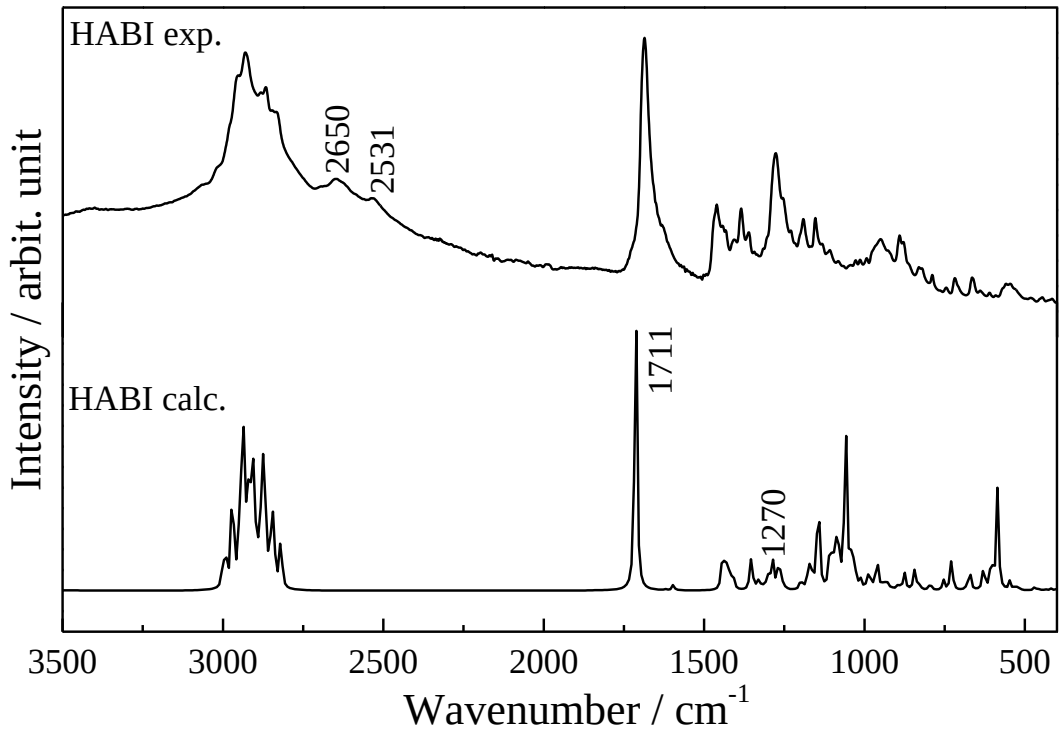

Figure D.3. Calculated and experimental FT-IR spectra of HABI.

By the chromatogram shown in **Figure D.4**, using a UV-Vis detector, it is possible to identify the early elution of less hydrophobic compounds that are present in low amount in the sample and the main product. HABI was eluted after around 38 min.

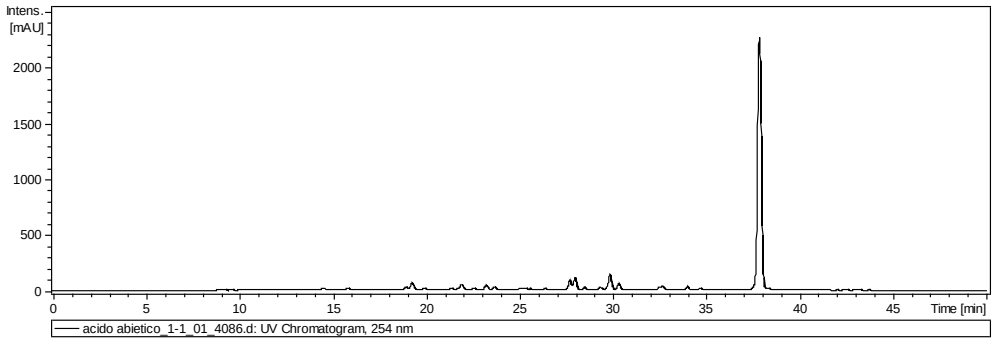

Figure D.4. Chromatogram of HABI applying UV-Vis detector.

By the chromatogram of HABI reagent applying mass detector shown (**Figure D.5**), impurities are better visualized compared to the data obtained from UV-Vis detector. Mass spectra of each eluted compound are shown from **Figures D.6** to **D.17**. It is interesting to note that all fragments present very high molar mass and higher than the mass of the ionized ABI. In **Figure D.17**, corresponding to the mass spectra of the

product eluted after 38.9 min, the main fragment has a m/z = 303.22 and corresponds to HABI. However, a very low intense fragment with m/z = 325.19 is observed.

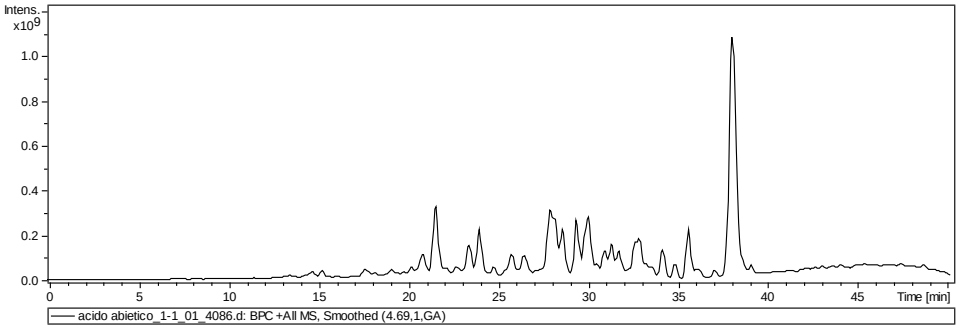

Figure D.5. Chromatogram of HABI applying mass detector, ESI+ mode.

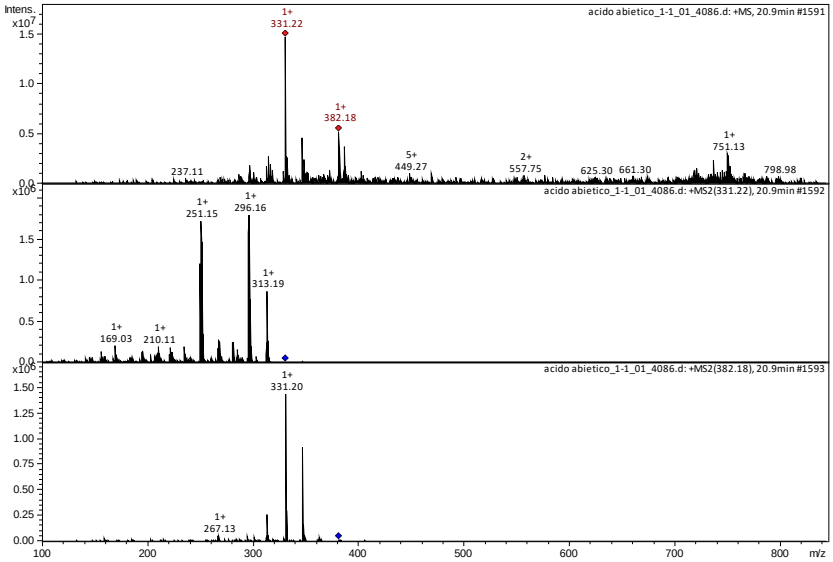

Figure D.6. Mass spectra of the compounds eluted after 20.9 min.

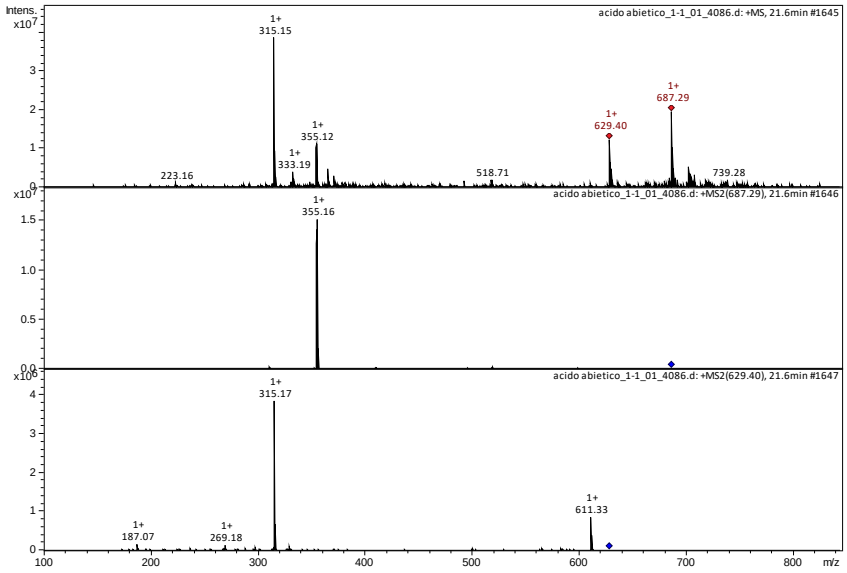

Figure D.7. Mass spectra of the compounds eluted after 21.6 min.

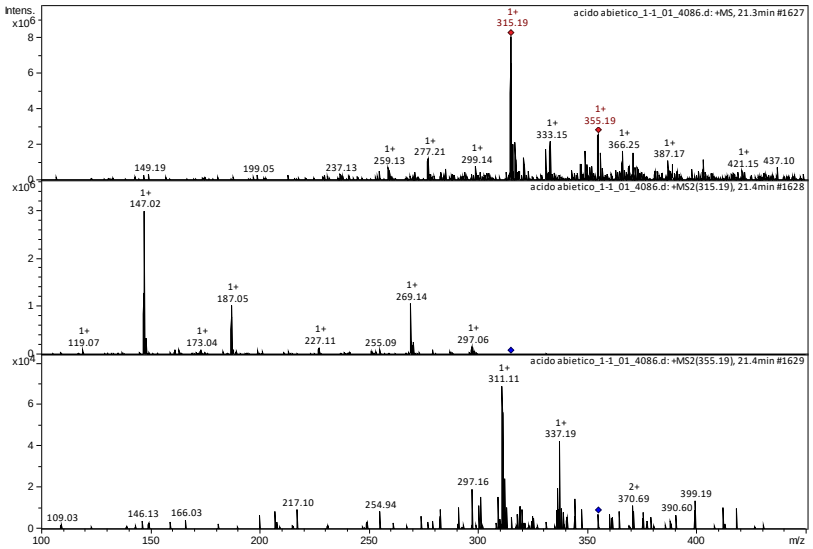

Figure D.8. Mass spectra of the compounds eluted after 21.3 min.

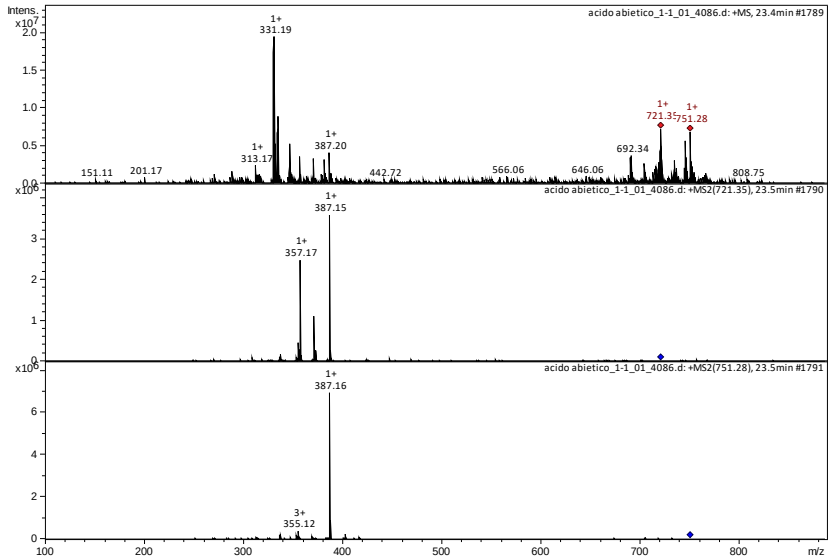

Figure D.9. Mass spectra of the compounds eluted after 23.4 min.

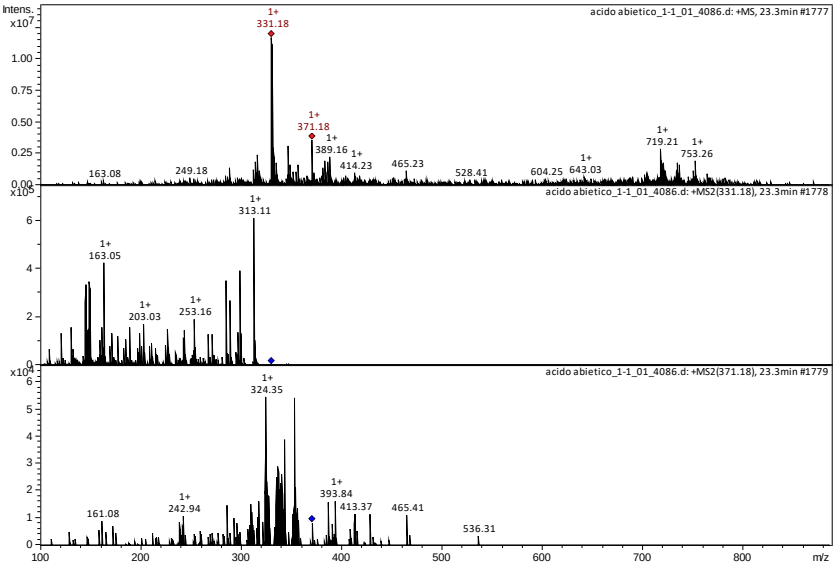

Figure D.10. Mass spectra of the compounds eluted after 23.3 min.

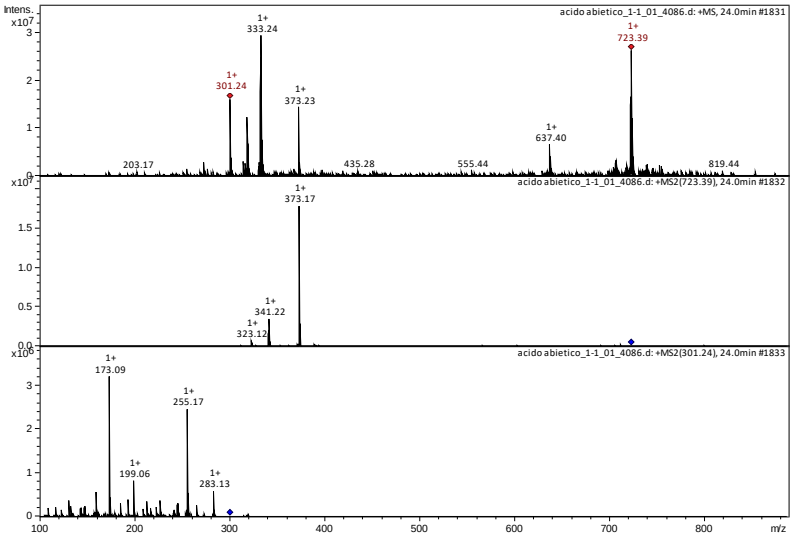

Figure D.11. Mass spectra of the compounds eluted after 24.0 min.

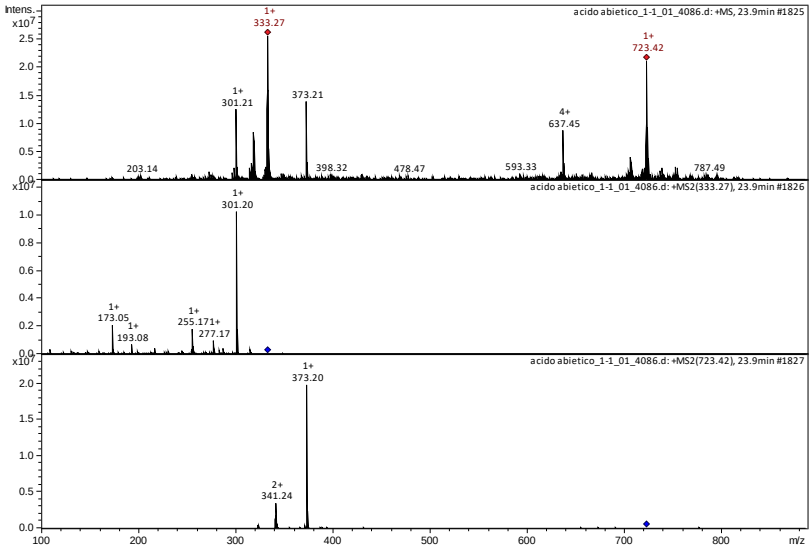

Figure D.12. Mass spectra of the compounds eluted after 23.9 min.

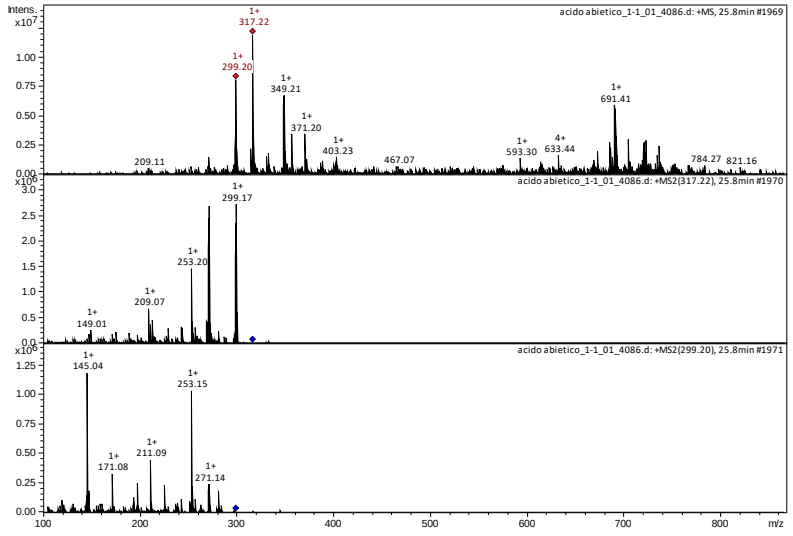

Figure D.13. Mass spectra of the compounds eluted after 25.8 min.

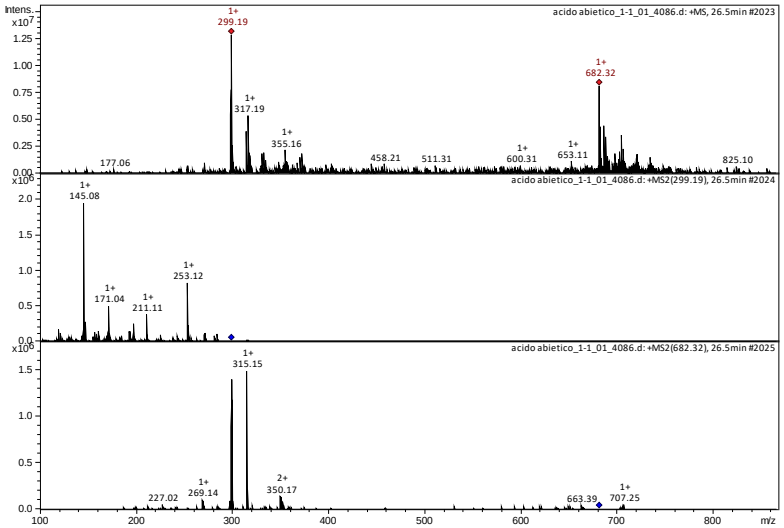

Figure D.14. Mass spectra of the compounds eluted after 26.5 min.

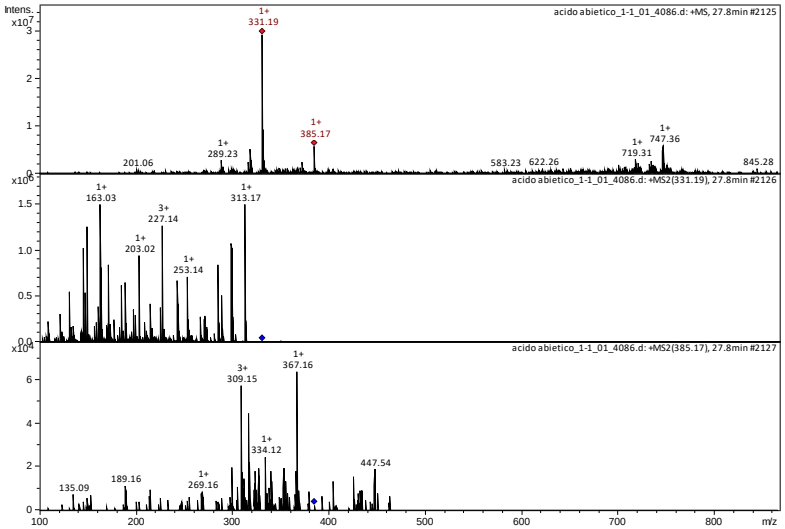

Figure D.15. Mass spectra of the compounds eluted after 27.8 min.

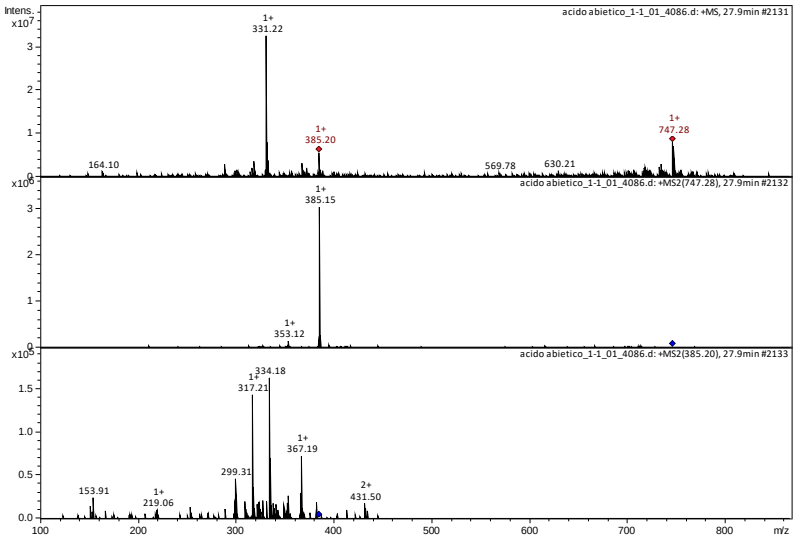

Figure D.16. Mass spectra of the compounds eluted after 27.9 min.

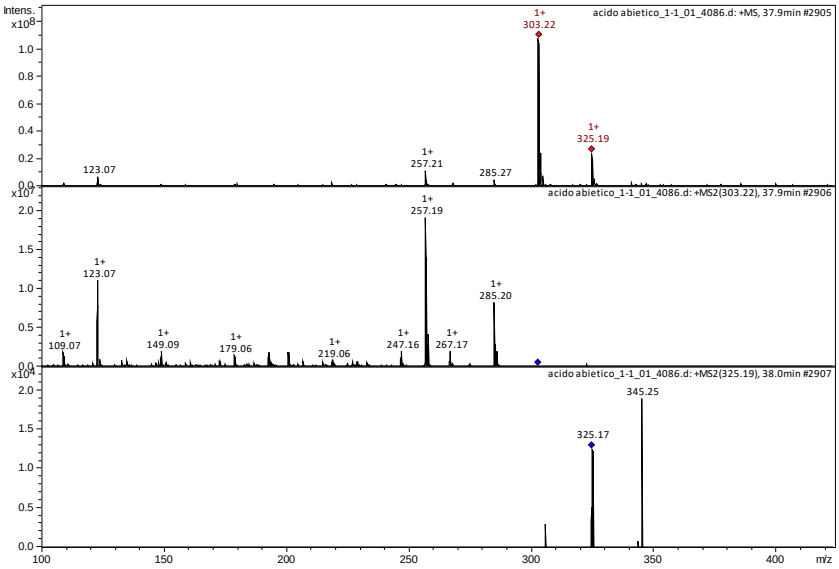

Figure D.17. Mass spectra of the compounds eluted after 38.9 min.

The results presented above suggest that the majority HABI reagent's impurities consist of structures with very high molar mass and, added to the results shown in the article, there is no evidence of intercalation or adsorption of such impurities in the Mg- or Zn-series of materials nor their presence in the NaABI salt.

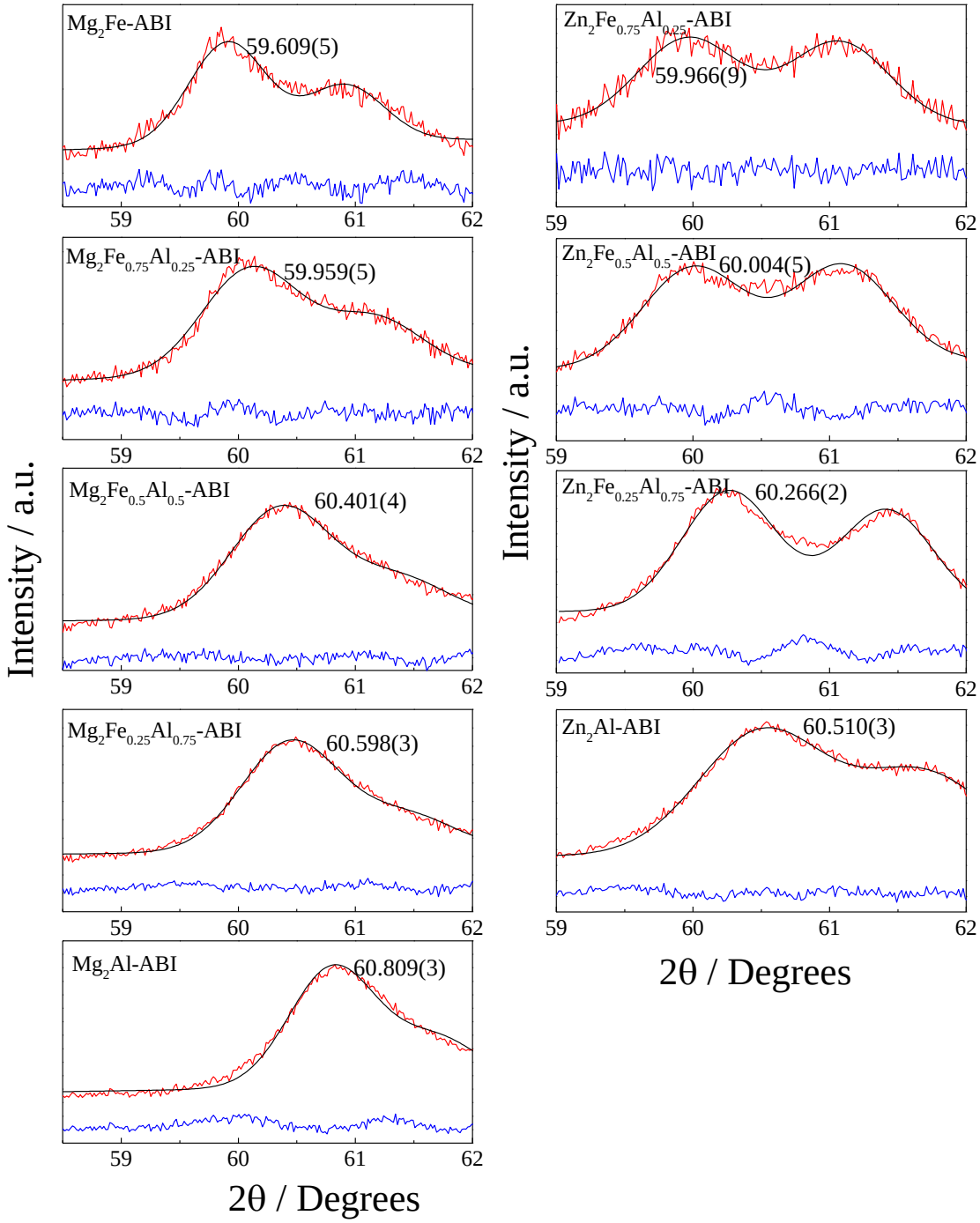

Figure D.18. Graphical presentation of the refinement of 110 and/or 113 peaks profile from XRD data of the $Mg_2Fe_yAl_{(1-y)}$-ABI and $Zn_2Fe_yAl_{(1-y)}$-ABI series (with exception of the Zn_2Fe-ABI sample): experimental XRD pattern (red), calculated pattern (black), and difference profiles (solid blue line).

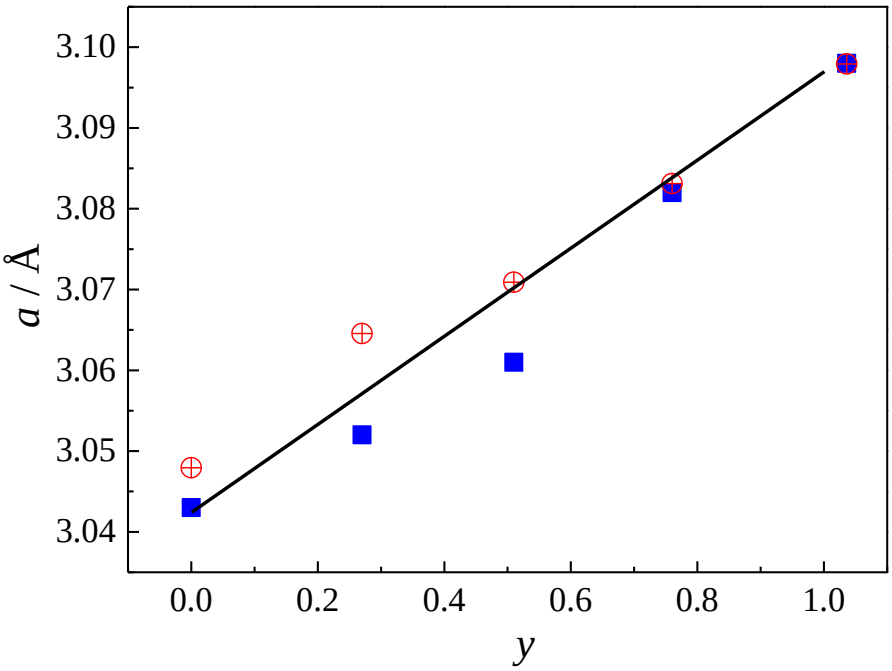

Figure D.19. Crossed-analysis of XRD and chemical analysis data for the $Mg_{1-x}Fe_yAl_{(1-y)}$-ABI series: variation of the lattice parameter *a* as a function of the composition of LDH layers in terms of *y*; experimental (filled squares) and expected (open circles) values of the *a* cell parameters for each experimental composition.

Appendix E. Supplementary data related to Chapter 6

Published paper related to the results shown in Chapter 6

Title: Design of 3D multi-layered electrospun membranes embedding iron-based layered double hydroxide for drug storage and control of sustained release

Abstract: Nowadays polymer dressings are expected to possess multiply functions. Besides acting as physical barriers, dressings may provide for the injured tissue species able to turn wound healing process faster and painless. In this way, dressings can be designed aiming to enable the release of drugs. The possibility to modulate drug release kinetics is a desired characteristic to be achieved in order to turn drug delivery systems adequate to specific treatments. However, hydrophilic drugs and hydrophobic polymers incompatibility hinders such modulation and a long-term release cannot be achieved efficiently. Here we present the design of poly(lactic acid) (PLA) membranes containing iron-based Layered Double Hydroxide (LDH) particles able to storage a hydrophilic anionic drug (derived from the non-steroidal anti-inflammatory naproxen). LDH particles are excellent candidates to compose multifunctional composites. They may present diverse biocompatible compositions, possess an elevated encapsulation capacity and tends to promote drugs sustained release by its own, besides assisting tissues regeneration process. Nanofibrous membranes were prepared by the combination of electrospun PLA and electrosprayed LDH as alternated layers (approach A) and also by both technics performed at the same time (approach B). In approach A, by varying the thickness of the PLA fibrous layers, it was possible to easily modulate the drug release rate. Half of drug content was released after 1, 4 and 17 days for the membranes containing the thinnest, the intermediate and the thicker PLA layers, respectively, and after 56 h for the membrane prepared by the approach B. Naproxen release was kept for 18 days for the thinnest membrane, 59 days for the membrane prepared by the approach B and 66 days for the thicker membranes. We believe that this work can inspire the development of new functional membranes with tunable drug release profile thanks to the versatile electrospinning and electrospraying techniques.

DOI link: https://doi.org/10.1016/j.eurpolymj.2020.109675

Optimization of the formulation of the LDH suspension used to prepare the LDH-PLA membranes

Variation of the LDH content in suspension

The capacity to cover the surface of the collector paper applying $Mg_2Fe_{0.5}Al_{0.5}$-Cl LDH / ethanol suspensions was evaluated using three weight percentages (0.5, 0.75 and 1 %) submitted to electrospraying for 30 min. Needle and collector voltages were kept at 25 and 0 kV, respectively, the working distance was equal to 16 cm, and the suspension rate flow equal to 6 mL h^{-1}. According to the results shown in **Figure E.1**, 1 % (w/w) LDH-ethanol suspension percentage was considered ideal by the efficacy and extension of surface covering.

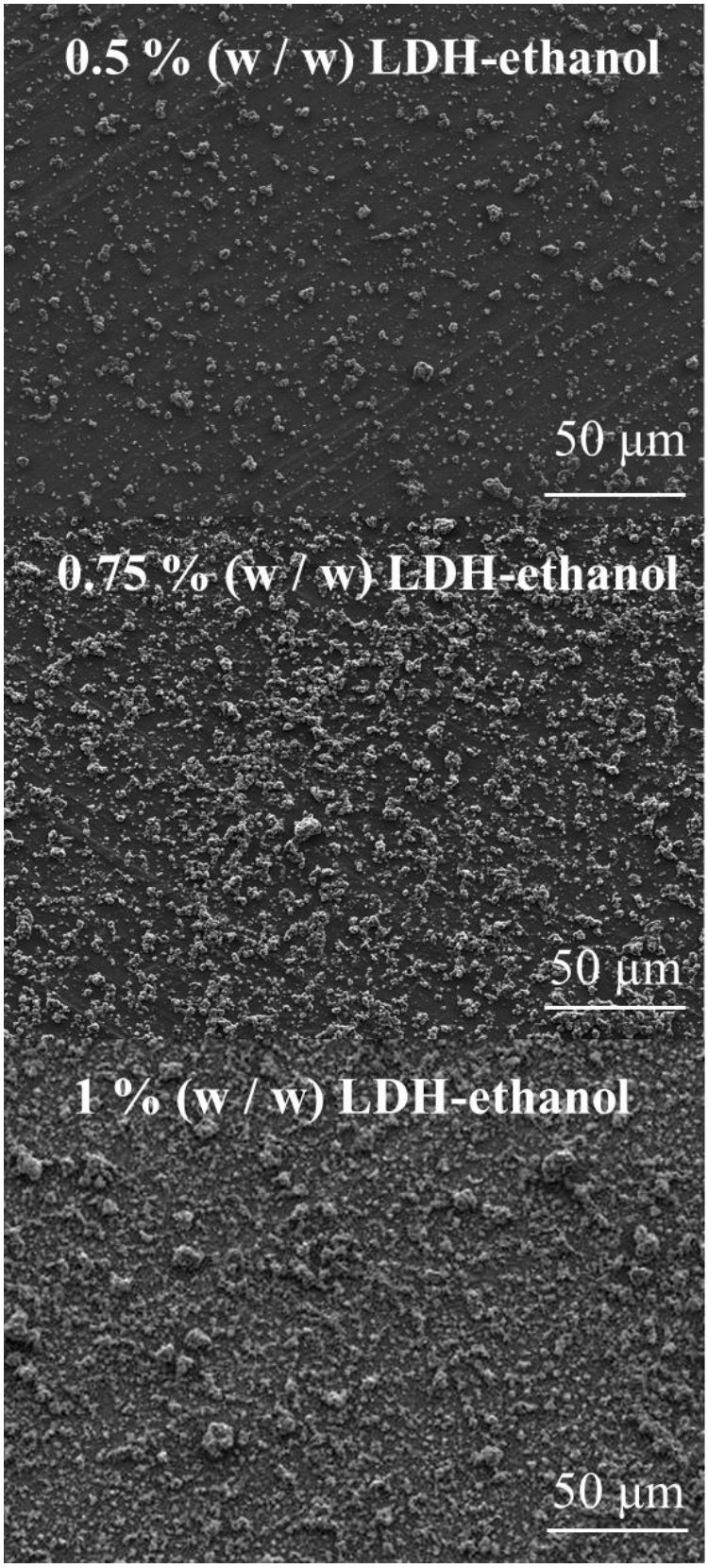

Figure E.1. SEM images of electrosprayed 0.5, 0.75, and 1 % (w / w) LDH-ethanol suspension. Samples were analyzed applying SE detector, 5 kV and work distance around 7.2 mm.

Evaluation of the effect of the ultrasonication treatment in the 1 % wt LDH/ethanol suspension stability used for electrospraying

To analyse the stability of the $Mg_2Fe_{0.5}Al_{0.5}$-Cl LDH in ethanol for electrospraying application, in relation to sedimentation, it was added 0.0797 g of LDH into 10 mL of ethanol (1 % wt) and the suspension was submitted to Ultrasonic Pointer (Branson digital sonifier) under ice bath. For the evaluation of the amplitude effect, 10, 20, 30 and 40 % amplitude were applied for a total of 3 min (2 s on alternated with 2 s off). After 2 min resting, when the flask was turned, deposited particles were visualized as can be seen in **Figure E2**. Less particles rested at the bottom of the flask for the sample ultrasonicated at 40 % of amplitude, indicating an effective reduction in aggregates size. Such condition was then applied for the optimization of the sonication time.

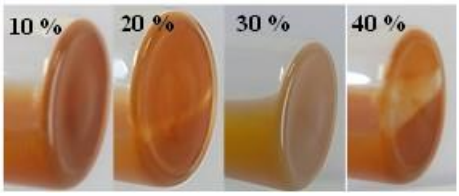

Figure E.2. Aspect of 1 % Cl-LDH / ethanol suspensions after ultrasound treatment at 10, 20, 30, and 40 % amplitude for a total of 3 minutes and resting time of 2 min.

After modification of the sonication amplitude, the sonication time was optimized and 6, 9, 20, and 30 min of treatment were tested. The systems were kept resting for 1 h and the turned flasks aspect after are present in **Figure E.3**. Even observing some deposited solids for the suspension ultrasonicated for 30 min, the result was considered satisfactory and the conditions were applied for the electrosprayed LDHs. Indeed, for the preparation of the membranes, the LDH suspensions were processed immediately after ultrasonication in order to minimize the sedimentation of LDH during electrospraying.

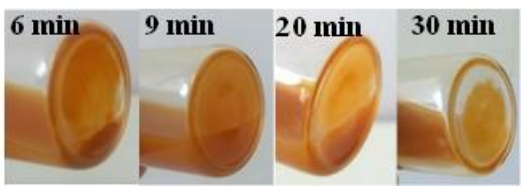

Figure E.3. Aspect of 1 % LDH-Cl / ethanol suspensions after ultrasonication at 40 % of amplitude for 6, 9, 20, and 30 minutes and resting time of 1 h.

Summarizing, the amplitude equal to 40 % and ultrasonication time of 30 min were considered the optimum conditions resulting in a satisfactory suspensions stability and were applied for the preparation of the nanofibers membranes.

$Mg_2Fe_{0.5}Al_{0.5}$-Cl and $Mg_2Fe_{0.5}Al_{0.5}$-3NAP_H materials characterization

Figure E.4. presents the XRD patterns of $Mg_2Fe_{0.5}Al_{0.5}$-Cl (precursor) and $Mg_2Fe_{0.5}Al_{0.5}$-3NAP_H samples. Precursor LDH diffractogram displays the characteristics peaks (narrow and well resolved) related to the LDH phase. On both diffractograms peaks are narrow revealing a structural organization. After NAP intercalation, the shift of the (ool) peaks to small angles region is observed, which indicates that the interplanar distances are higher, endorsing the organic anion intercalation. Moreover many (ool) harmonic peaks are visualized for the hybrid LDH. The presence of the residual $Mg_2Fe_{0.5}Al_{0.5}$-Cl phase in the $Mg_2Fe_{0.5}Al_{0.5}$-3NAP_H sample is evidenced by the permanence of the (113) peak, normally displaced to small angles region and not visualized for single phases LDHs intercalated with bulky anions, once it is dependent of the c crystallographic parameter.

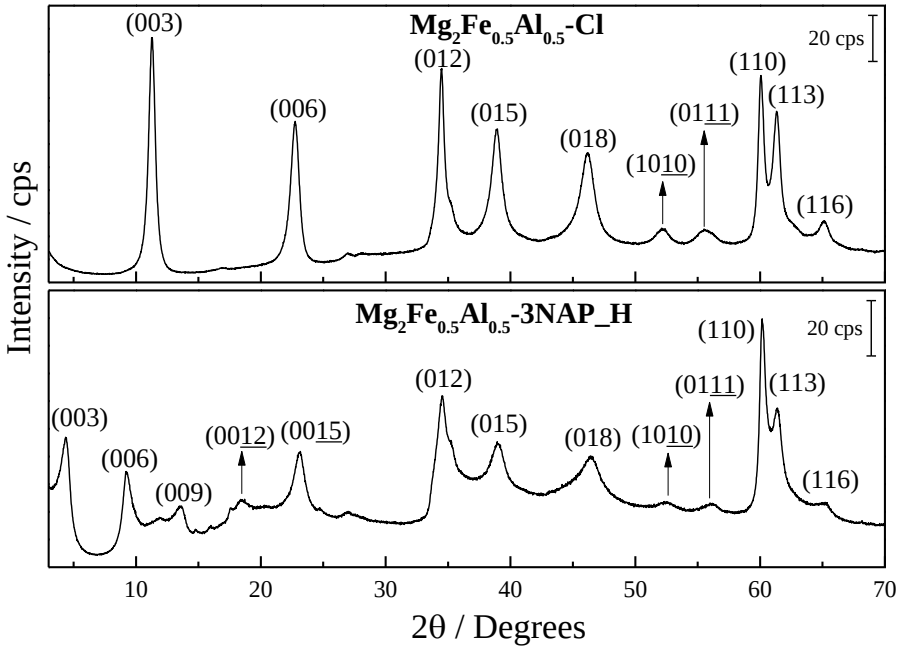

Figure E.4. XRD patterns of the LDH-Cl and LDH-NAP samples.

FT-IR spectra of the LDH materials are present in **Figure E.5**. The band at 1361 cm^{-1} is assigned to the antisymmetric stretching of the carbonate anions (contaminant), while the broad bands below 700 cm^{-1} are assigned to the metal-OH translation.[36] For the $Mg_2Fe_{0.5}Al_{0.5}$-3NAP_H sample the band at 1230 cm^{-1} is attributed to the in plane bending of the C-H bonds in the naphthalene ring. The bands at 1392 and 1545 cm^{-1} can be assigned to the stretching of the COO^- group.[131]

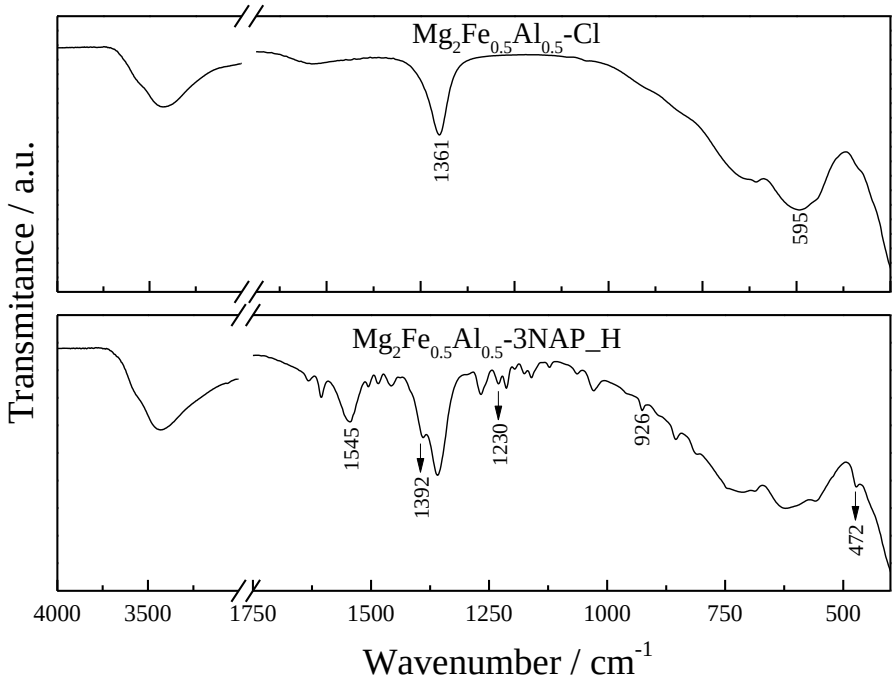

Figure E.5. FT-IR spectra of LDH-Cl and LDH-NAP samples.

FT-Raman spectra of the LDHs are presented in **Figure E.6**. For the precursor phase, the less intense band at 1062 cm^{-1} is assigned to the symmetric stretching of adsorbed carbonate anions.[331] The band at 540 cm^{-1} is assigned to metal-OH translation modes. For the $Mg_2Fe_{0.5}Al_{0.5}$-3NAP_H sample, the most intense bands at 1632 and 1416 cm^{-1} are attributed to C–C ring vibrations while the band at 1386 cm^{-1} is assigned to CH_3 deformation.[115]

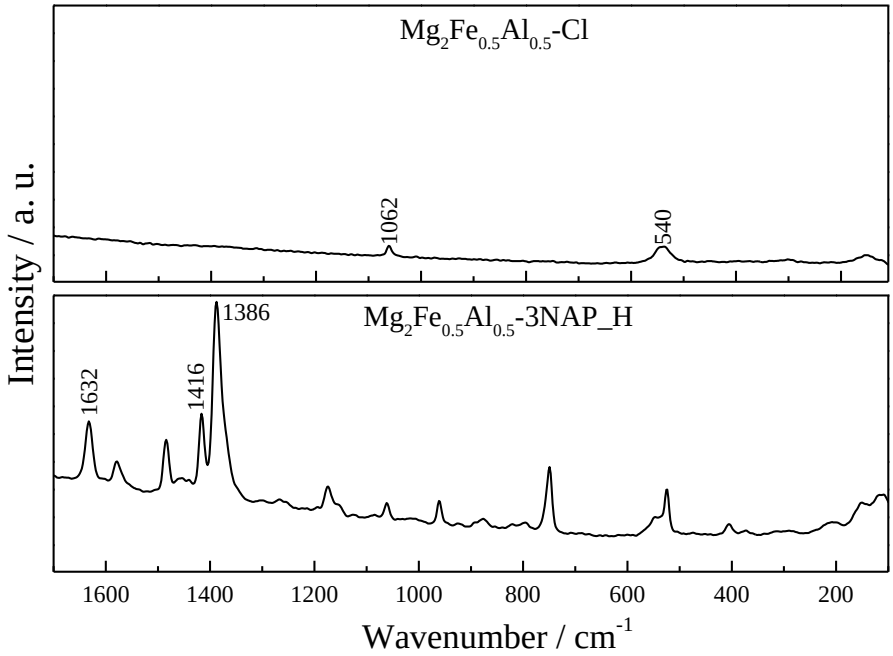

Figure E.6. FT-Raman spectra of LDH-Cl and LDH-NAP samples.

TGA curves of the $Mg_2Fe_{0.5}Al_{0.5}$-Cl and $Mg_2Fe_{0.5}Al_{0.5}$-3NAP_H materials are shown in Figures **E.7** and **E.8**, respectively. Three and four main mass loss events are observed, for the precursor and the hybrid LDH sample, respectively. For both compounds, the first and second events, occurring from room temperature up to 180 °C and 230 °C for the precursor LDH and for the hybrid material, respectively, are associated with the release of adsorbed and intercalated water molecules. For the $Mg_2Fe_{0.5}Al_{0.5}$-Cl sample, the third event, that occurs between 180 – 600 °C, is assigned to the matrix dehydroxylation. The residual mass corresponds to 59.5 % wt. For the $Mg_2Fe_{0.5}Al_{0.5}$-3NAP_H LDH, the third and fourth mass loss events correspond to the overlapping matrix dehydroxylation and NAP decomposition. The smaller residual mass (46.4 % wt) observed, in comparison with the precursor material, is in agreement with NAP presence.

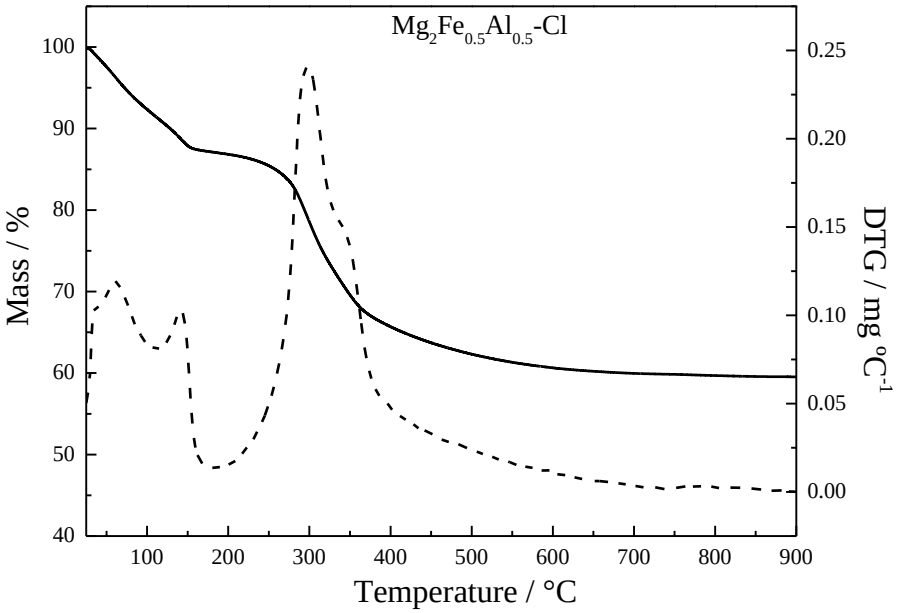

Figure E.7. TGA (solid line) and DTG (dashed line) curves of the $Mg_2Fe_{0.5}Al_{0.5}$-Cl sample.

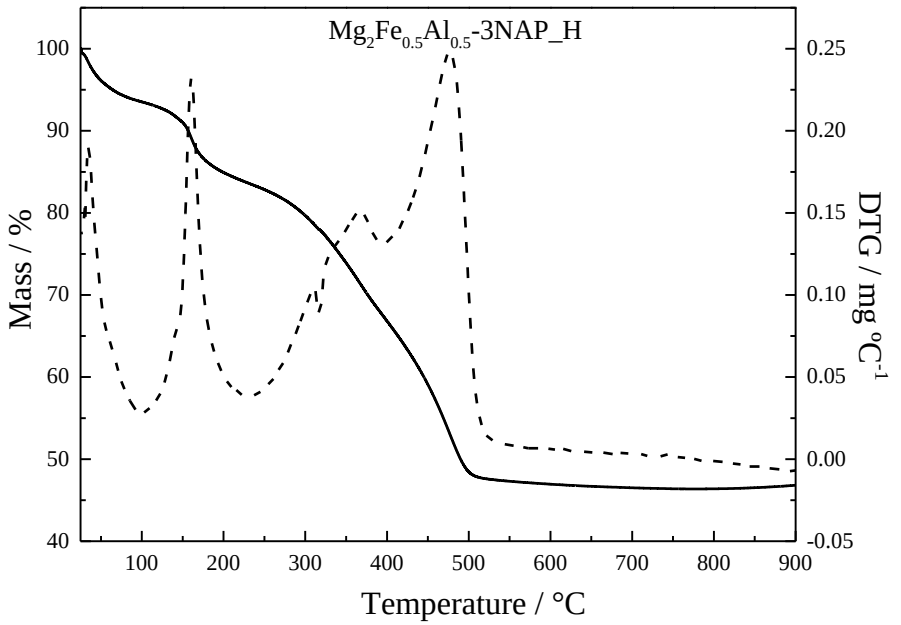

Figure E.8. TGA (solid line) and DTG (dashed line) curves of the $Mg_2Fe_{0.5}Al_{0.5}$-3NAP_H sample.

SEM micrographs of the $Mg_2Fe_{0.5}Al_{0.5}$-Cl and $Mg_2Fe_{0.5}Al_{0.5}$-3NAP_H samples are present in **Figure E.9**. For both samples, a sand rose morphology and many sets of 2D plates are visualized. The great similarity between the sample's morphology suggests that the chloride-exchange is a topotactic process, in which the final lattice is determined by the lattice of the pristine LDH.

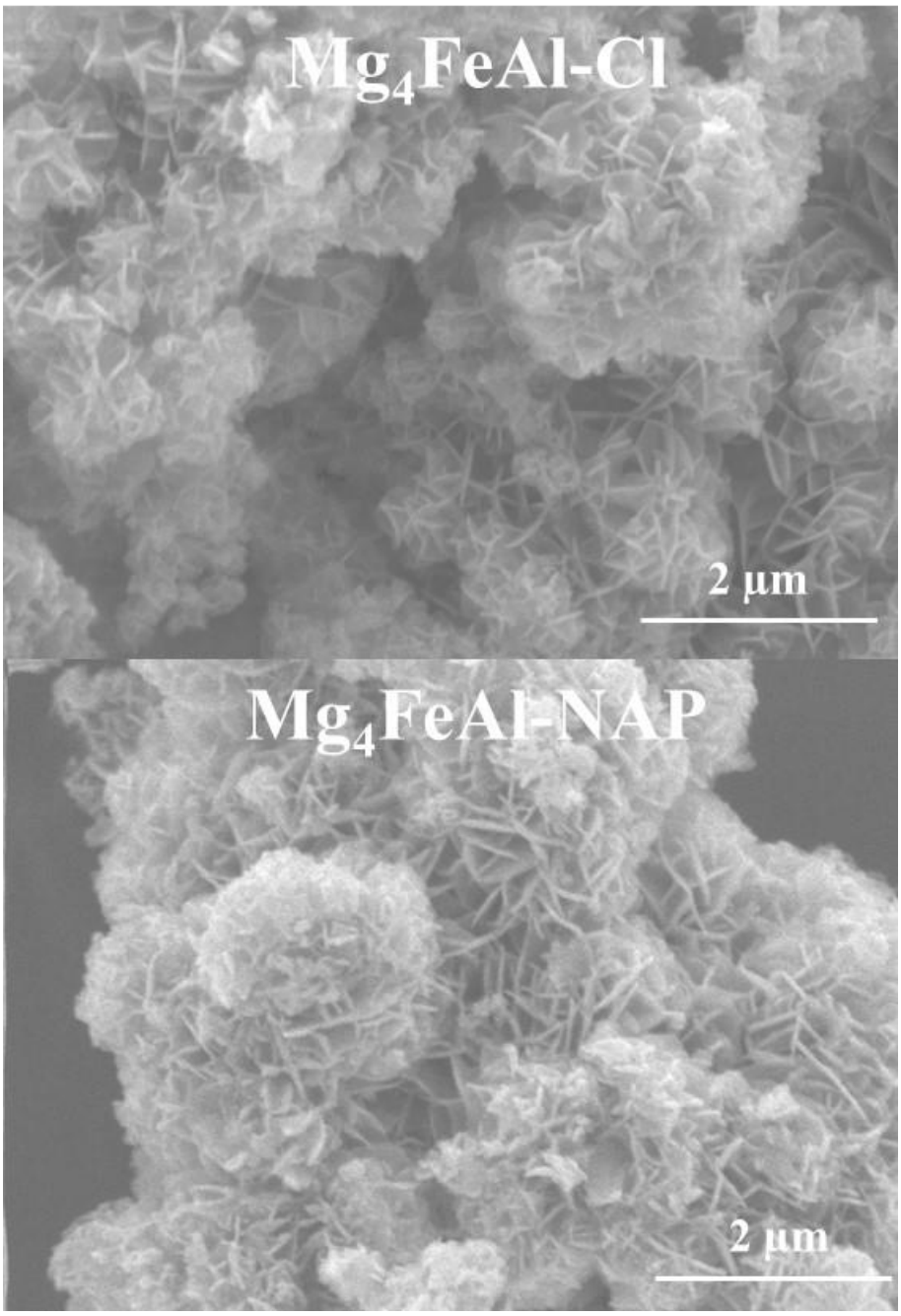

Figure E.9. SEM micrographs of the $Mg_2Fe_{0.5}Al_{0.5}$-Cl (top) and $Mg_2Fe_{0.5}Al_{0.5}$-3NAP_H (bottom) samples.

The elemental chemical composition of the $Mg_2Fe_{0.5}Al_{0.5}$-Cl and $Mg_2Fe_{0.5}Al_{0.5}$-3NAP_H LDHs, as well as the amount of water obtained by TGA experiments, are gathered in **Table E.1**. Molar ratio values between the metals are close to the nominal values. Naproxen anions were intercalated in appreciable amounts (36.17 g of NAP for 100 g of hybrid).

Table E.1. Elemental chemical composition of $Mg_2Fe_{0.5}Al_{0.5}$-Cl and $Mg_2Fe_{0.5}Al_{0.5}$-3NAP_H LDHs.

Sample	Mg/Al	Mg/Fe	Fe/Al	Mg / (Fe + Al)	% H_2O	wt % C	wt % NAP
$Mg_2Fe_{0.5}Al_{0.5}$-Cl	4.32	4.08	1.06	2.10	13.0	-----	-----
$Mg_2Fe_{0.5}Al_{0.5}$-3NAP_H	4.36	4.18	1.04	2.14	14.4	26.51	36.17

NaNAP calibration curve

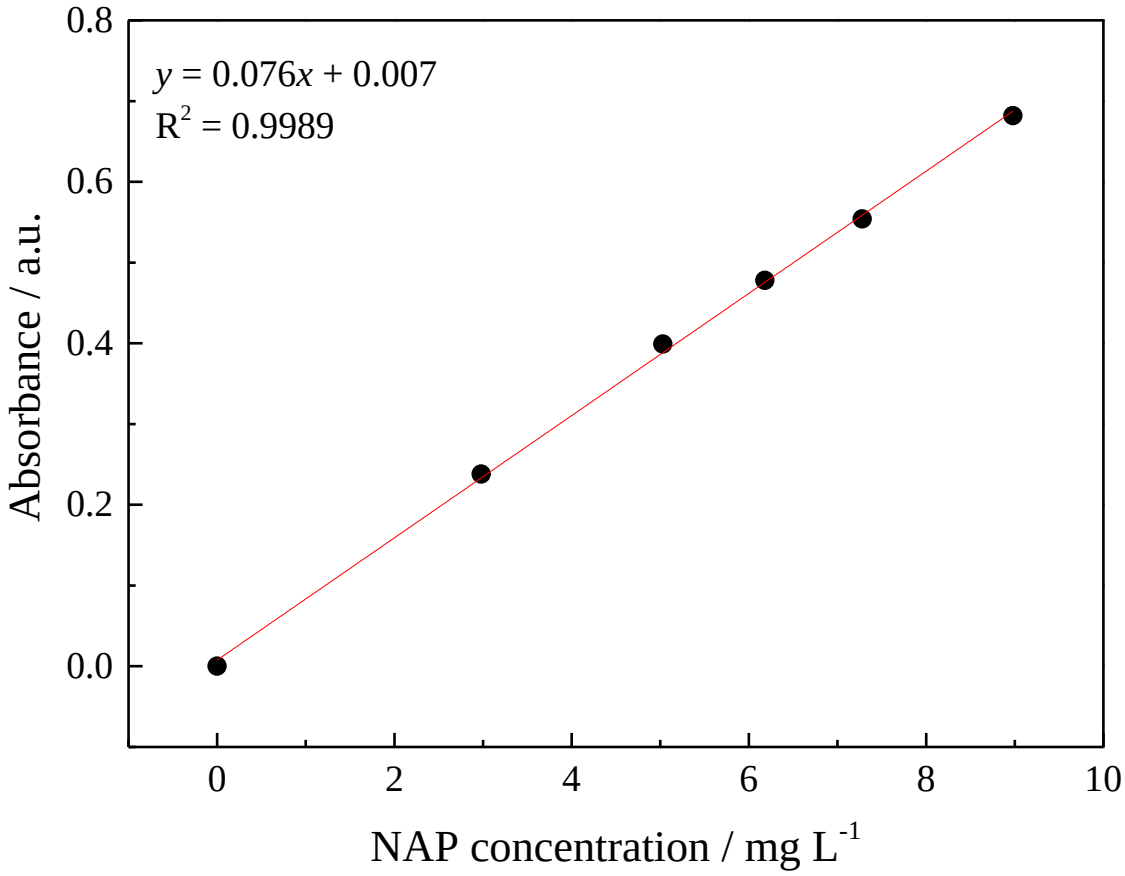

Figure E.10. Calibration curve: absorbance as a function of NAP concentration at λ = 230 nm.

Appendix F. Supplementary data related to Chapter 7

Published paper related to the results shown in Chapter 7

Title: Polymer/Iron-Based Layered Double Hydroxides as Multifunctional Wound Dressings

Abstract: This work presents the development of multifunctional therapeutic membranes based on a high-performance block copolymer scaffold formed by polyether (PE) and polyamide (PA) units (known as PEBA) and layered double hydroxide (LDH) biomaterials, with the aim to study their uses as wound dressings. Two LDH layer compositions were employed containing Mg^{2+} or Zn^{2+}, Fe^{3+} and Al^{3+} cations, intercalated with chloride anions, abbreviated as Mg-Cl or Zn-Cl, or intercalated with naproxenate (NAP) anions, abbreviated as Mg-NAP or Zn-NAP. Membranes were structurally and physically characterized, and the in vitro drug release kinetics and cytotoxicity assessed. PEBA-loading NaNAP salt particles were also prepared for comparison. Intercalated NAP anions improved LDH–polymer interaction, resulting in membranes with greater mechanical performance compared to the polymer only or to the membranes containing the Cl-LDHs. Drug release (in saline solution) was sustained for at least 8 h for all samples and release kinetics could be modulated: a slower, an intermediate and a faster NAP release were observed from membranes containing Zn-NAP, NaNAP and Mg-NAP particles, respectively. In general, cell viability was higher in the presence of Mg-LDH and the membranes presented improved performance in comparison with the powdered samples. PEBA containing Mg-NAP sample stood out among all membranes in all the evaluated aspects, thus being considered a great candidate for application as multifunctional therapeutic dressings.

DOI link: https://doi.org/10.3390/pharmaceutics12111130

Appendix G. Supplementary data related to Chapter 8

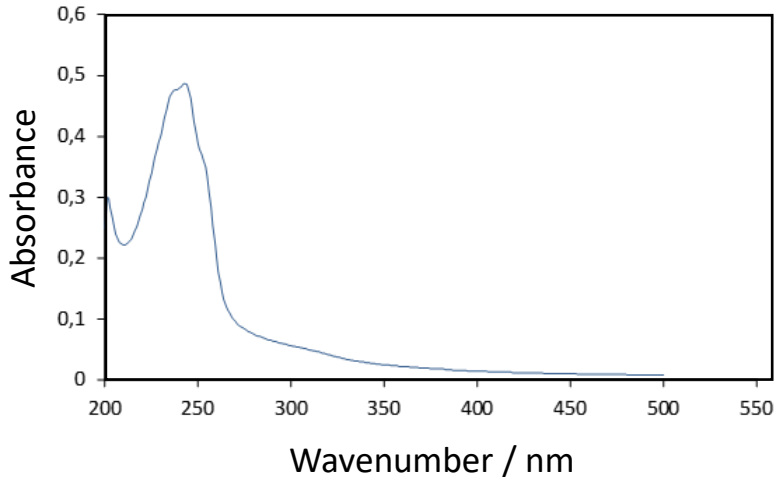

Figure G.1. Full-scan electronic spectra of ABI in physiologic solution at a concentration equal to 13.3 ppm.

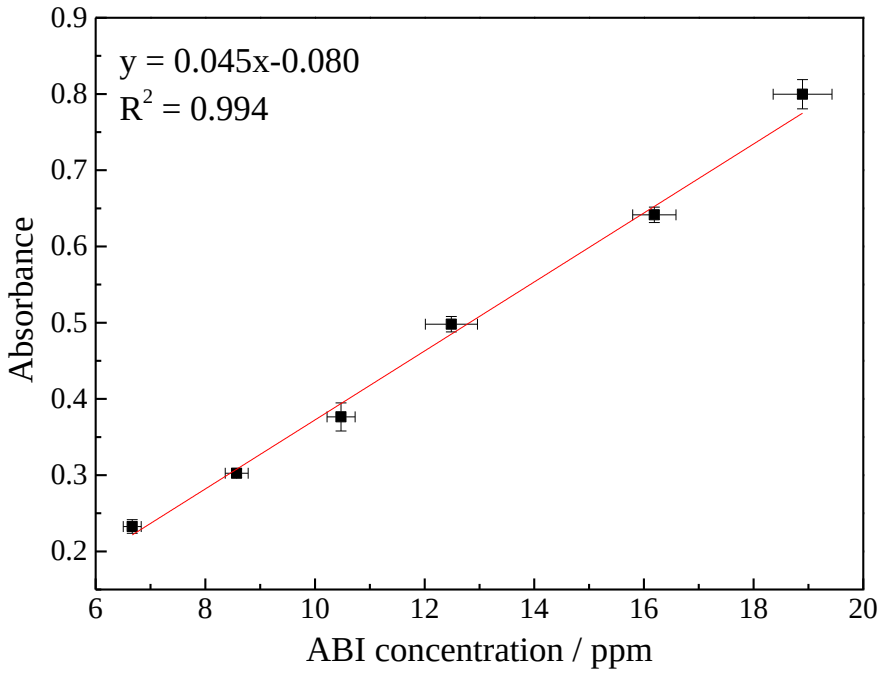

Figure G.2. Calibration curve: absorbance as a function of ABI concentration at λ = 243 nm.

NaABI and $Mg_2Fe_{0.5}Al_{0.5}$-ABI characterization

NaABI salt and LDH-ABI diffractograms are shown in **Figure G.3**. For the salt, a well-defined peak at (2θ) 4.23 ° and two broader peaks at (2θ) 15.23 and 29.10 ° are present. For the LDH-ABI sample, all peaks were indexed to the LDH phase. The elemental chemical composition of the $Mg_2Fe_{0.5}Al_{0.5}$-ABI LDH reveals a Mg^{2+} / (Fe^{3+} + Al^{3+}) and Fe^{3+}/Al^{3+} molar ratios equal to 2.07 and 1.04, respectively, thus very close to the nominal values. Carbon percentage was equal to 30.07 wt%, with corresponding ABI mass percentage equal to 37.77 %. Thus, LDH was able to intercalate a satisfactory amount of ABI.

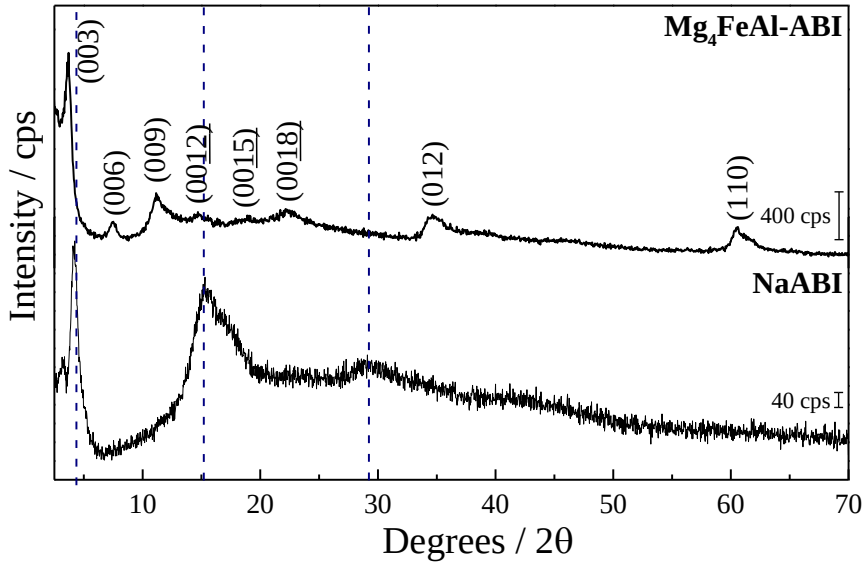

Figure G.3. XRD patterns of the NaABI and $Mg_2Fe_{0.5}Al_{0.5}$-ABI samples.

The FT-Raman and FT-IR spectra of the $Mg_2Fe_{0.5}Al_{0.5}$-ABI and NaABI samples (**Figures G.4** and **G.5**) do not review discrepancies compared to the results shown in **Chapter 5**.

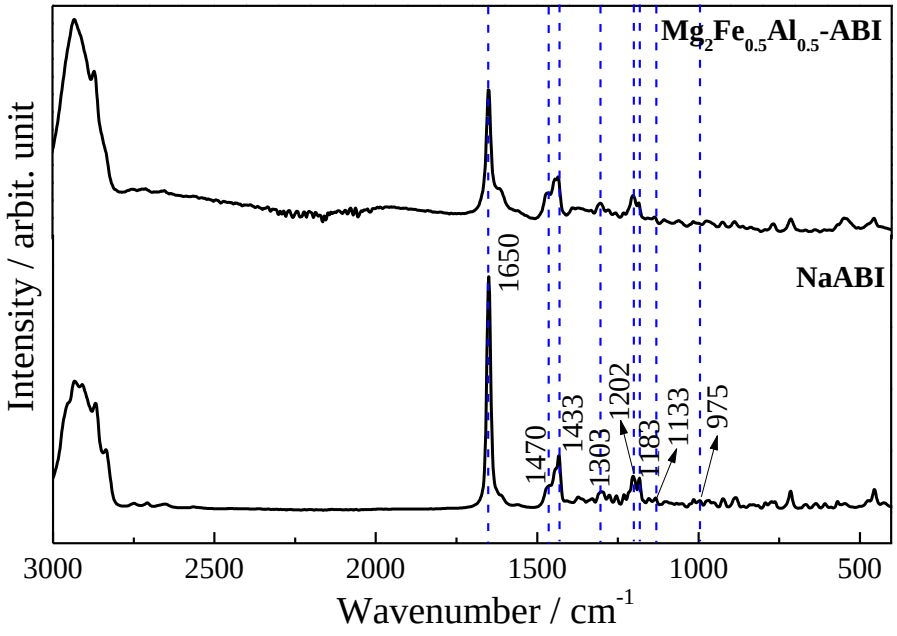

Figure G.4. FT-Raman spectra of the $Mg_2Fe_{0.5}Al_{0.5}$-ABI LDH and NaABI salt.

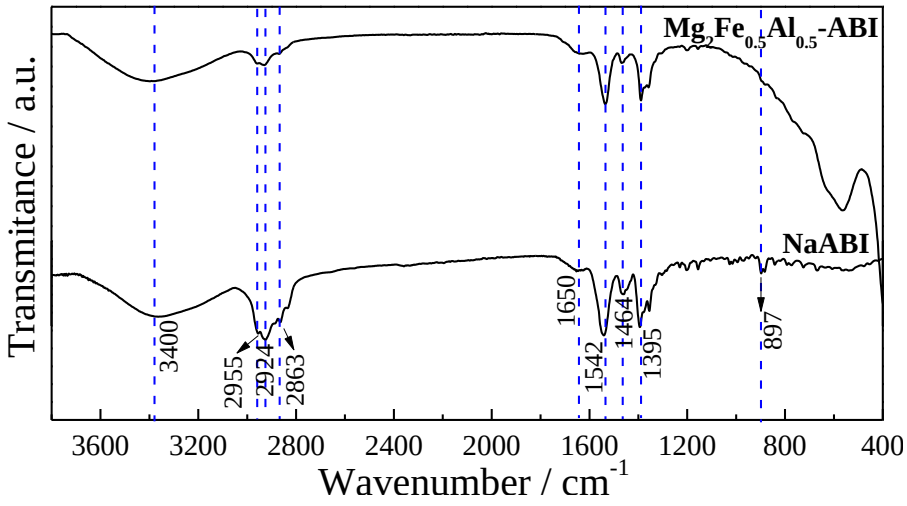

Figure G.5. FT-IR spectra of the $Mg_2Fe_{0.5}Al_{0.5}$-ABI LDH and NaABI salt.

REFERENCES

1. Iaquinta, M.; Mazzoni, E.; Manfrini, M.; D'Agostino, A.; Trevisiol, L.; Nocini, R.; Trombelli, L.; Barbanti-Brodano, G.; Martini, F.; Tognon, M. Innovative Biomaterials for Bone Regrowth. *Int. J. Mol. Sci.* **2019**, *20*, 618, doi:10.3390/ijms20030618.
2. Keller, L.; Pijnenburg, L.; Idoux-Gillet, Y.; Bornert, F.; Benameur, L.; Tabrizian, M.; Auvray, P.; Rosset, P.; María Gonzalo-Daganzo, R.; Gómez Barrena, E.; et al. Preclinical Safety Study of a Combined Therapeutic Bone Wound Dressing for Osteoarticular Regeneration. *Nat. Commun.* **2019**, *10*, 2156, doi:10.1038/s41467-019-10165-5.
3. Smoak, M.M.; Mikos, A.G. Advances in Biomaterials for Skeletal Muscle Engineering and Obstacles Still to Overcome. *Mater. Today Bio* **2020**, *7*, 100069, doi:10.1016/j.mtbio.2020.100069.
4. Dhivya, S.; Padma, V.V.; Santhini, E. Wound Dressings – a Review. *BioMed* **2015**, *5*, 22, doi:10.7603/s40681-015-0022-9.
5. Milan, P.B.; Kargozar, S.; Joghataie, M.T.; Samadikuchaksaraei, A. Chapter 11 - Nanoengineered biomaterials for skin regeneration. In *Nanoengineered Biomaterials for Regenerative Medicine*; Mozafari, M., Rajadas, J., Kaplan, D., Eds.; Elsevier, **2019**; pp. 265–283 ISBN 978-0-12-813355-2.
6. Giersiefen, H.; Hilgenfeld, R.; Hillisch, A. Modern methods of drug discovery: An introduction. In *Modern Methods of Drug Discovery*; Hillisch, A., Hilgenfeld, R., Eds.; Birkhäuser Basel: Basel, **2003**; pp. 1–18 ISBN 978-3-0348-7997-2.
7. Mizushima, T. Drug Discovery and Development Focusing on Existing Medicines: Drug Re-Profiling Strategy. *J. Biochem.* **2011**, *149*, 499–505, doi:10.1093/jb/mvr032.
8. Tiwari, G.; Tiwari, R.; Bannerjee, S.; Bhati, L.; Pandey, S.; Pandey, P.; Sriwastawa, B. Drug Delivery Systems: An Updated Review. *Int. J. Pharma. Investig.* **2012**, *2*, 2, doi:10.4103/2230-973X.96920.
9. Allen, T.M.; Cullis, P.R. Drug Delivery Systems: Entering the Mainstream. *Science* **2004**, *303*, 1818–1822, doi:10.1126/science.1095833.
10. Bulbake, U.; Doppalapudi, S.; Kommineni, N.; Khan, W. Liposomal Formulations in Clinical Use: An Updated Review. *Pharmaceutics* **2017**, *9*, 12, doi:10.3390/pharmaceutics9020012.
11. Werner, M.; Cummings, N.; Sethi, M.; Wang, E.; Sukumar, R.; Dominic, T.; Wang, A. Preclinical Evaluation of Genexol-PM, a Nanoparticle Formulation of Paclitaxel, as a Novel Radiosensitizer for the Treatment of Non-Small Cell Lung Cancer. Int. J. Radiat. Oncol. Biol. Phys. **2013**, *86*, 463–468, doi:10.1016/j.ijrobp.2013.02.009.
12. Mou, X.; Ali, Z.; Li, S.; He, N. Applications of Magnetic Nanoparticles in Targeted Drug Delivery System. *J. Nanosci. Nanotechnol.* **2015**, *15*, doi:10.1166/jnn.2015.9585.
13. Williams, D.F. On the Nature of Biomaterials. *Biomaterials* **2009**, *30*, 5897–5909, doi:10.1016/j.biomaterials.2009.07.027.
14. 6 - Drug delivery systems. In *Strategies to Modify the Drug Release from Pharmaceutical Systems*; Bruschi, M.L., Ed.; Woodhead Publishing, **2015**; pp. 87–194 ISBN 978-0-08-100092-2.
15. Ozdil, D.; Aydin, H.M. Polymers for Medical and Tissue Engineering Applications. *J. Chem. Technol. Biotechnol.* **2014**, *89*, doi:10.1002/jctb.4505.
16. Rattan, S.; Kargirwar, S.; Kondawar, S.; Ghosh, S.; Das, A.; Chakraborty, K.; Adhikari, J.; Mazumdar, P.; Sadasivuni, K. kumar; Mazumdar, Á.; et al. Polymer Nanocomposites in Biomedical Engineering. In; **2019**.

17. Williams, D.F. On the Mechanisms of Biocompatibility. *Biomaterials* **2008**, *29*, 2941–2953, doi:10.1016/j.biomaterials.2008.04.023.
18. Swetha, B.; Mathew, S.; Murthy, S.; Nagaraja, S.; Bhandi, S. Determination of Biocompatibility: A Review. *Int. Dent. Med. J. Adv. Res.* **2015**, *1*, 1–6, doi:10.15713/ins.idmjar.2.
19. Fadeel, B.; Pietroiusti, A.; Shvedova, A. *Adverse Effects of Engineered Nanomaterials: Exposure, Toxicology, and Impact on Human Health: Second Edition*; 2017; p. 468.
20. Allou, N.B.; Saikia, P.; Borah, A.; Goswamee, R.L. Hybrid Nanocomposites of Layered Double Hydroxides: An Update of Their Biological Applications and Future Prospects. *Colloid Polym. Sci.* **2017**, *295*, 725–747, doi:10.1007/s00396-017-4047-3.
21. Mishra, G.; Dash, B.; Pandey, S. Layered Double Hydroxides: A Brief Review from Fundamentals to Application as Evolving Biomaterials. *Appl. Clay Sci.* **2018**, *153*, 172–186, doi:10.1016/j.clay.2017.12.021.
22. Fan, G.; Li, F.; Evans, D.G.; Duan, X. Catalytic Applications of Layered Double Hydroxides: Recent Advances and Perspectives. *Chem. Soc. Rev.* **2014**, *43*, 7040–7066, doi:10.1039/C4CS00160E.
23. Xu, M.; Wei, M. Layered Double Hydroxide-Based Catalysts: Recent Advances in Preparation, Structure, and Applications. *Adv. Funct. Mater.* **2018**, *28*, 1802943, doi:10.1002/adfm.201802943.
24. Baig, N.; Sajid, M. Applications of Layered Double Hydroxides Based Electrochemical Sensors for Determination of Environmental Pollutants: A Review. *Tren. Environ. Anal. Chem.* **2017**, *16*, 1–15, doi:10.1016/j.teac.2017.10.003.
25. Shao, M.; Zhang, R.; Li, Z.; Wei, M.; Evans, D.G.; Duan, X. Layered Double Hydroxides toward Electrochemical Energy Storage and Conversion: Design, Synthesis and Applications. *Chem. Commun.* **2015**, *51*, 15880–15893, doi:10.1039/C5CC07296D.
26. Zubair, M.; Daud, M.; McKay, G.; Shehzad, F.; Al-Harthi, M.A. Recent Progress in Layered Double Hydroxides (LDH)-Containing Hybrids as Adsorbents for Water Remediation. *Appl. Clay Sci.* **2017**, *143*, 279–292, doi:10.1016/j.clay.2017.04.002.
27. Oh, J.-M.; Park, D.-H.; Choi, S.-J.; Choy, J.-H. LDH Nanocontainers as Bio-Reservoirs and Drug Delivery Carriers. *Recent Patents on Nanotechnology* **2012**, *6*, 200–217, doi:10.2174/187221012803531538.
28. Choi, G.; Eom, S.; Vinu, A.; Choy, J.-H. 2D Nanostructured Metal Hydroxides with Gene Delivery and Theranostic Functions; A Comprehensive Review. *Chem. Rec.* **2018**, *18*, 1033–1053, doi:10.1002/tcr.201700091.
29. Li, L.; Li, B.; Gu, W.; Xu, Z.P. Modifying Layered Double Hydroxide Nanoparticles for Tumor Imaging and Therapy. *Clays Clay Miner.* **2019**, *67*, 72–80, doi:10.1007/s42860-019-0006-z.
30. Fayyazbakhsh, F.; Solati-Hashjin, M.; Keshtkar, A.; Shokrgozar, M.A.; Dehghan, M.M.; Larijani, B. Novel Layered Double Hydroxides-Hydroxyapatite/Gelatin Bone Tissue Engineering Scaffolds: Fabrication, Characterization, and in Vivo Study. *Mater. Sci. Eng.* **2017**, *76*, 701–714, doi:10.1016/j.msec.2017.02.172.
31. Chatterjee, A.; Bharadiya, P.; Hansora, D. Layered Double Hydroxide Based Bionanocomposites. *Appl. Clay Sci.* **2019**, *177*, 19–36, doi:10.1016/j.clay.2019.04.022.
32. Choi, S.-J.; Oh, J.-M.; Choy, J.-H. Biocompatible Ceramic Nanocarrier for Drug Delivery with High Efficiency. *J. Ceram. Soc. Japan* **2009**, *117*, 543–549, doi:10.2109/jcersj2.117.543.
33. Cunha, V.R.R.; Guilherme, V.A.; de Paula, E.; de Araujo, D.R.; Silva, R.O.; Medeiros, J.V.R.; Leite, J.R.S.A.; Petersen, P.A.D.; Foldvari, M.; Petrilli, H.M.; et al. Delivery System for Mefenamic Acid Based on the Nanocarrier Layered Double Hydroxide:

Physicochemical Characterization and Evaluation of Anti-Inflammatory and Antinociceptive Potential. *Mater. Sci. Eng.* **2016**, *58*, 629–638, doi:10.1016/j.msec.2015.08.037.

34. Kuthati, Y.; Kankala, R.K.; Lee, C.-H. Layered Double Hydroxide Nanoparticles for Biomedical Applications: Current Status and Recent Prospects. *Appl. Clay Sci.* **2015**, *112–113*, 100–116, doi:10.1016/j.clay.2015.04.018.
35. Yan, M.; Yang, C.; Huang, B.; Huang, Z.; Huang, L.; Zhang, X.; Zhao, C. Systemic Toxicity Induced by Aggregated Layered Double Hydroxide Nanoparticles Available online: https://www.dovepress.com/systemic-toxicity-induced-by-aggregated-layered-double-hydroxide-nanop-peer-reviewed-article-IJN (accessed on 10 December 2019).
36. Cavani, F.; Trifiro, F.; Vaccari, A. Hydrotalcite-Type Anionic Clays: Preparation, Properties and Applications. *Catalysis Today* **1991**, 173–301, doi: 10.1016/0920-5861(91)80068-K.
37. Conterosito, E.; Palin, L.; Antonioli, D.; Viterbo, D.; Mugnaioli, E.; Kolb, U.; Perioli, L.; Milanesio, M.; Gianotti, V. Structural Characterisation of Complex Layered Double Hydroxides and TGA-GC-MS Study on Thermal Response and Carbonate Contamination in Nitrate- and Organic-Exchanged Hydrotalcites. *Chem. Eur. J.* **2015**, *21*, 14975–14986, doi:10.1002/chem.201500450.
38. Shannon, R.D. Revised Effective Ionic Radii and Systematic Studies of Interatomic Distances in Halides and Chalcogenides. *Acta Cryst A* **1976**, *32*, 751–767, doi:10.1107/S0567739476001551.
39. Forano, C.; Hibino, T.; Leroux, F.; Taviot-Guého, C. Chapter 13.1 Layered Double Hydroxides. In *Dev. Clay Sci*; Elsevier, **2006**; Vol. 1, pp. 1021–1095 ISBN 978-0-08-044183-2.
40. Jayanthi, K.; Vishnu Kamath, P.; Periyasamy, G. Electronic-Structure Calculations of Cation-Ordered II-III Layered Double Hydroxides: Origin of the Distortion of the Metal-Coordination Symmetry: Electronic-Structure Calculations of Cation-Ordered II-III Layered Double Hydroxides: Origin of the Distortion of the Metal-Coordination Symmetry. *Eur. J. Inorg. Chem.* **2017**, *2017*, 3675–3682, doi:10.1002/ejic.201700716.
41. Kwak, S. Bio-LDH Nanohybrid for Gene Therapy. *Solid State Ion.* **2002**, *151*, 229–234, doi:10.1016/S0167-2738(02)00714-2.
42. Choy, J.-H.; Oh, J.-M.; Park, M.; Sohn, K.-M.; Kim, J.-W. Inorganic–Biomolecular Hybrid Nanomaterials as a Genetic Molecular Code System. *Adv. Mater.* **2004**, *16*, 1181–1184, doi:10.1002/adma.200400027.
43. Xu, Z.P.; Walker, T.L.; Liu, K.; Cooper, H.M.; Lu, G.Q.M.; Bartlett, P.F. Layered Double Hydroxide Nanoparticles as Cellular Delivery Vectors of Supercoiled Plasmid DNA. *Int. J. Nanomedicine* **2007**, *2*, 163–174, doi:https://pubmed.ncbi.nlm.nih.gov/17722544.
44. Crepaldi, E.L.; Pavan, P.C.; Valim, J.B. Comparative Study of the Coprecipitation Methods for the Preparation of Layered Double Hydroxides. *Journal of the Brazilian Chemical Society* **2000**, *11*, 64–70, doi: 10.1590/S0103-50532000000100012.
45. Prasanna, S.V.; Kamath, P.V. Anion-Exchange Reactions of Layered Double Hydroxides: Interplay between Coulombic and H-Bonding Interactions. *Ind. Eng. Chem. Res.* **2009**, *48*, 6315–6320, doi:10.1021/ie9004332.
46. Xu, Z.P.; Lu, G.Q. (Max) Hydrothermal Synthesis of Layered Double Hydroxides (LDHs) from Mixed MgO and Al2O3: LDH Formation Mechanism. *Chem. Mater.* **2005**, *17*, 1055–1062, doi:10.1021/cm048085g.
47. Prince, J.; Montoya, A.; Ferrat, G.; Valente, J.S. Proposed General Sol−Gel Method to Prepare Multimetallic Layered Double Hydroxides: Synthesis, Characterization, and Envisaged Application. *Chem. Mater.* **2009**, *21*, 5826–5835, doi:10.1021/cm902741c.

48. Pushparaj, S.S.C.; Forano, C.; Prevot, V.; Lipton, A.S.; Rees, G.J.; Hanna, J.V.; Nielsen, U.G. How the Method of Synthesis Governs the Local and Global Structure of Zinc Aluminum Layered Double Hydroxides. *J. Phys. Chem. C* **2015**, *119*, 27695–27707, doi:10.1021/acs.jpcc.5b09490.
49. Kovanda, F.; Rojka, T.; Bezdička, P.; Jirátová, K.; Obalová, L.; Pacultová, K.; Bastl, Z.; Grygar, T. Effect of Hydrothermal Treatment on Properties of Ni–Al Layered Double Hydroxides and Related Mixed Oxides. *J. Solid State Chem.* **2009**, *182*, 27–36, doi:10.1016/j.jssc.2008.09.014.
50. Benito, P.; Herrero, M.; Labajos, F.; Rives, V. Effect of Post-Synthesis Microwave–Hydrothermal Treatment on the Properties of Layered Double Hydroxides and Related Materials. *Appl. Clay Sci.* **2010**, *48*, 218–227, doi:10.1016/j.clay.2009.11.051.
51. Gao, X.; Lei, L.; O'Hare, D.; Xie, J.; Gao, P.; Chang, T. Intercalation and Controlled Release Properties of Vitamin C Intercalated Layered Double Hydroxide. *J. Solid State Chem.* **2013**, *203*, 174–180, doi:10.1016/j.jssc.2013.04.028.
52. Ding, P.; Tang, S.F.; Li, Z.Z. Influence of Metal Cations on the Structure and Release Property of Layered Double Hydroxide-Ibuprofen Host-Guest Materials. *AMR* **2010**, *152–153*, 556–559, doi:10.4028/www.scientific.net/AMR.152-153.556.
53. Braterman, P.; Xu, Z.P.; Yarberry, F. Handbook of Layered Materials. *Layered Double Hydroxides (LDHs)* **2004**, 373–474.
54. Peterson, C.L.; Perry, D.L.; Masood, H.; White, J.L.; Hem, S.L.; Fritsch, C.; Haeusler, F. Characterization of Antacid Compounds Containing Both Aluminum and Magnesium. II. Codried Powders. *Pharm. Res.* **1993**, *10*, 1005–1007, doi:10.1023/A:1018910705853.
55. Schmassmann, A.; Tarnawski, A.; Gerber, H.A.; Flogerzi, B.; Sanner, M.; Varga, L.; Halter, F. Antacid Provides Better Restoration of Glandular Structures within the Gastric Ulcer Scar than Omeprazole. *Gut* **1994**, *35*, 896–904, doi:10.1136/gut.35.7.896.
56. Tarnawski, A.S.; Tomikawa, M.; Ohta, M.; Sarfeh, I.J. Antacid Talcid Activates in Gastric Mucosa Genes Encoding for EGF and Its Receptor. The Molecular Basis for Its Ulcer Healing Action. *J. Physiol. Paris* **2000**, *94*, 93–98, doi:10.1016/S0928-4257(00)00149-2.
57. Gusić, N.; Ivković, A.; VaFaye, J.; Vukasović, A.; Ivković, J.; Hudetz, D.; Janković, S. Nanobiotechnology and Bone Regeneration: A Mini-Review. *International Orthopaedics (SICOT)* **2014**, *38*, 1877–1884, doi:10.1007/s00264-014-2412-0.
58. Kapusetti, G.; Misra, N.; Singh, V.; Kushwaha, R.K.; Maiti, P. Bone Cement/Layered Double Hydroxide Nanocomposites as Potential Biomaterials for Joint Implant: Bone Cement and LDH Nanocomposite. *J. Biomed. Mater. Res.* **2012**, *100A*, 3363–3373, doi:10.1002/jbm.a.34296.
59. Rives, V.; del Arco, M.; Martín, C. Layered Double Hydroxides as Drug Carriers and for Controlled Release of Non-Steroidal Antiinflammatory Drugs (NSAIDs): A Review. *J. Control. Release* **2013**, *169*, 28–39, doi:10.1016/j.jconrel.2013.03.034.
60. Nakayama, H.; Wada, N.; Tsuhako, M. Intercalation of Amino Acids and Peptides into Mg-Al Layered Double Hydroxide by Reconstruction Method. *Int. J. Pharm.* **2004**, *269*, 469–478, doi:10.1016/j.ijpharm.2003.09.043.
61. Woo, M.A.; Woo Kim, T.; Paek, M.-J.; Ha, H.-W.; Choy, J.-H.; Hwang, S.-J. Phosphate-Intercalated Ca–Fe-Layered Double Hydroxides: Crystal Structure, Bonding Character, and Release Kinetics of Phosphate. *J. Solid State Chem.* **2011**, *184*, 171–176, doi:10.1016/j.jssc.2010.11.003.
62. Li, L.; Gu, W.; Chen, J.; Chen, W.; Xu, Z.P. Co-Delivery of SiRNAs and Anti-Cancer Drugs Using Layered Double Hydroxide Nanoparticles. *Biomaterials* **2014**, *35*, 3331–3339, doi:10.1016/j.biomaterials.2013.12.095.

63. Gu, Z.; Rolfe, B.E.; Xu, Z.P.; Campbell, J.H.; Lu, G.Q.M.; Thomas, A.C. Antibody-Targeted Drug Delivery to Injured Arteries Using Layered Double Hydroxide Nanoparticles. *Adv. Healthc. Mater.* **2012**, *1*, 669–673, doi:10.1002/adhm.201200069.
64. Peng, L.; Mei, X.; He, J.; Xu, J.; Zhang, W.; Liang, R.; Wei, M.; Evans, D.G.; Duan, X. Monolayer Nanosheets with an Extremely High Drug Loading toward Controlled Delivery and Cancer Theranostics. *Adv. Mater.* **2018**, *30*, 1707389, doi:https://doi.org/10.1002/adma.201707389.
65. Andrade, K.N.; Pérez, A.M.P.; Arízaga, G.G.C. Passive and Active Targeting Strategies in Hybrid Layered Double Hydroxides Nanoparticles for Tumor Bioimaging and Therapy. *Appl. Clay Sci.* **2019**, *181*, 105214, doi:10.1016/j.clay.2019.105214.
66. Hakeem, A.; Zhan, G.; Xu, Q.; Yong, T.; Yang, X.; Gan, L. Facile Synthesis of PH-Responsive Doxorubicin-Loaded Layered Double Hydroxide for Efficient Cancer Therapy. *J. Mater. Chem. B* **2018**, *6*, 5768–5774, doi:10.1039/C8TB01572D.
67. Choi, S.-J.; Oh, J.-M.; Choy, J.-H. Toxicological Effects of Inorganic Nanoparticles on Human Lung Cancer A549 Cells. *J. Inorg. Biochem.* **2009**, *103*, 463–471, doi:10.1016/j.jinorgbio.2008.12.017.
68. Kankala, R.K.; Kuthati, Y.; Sie, H.-W.; Shih, H.-Y.; Lue, S.-I.; Kankala, S.; Jeng, C.-C.; Deng, J.-P.; Weng, C.-F.; Liu, C.-L.; et al. Multi-Laminated Metal Hydroxide Nanocontainers for Oral-Specific Delivery for Bioavailability Improvement and Treatment of Inflammatory Paw Edema in Mice. *J. Colloid Interface Sci.* **2015**, *458*, 217–228, doi:10.1016/j.jcis.2015.07.044.
69. Menezes, J.; da Silva, T.; dos Santos, J.; Catari, E.; Meneghetti, M.; da Matta, C.; Alexandre-Moreira, M.; Santos-Magalhães, N.; Grillo, L.; Dornelas, C. Layered Double Hydroxides (LDHs) as Carrier of Antimony Aimed for Improving Leishmaniasis Chemotherapy. *Appl. Clay Sci.* **2014**, *91–92*, 127–134, doi:10.1016/j.clay.2013.12.029.
70. Liu, Z.-L.; Tian, D.-Y.; Li, S.-P.; Li, X.-D.; Lu, T.-H. MTX/LDHs Hybrids Synthesized from Reverse Microemulsions: Particle Control and Bioassay Study. *Int. J. Pharm.* **2014**, *473*, 414–425, doi:10.1016/j.ijpharm.2014.07.044.
71. Qiao, C.; Liu, J.; Yang, J.; Li, Y.; Weng, J.; Shao, Y.; Zhang, X. Enhanced Non-Inflammasome Mediated Immune Responses by Mannosylated Zwitterionic-Based Cationic Liposomes for HIV DNA Vaccines. *Biomaterials* **2016**, *85*, 1–17, doi:10.1016/j.biomaterials.2016.01.054.
72. Zhang, X.-Q.; Zeng, M.-G.; Li, S.-P.; Li, X.-D. Methotrexate Intercalated Layered Double Hydroxides with Different Particle Sizes: Structural Study and Controlled Release Properties. *Colloids Surf. B* **2014**, *117*, 98–106, doi:10.1016/j.colsurfb.2014.02.018.
73. Cunha, V.R.R.; de Souza, R.B.; da Fonseca Martins, A.M.C.R.P.; Koh, I.H.J.; Constantino, V.R.L. Accessing the Biocompatibility of Layered Double Hydroxide by Intramuscular Implantation: Histological and Microcirculation Evaluation. *Sci. Rep.* **2016**, *6*, 30547, doi:10.1038/srep30547.
74. Mold, M.; Shardlow, E.; Exley, C. Insight into the Cellular Fate and Toxicity of Aluminium Adjuvants Used in Clinically Approved Human Vaccinations. *Sci. Rep.* **2016**, *6*, 31578, doi:10.1038/srep31578.
75. Krewski, D.; Yokel, R.A.; Nieboer, E.; Borchelt, D.; Cohen, J.; Harry, J.; Kacew, S.; Lindsay, J.; Mahfouz, A.M.; Rondeau, V. Human Health Risk Assessment for Aluminium, Aluminium Oxide, and Aluminium Hydroxide. *J. Toxicol. Environ. Health B Crit. Rev.* **2007**, *10 Suppl 1*, 1–269, doi:10.1080/10937400701597766.
76. Kumar, V.; Gill, K. Aluminium Neurotoxicity: Neurobehavioural and Oxidative Aspects. *Archives of Toxicology* **2009**, *83*, 965–978, doi:10.1007/s00204-009-0455-6.

77. Bhagavan, N. V. *Medical Biochemistry*; 4th ed.; Academic Press, 2002;
78. Kishore, D.; Kannan, S. Double Bond Migration of Eugenol to Isoeugenol over As-Synthesized Hydrotalcites and Their Modified Forms. *Appl. Catal. A: Gen.* **2004**, *270*, 227–235, doi:10.1016/j.apcata.2004.05.008.
79. Choudhary, V.R.; Dumbre, D.K.; Uphade, B.S.; Narkhede, V.S. Solvent-Free Oxidation of Benzyl Alcohol to Benzaldehyde by Tert-Butyl Hydroperoxide Using Transition Metal Containing Layered Double Hydroxides and/or Mixed Hydroxides. *J. Mol. Catal. A Chem.* **2004**, *215*, 129–135, doi:10.1016/j.molcata.2004.01.009.
80. Benício, L.P.; Silva, R.; Lopes, J.; Eulálio, D.; Santos, R.; Aquino, L.; Vergutz, L.; Novais, R.; Costa, L.; Pinto, F.; et al. Layered Double Hydroxides: Nanomaterials for Applications in Agriculture. *Revista Brasileira de Ciência do Solo* **2015**, *39*, 1–13, doi:10.1590/01000683rbcs20150817.
81. Patel, R.; Park, J.T.; Patel, M.; Dash, J.K.; Gowd, E.B.; Karpoormath, R.; Mishra, A.; Kwak, J.; Kim, J.H. Transition-Metal-Based Layered Double Hydroxides Tailored for Energy Conversion and Storage. *J. Mater. Chem. A* **2018**, *6*, 12–29, doi:10.1039/C7TA09370E.
82. Gomes, A.; Cocke, D.; Tran, D.; Baksi, A. Layered Double Hydroxides in Energy Research: Advantages and Challenges. In; 2015; pp. 309–316 ISBN 978-1-119-08240-8.
83. Caporale, A.G.; Pigna, M.; Dynes, J.J.; Cozzolino, V.; Zhu, J.; Violante, A. Effect of Inorganic and Organic Ligands on the Sorption/Desorption of Arsenate on/from Al–Mg and Fe–Mg Layered Double Hydroxides. *J. Hazard. Mater.* **2011**, *198*, 291–298, doi:10.1016/j.jhazmat.2011.10.044.
84. Benselka-Hadj Abdelkader, N.; Bentouami, A.; Derriche, Z.; Bettahar, N.; de Ménorval, L.-C. Synthesis and Characterization of Mg–Fe Layer Double Hydroxides and Its Application on Adsorption of Orange G from Aqueous Solution. *Chem. Eng. J.* **2011**, *169*, 231–238, doi:10.1016/j.cej.2011.03.019.
85. Ahmed, A.A.A.; Talib, Z.A.; Hussein, M.Z.; Flaifel, M.H.; Al-Hada, N.M. Influence of Zn/Fe Molar Ratio on Optical and Magnetic Properties of ZnO and $ZnFe_2O_4$ Nanocrystal as Calcined Products of Layered Double Hydroxides. *J. Spectrosc.* **2014**, *2014*, 1–6, doi:10.1155/2014/732163.
86. Gasser, M.S.; Mohsen, H.T.; Aly, H.F. Humic Acid Adsorption onto Mg/Fe Layered Double Hydroxide. *Colloids and Surfaces A: Colloids Surf. A Physicochem. Eng. Asp.* **2008**, *331*, 195–201, doi:10.1016/j.colsurfa.2008.08.002.
87. Halajnia, A.; Oustan, S.; Najafi, N.; Khataee, A.R.; Lakzian, A. The Adsorption Characteristics of Nitrate on Mg–Fe and Mg–Al Layered Double Hydroxides in a Simulated Soil Solution. *Appl. Clay Sci.* **2012**, *70*, 28–36, doi:10.1016/j.clay.2012.09.007.
88. Yang, Y.; Gao, N.; Deng, Y.; Zhou, S. Adsorption of Perchlorate from Water Using Calcined Iron-Based Layered Double Hydroxides. *Appl. Clay Sci.* **2012**, *65–66*, 80–86, doi:10.1016/j.clay.2012.04.030.
89. Guo, Y.; Zhu, Z.; Qiu, Y.; Zhao, J. Enhanced Adsorption of Acid Brown 14 Dye on Calcined Mg/Fe Layered Double Hydroxide with Memory Effect. *Chem. Eng. J.* **2013**, *219*, 69–77, doi:10.1016/j.cej.2012.12.084.
90. Kang, D.; Yu, X.; Tong, S.; Ge, M.; Zuo, J.; Cao, C.; Song, W. Performance and Mechanism of Mg/Fe Layered Double Hydroxides for Fluoride and Arsenate Removal from Aqueous Solution. *Chem. Eng. J.* **2013**, *228*, 731–740, doi:10.1016/j.cej.2013.05.041.
91. Jiang, J.-Q.; Ashekuzzaman, S.M.; Hargreaves, J.S.J.; McFarlane, A.R.; Badruzzaman, A.B.M.; Tarek, M.H. Removal of Arsenic (III) from Groundwater Applying a Reusable

Mg-Fe-Cl Layered Double Hydroxide. *J. Chem. Technol. Biotechnol.* **2015**, *90*, 1160–1166, doi:10.1002/jctb.4607.
92. Peng, C.; Dai, J.; Yu, J.; Yin, J. Calcined Mg-Fe Layered Double Hydroxide as an Absorber for the Removal of Methyl Orange. *AIP Advances* **2015**, *5*, 057138, doi:10.1063/1.4921455.
93. Pigna, M.; Dynes, J.J.; Violante, A.; Sommella, A.; Caporale, A.G. Sorption of Arsenite on Cu-Al, Mg-Al, Mg-Fe, and Zn-Al Layered Double Hydroxides in the Presence of Inorganic Anions Commonly Found in Aquatic Environments. *Environ. Eng. Sci.* **2016**, *33*, 98–104, doi:10.1089/ees.2015.0131.
94. Gasser, M.S. Inorganic Layered Double Hydroxides as Ascorbic Acid (Vitamin C) Delivery System—Intercalation and Their Controlled Release Properties. *Colloids Surf. B* **2009**, *73*, 103–109, doi:10.1016/j.colsurfb.2009.05.005.
95. Chitrakar, R.; Tezuka, S.; Sonoda, A.; Sakane, K.; Hirotsu, T. A New Method for Synthesis of Mg−Al, Mg−Fe, and Zn−Al Layered Double Hydroxides and Their Uptake Properties of Bromide Ion. *Ind. Eng. Chem. Res.* **2008**, *47*, 4905–4908, doi:10.1021/ie0716417.
96. Vrbková, E.; Vyskočilová, E.; Semrádová, A.; Sekerová, L.; Červený, L. Mixed Oxides as Successful Sorption Materials for Some Active Pharmaceutical Ingredients. *Chem. Biochem. Eng. Q* . **2020**, *34*, doi:10.15255/CABEQ.2020.1774.
97. Web of Science Available online: https://www.webofknowledge.com (accessed on 5 August 2021).
98. Ding, Y.; Liu, L.; Fang, Y.; Zhang, X.; Lyu, M.; Wang, S. The Adsorption of Dextranase onto Mg/Fe-Layered Double Hydroxide: Insight into the Immobilization. *Nanomaterials* **2018**, *8*, 173, doi:10.3390/nano8030173.
99. Peng, F.; Wang, D.; Zhang, D.; Cao, H.; Liu, X. The Prospect of Layered Double Hydroxide as Bone Implants: A Study of Mechanical Properties, Cytocompatibility and Antibacterial Activity. *Appl. Clay Sci.* **2018**, *165*, 179–187, doi:10.1016/j.clay.2018.08.020.
100. Balcomb, B.; Singh, M.; Singh, S. Synthesis and Characterization of Layered Double Hydroxides and Their Potential as Nonviral Gene Delivery Vehicles. *ChemistryOpen* **2015**, *4*, 137–145, doi:10.1002/open.201402074.
101. Moaty, S.A.A.; Farghali, A.A.; Khaled, R. Preparation, Characterization and Antimicrobial Applications of Zn-Fe LDH against MRSA. *Mater. Sci. Eng. C* **2016**, *68*, 184–193, doi:10.1016/j.msec.2016.05.110.
102. Dias, A.; Cunha, L.; Vieira, A.C. Synthesis and Properties of A6B2(OH)16Cl2·4H2O (A=Mg, Ni, Zn, Co, Mn and B=Al, Fe) Materials for Environmental Applications. *Mater. Res. Bull.* **2011**, *46*, 1346–1351, doi:10.1016/j.materresbull.2011.05.022.
103. Xu, S.; Liao, M.-C.; Zeng, H.-Y.; Chen, C.-R.; Duan, H.-Z.; Liu, X.-J.; Du, J.-Z. Magnetic Hydrotalcites as Solid Basic Catalysts for Cellulose Hydrolysis. *Appl. Clay Sci.* **2015**, *115*, 124–131, doi:10.1016/j.clay.2015.07.039.
104. Morimoto, K.; Tamura, K.; Anraku, S.; Sato, T.; Suzuki, M.; Yamada, H. Synthesis of Zn–Fe Layered Double Hydroxides via an Oxidation Process and Structural Analysis of Products. *J. Solid State Chem.* **2015**, *228*, 221–225, doi:10.1016/j.jssc.2015.04.045.
105. Xia, S.-J.; Liu, F.-X.; Ni, Z.-M.; Xue, J.-L.; Qian, P.-P. Layered Double Hydroxides as Efficient Photocatalysts for Visible-Light Degradation of Rhodamine B. *J. Colloid Interface Sci.* **2013**, *405*, 195–200, doi:10.1016/j.jcis.2013.05.064.
106. Seftel, E.M.; Cool, P.; Lutic, D. Mg–Al and Zn–Fe Layered Double Hydroxides Used for Organic Species Storage and Controlled Release. *Mater. Sci. Eng. C* **2013**, *33*, 5071–5078, doi:10.1016/j.msec.2013.08.041.

107. Yang, B.; Liu, D.; Lu, J.; Meng, X.; Sun, Y. Phosphate Uptake Behavior and Mechanism Analysis of Facilely Synthesized Nanocrystalline Zn-Fe Layered Double Hydroxide with Chloride Intercalation. *Surf. Interface Anal* **2018**, *50*, 378–392, doi:10.1002/sia.6391.
108. Lu, H.; Zhu, Z.; Zhang, H.; Zhu, J.; Qiu, Y. Simultaneous Removal of Arsenate and Antimonate in Simulated and Practical Water Samples by Adsorption onto Zn/Fe Layered Double Hydroxide. *Chem. Eng. J.* **2015**, *276*, 365–375, doi:10.1016/j.cej.2015.04.095.
109. Morimoto, K.; Tamura, K.; Yamada, H.; Sato, T.; Suzuki, M. Determination and Reduction of Fe(III) Incorporated into Mg–Fe Layered Double Hydroxide Structures. *Appl. Clay Sci.* **2016**, *121–122*, 71–76, doi:10.1016/j.clay.2015.12.008.
110. Lung, Y.-F.; Sun, Y.-S.; Lin, C.-K.; Uan, J.-Y.; Huang, H.-H. Synthesis of Mg-Fe-Cl Hydrotalcite-like Nanoplatelets as an Oral Phosphate Binder: Evaluations of Phosphorus Intercalation Activity and Cellular Cytotoxicity. *Sci Rep* **2016**, *6*, 32458, doi:10.1038/srep32458.
111. 2018 Li Regulating the Local PH Level of Titanium via Mg-Fe Layered Double.Pdf.
112. Weizbauer, A.; Kieke, M.; Rahim, M.I.; Angrisani, G.L.; Willbold, E.; Diekmann, J.; Flörkemeier, T.; Windhagen, H.; Müller, P.P.; Behrens, P.; et al. Magnesium-Containing Layered Double Hydroxides as Orthopaedic Implant Coating Materials-An *in Vitro* and *in Vivo* Study, *J. Biomed. Mater. Res.* **2016**, *104*, 525–531, doi:10.1002/jbm.b.33422.
113. Aisawa, S.; Higashiyama, N.; Takahashi, S.; Hirahara, H.; Ikematsu, D.; Kondo, H.; Nakayama, H.; Narita, E. Intercalation Behavior of L-Ascorbic Acid into Layered Double Hydroxides. *Appl. Clay Sci.* **2007**, *35*, 146–154, doi:10.1016/j.clay.2006.09.003.
114. Kang, H.; Kim, M.; Feng, Q.; Lin, S.; Wei, K.; Li, R.; Choi, C.J.; Kim, T.-H.; Li, G.; Oh, J.-M.; et al. Nanolayered Hybrid Mediates Synergistic Co-Delivery of Ligand and Ligation Activator for Inducing Stem Cell Differentiation and Tissue Healing. *Biomaterials* **2017**, *149*, 12–28, doi:10.1016/j.biomaterials.2017.09.035.
115. Figueiredo, M.P.; Cunha, V.R.R.; Leroux, F.; Gueho, C.T.; Nakamae, M.N.; Kang, Y.R.; Souza, R.B.; Martins, A.M.C.R.P.F.; Koh, I.H.J.; Constantino, V.R.L. Iron-based layered double hydroxide implants: potential drug delivery carriers with tissue biointegration promotion and blood microcirculation preservation. *Acs Omega* **2018**, *3*, 18263–18274.
116. Li, Q.; Wang, D.; Qiu, J.; Peng, F.; Liu, X. Regulating the Local PH Level of Titanium: Via Mg-Fe Layered Double Hydroxides Films for Enhanced Osteogenesis. *Biomater. Sci.* **2018**, *6*, doi:10.1039/C8BM00100F.
117. Chahade, W.H.; Giorgi, R.D.N.; Szajubok, J.C.M. Antiinflamatórios não hormonais. *Einstein* **2008**, *6 (Supl 1)*, S166–S174.
118. Wongrakpanich, S.; Wongrakpanich, A.; Melhado, K.; Rangaswami, J. A Comprehensive Review of Non-Steroidal Anti-Inflammatory Drug Use in The Elderly. *Aging Dis.* **2018**, *9*, 143–150, doi:10.14336/AD.2017.0306.
119. Gordijo, C.R.; Barbosa, C.A.S.; Da Costa Ferreira, A.M.; Constantino, V.R.L.; Oliveira Silva, D. de Immobilization of Ibuprofen and Copper-Ibuprofen Drugs on Layered Double Hydroxides. *J. Pharm. Sci.* **2005**, *94*, 1135–1148, doi:10.1002/jps.20336.
120. Martino, P.D.; Barthélémy, C.; Joiris, E.; Capsoni, D.; Masic, A.; Massarotti, V.; Gobetto, R.; Bini, M.; Martelli, S. A New Tetrahydrated Form of Sodium Naproxen. *J. Pharm. Sci.* **2007**, *96*, 156–167, doi:10.1002/jps.20741.
121. del Arco, M.; Gutiérrez, S.; Martín, C.; Rives, V.; Rocha, J. Synthesis and Characterization of Layered Double Hydroxides (LDH) Intercalated with Non-

Steroidal Anti-Inflammatory Drugs (NSAID). *J. Solid State Chem.* **2004**, *177*, 3954–3962, doi:10.1016/j.jssc.2004.08.006.

122. Wei, M.; Shi, S.; Wang, J.; Li, Y.; Duan, X. Studies on the Intercalation of Naproxen into Layered Double Hydroxide and Its Thermal Decomposition by in Situ FT-IR and in Situ HT-XRD. *J. Solid State Chem.* **2004**, *177*, 2534–2541, doi:10.1016/j.jssc.2004.03.041.
123. Hou, W.-G.; Jin, Z.-L. Synthesis and Characterization of Naproxen Intercalated Zn–Al Layered Double Hydroxides. *Colloid Polym Sci* **2007**, *285*, 1449–1454, doi:10.1007/s00396-007-1704-y.
124. Berber, M.R.; Minagawa, K.; Katoh, M.; Mori, T.; Tanaka, M. Nanocomposites of 2-Arylpropionic Acid Drugs Based on Mg–Al Layered Double Hydroxide for Dissolution Enhancement. *Eur. J. Pharm. Sci.* **2008**, *35*, 354–360, doi:10.1016/j.ejps.2008.08.006.
125. Gunawan, P.; Xu, R. Synthesis of Unusual Coral-like Layered Double Hydroxide Microspheres in a Nonaqueous Polar Solvent/Surfactant System. *J. Mater. Chem.* **2008**, *18*, 2112, doi:10.1039/b719817e.
126. Carriazo, D.; del Arco, M.; Martín, C.; Ramos, C.; Rives, V. Influence of the Inorganic Matrix Nature on the Sustained Release of Naproxen. *Micropor. Mesopor. Mat.* **2010**, *130*, 229–238, doi:10.1016/j.micromeso.2009.11.014.
127. Rezvani, Z.; Sarkarat, M. Synthesis and Characterization of Magnetic Composites: Intercalation of Naproxen into Mg-Al Layered Double Hydroxides Coated on Fe3O4. *Z. anorg. allg. Chem.* **2012**, *638*, 874–880, doi:10.1002/zaac.201100487.
128. Jácome-Acatitla, G.; Tzompantzi, F.; López-González, R.; García-Mendoza, C.; Alvaro, J.M.; Gómez, R. Photodegradation of Sodium Naproxen and Oxytetracycline Hydrochloride in Aqueous Medium Using as Photocatalysts Mg-Al Calcined Hydrotalcites. *J. Photochem. Photobiol. A: Chem.* **2014**, *277*, 82–89, doi:10.1016/j.jphotochem.2013.12.014.
129. Rojas, R.; Jimenez-Kairuz, A.F.; Manzo, R.H.; Giacomelli, C.E. Release Kinetics from LDH-Drug Hybrids: Effect of Layers Stacking and Drug Solubility and Polarity. *Colloids Surf. A Physicochem. Eng. Asp.* **2014**, *463*, 37–43, doi:10.1016/j.colsurfa.2014.09.031.
130. Rojas, R.; Linck, Y.G.; Cuffini, S.L.; Monti, G.A.; Giacomelli, C.E. Structural and Physicochemical Aspects of Drug Release from Layered Double Hydroxides and Layered Hydroxide Salts. *Appl. Clay Sci.* **2015**, *109–110*, 119–126, doi:10.1016/j.clay.2015.02.030.
131. Delarco, M.; Fernandez, A.; Martin, C.; Rives, V. Release Studies of Different NSAIDs Encapsulated in Mg,Al,Fe-Hydrotalcites. *Appl. Clay Sci.* **2009**, *42*, 538–544, doi:10.1016/j.clay.2008.06.014.
132. Stephen C. McNeill; Russell O. Potts; Michael L. Francoeur Local Enhanced Topical Delivery (LETD) of Drugs: Does It Truly Exist? **1992**, *9*, 1422–1427, doi: 10.1023/a:1015854728278.
133. Attia, D.A. In Vitro and in Vivo Evaluation of Transdermal Absorption of Naproxen Sodium. *Aust. J. Basic & Appl. Sci* **2009**, 3 (3), 2154-2165.
134. Argemí, A.; Ellis, J.L.; Saurina, J.; Tomasko, D.L. Development of a Polymeric Patch Impregnated with Naproxen as a Model of Transdermal Sustained Release System. *J. Pharm. Sci.* **2011**, *100*, 992–1000, doi:10.1002/jps.22346.
135. Khatun, M.; Islam, S.A.; Akter, P.; Quadir, M.A.; Reza, Md.S. Controlled Release of Naproxen Sodium from Eudragit RS 100 Transdermal Film. *Dhaka Univ. J. Pharm. Sci* **1970**, *3*, doi:10.3329/dujps.v3i1.175.
136. Rodrigues, M.R.; Lanzarini, C.M.; Ricci-Junior, E. Preparation, in Vitro Characterization and in Vivo Release of Naproxen Loaded in Poly-Caprolactone

Nanoparticles. *Pharmaceutical Development and Technology* **2011**, *16*, 12–21, doi:10.3109/10837450903460475.
137. Üstündağ Okur, N.; Apaydın, Ş.; Karabay Yavaşoğlu, N.Ü.; Yavaşoğlu, A.; Karasulu, H.Y. Evaluation of Skin Permeation and Anti-Inflammatory and Analgesic Effects of New Naproxen Microemulsion Formulations. *Int. J. Pharm.* **2011**, S0378517311005606, doi:10.1016/j.ijpharm.2011.06.026.
138. Taviot-Guého, C.; Prévot, V.; Forano, C.; Renaudin, G.; Mousty, C.; Leroux, F. Tailoring Hybrid Layered Double Hydroxides for the Development of Innovative Applications. *Adv. Funct. Mater.* **2018**, *28*, 1703868, doi:10.1002/adfm.201703868.
139. Silvestre, A.J.D.; Gandini, A. Rosin: Major Sources, Properties and Applications. In *Monomers, Polymers and Composites from Renewable Resources*; Elsevier, **2008**; pp. 67–88 ISBN 978-0-08-045316-3.
140. San Feliciano, A.; Gordaliza, M.; Salinero, M.; del Corral, J. Abietane Acids: Sources, Biological Activities, and Therapeutic Uses. *Planta Med* **1993**, *59*, 485–490, doi:10.1055/s-2006-959744.
141. Fernández, M.A.; Tornos, M.P.; García, M.D.; de las Heras, B.; Villar, A.M.; Sáenz, M.T. Anti-Inflammatory Activity of Abietic Acid, a Diterpene Isolated from *Pimenta Racemosa* Var. Grissea. *J. Pharm. Pharmacol.* **2001**, *53*, 867–872, doi:10.1211/0022357011776027.
142. Neto, Í.; Faustino, C.; Rijo, P. Antimicrobial Abietane Diterpenoids against Resistant Bacteria and Biofilms. Book: The Battle Against Microbial Pathogens: Basic Science, Technological Advances and Educational ProgramsEdition: Microbiology Book Series, **2015**.
143. Mahizan, N.A.; Yang, S.-K.; Moo, C.-L.; Song, A.A.-L.; Chong, C.-M.; Chong, C.-W.; Abushelaibi, A.; Lim, S.-H.E.; Lai, K.-S. Terpene Derivatives as a Potential Agent against Antimicrobial Resistance (AMR) Pathogens. *Molecules* **2019**, 1–21, doi: 10.3390/molecules24142631.
144. Hsieh, Y.-S.; Yang, S.-F.; Hsieh, Y.-H.; Hung, C.-H.; Chu, S.-C.; Yang, S.-H.; Chen, P.-N. The Inhibitory Effect of Abietic Acid on Melanoma Cancer Metastasis and Invasiveness *In Vitro* and *In Vivo*. *Am. J. Chin. Med.* **2015**, *43*, 1697–1714, doi:10.1142/S0192415X15500962.
145. Park, J.Y.; Lee, Y.K.; Lee, D.-S.; Yoo, J.-E.; Shin, M.-S.; Yamabe, N.; Kim, S.-N.; Lee, S.; Kim, K.H.; Lee, H.-J.; et al. Abietic Acid Isolated from Pine Resin (Resina Pini) Enhances Angiogenesis in HUVECs and Accelerates Cutaneous Wound Healing in Mice. *J. Ethnopharmacol.* **2017**, *203*, 279–287, doi:10.1016/j.jep.2017.03.055.
146. Hamdan, S.; Pastar, I.; Drakulich, S.; Dikici, E.; Tomic-Canic, M.; Deo, S.; Daunert, S. Nanotechnology-Driven Therapeutic Interventions in Wound Healing: Potential Uses and Applications. *ACS Cent. Sci.* **2017**, *3*, 163–175, doi:10.1021/acscentsci.6b00371.
147. Vera Nyrén; Ernst Back The Ionization Constant, Solubility Product, and Solubility of Abietic and Dehydroabietic Acid. *Acta Chem. Scand.* **1958**, 5, doi:10.3891/acta.chem.scand.12-1516.
148. Huang, Y.; Chen, X.; Deng, Y.; Zhou, D.; Wang, L. A Novel Nickel Catalyst Derived from Layered Double Hydroxides (LDHs) Supported on Fluid Catalytic Cracking Catalyst Residue (FC3R) for Rosin Hydrogenation. *Chem. Eng. J.* **2015**, *269*, 434–443, doi:10.1016/j.cej.2015.01.098.
149. Yang, D.; Song, Z.; Qian, X. Adsorption of Abietic Acid from Colloidal Suspension by Calcined Mg/Al Hydrotalcite Compounds. *Ind. Eng. Chem. Res.* **2013**, *52*, 6956–6961, doi:10.1021/ie303513n.

150. Leroux, F.; Besse, J.-P. Polymer Interleaved Layered Double Hydroxide: A New Emerging Class of Nanocomposites. *Chem. Mater.* **2001**, *13*, 3507–3515, doi:10.1021/cm0110268.
151. Illaik, A.; Vuillermoz, C.; Commereuc, S.; Taviot-Guého, C.; Verney, V.; Leroux, F. Reactive and Functionalized LDH Fillers for Polymer. *Journal of Physics and Chemistry of Solids* **2008**, *69*, 1362–1366, doi:10.1016/j.jpcs.2007.10.019.
152. Liao, C.-S.; Ye, W.-B. Enhanced Ionic Conductivity in Poly(Ethylene Oxide)/Layered Double Hydroxide Nanocomposite Electrolytes. *J. Polym. Res.* **2003**, *10*, 241–246, doi:10.1023/B:JPOL.0000004619.00197.7a.
153. Kovanda, F.; Jindova, E.; Doušová, B.; Kolouskova, S.; Pleštil, J.; Sedlakova, Z. Layered Double Hydroxides Intercalated with Organic Anions and Their Application in Preparation of LDH/Polymer Nanocomposites. *Acta Geodyn. et Geomater.* **2009**, *6*, 111–119.
154. Hussan, S. A Review on Recent Advances of Enteric Coating. *IOSR J. Pharm.* **2012**, *2*, 05–11, doi:10.9790/3013-2610511.
155. Li, B.; He, J.; Evans, D.G.; Duan, X. Enteric-Coated Layered Double Hydroxides as a Controlled Release Drug Delivery System. *Int. J. Pharm.* **2004**, *287*, 89–95, doi:10.1016/j.ijpharm.2004.08.016.
156. Mahkam, M.; Davatgar, M.; Rezvani, Z.; Nejati, K. Preparation of PH-Sensitive Polymers/Layered Double Hydroxide Hybrid Beads for Controlled Release of Insulin. *Int. J. Polym. Mater.* **2013**, *62*, 57–60, doi:10.1080/00914037.2011.617337.
157. Xu, T.; Xu, X.; Gu, Y.; Fang, L.; Cao, F. Functional Intercalated Nanocomposites with Chitosan-Glutathione-Glycylsarcosine and Layered Double Hydroxides for Topical Ocular Drug Delivery. *Int. J Nanomedicine* **2018**, *13*, 917–937, doi:10.2147/IJN.S148104.
158. Perera, J.; Weerasekera, M.; Kottegoda, N. Slow Release Anti-Fungal Skin Formulations Based on Citric Acid Intercalated Layered Double Hydroxides Nanohybrids. *Chemistry Central Journal* **2015**, *9*, 27, doi:10.1186/s13065-015-0106-3.
159. Kim, M.H.; Park, D.-H.; Yang, J.-H.; Choy, Y.B.; Choy, J.-H. Drug-Inorganic-Polymer Nanohybrid for Transdermal Delivery. *Int. J. Pharm.* **2013**, *444*, 120–127, doi:10.1016/j.ijpharm.2012.12.043.
160. Salguero, Y.; Valenti, L.; Rojas, R.; García, M.C. Ciprofloxacin-Intercalated Layered Double Hydroxide-in-Hybrid Films as Composite Dressings for Controlled Antimicrobial Topical Delivery. *Mater. Sci. Eng. C* **2020**, *111*, 110859, doi:10.1016/j.msec.2020.110859.
161. Vasile, E.; Radu, I.-C.; Galateanu, B.; Rapa, M.; Hudita, A.; Jianu, D.; Stanescu, P.-O.; Cioflan, H.; Zaharia, C. Novel Nanocomposites Based on Bacterial Polyester/LDH-SDS Clay for Stem Cells Delivery in Modern Wound Healing Management. *Materials (Basel)* **2020**, *13*, 4488, doi:10.3390/ma13204488.
162. Sabu Thomas; Preetha Balakrishnan; Sreekala M.S. *Fundamental Biomaterials: Polymers*; Woodhead Publishing, 2018; ISBN ISBN: 978-0-08-102194-1.
163. Badar, M.; Rahim, M.I.; Kieke, M.; Ebel, T.; Rohde, M.; Hauser, H.; Behrens, P.; Mueller, P.P. Controlled Drug Release from Antibiotic-Loaded Layered Double Hydroxide Coatings on Porous Titanium Implants in a Mouse Model: Antibiotic-Loaded Layred Double Hydrocide Coatings. *J. Biomed. Mater. Res.* **2015**, *103*, 2141–2149, doi:10.1002/jbm.a.35358.
164. Li, M.; Sultanbawa, Y.; Xu, Z.P.; Gu, W.; Chen, W.; Liu, J.; Qian, G. High and Long-Term Antibacterial Activity against Escherichia Coli via Synergy between the Antibiotic Penicillin G and Its Carrier ZnAl Layered Double Hydroxide. *Colloids Surf. B* **2019**, *174*, 435–442, doi:10.1016/j.colsurfb.2018.11.035.

165. Munhoz, D.R.; Bernardo, M.P.; Malafatti, J.O.D.; Moreira, F.K.V.; Mattoso, L.H.C. Alginate Films Functionalized with Silver Sulfadiazine-Loaded [Mg-Al] Layered Double Hydroxide as Antimicrobial Wound Dressing. *Int. J. Biol. Macromol.* **2019**, *141*, 504–510, doi:10.1016/j.ijbiomac.2019.09.019.
166. Lambers, H.; Piessens, S.; Bloem, A.; Pronk, H.; Finkel, P. Natural Skin Surface PH Is on Average below 5, Which Is Beneficial for Its Resident Flora. *Int. J. Cosmet. Sci.* **2006**, *28*, 359–370, doi:10.1111/j.1467-2494.2006.00344.x.
167. Ghosal, K.; Agatemor, C.; Tucker, N.; Kny, E.; Thomas, S. CHAPTER 1 Electrical Spinning to Electrospinning: a Brief History. In *Electrospinning: From Basic Research to Commercialization*; The Royal Society of Chemistry, 2018; pp. 1–23 ISBN 978-1-78801-100-6.
168. Bhardwaj, N.; Kundu, S.C. Electrospinning: A Fascinating Fiber Fabrication Technique. *Biotechnol. Adv.* **2010**, *28*, 325–347, doi:10.1016/j.biotechadv.2010.01.004.
169. Li, D.; Xia, Y. Electrospinning of Nanofibers: Reinventing the Wheel? *Adv. Mater.* **2004**, *16*, 1151–1170, doi:10.1002/adma.200400719.
170. Boda, S.K.; Li, X.; Xie, J. Electrospraying an Enabling Technology for Pharmaceutical and Biomedical Applications: A Review. *J. Aerosol Sci.* **2018**, *125*, 164–181, doi:10.1016/j.jaerosci.2018.04.002.
171. Noruzi, M. Electrospun Nanofibres in Agriculture and the Food Industry: A Review: Electrospun Nanofibres in Agriculture and Food Science. *J. Sci. Food Agric.* **2016**, *96*, 4663–4678, doi:10.1002/jsfa.7737.
172. Li, Z.; Zhang, J.; Yu, L.; Zhang, J. Electrospun Porous Nanofibers for Electrochemical Energy Storage. *J Mater Sci* **2017**, *52*, 6173–6195, doi:10.1007/s10853-017-0794-2.
173. Liu, M.; Duan, X.-P.; Li, Y.-M.; Yang, D.-P.; Long, Y.-Z. Electrospun Nanofibers for Wound Healing. *Mater. Sci. Eng. C* **2017**, *76*, 1413–1423, doi:10.1016/j.msec.2017.03.034.
174. Valarezo, E.; Tammaro, L.; González, S.; Malagón, O.; Vittoria, V. Fabrication and Sustained Release Properties of Poly(ε-Caprolactone) Electrospun Fibers Loaded with Layered Double Hydroxide Nanoparticles Intercalated with Amoxicillin. *Appl. Clay Sci.* **2013**, *72*, 104–109, doi:10.1016/j.clay.2012.12.006.
175. Gao, Y.; Teoh, T.W.; Wang, Q.; Williams, G.R. Electrospun Organic–Inorganic Nanohybrids as Sustained Release Drug Delivery Systems. *J. Mater. Chem. B* **2017**, *5*, 9165–9174, doi:10.1039/C7TB01825H.
176. Yang, C.; Zhu, T.; Wang, J.; Chen, S.; Li, W. Synthesis and Characterization of Flurbiprofen Axetil-Loaded Electrospun MgAl-LDHs/Poly(Lactic-Co-Glycolic Acid) Composite Nanofibers. *RSC Adv.* **2015**, *5*, 69423–69429, doi:10.1039/C5RA11150A.
177. Tammaro, L.; Russo, G.; Vittoria, V. Encapsulation of Diclofenac Molecules into Poly(-Caprolactone) Electrospun Fibers for Delivery Protection. *Journal of Nanomaterials* **2009**, *2009*, 1–8, doi:10.1155/2009/238206.
178. Enrico Drioli; Lidietta Giorno *Encyclopedia of Membranes*; Springer-Verlag Berlin Heidelberg, 2016; ISBN ISBN 978-3-662-44323-1.
179. Enrico Drioli; Lidietta Giorno *Membranes Operation - Innovative Separations and Transformations*; WILEY-VCH, 2009; ISBN 978-3-527-32038-7.
180. Liang, N.; Liu, W.; Zuo, D.; Peng, P.; Qu, R.; Chen, D.; Zhang, H. Quaternized Polysulfone-Based Nanocomposite Membranes and Improved Properties by Intercalated Layered Double Hydroxide. *Polym Eng Sci* **2018**, *58*, 767–774, doi:10.1002/pen.24612.
181. Martos, A.M.; Herrero, M.; Várez, A.; Levenfeld, B. Synthesis and Characterization of New Membranes Based on Sulfonated Polysulfone/Zn,Al-Heptamolibdate LDH. *Materials Letters* **2015**, *152*, 125–127, doi:10.1016/j.matlet.2015.03.094.

182. Mohapi, M.; Sefadi, J.S.; Mochane, M.J.; Magagula, S.I.; Lebelo, K. Effect of LDHs and Other Clays on Polymer Composite in Adsorptive Removal of Contaminants: A Review. *Crystals* **2020**, *10*, 957, doi:10.3390/cryst10110957.
183. Oyarzabal, A.; Mugica, A.; Müller, A.J.; Zubitur, M. Hydrolytic Degradation of Nanocomposites Based on Poly(L-Lactic Acid) and Layered Double Hydroxides Modified with a Model Drug. *J. Appl. Polym. Sci.* **2016**, *133*, doi:10.1002/app.43648.
184. Pawar, R.; Tekale, S.; Shisodia, S.; Totre, J.; Domb, A. Biomedical Applications of Poly(Lactic Acid). *Recent Pat. Regen. Med.* **2014**, *4*, doi:10.2174/2210296504666140402235024.
185. Castro-Aguirre, E.; Iñiguez-Franco, F.; Samsudin, H.; Fang, X.; Auras, R. Poly(Lactic Acid)—Mass Production, Processing, Industrial Applications, and End of Life. *Adv. Drug Deliv. Rev.* **2016**, *107*, 333–366, doi:10.1016/j.addr.2016.03.010.
186. DeStefano, V.; Khan, S.; Tabada, A. Applications of PLA in Modern Medicine. *Engineered Regeneration* **2020**, *1*, 76–87, doi:10.1016/j.engreg.2020.08.002.
187. Stewart, S.; Domínguez-Robles, J.; McIlorum, V.; Mancuso, E.; Lamprou, D.; Donnelly, R.; Larrañeta, E. Development of a Biodegradable Subcutaneous Implant for Prolonged Drug Delivery Using 3D Printing. *Pharmaceutics* **2020**, *12*, 105, doi:10.3390/pharmaceutics12020105.
188. Liu, S.; Wu, G.; Chen, X.; Zhang, X.; Yu, J.; Liu, M.; Zhang, Y.; Wang, P. Degradation Behavior In Vitro of Carbon Nanotubes (CNTs)/Poly(Lactic Acid) (PLA) Composite Suture. *Polymers* **2019**, *11*, 1015, doi:10.3390/polym11061015.
189. Buckwalter, D.J.; Dennis, J.M.; Long, T.E. Amide-Containing Segmented Copolymers. *Prog. Polym. Sci.* **2015**, *45*, 1–22, doi:10.1016/j.progpolymsci.2014.11.003.
190. Kardani, R.; Asghari, M.; Mohammadi, T.; Afsari, M. Effects of Nanofillers on the Characteristics and Performance of PEBA-Based Mixed Matrix Membranes. *Rev. Chem. Eng.* **2018**, *34*, 797–836, doi:10.1515/revce-2017-0001.
191. Jang, Y.-T.; Liebmann, V.L.; Villman, G.S.; Amin, S.A. Nylon-PEBA Copolymer Catheter. Patent number: 4,898,591. Date of Patent: February 6th, **1990**.
192. Janes, D.W.; Chandrasekar, V.; Woolford, S.E.; Ludwig, K.B. Predicting the Effects of Composition, Molecular Size and Shape, Plasticization, and Swelling on the Diffusion of Aromatic Additives in Block Copolymers. *Macromolecules* **2017**, *50*, 6137–6148, doi:10.1021/acs.macromol.7b00690.
193. Warner, J.A.; Forsyth, B.; Zhou, F.; Myers, J.; Frethem, C.; Haugstad, G. Characterization of Pebax Angioplasty Balloon Surfaces with AFM, SEM, TEM, and SAXS: Characterization of PEBAX Angioplasty Balloon Surfaces. *J. Biomed. Mater. Res.* **2016**, *104*, 470–475, doi:10.1002/jbm.b.33414.
194. Zhang, C.; Dong, L.; Zhang, Y.; Bai, Y.; Gu, J.; Sun, Y.; Chen, M. Poly(Ether-b-Amide)/Tween20 Gel Membranes for CO_2/N_2 Separation. *Sep. Sci. Technol.* **2015**, 150527095459001, doi:10.1080/01496395.2015.1047851.
195. Nafisi, V.; Hägg, M.-B. Development of Dual Layer of ZIF-8/PEBAX-2533 Mixed Matrix Membrane for CO2 Capture. *J. Membr. Sci.* **2014**, *459*, 244–255, doi:10.1016/j.memsci.2014.02.002.
196. Ardestani, M.A.; Babaluo, A.A.; Peyravi, M.; Aghjeh, M.K.R.; Jannatdoost, E. Fabrication of PEBA/Ceramic Nanocomposite Membranes in Gas Sweetening. *Desalination* **2010**, *250*, 1140–1143, doi:10.1016/j.desal.2009.09.127.
197. Sarinthip Thanakkasaranee; Dowan Kim; Jongchul Seo Preparation and Characterization of Poly(Ether-Block-Amide)/Polyethylene Glycol Composite Films with Temperature-Dependent Permeation. *Polymers* **2018**, *10*, 225, doi:10.3390/polym10020225.

198. Cen, Y.; Staudt-Bickel, C.; Lichtenthaler, R.N. Sorption Properties of Organic Solvents in PEBA Membranes. *J. Membr. Sci.* **2002**, *206*, 341–349, doi:10.1016/S0376-7388(01)00767-0.
199. Liu, S.; Liu, G.; Shen, J.; Jin, W. Fabrication of MOFs/PEBA Mixed Matrix Membranes and Their Application in Bio-Butanol Production. *Sep. Purif. Technol.* **2014**, *133*, 40–47, doi:10.1016/j.seppur.2014.06.034.
200. Shirole, A.; Sapkota, J.; Foster, E.J.; Weder, C. Shape Memory Composites Based on Electrospun Poly(Vinyl Alcohol) Fibers and a Thermoplastic Polyether Block Amide Elastomer. *ACS Appl. Mater. Interfaces* **2016**, *8*, 6701–6708, doi:10.1021/acsami.6b00834.
201. da S. Oliveira, R.; Bizeto, M.A.; Liberatore, A.M.A.; Koh, I.H.J.; Camilo, F.F. A New Method for Producing Highly Concentrated Non-Aqueous Dispersions of Silver Nanoparticles and the Evaluation of Their Bactericidal Activity. *J. Nanopart. Res.* **2014**, *16*, 2723, doi:10.1007/s11051-014-2723-5.
202. Choi, S.-J.; Choy, J.-H. Effect of Physico-Chemical Parameters on the Toxicity of Inorganic Nanoparticles. *J. Mater. Chem.* **2011**, *21*, 5547, doi:10.1039/c1jm10167f.
203. Sun, X.; Neuperger, E.; Dey, S.K. Insights into the Synthesis of Layered Double Hydroxide (LDH) Nanoparticles: Part 1. Optimization and Controlled Synthesis of Chloride-Intercalated LDH. *J. Colloid Interface Sci.* **2015**, *459*, 264–272, doi:10.1016/j.jcis.2015.07.073.
204. Bail, A.L.; Duroy, H.; Fourquet, J.L. Ab-Initio Structure Determination of LiSbWO6 by X-Ray Powder Diffraction. *Mater. Res. Bull.* **1988**, *23*, 447–452, doi:https://doi.org/10.1016/0025-5408(88)90019-0.
205. Rodriguez-Carvajal, J. Recent Developments of the Program FULLPROF, Commission on Powder Diffraction. *IUCr Newsl.* **2001**, *26*.
206. Evans, D.G.; Slade, R.C.T. Structural Aspects of Layered Double Hydroxides. In; Springer-Verlag: Berlin/Heidelberg, **2005**, doi: 10.1007/430_005.
207. Popa, N.C.; Balzar, D. Size-Broadening Anisotropy in Whole Powder Pattern Fitting. Application to Zinc Oxide and Interpretation of the Apparent Crystallites in Terms of Physical Models. *Journal of Applied Crystallography* **2008**, *41*, 615–627, doi:10.1107/S0021889808012223.
208. Meier, R. On Art and Science in Curve-Fitting Vibrational Spectra. *Vibrational Spectroscopy - VIB SPECTROSC* **2005**, *39*, 266–269, doi:10.1016/j.vibspec.2005.03.003.
209. Jayanthi, K.; Kamath, P.V. A Crystal Chemical Approach to a Cation-Ordered Structure Model for Carbonate-Intercalated Layered Double Hydroxides. *Crystal Growth & Design* **2016**, *16*, 4450–4456, doi:10.1021/acs.cgd.6b00562.
210. Das, S.; Hendry, M.J.; Essilfie-Dughan, J. Transformation of Two-Line Ferrihydrite to Goethite and Hematite as a Function of PH and Temperature. *Environ. Sci. Technol.* **2011**, *45*, 268–275, doi:10.1021/es101903y.
211. Frau, F.; Addari, D.; Davide, A.; Biddau, R.; Cidu, R.; Rossi, A. Influence of Major Anions on As(V) Adsorption by Synthetic 2-Line Ferrihydrite. Kinetic Investigation and XPS Study of the Competitive Effect of Bicarbonate. *Water, Air, and Soil Pollution* **2009**, *205*, 25–41, doi:10.1007/s11270-009-0054-4.
212. Ristić, M.; De Grave, E.; Musić, S.; Popović, S.; Orehovec, Z. Transformation of Low Crystalline Ferrihydrite to α-Fe2O3 in the Solid State. *J. Mol. Struct.* **2007**, *834–836*, 454–460, doi:10.1016/j.molstruc.2006.10.016.
213. Wang, M.; Zhou, Y.; Zhang, Y.; Hahn, S.H.; Kim, E.J. From Zn(OH)2 to ZnO: A Study on the Mechanism of Phase Transformation. *CrystEngComm* **2011**, *13*, 6024, doi:10.1039/c1ce05502j.

214. Giannakoudakis, D.A.; Arcibar-Orozco, J.A.; Bandosz, T.J. Key Role of Terminal Hydroxyl Groups and Visible Light in the Reactive Adsorption/Catalytic Conversion of Mustard Gas Surrogate on Zinc (Hydr)Oxides. *Appl. Catal. B: Environmental* **2015**, *174–175*, 96–104, doi:10.1016/j.apcatb.2015.02.028.
215. Kirkpatrick, R.J.; Kalinichev, A.G.; Wang, J.; Hou, X.; Amonette, J.E. Molecular Modeling of the Vibrational Spectra of Interlayer and Surface Species of Layered Double Hydroxides. In *The Application of Vibrational Spectroscopy to Clay Minerals and Layered Double Hydroxides*; Clay Minerals Society, **2005** ISBN 978-1-881208-33-4.
216. Https://Rruff.Info/ (RRUFF ID R060027).
217. Vaccari, A. Layered Double Hydroxides: Present and Future: V. Rives (Ed.), Nova Science Publishers, Inc., New York, 2001, IX+439 Pp., ISBN 1-59033-060-9. *Appl. Clay Sci.* **2002**, *22*, 75–76, doi:10.1016/S0169-1317(02)00112-6.
218. Kloprogge, J.T.; Hickey, L.; Frost, R.L. FT-Raman and FT-IR Spectroscopic Study of Synthetic Mg/Zn/Al-Hydrotalcites. *J. Raman Spectrosc.* **2004**, *35*, 967–974, doi:10.1002/jrs.1244.
219. Kloprogge, J.T.; Frost, R.L. Fourier Transform Infrared and Raman Spectroscopic Study of the Local Structure of Mg-, Ni-, and Co-Hydrotalcites. *J. Solid State Chem.* **1999**, *146*, 506–515, doi:10.1006/jssc.1999.8413.
220. Palmer, S.J.; Frost, R.L.; Spratt, H.J. Synthesis and Raman Spectroscopic Study of Mg/Al,Fe Hydrotalcites with Variable Cationic Ratios. *J. Raman Spectrosc.* **2009**, *40*, 1138–1143, doi:10.1002/jrs.2198.
221. Nakamoto, K. *Infrared and Raman Spectra of Inorganic and Coordination Compounds, Part A: Theory and Applications in Inorganic Chemistry*; 6th ed.; WILEY, **2009**; ISBN 978-0-471-74339-2.
222. Seftel, E.M.; Popovici, E.; Mertens, M.; Cool, P.; Vansant, E.F. Infrared and Raman Spectroscopic Study of Sn-Containing Zn/Al-Layered Double Hydroxides. *J. Optoelectron. Adv.* **2008**, *10 (12)*, 3477-3481, ISSN: 1454-4164.
223. Pereira, R.C.; Anizelli, P.R.; Di Mauro, E.; Valezi, D.F.; da Costa, A.C.S.; Zaia, C.T.B.V.; Zaia, D.A.M. The Effect of PH and Ionic Strength on the Adsorption of Glyphosate onto Ferrihydrite. *Geochem Trans* **2019**, *20*, 3, doi:10.1186/s12932-019-0063-1.
224. Xiao, W.; Jones, A.M.; Collins, R.N.; Bligh, M.W.; Waite, T.D. Use of Fourier Transform Infrared Spectroscopy to Examine the Fe(II)-Catalyzed Transformation of Ferrihydrite. *Talanta* **2017**, *175*, 30–37, doi:10.1016/j.talanta.2017.07.018.
225. Mazzetti, L.; Thistlethwaite, P.J. Raman Spectra and Thermal Transformations of Ferrihydrite and Schwertmannite. *J. Raman Spectrosc.* **2002**, *33*, 104–111, doi:10.1002/jrs.830.
226. Peter Atkins; Tina Overton; Jonathan Rourke; Mark Weller; Fraser Armstrong *Inorganic Chemistry*; fifth.; OUP Oxford, **2009**; ISBN ISBN 978–1–42–921820–7.
227. Hawkes, S.J. All Positive Ions Give Acid Solutions in Water. *J. Chem. Educ.* **1996**, *73*, 516, doi:10.1021/ed073p516.
228. Saito, K.; Nakagawa, M.; Ishikita, H. PKa of the Ligand Water Molecules in the Oxygen-Evolving Mn4CaO5 Cluster in Photosystem II. *Commun. Chem.* **2020**, *3*, 89, doi:10.1038/s42004-020-00336-7.
229. Li, K.; Xue, D. Estimation of Electronegativity Values of Elements in Different Valence States. *J. Phys. Chem. A* **2006**, *110*, 11332–11337, doi:10.1021/jp062886k.
230. Scholz, F.; Kahlert, H. The Calculation of the Solubility of Metal Hydroxides, Oxide-Hydroxides, and Oxides, and Their Visualisation in Logarithmic Diagrams. *ChemTexts* **2015**, *1*, 7, doi:10.1007/s40828-015-0006-0.

231. Gordy, W. A Relation between Bond Force Constants, Bond Orders, Bond Lengths, and the Electronegativities of the Bonded Atoms. *J. Chem. Phys.* **1946**, *14*, 305–320, doi:10.1063/1.1724138.
232. Nieboer, E.; Richardson, D.H.S. The Replacement of the Nondescript Term 'Heavy Metals' by a Biologically and Chemically Significant Classification of Metal Ions. *Environmental Pollution Series B, Chemical and Physical* **1980**, *1*, 3–26, doi:10.1016/0143-148X(80)90017-8.
233. Lutz, H.D.; Möller, H.; Schmidt, M. Lattice Vibration Spectra. Part LXXXII. Brucite-Type Hydroxides M(OH)2 (M = Ca, Mn, Co, Fe, Cd) — IR and Raman Spectra, Neutron Diffraction of Fe(OH)2. *J. Mol. Struct.* **1994**, *328*, 121–132, doi:10.1016/0022-2860(94)08355-X.
234. Brindley, G.W.; Kao, C.-C. Structural and IR Relations among Brucite-like Divalent Metal Hydroxides. *Phys. Chem. Minerals* **1984**, *10*, 187–191, doi:10.1007/BF00311476.
235. Lewis, D.G.; Farmer, V.C. Infrared Absorption of Surface Hydroxyl Groups and Lattice Vibrations in Lepidocrocite (γ-FeOOH) and Boehmite (γ-AlOOH). *Clay Miner.* **1986**, *21*, 93–100, doi:10.1180/claymin.1986.021.1.08.
236. Besson, G. Refined Relationships between Chemical Composition of Dioctahedral Fine-Grained Mica Minerals and Their Infrared Spectra within the OH Stretching Region. Part I: Identification of the OH Stretching Bands. *Clays Clay Miner.* **1997**, *45*, 158–169, doi:10.1346/CCMN.1997.0450204.
237. Salak, A.N.; Tedim, J.; Kuznetsova, A.I.; Vieira, L.G.; Ribeiro, J.L.; Zheludkevich, M.L.; Ferreira, M.G.S. Thermal Behavior of Layered Double Hydroxide Zn–Al–Pyrovanadate: Composition, Structure Transformations, and Recovering Ability. *J. Phys. Chem. C* **2013**, *117*, 4152–4157, doi:10.1021/jp312512y.
238. Constantino', V.R.L.; Hnnavaia, T.J. Basic Properties of Mg2+1-x,Al3+x Layered Double Hydroxides Intercalated by Carbonate, Hydroxide, Chloride, and Sulfate Anions. *Physical Inorganic Chemistry* **1995**, doi: 10.1002/chin.199525006.
239. Rozov, K.; Berner, U.; Taviot-Gueho, C.; Leroux, F.; Renaudin, G.; Kulik, D.; Diamond, L.W. Synthesis and Characterization of the LDH Hydrotalcite–Pyroaurite Solid-Solution Series. *Cem. Concr. Res.* **2010**, *40*, 1248–1254, doi:10.1016/j.cemconres.2009.08.031.
240. Dietmann, K.M.; Linke, T.; Trujillano, R.; Rives, V. Effect of Chain Length and Functional Group of Organic Anions on the Retention Ability of MgAl- Layered Double Hydroxides for Chlorinated Organic Solvents. *ChemEngineering* **2019**, *3*, 89, doi:10.3390/chemengineering3040089.
241. U. Schwertmann; Dr. R. M. Cornell *Iron Oxides in the Laboratory: Preparation and Characterization*; Second edition.; WILEY-VCH Verlag GmbH, **2000**; ISBN 978-3-527-61322-9.
242. Rocha, M.A.; Petersen, P.A.D.; Teixeira-Neto, E.; Petrilli, H.M.; Leroux, F.; Taviot-Gueho, C.; Constantino, V.R.L. Layered Double Hydroxide and Sulindac Coiled and Scrolled Nanoassemblies for Storage and Drug Release. *RSC Adv.* **2016**, *6*, 16419–16436, doi:10.1039/C5RA25814F.
243. Vegard, L. Die Konstitution Der Mischkristalle Und Die Raumfüllung Der Atome. *Zeitschrift für Physik* **1921**, *5*, 17–26, doi:10.1007/BF01349680.
244. Richardson, I.G. The Importance of Proper Crystal-Chemical and Geometrical Reasoning Demonstrated Using Layered Single and Double Hydroxides. *Acta Crystallogr. B Struct. Sci. Cryst. Eng. Mater.* **2013**, *69*, 150–162, doi:10.1107/S205251921300376X.

245. Richardson, I.G. Zn- and Co-Based Layered Double Hydroxides: Prediction of the It a Parameter from the Fraction of Trivalent Cations and It Vice Versa. *Acta Crystallographica Section B* **2013**, *69*, 414–417, doi:10.1107/S2052519213017545.
246. Faour, A.; Mousty, C.; Prevot, V.; Devouard, B.; De Roy, A.; Bordet, P.; Elkaim, E.; Taviot-Gueho, C. Correlation among Structure, Microstructure, and Electrochemical Properties of NiAl–CO3 Layered Double Hydroxide Thin Films. *J. Phys. Chem. C* **2012**, *116*, 15646–15659, doi:10.1021/jp300780w.
247. Page, K.; Proffen, T.; Mclain, S.; Clausen, B.; Darling, T.; TenCate, J.; Lee, S.-Y.; Ustundag, E. Atomic Pair Distribution Analysis of Materials Containing Crystalline and Amorphous Phases. *Zeitschrift fur Kristallographie* **2005**, *220*, doi:10.1524/zkri.2005.220.12.1002.
248. Billinge, S.J.L. The Rise of the X-Ray Atomic Pair Distribution Function Method: A Series of Fortunate Events. *Philosophical Transactions of the Royal Society A: Mathematical, Physical and Engineering Sciences* **2019**, *377*, doi:10.1098/rsta.018.0413.
249. Boily, J.-F.; Song, X. Direct Identification of Reaction Sites on Ferrihydrite. *Commun. Chem.* **2020**, *3*, 79, doi:10.1038/s42004-020-0325-y.
250. Tang, Y.; Michel, F.M.; Zhang, L.; Harrington, R.; Parise, J.B.; Reeder, R.J. Structural Properties of the Cr(III)−Fe(III) (Oxy)Hydroxide Compositional Series: Insights for a Nanomaterial "Solid Solution." *Chem. Mater.* **2010**, *22*, 3589–3598, doi:10.1021/cm1000472.
251. Rozov, K.B.; Berner, U.; Kulik, D.A.; Diamond, L.W. Solubility and Thermodynamic Properties of Carbonate-Bearing Hydrotalcite—Pyroaurite Solid Solutions with A 3:1 Mg/(Al+Fe) Mole Ratio. *Clays Clay Miner.* **2011**, *59*, 215–232, doi:10.1346/CCMN.2011.0590301.
252. Mandal, S.; Mayadevi, S.; Kulkarni, B.D. Adsorption of Aqueous Selenite [Se(IV)] Species on Synthetic Layered Double Hydroxide Materials. *Ind. Eng. Chem. Res.* **2009**, *48*, 7893–7898, doi:10.1021/ie900136s.
253. Parida, K.M.; Mohapatra, L. Carbonate Intercalated Zn/Fe Layered Double Hydroxide: A Novel Photocatalyst for the Enhanced Photo Degradation of Azo Dyes. *Chem. Eng. J.* **2012**, *179*, 131–139, doi:10.1016/j.cej.2011.10.070.
254. Jolivet, J.-P.; Chanéac, C.; Tronc, E. Iron Oxide Chemistry. From Molecular Clusters to Extended Solid Networks. *Chem. Commun.* **2004**, 477–483, doi:10.1039/B304532N.
255. Liu, C.; Zhu, Z.; Li, F.; Liu, T.; Liao, C.; Lee, J.-J.; Shih, K.; Tao, L.; Wu, Y. Fe(II)-Induced Phase Transformation of Ferrihydrite: The Inhibition Effects and Stabilization of Divalent Metal Cations. *Chem. Geol.* **2016**, *444*, 110–119, doi:10.1016/j.chemgeo.2016.10.002.
256. Waychunas, G.A.; Fuller, C.C.; Davis, J.A.; Rehr, J.J. Surface Complexation and Precipitate Geometry for Aqueous Zn(II) Sorption on Ferrihydrite: II. XANES Analysis and Simulation. *Geochim. Cosmochim. Acta* . **2003**, *67*, 1031–1043, doi:10.1016/S0016-7037(02)01280-2.
257. Islam, S.; Das, S.; Mishra, G.; Das, B.; Malakar, A.; Carlomagno, I.; Meneghini, C.; De Giudici, G.; Gonçalves, L.P.L.; Sousa, J.P.S.; et al. Coagulating and Flocculating Ferrihydrite: Application of Zinc Acetate Salt. *Environ. Sci.: Water Res. Technol.* **2020**, *6*, 2057–2064, doi:10.1039/D0EW00357C.
258. Nachtegaal, M.; Sparks, D.L. Effect of Iron Oxide Coatings on Zinc Sorption Mechanisms at the Clay-Mineral/Water Interface. *J. Colloid Interface Sci.* **2004**, *276*, 13–23, doi:10.1016/j.jcis.2004.03.031.

259. Stec, M.; Jagustyn, B.; Słowik, K.; Sciazko, M.; Iluk, T. Influence of High Chloride Concentration on PH Control in Hydroxide Precipitation of Heavy Metals. *J. Sustain. Met.* **2020**, *6*, doi:10.1007/s40831-020-00270-x.
260. Cousy, S.; Gorodylova, N.; Svoboda, L.; Zelenka, J. Influence of Synthesis Conditions over Simonkolleite/ZnO Precipitation. *Chemical Papers* **2017**, *71*, 2325–2334, doi:10.1007/s11696-017-0226-4.
261. Moezzi, A.; Cortie, M.; McDonagh, A. Transformation of Zinc Hydroxide Chloride Monohydrate to Crystalline Zinc Oxide. *Dalton Trans.* **2016**, *45*, 7385–7390, doi:10.1039/C5DT04864H.
262. Boclair, J.W.; Braterman, P.S. Layered Double Hydroxide Stability. 1. Relative Stabilities of Layered Double Hydroxides and Their Simple Counterparts. *Chem. Mater.* **1999**, *11*, 298–302, doi:10.1021/cm980523u.
263. Shannon, R.D. Revised Effective Ionic Radii and Systematic Studies of Interatomic Distances in Halides and Chalcogenides. *Acta Crystallographica Section A* **1976**, *32*, 751–767, doi:10.1107/S0567739476001551.
264. Saji, R.S.; Prasana, J.C.; Muthu, S.; George, J.; Kuruvilla, T.K.; Raajaraman, B.R. Spectroscopic and Quantum Computational Study on Naproxen Sodium. *Spectrochimica Acta Part A: Molecular and Biomolecular Spectroscopy* **2020**, *226*, 117614, doi:10.1016/j.saa.2019.117614.
265. Berber, M.; Hafez, I.; Minagawa, K.; Mori, T.; Tanaka, M. Versatile Nanocomposite Formulation System of Non-Steroidal Anti-Inflammatory Drugs of the Arylalkanoic Acids. In; **2011** ISBN 978-953-307-347-7.
266. Jayanthi, K.; Nagendran, S.; Kamath, P.V. Layered Double Hydroxides: Proposal of a One-Layer Cation-Ordered Structure Model of Monoclinic Symmetry. *Inorg. Chem.* **2015**, *54*, 8388–8395, doi:10.1021/acs.inorgchem.5b01050.
267. Brody, R.H.; Edwards, H.G.M.; Pollard, A.M. Fourier Transform-Raman Spectroscopic Study of Natural Resins of Archaeological Interest. *Biopolymers* **2002**, *67*, 129–141, doi:10.1002/bip.10059.
268. Nong, W.J.; Chen, X.P.; Liang, J.Z.; Wang, L.L.; Tong, Z.F.; Huang, K.L.; Wu, R.; Xie, Q.R.; Jia, Y.H.; Li, K.X. Isolation and Characterization of Abietic Acid. *AMR* **2014**, *887–888*, 551–556, doi:10.4028/www.scientific.net/AMR.887-888.551.
269. Landucci, L.L.; Zinkel, D.F. The 1H and 13C NMR Spectra of the Abietadienoic Resin Acids. **1991**, *45*, 341–346, doi:doi:10.1515/hfsg.1991.45.5.341.
270. Lavielle, N.; Hébraud, A.; Thöny-Meyer, L.; Rossi, R.M.; Schlatter, G. 3D Composite Assemblies of Microparticles and Nanofibers for Tailored Wettability and Controlled Drug Delivery. *Macromol. Mater. Eng.* **2017**, *302*, 1600458, doi:10.1002/mame.201600458.
271. Cai, Y.; Lv, J.; Feng, J. Spectral Characterization of Four Kinds of Biodegradable Plastics: Poly (Lactic Acid), Poly (Butylenes Adipate-Co-Terephthalate), Poly (Hydroxybutyrate-Co-Hydroxyvalerate) and Poly (Butylenes Succinate) with FTIR and Raman Spectroscopy. *J. Polym. Environ.* **2013**, *21*, 108–114, doi:10.1007/s10924-012-0534-2.
272. Ritger, P.L.; Peppas, N.A. A Simple Equation for Description of Solute Release I. Fickian and Non-Fickian Release from Non-Swellable Devices in the Form of Slabs, Spheres, Cylinders or Discs. *J. Control. Release* **1987**, *5*, 23–36, doi:10.1016/0168-3659(87)90034-4.
273. Haroosh, H.J.; Dong, Y.; Ingram, G.D. Synthesis, Morphological Structures, and Material Characterization of Electrospun PLA:PCL/Magnetic Nanoparticle Composites for Drug Delivery. *J. Polym. Sci. B Polym. Phys.* **2013**, *51*, 1607–1617, doi:10.1002/polb.23374.

274. Fahami, A.; Fathi, M. Development of Cress Seed Mucilage/PVA Nanofibers as a Novel Carrier for Vitamin A Delivery. *Food Hydrocolloids* **2018**, *81*, 31–38, doi:10.1016/j.foodhyd.2018.02.008.
275. Chakraborty, M.; Dasgupta, S.; Sengupta, S.; Chakraborty, J.; Ghosh, S.; Ghosh, J.; Mitra, M.K.; Mishra, A.; Mandal, T.K.; Basu, D. A Facile Synthetic Strategy for Mg-Al Layered Double Hydroxide Material as Nanocarrier for Methotrexate. *Ceramics International* **2012**, *38*, 941–949, doi:10.1016/j.ceramint.2011.08.014.
276. Zhang, X.-Q.; Zeng, M.-G.; Li, S.-P.; Li, X.-D. Methotrexate Intercalated Layered Double Hydroxides with Different Particle Sizes: Structural Study and Controlled Release Properties. *Colloids Surf. B Colloid Surface B* **2014**, *117*, 98–106, doi:10.1016/j.colsurfb.2014.02.018.
277. Sparks, D.L. Kinetics and Mechanisms of Chemical Reactions at the Soil Mineral/Water Interface Available online: https://www.taylorfrancis.com/ (accessed on 10 December 2019).
278. O'Hara, T.; Dunne, A.; Butler, J.; Devane, J. A Review of Methods Used to Compare Dissolution Profile Data. *Pharmaceut Sci. Tech. Today* **1998**, *1*, 214–223, doi:10.1016/S1461-5347(98)00053-4.
279. *Congresso Brasileiro de Polímeros (15.:**2019**: Bento Gonçalves-RS) - Anais Do 15º Congresso Brasileiro de Polímeros/Associação Brasileira de Polímeros*; São Carlos; ISBN 978-85-63273-41-3.
280. Figueiredo, M.P.; Layrac, G.; Hébraud, A.; Limousy, L.; Brendle, J.; Schlatter, G.; Constantino, V.R.L. Design of 3D Multi-Layered Electrospun Membranes Embedding Iron-Based Layered Double Hydroxide for Drug Storage and Control of Sustained Release. *Eur. Polym. J.* **2020**, *131*, 109675, doi:10.1016/j.eurpolymj.2020.109675.
281. Vatani, M.; Raisi, A.; Pazuki, G. Pervaporation Separation of Ethyl Acetate from Aqueous Solutions Using ZSM-5 Filled Dual-Layer Poly(Ether- *Block* -Amide)/Polyethersulfone Membrane. *RSC Adv.* **2018**, *8*, 4713–4725, doi:10.1039/C7RA13382K.
282. Delgado, D.R.; Ruidiaz, M.A.; Gómez, S.M.; Gantiva, M.; Martínez, F. Thermodynamic Study of the Solubility of Sodium Naproxen in Some Ethanol + Water Mixtures. *Quím. Nova* **2010**, *33*, 1923–1927, doi:10.1590/S0100-40422010000900019.
283. Sanaeepur, H.; Mashhadikhan, S.; Mardassi, G.; Ebadi Amooghin, A.; Van der Bruggen, B.; Moghadassi, A. Aminosilane Cross-Linked Poly Ether-Block-Amide PEBAX 2533: Characterization and CO2 Separation Properties. *Korean J. Chem. Eng.* **2019**, *36*, 1339–1349, doi:10.1007/s11814-019-0323-x.
284. Hatfield, G.R.; Guo, Y.; Killinger, W.E.; Andrejak, R.A.; Roubicek, P.M. Characterization of Structure and Morphology in Two Poly(Ether-Block-Amide) Copolymers. *Macromolecules* **1993**, *26*, 6350–6353, doi:10.1021/ma00076a008.
285. Kardani, R.; Asghari, M.; Mohammadi, T.; Afsari, M. Effects of Nanofillers on the Characteristics and Performance of PEBA-Based Mixed Matrix Membranes. *Rev. Chem. Eng.* **2018**, *34*, 797–836, doi:10.1515/revce-2017-0001.
286. de Campos, B.M.; Calefi, P.S.; Ciuffi, K.J.; de Faria, E.H.; Rocha, L.A.; Nassar, E.J.; Silva, J.V.L.; Oliveira, M.F.; Maia, I.A. Coating of Polyamide 12 by Sol–Gel Methodology. *J. There. Anal. Calorim.* **2014**, *115*, 1029–1035, doi:10.1007/s10973-013-3384-9.
287. Li, D.; Xu, X.; Xu, J.; Hou, W. Poly(Ethylene Glycol) Haired Layered Double Hydroxides as Biocompatible Nanovehicles: Morphology and Dispersity Study. *Colloids Surf. A Physicochem. Eng. Asp.* **2011**, *384*, 585–591, doi:10.1016/j.colsurfa.2011.05.012.

288. *Introduction to Spectroscopy*; Pavia, D.L., Ed.; 4th ed.; Brooks/Cole, Cengage Learning: Belmont, CA, **2009**; ISBN 978-0-495-11478-9.
289. Sheth, J.P.; Xu, J.; Wilkes, G.L. Solid state structure–property behavior of semicrystalline poly(ether-block-amide) PEBAX® thermoplastic elastomers. *Polymer* **2003**, 44 (3), 743-756, doi: 10.1016/S0032-3861(02)00798-X.
290. Zhang, C.; Dong, L.; Zhang, Y.; Bai, Y.; Gu, J.; Sun, Y.; Chen, M. Poly(Ether-b-Amide)/Tween20 Gel Membranes for CO_2/N_2 Separation. *Sep. Sci. Technol.* **2015**, 150527095459001, doi:10.1080/01496395.2015.1047851.
291. Di Martino, P.; Barthélémy, C.; Palmieri, G.F.; Martelli, S. Physical Characterization of Naproxen Sodium Hydrate and Anhydrate Forms. *Eur. J. Pharm. Sci.* **2001**, *14*, 293–300, doi:10.1016/S0928-0987(01)00179-8.
292. Smallwood, I.M. *Handbook of Organic Solvent Properties*; Arnold ; Halsted Press: London : New York, **1996**; ISBN 978-0-340-64578-9.
293. Pagano, C.; Perioli, L.; Latterini, L.; Nocchetti, M.; Ceccarini, M.R.; Marani, M.; Ramella, D.; Ricci, M. Folic Acid-Layered Double Hydroxides Hybrids in Skin Formulations: Technological, Photochemical and in Vitro Cytotoxicity on Human Keratinocytes and Fibroblasts. *Appl. Clay Sci.* **2019**, *168*, 382–395, doi:10.1016/j.clay.2018.12.009.
294. William M. Haynes *CRC Handbook of Chemistry and Physics*; 97th ed.; **2016**.
295. Kura, A.U.; Hussein-Al-Ali, S.; Hussein, M.Z.; Fakurazi, S.; Arulselvan, P. Development of a Controlled-Release Anti-Parkinsonian Nanodelivery System Using Levodopa as the Active Agent. *IJN* **2013**, 1103, doi:10.2147/IJN.S39740.
296. Bullo, S.; Arulselvan, P.; El Zowalaty, M.; Sharida Fakurazi, S.; Webster, T.J.; Geilich, B.; Hussein, M. Development of a Biocompatible Nanodelivery System for Tuberculosis Drugs Based on Isoniazid-Mg/Al Layered Double Hydroxide. *IJN* **2014**, 4749, doi:10.2147/IJN.S63608.
297. Megat Nabil Mohsin, S.; Hussein, M.Z.; Sarijo, S.H.; Fakurazi, S.; Arulselvan, P.; Taufiq-Yap, Y.H. Nanolayered Composite with Enhanced Ultraviolet Ray Absorption Properties from Simultaneous Intercalation of Sunscreen Molecules. *IJN* **2018**, *Volume 13*, 6359–6374, doi:10.2147/IJN.S171390.
298. Figueiredo, M.P.; Borrego-Sánchez, A.; García-Villén, F.; Miele, D.; Rossi, S.; Sandri, G.; Viseras, C.; Constantino, V.R.L. Polymer/Iron-Based Layered Double Hydroxides as Multifunctional Wound Dressings. *Pharmaceutics* **2020**, *12*, 1130, doi:10.3390/pharmaceutics12111130.
299. Vatani, M.; Raisi, A.; Pazuki, G. Pervaporation Separation of Ethyl Acetate from Aqueous Solutions Using ZSM-5 Filled Dual-Layer Poly(Ether- *Block* -Amide)/Polyethersulfone Membrane. *RSC Adv.* **2018**, *8*, 4713–4725, doi:10.1039/C7RA13382K.
300. Matusik, J.; Deng, Y. Fumonisin B1 Interaction with Mg-Al and Mg-Fe Layered Double Hydroxides: Removal Efficiency and Mechanisms. *Materials* **2020**, *13*, 4344, doi:10.3390/ma13194344.
301. Kim, T.-H.; Lundehøj, L.; Nielsen, U.G. An Investigation of the Phosphate Removal Mechanism by MgFe Layered Double Hydroxides. *Appl. Clay Sci.* **2020**, *189*, 105521, doi:10.1016/j.clay.2020.105521.
302. Maderuelo-Solera, R.; López-Asensio, R.; Cecilia, J.A.; Jiménez-Gómez, C.P.; García Sancho, C.; Moreno-Tost, R.; Maireles-Torres, P. Catalytic Transfer Hydrogenation of Furfural to Furfuryl Alcohol over Calcined MgFe Hydrotalcites. *Appl. Clay Sci.* **2019**, *183*, 105351, doi:10.1016/j.clay.2019.105351.
303. Soukane, S.; K., B.; Naceur, W.; S., H.; Laidi, M.; Drouiche, N.; Alpatova, A. Adsorption of Humic Acid from Seawater on Organo Mg-Fe-Layered Double

Hydroxides: Isotherm, Kinetic Modeling, and Ionic Strength. *Desalination and water treatment* **2020**, *195*, 114–127, doi:10.5004/dwt.2020.25847.

304. Guo, Y.; Gong, Z.; Li, C.; Gao, B.; Li, P.; Wang, X.; Zhang, B.; Li, X. Efficient Removal of Uranium (VI) by 3D Hierarchical Mg/Fe-LDH Supported Nanoscale Hydroxyapatite: A Synthetic Experimental and Mechanism Studies. *Chem. Eng. J.* **2019**, *392*, 123682, doi:10.1016/j.cej.2019.123682.
305. Shi, Z.; Wang, Y.; Sun, S.; Zhang, C.; Wang, H. Removal of Methylene Blue from Aqueous Solution Using Mg-Fe, Zn-Fe, Mn-Fe Layered Double Hydroxide. *Water Sci. Technol.* **2020**, *81*, doi:10.2166/wst.2020.313.
306. Liu, Y.; Liu, Y.; He, Q.; Guo, P.; Chen, J.; Wan, D.; Xiao, S. Utilizing the "Memory Effect" of Bimetallic-Supported Hydrotalcites for Adsorption and Reduction of Perchlorate in Water. *Colloids Surf. A Physicochem. Eng. Asp.* **2020**, *593*, 124641, doi:10.1016/j.colsurfa.2020.124641.
307. Gonçalves, R.G.L.; Mendes, H.M.; Bastos, S.L.; D'Agostino, L.C.; Tronto, J.; Pulcinelli, S.H.; Santilli, C.V.; Neto, J.L. Fenton-like Degradation of Methylene Blue Using Mg/Fe and MnMg/Fe Layered Double Hydroxides as Reusable Catalysts. *Appl. Clay Sci.* **2020**, *187*, 105477, doi:10.1016/j.clay.2020.105477.
308. Puzyrnaya, L.; Pshinko, G.; Zub, V.; Zuy, O. Removal of Cu(II), Co(II) and Cd(II) from Water Solutions by Layered-Double Hydroxides with Different [Mg(II)]/[Fe(III)] Molar Ratios. *Bull. Mater. Sci.* **2020**, *43*, doi:10.1007/s12034-019-1969-z.
309. Santos, L.; Silva, A.F.; Lins, P.; Duarte, J.; Ide, A.; Meili, L. Mg-Fe Layered Double Hydroxide with Chloride Intercalated: Synthesis, Characterization and Application for Efficient Nitrate Removal. *Environ. Sci. Pollut. Res.* **2020**, *27*, doi:10.1007/s11356-019-07364-4.
310. Zhang, Q.; Ji, F.; Zhao, T.; Shen, Q.; Fang, D.; Kuang, L.; Jiang, L.; Ding, S. Systematic Screening of Layered Double Hydroxides for Phosphate Removal and Mechanism Insight. *Appl. Clay Sci.* **2019**, *174*, 159–169, doi:10.1016/j.clay.2019.03.030.
311. Kim, J.-H.; Kang, J.-K.; Lee, S.-C.; Kim, S.-B. Immobilization of Layered Double Hydroxide in Poly(Vinylidene Fluoride)/Poly(Vinyl Alcohol) Polymer Matrices to Synthesize Bead-Type Adsorbents for Phosphate Removal from Natural Water. *Appl. Clay Sci.* **2019**, *170*, 1–12, doi:10.1016/j.clay.2019.01.004.
312. Dalla Nora, F.B.; Lima, V.V.C.; Oliveira, M.L.S.; Hosseini-Bandegharaei, A.; de Lima Burgo, T.A.; Meili, L.; Dotto, G.L. Adsorptive Potential of Zn–Al and Mg–Fe Layered Double Hydroxides for the Removal of 2–Nitrophenol from Aqueous Solutions. *J. Environ. Chem. Eng.* **2020**, *8*, 103913, doi:10.1016/j.jece.2020.103913.
313. Meng, W.; Li, F.; Evans, D.G.; Duan, X. Preparation and Intercalation Chemistry of Magnesium–Iron(III) Layered Double Hydroxides Containing Exchangeable Interlayer Chloride and Nitrate Ions. *Mater. Res. Bull.* **2004**, *39*, 1185–1193, doi:10.1016/j.materresbull.2004.04.016.
314. Hájek, M.; Kocík, J.; Frolich, K.; Vávra, A. Mg-Fe Mixed Oxides and Their Rehydrated Mixed Oxides as Catalysts for Transesterification. *J. Clean. Prod.* **2017**, *161*, 1423–1431, doi:10.1016/j.jclepro.2017.05.199.
315. Dabholkar, V.; Kurade, S.; Badhe, K. One-Pot Synthesis of 5-Amino-1H-Pyrazole-4-Carbonitrile Using Calcined Mg-Fe Hydrotalcite Catalyst. *Curr. Organocatalysis* **2018**, *05*, doi:10.2174/2213337205666180516094624.
316. Yu, J.; Zhu, Z.; Zhang, H.; Qiu, Y.; Yin, D. Mg–Fe Layered Double Hydroxide Assembled on Biochar Derived from Rice Husk Ash: Facile Synthesis and Application in Efficient Removal of Heavy Metals. *Environ. Sci. Pollut. Res.* **2018**, *25*, 24293–24304, doi:10.1007/s11356-018-2500-6.

317. Matusik, J.; Rybka, K. Removal of Chromates and Sulphates by Mg/Fe LDH and Heterostructured LDH/Halloysite Materials: Efficiency, Selectivity, and Stability of Adsorbents in Single- and Multi-Element Systems. *Materials* **2019**, *12*, 1373, doi:10.3390/ma12091373.
318. Zhu, E.; Hong, X.; Ye, Z.; Hui, K.S.; Hui, K.N. Influence of Various Experimental Parameters on the Capacitive Removal of Phosphate from Aqueous Solutions Using LDHs/AC Composite Electrodes.*Sep. Purif. Technol.* **2019**, *215*, 454–462, doi:10.1016/j.seppur.2019.01.004.
319. Wang, D.; Zhang, X.; Zhao, W.; Peng, W.; Zhao, N.; Xiao, F.; Wei, W.; Sun, Y. Synthesis of Dimethyl Carbonate from Methyl Carbamate and Methanol Catalyzed by Mixed Oxides from Hydrotalcite-like Compounds. *J. Phys. Chem. Solids* **2010**, *71*, 427–430, doi:10.1016/j.jpcs.2009.12.005.
320. Rahmanian, O.; Amini, S.; Dinari, M. Preparation of Zinc/Iron Layered Double Hydroxide Intercalated by Citrate Anion for Capturing Lead (II) from Aqueous Solution. *J. Mol. Liq.* **2018**, *256*, 9–15, doi:10.1016/j.molliq.2018.02.018.
321. Adlnasab, L.; Ezoddin, M.; Shabanian, M.; Mahjoob, B. Development of Ferrofluid Mediated CLDH@Fe3O4@Tanic Acid- Based Supramolecular Solvent: Application in Air-Assisted Dispersive Micro Solid Phase Extraction for Preconcentration of Diazinon and Metalaxyl from Various Fruit Juice Samples. *Microchemical Journal* **2019**, *146*, 1–11, doi:10.1016/j.microc.2018.12.020.
322. Gu, N.; Gao, J.; Wang, K.; Li, B.; Dong, W.; Ma, Y. Microcystis Aeruginosa Inhibition by Zn–Fe–LDHs as Photocatalyst under Visible Light. *J. Taiwan Inst. Chem. Eng* . **2016**, *64*, 189–195, doi:10.1016/j.jtice.2016.04.016.
323. Moustafa, D.; Mahmoud, R.; Abd El-salam, H.; Shehata, N. Utilization of Residual Zinc–Iron-Layered Double Hydroxide after Methyl Orange Management as a New Sorbent for Wastewater Treatment. *Appl. Nanosci.* **2021**, *11*, doi:10.1007/s13204-020-01632-3.
324. Bouteraa, S.; Saiah, F.; Saiah, D.; Hamouda, S.; Nourredine, B. Zn-M-CO3 Layered Double Hydroxides (M=Fe, Cr, or Al): Synthesis, Characterization, and Removal of Aqueous Indigo Carmine. *Bull. Chem. React. Eng.* **2020**, *15*, doi:10.9767/bcrec.15.1.5053.43-54.
325. Younes, H.A.; Khaled, R.; Mahmoud, H.M.; Nassar, H.F.; Abdelrahman, M.M.; Abo El-Ela, F.I.; Taha, M. Computational and Experimental Studies on the Efficient Removal of Diclofenac from Water Using ZnFe-Layered Double Hydroxide as an Environmentally Benign Absorbent. *J. Taiwan Inst. Chem. Eng* . **2019**, *102*, 297–311, doi:10.1016/j.jtice.2019.06.018.
326. Mostafa, S.; Farghali, A.; Khalil, M. Novel Zn-Fe LDH/MWCNT s and Graphene/MWCNTs Nanocomposites Based Potentiometric Sensors for Benzydamine Determination in Biological Fluids and Real Water Samples. *Electroanalysis* **2021**, *33*, doi:10.1002/elan.202060455.
327. Ahmed, A.A.A.; Abdulwahab, A.M.; Talib, Z.A.; Salah, D.; Flaifel, M.H. Magnetic and Optical Properties of Synthesized ZnO–ZnFe2O4 Nanocomposites via Calcined Zn–Fe Layered Double Hydroxide. *Opt. Mater.* **2020**, *108*, 110179, doi:10.1016/j.optmat.2020.110179.
328. Zaher, A.; Taha, M.; Farghali, A.; Mahmoud, R. Zn/Fe LDH as a Clay-like Adsorbent for the Removal of Oxytetracycline from Water: Combining Experimental Results and Molecular Simulations to Understand the Removal Mechanism. *Environ. Sci. Pollut. Res.* **2020**, *27*, doi:10.1007/s11356-020-07750-3.

329. Wu, L.; Zheng, Z.; Pan, F.-S.; Tang, A.; Zhang, G.; Liu, L. Influence of Reaction Temperature on the Controlled Growth of Mg-Al LDH Film. *Int. J. Electrochem. Sci.* **2017**, *12*, 6352–6364, doi:10.20964/2017.07.74.
330. Favvas, E.P.; Kouvelos, E.P.; Papageorgiou, S.K.; Tsanaktsidis, C.G.; Mitropoulos, A.Ch. Characterization of Natural Resin Materials Using Water Adsorption and Various Advanced Techniques. *Appl. Phys. A* **2015**, *119*, 735–743, doi:10.1007/s00339-015-9022-6.
331. Faria, D.L.A. de; Constantino, V.R.L.; Baldwin, K.J.; Batchelder, D.N.; Pinnavaia, T.J.; Chibwe, M. Raman Microspectroscopy of Phthalocyanine Intercalates: Tetrasulphonated Cobalt and Nickel Phthalocyanines in Layered Double Hydroxide. *J. Raman Spectrosc.* **1998**, *29*, 103–108, doi:10.1002/(SICI)1097-4555(199802)29:2<103::AID-JRS199>3.0.CO;2-J.

INDEX

Curriculum Vitae

Mariana Pires Figueiredo

email: mpiresfigueiredo@gmail.com

LinkedIn: www.linkedin.com/in/mpfig

Currículo lattes: http://lattes.cnpq.br/7440615362378556

ORCID: https://orcid.org/0000-0002-9389-2057

Google acadêmico: https://scholar.google.com/citations?user=7xflwVkAAAAJ

Web of Science ResearcherID: AAO-3097-2020

EDUCATION

2016 – 2021 | Institute of Chemistry (USP), Brazil – PhD

- 1st place in the graduate entrance exam

2014 – 2017 | Institute of Chemistry (USP), Brazil - Bachelor's emphasis in Biotechnology

2012 – 2015 | Institute of Chemistry (USP), Brazil - Bachelor's degree in Chemistry

2009 – 2011 | Faculdades Oswaldo Cruz (FOC), Brazil - Bachelor's degree in Chemical Engineering. Interrupted

RESEARCH EXPERIENCE

Mar 2016 – August 2021 | Institute of Chemistry, University of São Paulo (USP), Brazil

PhD student

Supervisor: Professor Vera Regina Leopoldo Constantino

Scholarship: FAPESP, **Grant 2016/13862-9**

- Developed Layered Double Hydroxides (LDH) materials composed by endogenous metals to act as drug carriers for anti-inflammatory drugs and natural products, and performed their compositional and extended structural characterization
- Studied the incorporation of Fe^{3+} cations into LDH structure and the intercalation of the bioactive species into LDH by coprecipitation and ion-exchange methods

- Developed and characterized iron-based LDH/polymer composites aiming multifunctional therapeutics dressings able to sustain drug release and to assist tissues regeneration
- This work, also related to two internships abroad, resulted in 9 scientific publications, where 4 are already published, 4 were submitted to publication, and 1 (a review article) is in writing

Jan 2020 – Jul 2020 | Faculty of Pharmacy, University of Granada (UGR), Spain

Visiting PhD student (internship abroad related to the PhD project in Brazil)

Supervisor: Professor César Viseras

Scholarship: FAPESP, **Grant 2018/22782-4**

- Worked on drug solubility essays
- Evaluated the pharmaceutical performance of membranes aiming multifunctional therapeutic dressings composed by iron-based LDH drug carriers loading naproxenate species and the PEBAX®2533 block copolymer
- *In vitro* naproxen release assays from membranes and composite membranes were performed in Franz cells apparatus and showed a sustained release
- *In vitro* biocompatibility of powered LDH, LDH loading drug, as well as their polymer composites, were assessed by MTT method and showed a synergism between LDH drug carrier and polymer

Feb 2018 – Jul 2018 | Mulhouse Materials Science Institute (IS2M) and Institute for Chemistry and Processes for Energy, the Environment and Health (ICPEES) – University of Strasbourg, France

Visiting PhD student (internship abroad related to the PhD project in Brazil)

Supervisor: Professor Guy Schlatter, Professor Dr. Jocelyne Brendlé and Professor Lionel Limousy

Scholarship: FAPESP, **Grant 2018/22726**

- Developed and characterized polymeric membranes aiming implantable medical devices containing iron-based LDH drug carrier loading naproxenate species
- Electrospinning of poly(L,D lactic acid) and electrospraying of LDH particles were combined to produce membranes with different designs which propitiated easy and effective modulation of the drug release rate

Oct 2014 – Dec 2015 | Institute of Chemistry, University of São Paulo (USP), Brazil

Undergraduate Researcher

Supervisor: Professor Vera Regina Leopoldo Constantino

Scholarship: FAPESP, **Grant 2014/15900-0**

- Synthesized and characterized LDH drug carriers consisting of essential metals loading anti-inflammatory species (*e.g.* naproxenate and mefenamate)
- *In vitro* naproxenate dissolution test aiming oral dosage forms showed a sustained drug release for four days against two hours release from non-encapsulated drug formulation
- Carrier's biocompatibility and participation in collagen neogenesis were attested through *in vivo* intramuscular materials implantation in rats

Jul 2013 – Jul 2014 | Institute of Chemistry, University of São Paulo (USP), Brazil

Undergraduate Researcher

Supervisor: Professor Vera Regina Leopoldo Constantino

- Optimized the synthesis and ion-exchange processes of the layered hexaniobate $K_4Nb_6O_{17}$
- The production time of the acid $H_xK_{4-x}Nb6O_{17}$ phase was reduced from 24 to 6h
- It was verified that protons exchange percentage can be higher than 50 %, an open issue in the literature
- A paper was published in the *Eclética Química Journal*

EMPLOYMENT

Sep 2009 – Mar 2011 | Laboratory of Unit Operations, Faculdades Oswaldo Cruz, São Paulo, Brazil

Technical auxiliary

- Designed experiments and worked on equipment's maintenance
- Assisted experimental classes on U-tube manometers, granulometric analysis, turbulent and laminar flow in tubes, agitation, flocculation, sieving, filtration in filter press, turbines, and pumps
- Expanded the uses of the laboratory to the faculty community and the local community through the development of short courses

TECHNICAL SKILLS

Materials Preparation

- **Polymeric membranes and composites:** application of electrospinning, electrospraying and solvent casting methods
- **Synthesis of solid layered materials:** preparation of inorganic and hybrid organic-inorganic layered solid materials by solid state, coprecipitation, ion-exchange reactions
- **Samples preparation:** preparation of powdered and polymeric films samples for analysis by scanning electron microscopy, atomic emission spectrometry and X-ray diffractometry

Materials Characterization

- **Mechanical tension:** operation of the TA Instruments Discovery HR-3 hybrid rheometer
- **Thermogravimetric analysis:** operation of the TA instrument Q5000 model and of the 202 netzsch thermoanalyser model TGA/DSC 490 PC Luxx coupled to an Aëolos 403 C mass 203 spectrometer
- **Differential scanning calorimeter:** operation of the Q200 instrument from TA Instruments
- **Scanning electron microscopy:** operation of the VEGA3SEM equipment
- ***In vitro* drug release assays:** experience in Franz Cell and oral dissolution apparatus

TEACHING EXPERIENCE

Aug 2020 – Dec 2020 | Inorganic chemistry I – Chemistry of the Elements Course
Teaching Assistant
Corrected reports and activities, and taught in classes for exercises resolution
Jul 2018 – Nov 2018 | Experimental Physical Chemistry Course
Teaching Assistant
Tested experiments for application in the laboratory classes, assisted laboratory classes, corrected reports and activities, and evaluated seminars presented by the students
Jul 2017 – Nov 2017 | General Chemistry Course
Teaching Assistant
Tested experiments for application in laboratory classes, assisted laboratory classes, corrected reports and activities, and taught in classes for exercises resolution

SUPERVISION

Oct 2014 – Sep 2015 | Undergraduate scientific initiation mentor
Developed mentoring and interpersonal skills

May 2020 – Oct 2020 | Co-supervision of undergraduate monograph
Developed mentoring and leadership skills

DEPARTMENT COMMITTEES AND RESPONSABILITY

Aug 2017 – Aug 2018 | Council of the Institute of Chemistry, University of São Paulo (USP), São Paulo, Brazil
Graduate student representative

Aug 2017 – Aug 2018 | Coordination of Graduate Program Committee of the Institute of Chemistry, University of São Paulo (USP), São Paulo, Brazil
Graduate student representative
Apr 2016 – Apr 2017 | Coordination of Graduate Program Committee of the Institute of Chemistry, University of São Paulo (USP), São Paulo, Brazil
Graduate student representative

Apr 2016 – Apr 2017 | Ethics and Human Rights Committee, University of São Paulo (USP), São Paulo, Brazil
Graduate student representative

SCIENTIFIC PUBLICATIONS

Articles in Journals

- **Pires Figueiredo, M.**; Constantino, V.R.L. *K4Nb6O17 layered hexaniobate: revisiting the proton-exchanged reaction*. Eclética Química Journal, **2021**, accepted for publication.
- **Pires Figueiredo, M.**; Leroux, F.; Taviot-Gueho, C.; Constantino,V.R.L. *Influence of iron(III) content in the loading of naproxen into iron-based layered double hydroxides by ion-exchange reaction*. ChemistrySelect, **2021**, submitted.
- **Pires Figueiredo, M.**; Borrego-Sánchez, A.; Pimentel, C.; Pérez de la Luz, A.; Viseras, C.; Sainz-Díaz, C.I. *Experimental and theoretical studies on the intercalation ofnaproxen into the Mg_2Al and Zn_2Al Layered Double Hydroxides by ion-exchange reaction*. Applied Clay Science, **2021**, submitted.
- **Pires Figueiredo, M.**; Lini,B.; García-Villén, F.; Borrego-Sánchez, A.; Rossi,A.; Viseras, C.; Constantino, V.R.L. *Development of an innovative membrane containing layered double hydroxide particles intercalated with natural abietate-type diterpenoid aiming wound dressing***.** Applied Clay Science, **2021**, submitted.
- **Pires Figueiredo, M.**; Duarte, A.; Vendruscolo, V.; Thirouard, R.; Constantino, V.R.; Taviot-Guého, C. *Investigation about iron(III) incorporation into layered double hydroxides: compositional and structural properties of $Mg_2Fe_yAl_{(1-y)}(OH)_6$-Cl and $Zn_2Fe_yAl_{(1-y)}(OH)_6$-Cl.* Journal of Alloys and Compounds, 886, p. 161184, **2021**.
- **Pires Figueiredo, M.**; Borrego-Sánchez, A.; García-Villén, F.; Miele, D.; Rossi, S.; Sandri, G., Viseras, C.; Constantino, V.R.L.C. *Polymer/Iron-Based Layered Double Hydroxides as Multifunctional Wound Dressings.* Pharmaceutics, 12(11), p. 1130, **2020.**
- **Pires Figueiredo, M.**; Layrac, G.; Hebraud, A.; Limousy, L.; Brendle, J.; Constantino, V.R.L.; Schlatter, G. *Design of 3D Multi-Layered Electrospun Membranes Embedding Iron-Based Layered Double Hydroxide for Drug Storage and Control of Sustained Release*. European Polymer Journal, p. 109675, **2020.**
- **Pires Figueiredo, M.**; Cunha, V.R.R.; Leroux, F.; Taviot-Gueho, C.; Nakamae, M.N.; Kang, Y.R.; Souza, R.B.; Martins, A.M.C.R.P.F.; Koh, I.H.J.; Constantino, V.R.L.C. *Iron-Based Layered Double Hydroxide Implants: Potential Drug Delivery Carriers with Tissue Biointegration Promotion and Blood Microcirculation Preservation*. ACS Omega, v. 3, p. 18263, **2018.**
- Cosendey, M.E.E.; **Pires Figueiredo, M.**; Shiguihara, A. L.; Constantino, V.R.L.; Amim Júnior, J. *Thermal and morphological study of poly(acrylamide-co-diallyldimethylammonium chloride)/nanoclay composite films*. Brazilian Journal of Thermal Analysis, v. 7, p. 1, **2018.**

Working Papers

- **Pires Figueiredo, M.**; Eulálio, D.; Constantino, V.R.L. (Review Article) Iron-based Layered Double Hydroxides as biomaterials: advances and challenges.
- **Pires Figueiredo, M.**; Suarez, E.; Taviot-Guého, C.; Leroux, F.; Petrilli, H.; Constantino, V.R.L. One-pot intercalation a natural bioactive diterpenoid into iron-based layered double hydroxides.
- Eulálio, D; **Pires Figueiredo, M.**; Taviot-Gueho,C; Leroux,F; Araújo de Faria, DL; Constantino,VRL). (2021). Hybrid materials based on Layered Hydroxides and the dipeptide N-acetyl-L-cysteine

Book Chapter

- Constantino, V.R.L.; Cunha, V.R.R., Rocha, M.A.; **Pires Figueiredo, M.**; Magri, V.R.; Eulálio, D.; Perotti, G.F.; Bizeto, M.A.; Zambuzzi, W.F.; and Koh, I.H.J. *Layered Double Hydroxides: Characterization, Biocompatibility and Therapeutic Purposes.* Accepted for publication in the book "Series on Chemistry, Energy and the Environment: Progress in Layered Double Hydroxides - From Synthesis to New Applications" published by World Scientific under the general topic of "Chemistry, Energy and the Environment." Edited by Karl Kadish and Roger Guilard as series editors.

Conference Proceedings

- **Pires Figueiredo, M.**; Lini, B.; García-Villén, F; Borrego-Sánchez, A.; Viseras, C.; Constantino, V.R.L. Hidróxidos Duplos Lamelares *Baseados de Fe^{3+} como Carregadores para Ânions Abietato e seus Compósitos Poliméricos como Potenciais Curativos Terapêuticos*
  IV Workshop of Inorganic Chemistry, Federal University of Amazonas, Amazonas, Brazil, **2020**. ISBN 978-65-5941-074-3
- **Pires Figueiredo, M.**; Koh, I.H.J.; Taviot-Gueho, C.; Constantino, V. R. L. *Characterization of Poly(ether-b-amide)/Iron-based Layered Double Hydroxides composites for wound healing purposes*
  XV Brazilian Polymer Conference, XV CBPOL, Brazil, **2019**. ISBN: 978-85-63273-41-3
- **Pires Figueiredo, M.**; Duarte, A.; Taviot-Chého, C.;Leroux, F.; Constantino, V.R.L. *Iron-based Layered double hydroxides as drug carriers: advantages and challenges.* Scientific Research Abstracts – International conference on clay science and technology (Euroclay) 2019, Paris - France.
- **Pires Figueiredo, M.**; Layrac, G.; Hebraud, A.; Limously, L.; Bredle, J.; Constantino, V.R.L.; Schlatter, G. *Poly(lactic acid) / Layered Double Hydroxides membranes: drug storage and release modulation*
  5th Annual meeting of applied clays, **2019**. (available online in https://3f593d6f-0b28-4c7f-b61a-06666c615d91.filesusr.com/ugd/72c0ae_f316e16a79384534b9c0477d5941a5b0.pdf

- **Pires Figueiredo, M.**; Constantino, V.R.L.; Cunha, V.R.R. *Iron-Based Layered Double Hydroxides: Synthesis, Characterization and Insights Upon Pharmacological Applications*
  Scientific Research Abstracts – International clay conference **2017**, Granada - Spain. (Available online in file:///C:/Users/mpire/Downloads/pdfjoiner.pdf)
- **Pires Figueiredo, M.**; Taviot-Gueho, C.; Constantino, V.R.L. *Influence of Fe^{3+} Cations on the Obtainment of Layered Double Hydroxides for Application as Drug Carriers*
  4th Annual meeting of Applied Clays, Teresina, Brazil, **2018**
- **Pires Figueiredo, M.**; Constantino, V.R.L.; Taviot-Gueho, C.; Leroux, F. *Layered Double Hydroxide as a carrier for Natural Bioactive Species*
  III annual meeting of Applied Clays, São Paulo, Brazil, **2017**

REFEREE DUTIE

- **Reviewer for *The Scientific World Journal*, 2021**
- **Reviewer for the *Journal of Tissue Viability*, 2021**
- **27th USP International Scientific and Technological Initiation Symposium (SIICUSP) | University of São Paulo, Brazil, 2019**
  Evaluated research works of undergraduate students competing for the international stage of the competition
- **27th USP International Scientific and Technological Initiation Symposium (SIICUSP) | Institute of Chemistry of the University of São Paulo, Brazil, 2019**
  Evaluated research works of undergraduate students competing in the first stage of the competition
- **26th USP International Scientific and Technological Initiation Symposium (SIICUSP) | Institute of Chemistry of the University of São Paulo, Brazil, 2018**
  Evaluated research works of undergraduate students competing in the first stage of the competition

DEVELOPED AND TAUGHT SHORT COURSES

- **IV Workshop of Inorganic Chemistry, Federal University of Amazonas, Amazonas, Brazil, 2020**
  Title: *Layered Materials: Structure and Properties*

  This short-term course addresses materials such as Clay and Clay minerals, Layered Double Hydroxides (LDH), Layered Niobates, and Graphite/Graphene focusing on their structure and properties. The short-term course also presents methods for modulating properties of different layered materials, as well as materials applications. The authorship of this course is shared with the Ph.D. student Vagner Roberto Magri).

- **Faculdades Oswaldo Cruz Week, São Paulo, Brazil, 2010**
  Title: *Homemade Soap Production* for environmental, chemical and production

engineering students during the event FOC Week 2010 (1st edition)

This short course aims to provide chemical concepts involved in the saponification reaction, *i.e.* in the synthesis of soap from the alkaline hydrolysis of esters or triglycerides, such as cooking oil. In addition, the course consisted also of a practical laboratory class, where students prepare their own soaps. Finally, the course aims to provide a sustainable alternative to the high amount of cooking oil waste, often improperly disposed of in the environment.

- **Faculdades Oswaldo Cruz Open Doors, São Paulo, Brazil, 2010**
  Title: *Homemade Soap Production* for the local public during the event Social Responsibility Day (2nd edition)

  This short course aims to provide a sustainable alternative to the high amount of cooking oil waste, often improperly disposed of in the environment, and also an alternative to turn waste into value-added products, being a possible source of income for people in an economic vulnerability situation. Since the short course aimes at the general public, regardless of education level, it reinforces issues of safety and protection necessary for homemade soap production (contributions: Prof. Germano Ribeiro).

EVENTS ORGANIZATION

- **IV Institutional Congress - The Institute of Chemistry: challenges and perspectives. Institute of Chemistry, USP, Brazil, 2018**
  Coordinated lectures sections directed to the community of graduate students and acted as lecturer
- **Welcome event for graduate courses freshmen. Institute of Chemistry, USP, Brazil, 2017**
  Scheduled meetings and performed a talk
- **3th Annual Meeting of Applied Clays. Institute of Chemistry, USP, Brazil, 2017**
  Worked in the logistics of physical spaces, participated of the creation of the event logo, recaptioned participants and managed kits assembly and distribution
- **33th Chemistry Week. Institute of Chemistry, USP, Brazil, 2017**
  Managed the "Workshop of Chemical Waste" and worked on the reception and registration of the participants

SCIENTIFIC EVENTS PARTICIPATION

Oral Presentations

- **Pires Figueiredo, M.**; Duarte, A.; Taviot-Gueho, C.; Leroux, F.; Constantino, V.R.L. *Iron Based Layered Double Hydroxides as Drug Carriers: Advantages and Challenges*
  International Conference on Clay Science and Technology (EUROCLAY), **2019**

- **Pires Figueiredo, M.**; Layrac, G.; Hebraud, A.; Limously, L.; Bredle, J.; Constantino, V.R.L.; Schlatter, G. *Poly(lactic acid) / Layered Double Hydroxides Membranes: Drug Storage and Release Modulation*
  5th Annual meeting of applied clays, **2019**
- **Pires Figueiredo, M.**; Koh, I.H.J.; Taviot-Gueho, C.; Constantino, V. R. L. *Characterization of Poly(ether-b-amide)/Iron-based Layered Double Hydroxides Composites for Wound Healing Purposes*
  XV Brazilian Polymer Conference, XV CBPOL, Brazil, **2019**

Poster Presentations

- **Pires Figueiredo, M.**; Borrego-Sanchez, A.; Garcia-Villen, F.; Viseras, C.; Constantino, V.R.L. *Hidróxidos Duplos Lamelares Baseados em Fe^{3+} como Carregadores Para Ânions Abietato e Seus Compósitos Poliméricos Como Potenciais Curativos Terapêuticos*
  IV Workshop of Inorganic Chemistry, Federal University of Amazonas, Amazonas, Brazil, **2020**
- **Pires Figueiredo, M.**; Borrego-Sanchez, A.; Garcia-Villen, F.; Viseras, C.; Constantino, V.R.L. *PEBA/Layered Double Hydroxides as Multifunctional Therapeutic Dressings*
  43ª Virtual Annual Meeting, Brazil, **2020**
- **Pires Figueiredo, M.**; Koh, I.H.J.; Taviot-Gueho, C.; Leroux, F.; Constantino, V.R.L.
  Iron-based Layered Double Hydroxides Polymer Composites as Drug Delivery Devices: Preliminary Considerations
  Annual Meeting of the French Group for the Study of Insertion Compounds, Obernai, France, **2019**
- **Pires Figueiredo, M.**; Layrac, G.; Hebraud, A.; Limously, L.; Bredle, J.; Constantino, V.R.L.; Schlatter, G. *Poly(lactic acid) / Layered Double Hydroxides Membranes: Drug Storage and Release Modulation*
  5th Annual meeting of applied clays, Franca, Brazil, **2019**
- **Pires Figueiredo, M.**; Constantino, V.R.L.; Taviot-Gueho, C.; Leroux, F.; Constantino, V.R.L. *Influence of Fe^{3+} Cations on the Obtainment of Layered Double Hydroxides for Application as Drug Carriers*
  4th Annual meeting of Applied Clays, Teresina, Brazil, **2018**
- **Pires Figueiredo, M.**; Constantino, V.R.L.; Cunha, V.R.R. *New iron-based layered double hydroxides: from characterization to pharmacological applications*
  International Clay Conference (ICC), Granada, Spain, **2017**
- **Pires Figueiredo, M.**; Constantino, V.R.L.; Taviot-Gueho, C.; Leroux, F. *Layered Double Hydroxide as a carrier for Natural Bioactive Species*
  III annual meeting of Applied Clays, São Paulo, Brazil, **2017**
- **Pires Figueiredo, M.**; Taviot-Gueho, C.; Leroux, F.; Constantino, V.R.L. *Layered Double Hydroxide as a Carrier for Abietate Species*
  International Symposium on Intercalation Compounds (ISIC), Assisi, Italy, **2017**

- Amim Junior, J.; Machado, L.C.; **Pires Figueiredo, M.**; Shiguihara, A.L.; Constantino, V.R.L. *Thermal Analysis and Spectroscopic Study of PVP Films in the Presence of Sorbitan Derivative Surfactants*
  XIV Brazilian Polymer Conference, XV CBPOL, Brazil, **2017**
- Vendruscolo, V.; **Pires Figueiredo, M.**; Constantino, V.R.L. *New Insights in the Proton-Exchange Properties and Exfoliation of the Layered Potassium Hexaniobate*
  IUPAC - 46th World Chemistry Congress, São Paulo, Brazil, **2017**
- Henriques, R.R.; Celestino, G.G.; **Pires Figueiredo, M.**; Constantino, V.R.L.; Shiguihara, A.L.; Amim Junior, J. *Preparo e Caracterização da Argila Nanomer PGV Moficada com Hidroxietilcelulose Etoxilado Quaternizada.*
  AutoOrg, Florianópolis, Brazil, **2016**
- Consendey, M.E.E.; **Pires Figueiredo, M.**; Constantino, V.R.L.; Shiguihara, A.L.; Amim Junior, J. Caracterização de Filmes dos Compósitos Formados por Poli(acrilamida-co-dialildimetillamônio)/argila
  AutoOrg, Florianópolis, Brazil, **2016**
- **Pires Figueiredo, M.**; Constantino, V.R.L. Reinvestigation of Proton-Exchanged Layered Hexaniobate Phase
  38th Annual Meeting of the Brazilian Chemical Society, Águas de Lindóia, Brazil, **2015**

Invited speaker

- **Pires Figueiredo, M.**, Representing Graduate Students in Committees of the Institute of Chemistry
  IV Institutional Congress - The Institute of Chemistry: challenges and perspectives. University of São Paulo, Brazil, **2017**

Audience

- 1st Regional Meeting of the National Institute of Organic Electronics (INEO) organized by Polo São Paulo at Escola Politécnica (USP), **2018**
- VII Symposium on Biological and Biotechnological Innovations Applied to Health - Science against Time, **2018**
- USP Nanotechnology Conference - Workshop NAP-NN, **2014**

COURSES AND CERTIFICATIONS

- Excel for Business: Intermediate I. Macquarie University, Australia, 2021.
- Excel for Business: Essentials. Macquarie University, Australia, 2021.
- Materials in Dental Health. Hong Kong University, China, 2021.
- Introduction to the Biology of Cancer. Johns Hopkins University, United States of America, **2021**
- What is “the mind” and what is artificial intelligence? University of Colorado, United States of America, **2020**

- Physical Chemistry of Surfactants Applied to Cosmetics. Brazilian Chemical Society - 43ª Virtual Annual Meeting, Brazil, **2020**
- Management of Chemical Waste. Institute of Chemistry of the University of São Paulo, Brazil, **2020**
- Compatibility and storage of chemicals. *Comissão de Desenvolvimento e Treinamento* of the Institute of Chemistry, University of São Paulo, Brazil, **2020**
- Chemical's labeling. *Comissão de Desenvolvimento e Treinamento* of the Institute of Chemistry, University of São Paulo, Brazil, **2020**
- Polymer Physics: Polymeric Networks. XV Brazilian Polymer Conference, XV CBPOL, Brazil, **2019**
- Entrepreneurship: from the design of scientific projects to the validation of essays. Universidade de Franca, UNIFRAN, Brazil, **2019**
- Training in the Use and Management of Laboratory Animals. University of São Paulo, USP, Brazil, **2019**
- Teaching in Graduation Level: First approximation. University of São Paulo, USP, Brazil, **2018**
- High performance liquid chromatography (HPLC) - Basic Theory and Practice, University of São Paulo, Institute of Chemistry, São Paulo, Brazil, **2018**
- Introduction to Rietveld Refinement for Argilominerals, Federal University of Piauí, Teresina, Brazil, **2018**
- Light scattering - Particle size, zeta potential and weight. Brookhaven Instruments, University of São Paulo, Institute of Physics, São Paulo, Brazil, **2017**
- 5th School of SAXS data analysis. Brazilian synchrotron light laboratory, Campinas, Brazil, **2016**
- 1st User Workshop on Coherent X-ray Imaging and Small Angle X-ray Scattering. Brazilian synchrotron light laboratory, Campinas, Brazil, **2016**
- Vibros III – Prof. Oswaldo Sala vibrational spectroscopy course (Raman spectroscopy). University of São Paulo, Institute of Chemistry, São Paulo, Brazil, **2015**
- Thermal analysis of nanomaterials – Netzsch. ABC Federal University, Santo André, Brazil, **2015**
- Vibrational spectroscopy – FT-IR, Escola Senai Mario Amato, São Bernardo do Campo, Brazil, **2009**

HONORS AND AWARDS

- Best Student Oral Presentation in the International Conference on Clay Science and Technology (EUROCLAY) - *Association Internationale Pour L'etude des Argiles (AIPEA)*, Paris, France, **2019**
- Best poster presentation in the *V Reunião Anual de Argilas Aplicadas (RAA)* (V annual meeting of Applied Clays), Franca, Brazil, **2019**
- Student Travel Award 2017 in the 16th International Clay Conference (ICC) - *Association Internationale Pour L'etude des Argiles (AIPEA)*, Granada, Spain, **2017**
- Travel Grant in the 19th International Symposium on Intercalation Compounds (ISIC) (Assisi, Italy), Assisi, Italy, **2017**

BROADCAST INTERVIEWS

02/04/2020 | Topic: The situation of Brazilians who were living in countries most affected by the SARs-CoV2 pandemic in April 2020 and the sanitary restrictions imposed by the governments to contain the pandemic, Novo Dia, TV jornal Interior.

LANGUAGE SKILLS

English | Advanced

Spanish | Intermediate

French | Intermediate

Portuguese | Native Speaker

VOLUNTEER EXPERIENCE

Fev 2014 – Jul 2014 | *Inova Química Júnior*

Member of the group of Projects

Inova Química Júnior is a non-profit organization created and maintained by undergraduate students from the Institute of Chemistry of the University of São Paulo (USP) and provides research and consultancy services for companies and other institutions, as well as organize events for undergraduate students of IQ-USP, such as technical visits to chemical companies, aiming for promoting the entry of students into the labor market.

Apr 2013 – Sep 2013 | Buddha's Light International Association (BLIA)

Tai Chi Chuan e Kung Fu Instructor

Taught Tai Chi Chuan and Kung Fu to kids belonging to the social project "Buddha's Children" (linked to BLIA), which aims to promote art, culture, and education in the local community of Cotia, São Paulo, Brazil.

Jan 2003 – Fev 2007 | Amateur theatre artist, Grupo Teatral Voz da Terra

I was member of the *Associação Voz da Terra* (https://www.ciavozdaterra.art/) that promotes access to the universe of theater and the dissemination of culture in São Tomé das Letras city, Minas Gerais, Brazil.